Western Australian School of Mines
Department of Spatial Sciences

Advanced Satellite Radar Interferometry for Small-Scale Surface Deformation Detection

Ireneusz Baran

This thesis is presented for the Degree of
Doctor of Philosophy
of
Curtin University of Technology

January 2004

Declaration

This thesis contains no material which has been accepted for the award of any other degree or diploma in any university.

To the best of my knowledge and belief this thesis contains no material previously published by any other person except where due acknowledgement has been made.

Signature: ……..……

Date: …….

ABSTRACT

Synthetic aperture radar interferometry (InSAR) is a technique that enables generation of Digital Elevation Models (DEMs) and detection of surface motion at the centimetre level using radar signals transmitted from a satellite or an aeroplane. Deformation observations can be performed due to the fact that surface motion, caused by natural and human activities, generates a local phase shift in the resultant interferogram. The magnitude of surface deformation can be estimated directly as a fraction of the wavelength of the transmitted signal. Moreover, differential InSAR (DInSAR) eliminates the phase signal caused by relief to yield a differential interferogram in which the signature of surface deformation can be seen.

Although InSAR applications are well established, the improvement of the interferometry technique and the quality of its products is highly desirable to further enhance its capabilities. The application of InSAR encounters problems due to noise in the interferometric phase measurement, caused by a number of decorrelation factors. In addition, the interferogram contains biases owing to satellite orbit errors and atmospheric heterogeneity. These factors dramatically reduce the effectiveness of radar interferometry in many applications, and, in particular, compromise detection and analysis of small-scale spatial deformations.

The research presented in this thesis aim to apply radar interferometry processing to detect small-scale surface deformations, improve the quality of the interferometry products, determine the minimum and maximum detectable deformation gradient and enhance the analysis of the interferometric phase image.

The quality of DEM and displacement maps can be improved by various methods at different processing levels. One of the methods is filtering of the interferometric phase. However, while filtering reduces noise in the interferogram, it does not necessarily enhance or recover the signal. Furthermore, the impact of the filter can significantly change the structure of the interferogram. A new adaptive radar interferogram filter has been developed and is presented herein. The filter is based on a modification to the Goldstein radar interferogram filter making the filter parameter dependent on coherence so that incoherent areas are filtered more than

coherent areas. This modification minimises the loss of signal while still reducing the level of noise.

A methodology leading to the creation of a functional model for determining minimum and maximum detectable deformation gradient, in terms of the coherence value, has been developed. The sets of representative deformation models have been simulated and the associated phase from these models has been introduced to real SAR data acquired by ERS-1/2 satellites. A number of cases of surface motion with varying magnitudes and spatial extent have been simulated. In each case, the resultant surface deformation has been compared with the 'true' surface deformation as defined by the deformation model. Based on those observations, the functional model has been developed.

Finally, the extended analysis of the interferometric phase image using a wavelet approach is presented. The ability of a continuous wavelet transform to reveal the content of the wrapped phase interferogram, such as (i) discontinuities, (ii) extent of the deformation signal, and (iii) the magnitude of the deformation signal is examined. The results presented represent a preliminary study revealing the wavelet method as a promising technique for interferometric phase image analysis.

ACKNOWLEDGEMENTS

I would like to express my gratitude to my supervisor, Associate Professor Mike Stewart, for his overall guidance and encouragement throughout my studies. If it were not for his support, I would not have completed my studies. I am indebted to him not only for his scientific supervision, but also for his understanding, help, and friendship. My grateful thanks also go to Professor Peter Lilly and Dr Zbigniew Perski (the University of Silesia, Poland), my associate supervisors, for their continued guidance and help throughout this research.

In addition, my thanks go to all of the friendly team members, both staff and students, of the Western Australian School of Mines and the Western Australian Centre for Geodesy, for their help and advice, particularly to the colleagues who worked with me in the lab, Mr Sten Claessens, Dr Xiaoli Deng, Mr Stuart Gordon and Dr Simon Holmes. My thanks go to staff members Professor Will Featherstone, Dr Michael Kuhn, Dr Jonathan Kirby, Dr Nigel Penna, Mr Luke Shepherd, Professor Ernesto Villaescusa and Dr Eleonora Widzyk-Capehart for their helpful comments and support. Special thanks go to Dr Jadwiga Maciaszek and Professor Jacek Szewczyk (the University of Mining and Metallurgy, Krakow, Poland) for inspiring me to undertake these studies as well as for their help and support.

Thanks are expressed to Mr Bert Kampes (Delft University, the Netherlands), the main developer of the interferometry processing software 'Doris', for providing valuable comments and remarks. In-kind support was also received from the Western Mining Corporation and the European Space Agency who supplied research data. I gratefully acknowledge the scholarship provided by International Postgraduate Research Scholarship (IPRS) scheme, the Western Australian School of Mines and the Department of Spatial Sciences, without which this work could not have been undertaken.

Finally, I would like to thank my family for their continued support, especially to my wife Iwonka, for all her love, help and patience that have helped make this work possible.

TABLE OF CONTENTS

Abstract iii
Acknowledgements v
Table of Contents vi
List of Figures x
List of Tables xviii
List of Acronyms xix
List of Symbols xxi
1 Introduction 1
1. 1 Remote Sensing 1
1.1.1 Satellite Radar Remote Sensing Systems 2
1.1.2 Synthetic Aperture Radar Interferometry 3
1. 2 Application of InSAR for Deformation Monitoring 3
1.2.1 Glacier and Ice Motions 4
1.2.2 Volcano Deformation 4
1.2.3 Earthquake Deformation 5
1.2.4 Landslides 5
1.2.5 Mining Subsidence 6
1. 3 Conventional Deformation Monitoring Techniques 9
1. 4 Aims of this Research 9
1. 5 Thesis Structure 11
2 Synthetic Aperture Radar Interferometry Background 13
2. 1 Radar 13
2. 2 Basic SAR principles 14
2. 3 Factors Affecting Reflectivity 19
2. 4 Topographic Effects on Image Geometry 20
2. 5 Principles of InSAR 21
2. 6 Differential Interferometry 29
2. 7 Interferometric Phase Statistics 31
2.7.1 Coherence 31
2.7.2 The Multilook Phase Difference Distribution 32
2. 8 Sources of Decorrelation 34
2.8.1 Thermal Decorrelation 34

2.8.2 Temporal Decorrelation 35
2.8.3 Geometric Decorrelation 35
2.8.4 Doppler Centroid Decorrelation 37
2.8.5 Processing Induced Decorrelation 37
2. 9 Orbital Error 37
2. 10 Atmospheric Heterogeneities 38
2. 11 Summary 40
3 Study Areas and Research Data 41
3. 1 Location and Characteristic of the Study Areas 41
3.1.1 The Leinster Study Area 41
3.1.2 The Silesia Study Area 44
3. 2 Satellite Radar Data 46
3.2.1 Sensor Characteristics 46
3.2.2 Satellite Data Selection 47
3.2.3 SAR Data Limitations at Leinster Study Area 49
3.2.4 Satellite Orbit Coordinates 49
3. 3 Other Reference Data 50
3.3.1 Digital Elevation Model 50
3.3.2 Meteorological Data 51
3. 4 Summary 53
4 Interferometry Processing and Interferogram Interpretation 54
4. 1 Processing Software and Hardware 54
4. 2 Interferometry Processing 55
4.2.1 Image Reading 56
4.2.2 Satellite Orbit Interpolation 57
4.2.3 Image Coregistration 58
4.2.3.1 Image Offset Estimation 58
4.2.3.2 Offset Vector Modelling 61
4.2.3.3 Resampling 62
4.2.4 Interferometric Product Generation 63
4.2.4.1 Interferogram 63
4.2.4.2 Reference Phase Correction 64
4.2.4.3 Coherence Map 66
4.2.4.4 DEM Radar Coding 68

4.2.4.5 Differential Interferogram 69
4.2.5 Phase Unwrapping 72
4.2.6 Phase to Height Conversion 74
4.2.7 Geocoding 75
4. 3 Interferogram Interpretation of the Leinster Mine Site 76
4. 4 Interferogram Interpretation of the Silesia Study Area 79
4. 5 Limitation and Weaknesses of InSAR 83
4. 6 Summary 84
5 A New Adaptive Radar Interferogram Filter 85
5. 1 Background to the Phase Filtering 85
5.1.1 Filtering in Space Domain 86
5.1.2 Filtering in the Frequency Domain 89
5.1.3 Adaptive Filters 91
5. 2 Goldstein Radar Interferogram Filter 92
5. 3 A New Interferogram Phase Filter 92
5. 4 Data Simulations 95
5.4.1 Simulation of the Interferogram 95
5.4.2 Simulation of the Coherence Map 96
5.4.2.1 Geometrical Decorrelation 96
5.4.2.2 Thermal Decorrelation 98
5.4.2.3 Temporal Decorrelation 98
5.4.2.4 Total Decorrelation 99
5.4.3 Phase Noise Modelling 100
5. 5 Numerical Validation Using Simulated Data Set 102
5. 6 Numerical Validation Using Real Data Set 107
5.6.1 Filter Impact on DEMs 107
5.6.2 Filter Impact on Small-Scale Deformation Detection 110
5. 7 Discussion 113
5. 8 Summary 114
6 A New Functional Model for Determining Minimum and Maximum Detectable Deformation Gradient 115
6. 1 Introduction 115
6. 2 Small-Scale Surface Deformation Simulation 116
6. 3 Interferometry Analysis of the Simulated Deformation Models 119

6. 4 Functional Model 122
6.4.1 Model Parameters 122
6.4.2 Model Determination 125
6.4.3 Validation of the Functional Model 128
6. 5 Discussion 130
6. 6 Summary 132
7 Advanced Interferogram Analysis Using A Wavelet Approach 134
7. 1 The Wavelet Transform 134
7. 2 Wavelet Selection 136
7. 3 Extended Analysis of the Interferogram Using the Halo Wavelet 141
7.3.1 Simulated Interferometric Phase Images 141
7.3.2 Real Interferometric Phase Image 151
7. 4 Discussion 154
7. 5 Summary 156
8 Conclusions and Recommendations 157
8. 1 Summary 157
8. 2 Research Outcomes 158
8.2.1 Application of InSAR for Small-Scale Deformation Detection 158
8.2.2 Improved Adaptive Radar Interferogram Filter 160
8.2.3 New Functional Model for Determining Minimum and Maximum Detectable Deformation Gradient 160
8.2.4 Advanced Interferogram Analysis using a Wavelet Approach 161
8. 3 Recommendations for Future Research 161
REFERENCES 164

LIST OF FIGURES

Figure 1.1 *Interferometric fringes overlaid with underground mine activity (after Stow and Wright, 1997).* 6
Figure 1.2 *Thesis structure.* 12
Figure 2.1 *The electromagnetic spectrum and atmospheric transmission capabilities (after Henderson and Lewis, 1998, p3).* 14
Figure 2.2 *Sensor-target geometry (single pass).* 15
Figure 2.3 *Three-dimensional view of the scanning configuration for a side looking SAR system.* 16
Figure 2.4 *Real antenna forming a synthetic aperture.* 17
Figure 2.5 *Determination of the effective resolution element (adapted from Lillesand and Kiefer, 2000, p623).* 18
Figure 2.6 *Terrain elevation affecting the image geometry. Area (1) indicates foreshortening, (2) layover and (3) shadow. Black strip (3) indicates weak backscattered signal.* 20
Figure 2.7 *Wave phase difference (left-hand side), and addition of two waves (right-hand side).* 21
Figure 2.8 *a (left-hand side) Young's two-slit experiment set up and b (right-hand side) interferometric fringes (adapted from Ghiglia and Pritt (1998, p10 and p13).* 22
Figure 2.9 *Cross-section through Young's experiment set up (adapted from Ghiglia and Pritt; 1998, p11).* 23
Figure 2.10 *Side-looking SAR set up with two radar antennas (perspective view).* 24
Figure 2.11 *Definitions of amplitude and phase.* 24
Figure 2.12 *InSAR geometry in the plane orthogonal to the satellite trajectories.* 26
Figure 2.13 *Interferometry pattern caused by topography.* 29
Figure 2.14 *Two-pass DInSAR geometry in the plane orthogonal to the satellite trajectories.* 30
Figure 2.15 *Probability Density Functions for different multilook (L) values (γ = 0.75, ϕ_0 = 0).* 33
Figure 2.16 *Probability Density Functions for different coherence levels (L=1).* 33
Figure 2.17 *Interferometric image geometry on the Earth's surface.* 35
Figure 2.18 *Geometric decorrelation for ERS-1/2 (after Hanssen, 2001, p103).* 36

Figure 2.19 *a (left-hand side) Two orbits (master and slave) and associated error ellipses, b (right-hand side) radial and across-track errors influencing the baseline vertical (B_v) and horizontal (B_h) components (after Hanssen, 2001, p121).* 38

Figure 3.1 *(a) Location of the Leinster study area and (b) map of crustal elements (cratonic regions) in Western Australia (after Geoscience Australia 2003). The rectangular frame indicates the location of image frame 4164 (relative scale).* 42

Figure 3.2 *(a) Deformation at the Leinster mine site, and different scale of surface cracks observed at (b) 100 m, (c) 200 m, and 400 m from the pit crest.* 43

Figure 3.3 *Aerial photograph showing the Leinster mine site taken in 2001. Sparse vegetation cover over the deformation zone can be seen.* 44

Figure 3.4 *Location of the Silesia study area in Poland (relative scale). The rectangular frame indicates the location of image frame 2592.* 45

Figure 3.5 *DESCW graphical interface.* 48

Figure 3.6 *Meteorological data (relative humidity, temperature, and MSL pressure) 24 hours before and after the image acquisitions AQ-I and AQ-II.* 53

Figure 4.1 *Interferometry processing chain.* 56

Figure 4.2 *Intensity image. The rectangular shape shows the mine site area. Two open pits (P) and the airstrip (A) are clearly visible. The white colour represents high intensity whereas the dark indicates areas of low intensity of the returned signal.* 57

Figure 4.3 *The spectrum of master (a) and slave (c) images before azimuth filtering. Plots (b) and (d) show the overlaying spectrum of both images as a consequence of the spectral filtering.* 60

Figure 4.4 *The absolute error (e) in range direction (estimated offset minus observed offset) for the number of correlation windows.* 62

Figure 4.5 *The absolute error (e) in azimuth direction (estimated offset minus observed offset) for the number of correlation windows.* 62

Figure 4.6 *Phase image with visible flat Earth pattern (pixel size is 20x20 m).* 64

Figure 4.7 *The phase image of the complex interferogram. The reference phase has been subtracted. Visible fringes corresponding to local topography (1 fringe ≈ 41 m)* 65

Figure 4.8 *Estimated coherence map over the Leinster study area. The white colour indicates area where the coherence is high. Simple land classification based on coherence value: (1) valley, (2) bush, (3) hills, and(4) streams.* 67
Figure 4.9 *Wrapped phase of the radar coded 9"DEM.* 68
Figure 4.10 *Differential interferogram. Topographic information has been removed from the complex interferogram using 9"DEM. The rectangular window indicates the mine site location.* 70
Figure 4.11 *Residual fringes due to radial and across-track state vector RMS errors with 95% confidence level that the maximum amount of fringes is less than shown (after Hanssen, 2001, p124).* 71
Figure 4.12 *Reconstructed residual phase trend for the whole frame 4164.* 71
Figure 4.13 *Wrapped phase interferogram – unfiltered.* 73
Figure 4.14 *Wrapped phase interferogram – filtered using Goldstein radar interferogram filter.* 73
Figure 4.15 *Unwrapped phase image. Visible phase variation over the mine site area (rectangular box).* 74
Figure 4.16 *InSAR geometry with respect to the Cartesian (x,y,z) and geodetic (lon,lat,h) reference systems.* 75
Figure 4.17 *DEM derived from InSAR over the Leinster study area.* 76
Figure 4.18 *(a) differential interferogram, (b) coherence map, (c) magnitude-phase mix, and (d) magnitude image of the differential interferogram over the Leinster mine site. Pixel size is 20x20 m.* 78
Figure 4.19 *Coherence map over the Silesia study area.* 80
Figure 4.20 *Interferogram over the Silesia study area with a number of visible fringes corresponding to surface deformation due to underground mining activities.* 80
Figure 4.21 *(a) interferogram, (b) coherence map, (c) magnitude-phase mix, and (d) magnitude image of the interferogram over the part of Silesia study area (Bytom city). Pixel size is 20x20 m.* 81
Figure 4.22 *(a) Interferometric phase image (colour bar in radians) and (b) surface subsidence (colour bar in millimetres). Interferogram was filtered using Goldstein radar interferogram filter.* 82
Figure 4.23 *Three-dimensional model of surface subsidence based on InSAR data (colour bar in millimetres).* 82

Figure 5.1 *Kernel of a mean filter with n x n neighbourhood.* 86
Figure 5.2 *An example convolution of the image (I) with kernel (K) with the boundary effect.* 86
Figure 5.3 *An example convolution of image (I) with kernel (K) with no boundary effect.* 87
Figure 5.4 *(a) Simulated noisy interferogram (120x120 pixels), (b) Interferogram after applying of the mean filter (kernel 3x3).* 88
Figure 5.5 *Interferogram after applying of the median filter (kernel 3x3).* 89
Figure 5.6 *Four types of ideal filters: (a) low-pass filter, (b) high-pass filter, (c) band-pass filter, (d) notch filter.* 91
Figure 5.7 *Phase standard deviation (σ_φ) versus coherence (L indicates the multi-look number).* 93
Figure 5.8 *New adaptive radar interferogram filter diagram.* 94
Figure 5.9 *Digital Elevation Model (pixel size is 50 m).* 95
Figure 5.10 *Simulated wrapped phase interferogram based on DEM. The horizontal line indicates the cross-section location (see Section 5.5).* 96
Figure 5.11 *Map of slopes (in degrees) based on the given DEM.* 97
Figure 5.12 *Simulated coherence map based on geometrical decorrelation.* 98
Figure 5.13 *Simulated coherence map based on fractal surface.* 99
Figure 5.14 *Modelled coherence map based on all decorrelation factors.* 100
Figure 5.15 *Phase standard deviation (σ_φ) based on coherence map (L=1).* 101
Figure 5.16 *Simulated interferometric phase noise.* 101
Figure 5.17 *Histogram showing noise distribution (mean = 0.2, STD = 72.9).* 102
Figure 5.18 *Simulated interferogram with added noise.* 102
Figure 5.19 *A cross-section over the simulated interferogram without noise. Each line shows the phase after filtering for different value of the filter exponent. The phase offset (φ_V) is clearly visible.* 103
Figure 5.20 *±max phase differences versus coherence caused by the Goldstein filter for α = 0.75 and α = 0.5 (bold lines), and the new filter (dashed line).* 104
Figure 5.21 *Filtered wrapped phase of the simulated interferogram using Goldstein radar interferogram filter.* 105
Figure 5.22 *Difference between filtered and not filtered interferogram for Goldstein radar interferogram filter. Remaining features indicate loss of resolution.* ... 105

Figure 5.23 *Filtered wrapped phase of the simulated interferogram using the new filter.* 106

Figure 5.24 *Difference between filtered and not filtered interferogram for the new filter. Remaining features indicate loss of resolution.* 106

Figure 5.25 *Filtered wrapped phase interferogram using the Goldstein radar interferogram filter.* 107

Figure 5.26 *Filtered wrapped phase interferogram using the new filter. Horizontal line indicates cross-section location.* 108

Figure 5.27 *Coherence map.* 108

Figure 5.28 *The cross-section over the unfiltered and filtered wrapped phase interferogram.* 109

Figure 5.29 *The cross-section over the reconstructed surface heights.* 109

Figure 5.30 *(a) Raw interferogram, (b) coherence map, (c) filtered interferogram using the Goldstein (α = 0.9) and (d) the new radar interferogram filter (colour bars in radians).* 110

Figure 5.31 *(a) Surface subsidence reconstructed from the filtered interferogram using the Goldstein and (b) the new radar interferogram filter (colour bars in millimetres). Horizontal line indicates the cross-section location.* 111

Figure 5.32 *The cross-section along the reconstructed surface subsidences.* 111

Figure 5.33 *Loss of deformation signal due to over-filtering. Based on differences between the reconstructed surface subsidences based on filtered interferograms using the new and Goldstein radar interferogram filter (colour bar in millimetres).* 112

Figure 5.34 *New three-dimensional model of surface subsidence (colour bar in millimetres).* 113

Figure 6.1 *Geometry of the simulated deformation model.* 117

Figure 6.2 *Definitions of amplitude and phase for the new image.* 118

Figure 6.3 *Proposed methodology.* 119

Figure 6.4 *Phase images of the simulated models M0 to M6 and their signature after interferometry processing for different coherence value (rows A to E). The left-hand side column shows the corresponding coherence map and the average value over the area.* 120

Figure 6.5 *Phase images of the simulated models N0 to N4 and their signature after interferometry processing for different coherence value (rows A to E). The left-*

hand side column shows the corresponding coherence map and the average value over the area. 121

Figure 6.6 *Phase images of the simulated models O0 to O3 and their signature after interferometry processing for different coherence value (rows A to E). The left-hand side column shows the corresponding coherence map and the average value over the area.* 122

Figure 6.7 *Observations and the linear models:* $d_{min}(\gamma)$ *and* $d_{max}(\gamma)$. 125

Figure 6.8 *The new functional model for determination of the min/max detectable deformation gradient (d) in terms of coherence value (*γ*). This model is valid for the satellites ERS-1/2 (*λ*=5.66 cm) and interferogram resolution 20x20 m.* 127

Figure 6.9 *(a) Deformation fringe over the Silesia study area and (b) the corresponding coherence map (mean coherence over the area is 0.61).* 128

Figure 6.10 *(a) Deformation fringes over the Silesia study area and (b) the corresponding coherence map.* 129

Figure 6.11 *Validation of the functional model. (The three test cases (*K_1, K_{2A}, K_{2B}*) agree with the new functional model).* 130

Figure 7.1 *Basic concept of the wavelet transform (one-dimension case at* y_0*).* 135

Figure 7.2 *(a) Wrapped phase of the 'M4' deformation model and (b) its interferogram signature 'M4E' (colour bars in radian).* 137

Figure 7.3 *The global wavelet power spectrum in comparison to the radially-averaged Fourier power spectrum for (a) Halo, (b) Perrier, (c) Paul, (d) Poisson wavelets. Power spectrum is shown in arbitrary units.* 138

Figure 7.4 *Fourier power spectra of the wavelets (a) Halo, (b) Perrier, (c) Paul, and (d) Poisson at different scale values (s). Scales are shown in meters while the power spectrum is shown in arbitrary units.* 139

Figure 7.5 *The scalograms showing the wavelet power spectra of the interferometric wrapped phase image of the 'M4' deformation model for the (a) Halo, (b) Perrier, (c) Paul, and (d) Poisson wavelet. The horizontal scale bar illustrates the magnitude of the power.* 140

Figure 7.6 *Scalograms of the deformation model 'M4' (left-hand side) and its interferogram signature 'M4E' (right-hand side) indicating a series of cross-*

sections at different scale values using the Halo wavelet. Horizontal scale bar shows the magnitude of the power. 142

Figure 7.7 *The scalograms of the deformation model 'M4' representing two fringes (left-hand side) and its interferogram signature 'M4E' (right-hand side). (A,A') show horizontal cross-section for scale equal to 150 m, (B,B') vertical cross-section along the Azimuth direction (Range = 600 m), and (C,C') corresponding cross-sections along the azimuth direction over the wrapped phase. Numbers 1 to 4 indicates spectral features. The vertical axis illustrates different scale values, while the horizontal scale bar is the magnitude of the power.* 144

Figure 7.8 *The scalograms of the deformation model 'M2' representing half of the fringe (left-hand side) and its interferogram signature 'M2B' (right-hand side). The horizontal scale bar illustrates the magnitude of the wavelet power.*..... 145

Figure 7.9 *The scalograms of the deformation model 'M4' representing two fringes (left-hand side) and its interferogram signature 'M4B' (right-hand side). The horizontal scale bar illustrates the magnitude of the wavelet power.* 146

Figure 7.10 *The scalograms of the deformation model 'M6' representing four fringes (left-hand side) and its interferogram signature 'M6E' (right-hand side). The horizontal scale bar illustrates the magnitude of the wavelet power.* 147

Figure 7.11 *The scalograms of the deformation model 'N2' representing half of the fringe (left-hand side) and its interferogram signature 'N2B' (right-hand side). The horizontal scale bar illustrates the magnitude of the wavelet power.*..... 148

Figure 7.12 *The scalograms of the deformation model 'N2' representing half of the fringe (left-hand side) and its interferogram signature 'N2E' (right-hand side). The horizontal scale bar illustrates the magnitude of the wavelet power.*..... 149

Figure 7.13 *The scalograms of the deformation model 'N4' representing two fringes (left-hand side) and its interferogram signature 'N4E' (right-hand side). The horizontal scale bar illustrates the magnitude of the wavelet power.* 150

Figure 7.14 *Interferometric phase images extracted from wrapped phase interferogram over Silesia study area. (a) Represents two interferometric fringes and (b) one interferometric fringe (colour bars in radian).* 151

Figure 7.15 *The scalogram of the real phase image representing four fringes (Figure 6.10.a) related to surface subsidence over Silesia study area. The horizontal scale bar illustrates the magnitude of the wavelet power.* 152

Figure 7.16 *The scalogram of the real phase image representing two fringes (Figure 7.14.a) related to surface subsidence over Silesia study area. The horizontal scale bar illustrates the magnitude of the wavelet power.* 153

Figure 7.17 *The scalogram of the real phase image representing one fringe (Figure 7.14.b) related to surface subsidence over Silesia study area. The horizontal scale bar illustrates the magnitude of the wavelet power.* 154

LIST OF TABLES

Table 3.1 *ERS-1/2 SAR sensor parameters (after Franceschetti and Lanari, 1999, p11)* 47
Table 3.2 *Satellite data for Leinster study area (SLC images)* 48
Table 3.3 *Satellite data for Silesia study area (SLC images)* 49
Table 3.4 *Daily Rainfall data at Leinster study area (AQ-I)* 52
Table 3.5 *Daily Rainfall data at Leinster study area (AQ-II)* 52
Table 4.1 *UNIX workstation specifications* 55
Table 5.1 *Geometrical decorrelation simulation parameters* 97
Table 5.2 *Filter parameters* 103
Table 6.1 *Deformation models parameters* 117
Table 6.2 *Model parameters (observations)* 124

LIST OF ACRONYMS

9”DEM	9-second Digital Elevation Model
AHD	Australian Height Datum
AMI	Active Microwave Instrument
ATSR-2	Along-Track Scanning Radiometer
CR	Corner Reflector
Delft	Delft University of Technology, Delft, the Netherlands
DEM	Digital Elevation Model
DEOS	Delft Institute for Earth-Oriented Space Research
DGM-E04	Delft Gravity Model
DIDP	Double Interpolation and Double Prediction
DInSAR	Differential Synthetic Aperture Radar Interferometry
EGM96	Earth Geopotential Model 1996
ESA	European Space Agency
ERS-1, ERS-2	European Remote Sensing Satellites
FDC	Doppler Centroid Frequency
GPS	Global Positioning System
GDA94	Geodetic Datum of Australia 1994
GOME	Global Ozone Monitoring Experiment
InSAR	Synthetic Aperture Radar Interferometry
LRR	Laser Retroreflectors
MSL	Mean Sea Level
ODRs	Orbital Data Records
PAF	Processing and Archiving Centre
PRARE	Precise Range and Range-rate Equipment
PS	Permanent Scatterer
PRF	Pulse Repetition Frequency
RA	Radar Altimeter
RMS	Root Mean Square
SAR	Synthetic Aperture Radar
SIR	Shuttle Imaging Radar
SLR	Satellite Laser Ranging
SLC	Single Look Complex Image

SNR	Signal-to-Noise Ratio
UT	Universal Time

LIST OF SYMBOLS

$B_{\perp}$	Perpendicular baseline
$B_{\perp}^{\circ}$	Perpendicular baseline for the resolution pixel on the reference surface
$B_{\perp,C}$	Critical perpendicular baseline
$B_{\|\|}$	Parallel baseline (path difference)
c	Speed of light
E	Image intensity
H	Satellite altitude
N	Geoid-ellipsoid separation (geoid height)
R_i	Slant range distance from the satellite to the ground
λ	Wavelength
f_{DC}^{M}, f_{DC}^{S}	Doppler centroid frequency for master and slave image
α	Baseline orientation angle
I	Complex interferogram
D, L	Radar antenna dimensions
d	Deformation gradient
d_x	Maximum detectable deformation gradient (old definition)
d_{min}	Minimum detectable deformation gradient (new definition)
d_{max}	Maximum detectable deformation gradient (new definition)
h	Deformation magnitude
α_t	Terrain slope angle
B_A	Azimuth bandwidth
B_w	Range bandwidth
γ	Coherence absolute value
γ_{total}	Total decorrelation value
γ_{geom}	Geometric decorrelation
$\gamma_{temporal}$	Temporal decorrelation
$\gamma_{thermal}$	Thermal decorrelation
γ_{FDC}	Doppler centroid decorrelation
γ_{proc}	Processing induced decorrelation
τ	Pulse duration of the transmitted signal

f	Frequency
θ	Look angle
θ_{inc}	Incidence angle
θ_0	Nominal incidence angle on the ellipsoid
P_S	Power spectrum of the signal
ps	Pixel size
P_N	Power spectrum of the noise
Δr_g	Ground range resolution
s	Wavelet scale ('width')
S_M, S_S	Master and slave satellite respectively
S_m, S_n	Slope values
$O^C_{A,R}$	Coarse offset between two registered images
$\phi^M_{i,j}, \phi^S_{i,j}, \phi^R_{i,j}, \phi^I_{i,j}$	The Phase Value of the Master, Slave, Reference and Interferogram at pixel location i,j.
$W(\vec{b}, s)$	Wavelet coefficients
$\Psi(\vec{b}, s)$	Wavelet function
Δr	The slant range resolution
ΔA	Azimuth resolution
Ω	Decision value

1 INTRODUCTION

Prior to commencing into an investigation of the use of satellite-borne radar imaging to detect and research small-scale surface deformation, a review of the origin of remote sensing, radar imaging and the Synthetic Aperture Radar Interferometry (InSAR) is presented in this chapter. Given an introduction to this technology and its application, the scope and hypothesis of this dissertation are laid out.

1. 1 Remote Sensing

The term *remote sensing* was established in the 1960s by geographers at the US Office of Naval Research and is used to denote images acquired from aircraft and artificial satellites (Curran, 1985, p2). Providing an accurate and comprehensive definition of remote sensing is very difficult and varies depending on the degree of complexity used. Different definitions of remote sensing can be found, for instance in Lillesand and Kiefer (2000, p1) and Lintz and Simonett (1976, p1). However, having taken the similarities between these definitions into account, remote sensing can be defined as a technique that involves acquisition of information about an object without being in direct contact with it. Remote sensing has a long history that Harris (1987, pp2-4) divides into five different stages. However, in the past decade, a very dynamic development of both airborne and satellite remote sensors has been experienced. A variety of sensors carried on board satellites and operating at different electromagnetic spectra have provided a wide range of scientific data, such as optical and radar images of the Earth's surface.

Based on the sensor's characteristics, satellite remote sensing systems can be divided into 'active' and 'passive' systems (Legg, 1994, p17). Passive systems use an external source of energy, such as solar illumination from the surface of the Earth. These record reflected or emitted electromagnetic radiation, mostly in the optical spectrum, which extends from 0.3 μm to 14 μm and includes ultra violet (UV), visible, near visible and thermal infrared wavelengths (Lillesand and Kiefer, 2000,

pp373-374). Active systems use their own energy source, which is first transmitted to the object (*e.g.* the Earth) and then the backscattered signal is detected and processed. The active system usually employs electromagnetic energy in the microwave part of the spectrum. The advantage of microwave sensing is its independence of weather conditions and daylight. Since the radar system operates in the microwave portion of the electromagnetic spectrum, it can provide information that cannot be obtained by visible and infrared images. In addition, radar imaging achieves the quality and resolution comparable to the traditional optical imagery.

1.1.1 Satellite Radar Remote Sensing Systems

Satellite remote sensing is an extension of airborne remote sensing which was established in the 1960s and 1970s. The first space borne radar system *Seasat* was launched in 1978 and was primarily dedicated to ocean studies. Although its mission finished prematurely after 100 days of operation, the Synthetic Aperture Radar (SAR) imagery was impressive, and enabled SAR systems to be included in numerous satellite missions, such as Shuttle Imaging Radar (SIR) and the Soviet *Cosmos* launched in the 1980s. In the early 1990s, three other radar satellites were launched: *Almaz-1* by the former Soviet Union, *ERS-1* by the European Space Agency (ESA), and *JERS-1* by Japan. In 1995, Canada's Radarsat and ESA's *ERS-2* followed (Campbell, 1996, pp228-235).

All remote sensing satellites have a set of instruments for observing the Earth's surface and its atmosphere. Each system has various sensors and supporting instrumentation necessary to receive operating instructions from the ground control stations. The design, construction and launch of a new satellite span several years. For example, the ESA ERS-1 satellite, launched in 1991, was mainly constructed before 1986, and most of the electronics date back to the early 1980s (Legg, 1994, pp11-13). For more details and different sensor parameters the reader is referred to Franceschetti and Lanari (1999, pp4-13).

The new Earth observation satellite programs, such as ENVISAT, developed by ESA and launched in March 2002 (ESA Service, 2002), and the proposed future programs, such as LIGHTSAR (USA), ECHO (USA), COSMO-SKYMED (Italy), and SMART

SAR (Germany), aim to reduce mission and operational costs of the satellite radar remote systems (Desnos *et al.*, 2000; Louet and Bruzzi, 1999).

1.1.2 Synthetic Aperture Radar Interferometry

Synthetic Aperture Radar Interferometry is a valuable technique for creating Digital Elevation Models (DEM) and deformation detection studies based on remotely sensed data.

Various terms are used to describe the InSAR technique and its applications. In this thesis, the term InSAR or radar interferometry denotes a combination of two or more SAR images covering the same area to obtain accurate surface topography or deformation information (Rees, 1999, p101). The term Differential Synthetic Aperture Radar Interferometry (DInSAR) is used to describe the technique that provides accurate surface deformation by eliminating topographic effects from an InSAR interferogram (Guarnieri and Rocca, 1999).

1. 2 Application of InSAR for Deformation Monitoring

InSAR technology was originally developed for military purposes. Nowadays, it is available and widely used for a variety of civilian applications (Capes, 1999; Ehrismann *et al.*, 1999). Since the late 1980s, many applications of radar interferometry have been developed, including the observation of ground motion over agricultural areas by Gabriel *et al.* (1989), the creation of high accuracy DEM (Zebker and Goldstein, 1986), and deformation monitoring of the Earth's crust with millimetre per year accuracy at very dense spatial sampling (Strozzi *et al.*, 2000). The following paragraphs review the application of InSAR to many forms of surface deformation that can be categorised as follows: (i) glacier and ice motions, (ii) volcano deformations, (iii) earthquake deformation, (iv) landslides and (v) mining subsidence.

1.2.1 Glacier and Ice Motions

On account of the inaccessibility of some terrain (*e.g.* Antarctica), satellite radar interferometry is a valuable technique that enables measurements of glacier and ice motions. According to an earlier study conducted by Goldstein *et al.* (1993), glacier motions and sea ice dynamics can be studied and monitored using radar interferometry. Madsen *et al.* (1999) state that such monitoring is very important for assessing glacier mass transport and changes in glacier volume, which may have significant implications for global climate change assessment. However, the satellite repeat interval (35 days for the ERS-1/2 satellites) has been found to be the major factor limiting the interferometry application in cases of high glacier velocity. Some further results of satellite radar interferometry application for glacier and ice motion measurements are demonstrated by Haarpainter *et al.* (2000), Hall (1998), Rack *et al.* (1998), Dammert *et al.* (1997), Mohr and Madsen (1996), and Cumming *et al.* (1996).

1.2.2 Volcano Deformation

Massonnet *et al.* (1995) evaluated space born radar interferometry as a highly effective method for volcano deformation detection studies. It was successfully demonstrated that radar images, acquired by the ERS-1 satellite, could be applied to detect the inflation of volcanic edifices that usually precede eruptions. Further studies conducted on the Mt. Etna volcano also showed the suitability of the InSAR for volcano eruption monitoring (Sansosti *et al.*, 1998; Lanari *et al.*, 1998). Amelung *et al.* (2000) studied deformation of eight volcanoes on the Galápagos Islands during 1992-99, using radar interferometry. The results of this investigation provided displacement maps of volcanoes, indicating uplift rates ranging from several millimetres up to 0.9 m per year. Further information about the application of InSAR for volcanic deformation monitoring may be found in Dzurisin (2003), Mann *et al*. (2002), Tokunaga and Thuy (2000), Vadon and Massonnet (2000), Amelung *et al.* (1999a), Kobayashi *et al.* (1999), and Berardino *et al.* (1999). In summary, these studies show that measurements of pre-eruptive, co-eruptive and post-eruptive volcano deformation using radar interferometry can be performed.

1.2.3 Earthquake Deformation

One of the first applications of InSAR technology for earthquake motion detection was carried out in Landers, California in 1992 (Massonnet *et al.*, 1993). The observed deformations were evaluated against surveying measurements, demonstrating the high accuracy of InSAR technology for earthquake related motion monitoring. Furthermore, the researchers indicated the advantages of the InSAR technique over standard geodetic techniques for ground deformation monitoring, due to the very dense spatial sampling and its high vertical accuracy. In addition, it is evident that the InSAR technique is becoming a new geodetic tool, helping to better understand earthquake origins and their characteristics. More information about the application of InSAR for earthquake deformation monitoring can be found in Amelung and Bell (2003), Zeng and Ohkura (2000), Stramondo *et al.* (1999), Feigl *et al.* (1999), Peltzer *et al.* (1996), and Peltzer and Rosen (1995).

1.2.4 Landslides

The application of radar interferometry to monitor natural ground displacement phenomena with the accuracy required for landslide monitoring was demonstrated by Fruneau *et al.* (1996). In this study, a small spatial extent (800x800 m) with a high topographic variability was examined and the model of surface displacements was constructed. Rott and Siegel (1999) successfully applied satellite radar interferometry to monitor mass movements and to detect hazard zones in the Austrian Alps. Studies of InSAR for land subsidence mapping in urban areas also show high capability to detect, monitor and quantify subtle ground deformations over a specific period of time and over vast areas (Berardino *et al.*, 2000; Wegmüller *et al.*, 1999, 1998; Fruneau *et al.*, 1999; Strozzi and Wegmüller, 1999; Haynes *et al.*, 1997). Refice *et al.* (2000), however, state that the application of InSAR to slope stability studies of a small spatial extent is strongly limited by weather conditions. Some further results of InSAR application for subsidence monitoring are demonstrated by Schmidt and Bürgmann (2003), Nakagawa *et al.* (2000), Yonezawa and Takeuchi (2000), Amelung *et al.* (1999b), and Cohen *et al.* (1998).

1.2.5 Mining Subsidence

Subsidence and its effects on surface-level structures poses serious problems for the development and maintenance of building stock and other human-made structures, such as roads and railway lines (Wodyński and Kocot, 2000). Therefore, the effective protection and management of mining induced deformation is one of the main concerns for the mining industry as well as for local communities. First attempts to apply InSAR for mining subsidence monitoring proved the method's viability to measure such a deformation with vertical accuracy of a few millimetres (Stow *et al.*, 1999; Stow and Wright, 1997; Stow, 1996). According to this research, remotely acquired SAR images have the potential to improve subsidence-modelling accuracy by increasing the quantity and quality of collected data, as compared to the conventional surveying techniques. The achieved interferogram (Figure 1.1) shows two distinctive concentric fringe features indicating subsidence aligning with areas of underground mining activity over the Selby coalfield, UK. Geotechnical interpretation of the fringe features was possible and the associated subsidence was established as between 3 and 12 cm.

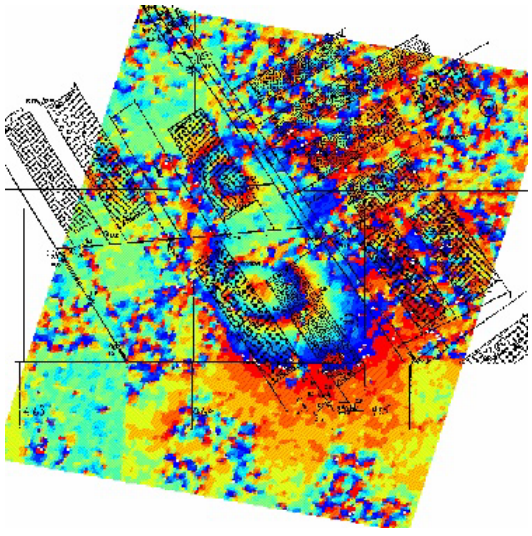

Figure 1.1 *Interferometric fringes overlaid with underground mine activity (after Stow and Wright, 1997).*

This research shows that mining subsidence can be successfully detected using the 35-day repeat SAR data and radar interferometry techniques. Furthermore, researchers indicate that the balance between adopting a useable temporal baseline (in terms of interferogram coherence) and allowing a suitable length of time to lapse

for a measurable amount of subsidence to occur needs to be found. In addition, agricultural land and unfavourable weather conditions during data acquisition considerably increase the interferometric phase noise and reduce the ability of radar interferometry for deformation detection studies.

Timmen *et al.* (1996) assessed the ability of InSAR and its accuracy for surface deformation monitoring over a uranium ore mining site in Thuringia, Germany. In principle, the reference network of specially developed corner reflectors (CR) was deployed and measured using terrestrial geodetic techniques. Than, the interferometric phase images were investigated with the objective of detecting the CR movements. It was demonstrated that the sub-centimetre accuracy of InSAR derived data in surface motion detection is achievable under favourable environmental conditions. Moreover, Timmen *et al.* (1996) report that significant change in weather and seasonal conditions between two epochs destroyed the coherence and provided no result.

The application of InSAR for deformation monitoring undertaken in 1997 by Perski (1998) confirms the usefulness of this technique in environmental monitoring as well as in detecting the dynamics of land subsidence caused by underground mining activities over the Upper Silesian Coal Basin, Poland. Perski indicated the negative aspect of high magnitude mining activities in this region, which is one of Europe's biggest mining centres. Changes of topography and hydrography as well as damage to buildings and other structures due to mining in this region are significant. The results of his experiment showed that mining-related surface deformation could be monitored with good quality and quantity using ERS-1/2 satellites data and a 35-day repeat cycle. Furthermore, using InSAR data, Perski derived a complete map of terrain deformation over the Upper Silesia. Moreover, the high accuracy of this map was demonstrated by its agreement with the ground control points measured using conventional surveying techniques (Perski, 2000, 1999; Perski and Jura, 1999).

A slow and local phenomenon of subsidence caused by underground coal mining has been observed near Gardanne in France (Carnec and Delacourt, 1999). The series of radar images acquired by both ERS-1 and ERS-2 satellites were processed and the achieved interferogram demonstrated the ability of radar interferometry to detect

surface subsidence. Validation of the interferometry data with levelling observations showed a high level of agreement.

A similar study demonstrated by Wegmüller *et al.* (2000) showed that radar interferometry has substantial potential for monitoring deformation caused by subsurface mining activities. However, Wegmüller *et al.* (2000) indicate that the main limitation of InSAR is the temporal decorrelation, which does not allow the estimation of surface deformation in forested and most agricultural areas.

As indicated by Ge *et al.* (2001a, 2001b, 2001c, 2000a, 2000b), a network of GPS points is not sufficiently dense to monitor surface subsidence caused by underground mining as well as the crustal deformation due to an active seismic fault or volcanic activity. They proposed the integrated GPS and InSAR called "Double Interpolation and Double Prediction" (DIDP) method to improve the monitoring of surface deformation. In the proposed DIDP approach, the atmospheric corrections and the satellite orbit errors are obtained from GPS measurements and incorporated in the InSAR process to improve the accuracy of the ground displacement measurements. The InSAR data however, give the high-density map of physical phenomena being studied.

According to Popiołek *et al.* (2002), the application of InSAR for deformation monitoring can be potentially extended over surface mining activities to examine the following dynamic phenomena: (i) landslides and motions of excavation slopes and floor, (ii) the mass movement of waste dumps, (iii) depression and deformation due to drainage and (iv) mining progress.

In conclusion, many types of surface deformation can be monitored using the InSAR technique. However, the horizontal resolution is limited by the size of the resolution pixel (20 m in case of satellite ERS-1/2) whereas the vertical accuracy is much higher (up to a few millimetres). In addition, while the weather conditions do not prevent a radar system from acquiring an image, the changes in weather conditions from times of image acquisition reduce the applicability of radar interferometry for deformation detection studies.

1. 3 Conventional Deformation Monitoring Techniques

Conventional surface deformation monitoring techniques can be divided into two categories, namely surveying and geotechnical (Ding *et al.*, 1998, pp3-12; Thompson *et al.*, 1993). For the surveying techniques, survey instruments, such as levels, theodolites, total stations, GPS receivers, and photogrammetric cameras, are usually employed to collect data. Surface deformation monitoring systems employ a levelling line or mesh of points to obtain vertical movement. Currently, highly accurate surveying systems are able to determine all three spatial coordinates (x,y,z), by establishing the positions of the surveyed targets in relation to a stable set of reference points. The indication of movement of the coordinated targets can be determined by comparing the coordinates from at least two different survey epochs. Surveying techniques can be used to determine the absolute position and positional changes of any point on the surface with respect to the reference point(s).

Geotechnical monitoring techniques usually employ instrumentation to measure deformation or displacement with a very high accuracy over a relatively small spatial extent. Common geotechnical instrumentations used in small-scale deformation surveys include (i) extensometers, (ii) inclinometers, piezometers, (iii) crack meters, and (iv) microseismic geophones, which are directly attached to the deforming body (Ding *et al.*, 1998, pp 12-14; Logan *et al.*, 1993; Loubser, 1993).

Surveying and geotechnical monitoring systems are usually established in areas where the likelihood of deformation is very high. The main advantage of the surveying and geotechnical monitoring techniques used for deformation control is the high accuracy of measurements. However, major disadvantages include the complicated instrumentation, the small number of observations obtained, poor spatial resolution and high cost of surveys.

1. 4 Aims of this Research

Although InSAR applications are well established, the improvement of the interferometry technique and the quality of its products is desirable to further enhance its capabilities. The aim of this research is to apply, test and enhance the radar interferometry technique to determine surface deformation, with the major

focus on small-scale surface deformation such as that associated with mining activities.

In this thesis, three research problems and objectives have been identified. First, radar interferometry encounters problems due to noise in the interferometric phase measurement, caused by a number of decorrelation factors. Moreover, the interferogram contains biases due to satellite orbit errors and atmospheric heterogeneity. These factors dramatically reduce the capabilities of radar interferometry in many applications and, in particular, compromise detection and the analysis of spatially small-scale surface deformations. By filtering the interferometric phase, the quality of deformation maps can be improved. However, while filtering reduces noise in the interferogram it reduces the deformation signal.

Secondly, the following problem is related to the radar interferometry limits. What is the minimum and maximum deformation gradient that the radar interferometry can detect? While Massonnet and Feigl (1998) defined the maximum detectable deformation gradient, they did not include the effects of decorrelation that are responsible for the phase noise. Therefore, such a definition does not describe the problem realistically.

Finally, as the analyses of the interferometric phase are based on the visual inspection of the phase image (interferogram), the question emerges whether the interpretation of the interferometric information could be extended. If this is possible, the additional information, invisible to the human eye, could be revealed. Moreover, the deformation detection could be automated.

The key objectives of this research may therefore be summarised as follows:

- Determine suitability of InSAR for small-scale surface deformation detection;
- Reduce the interferometric phase noise via implementation of a developed filtering algorithm;
- Develop a functional model for determining the minimum and maximum detectable deformation gradient accounting for the effects of decorrelation; and
- Advanced analysis of the interferometric phase image;

1. 5 Thesis Structure

This thesis comprises eight chapters (Figure 1.2). Chapter 1 has considered the concept of remote sensing, InSAR origin, and reviewed the application of radar interferometry for deformation detection, focusing on small-scale deformation detection (*e.g.* mining related surface subsidence). Furthermore, the objectives of the research have been defined. Chapter 2 provides an overview of the background and theory required for DEM generation and surface deformation detection using the satellite radar interferometry technique. It discusses radar, synthetic aperture radar and interferometry principles followed by sources of errors. Chapter 3 presents the case study areas and describes the deformation characteristics of the areas to be analysed using radar interferometry. Moreover, the key characteristics of the satellite and reference data are outlined. The sequences of the processing steps necessary to create a repeat pass interferogram and a differential interferogram from SAR data are given and discussed in Chapter 4. In this chapter, the interferometric data from the two study areas are presented and analysed in terms of small-scale surface deformation detection. In addition, the problems associated with interferometry processing as well as interferogram interpretation have been identified. A new adaptive radar interferogram filter that minimises the loss of signal while still reducing the level of noise is proposed in Chapter 5. The validation of the new filter is undertaken on simulated and real data. In Chapter 6, a functional model for determining the minimum and maximum detectable deformation gradient in terms of the coherence value is developed. The extended analysis of the interferometric phase image using the wavelet transform is presented in Chapter 7. Finally, Chapter 8 concludes with a summary of the major findings of this research and includes recommendations for future work.

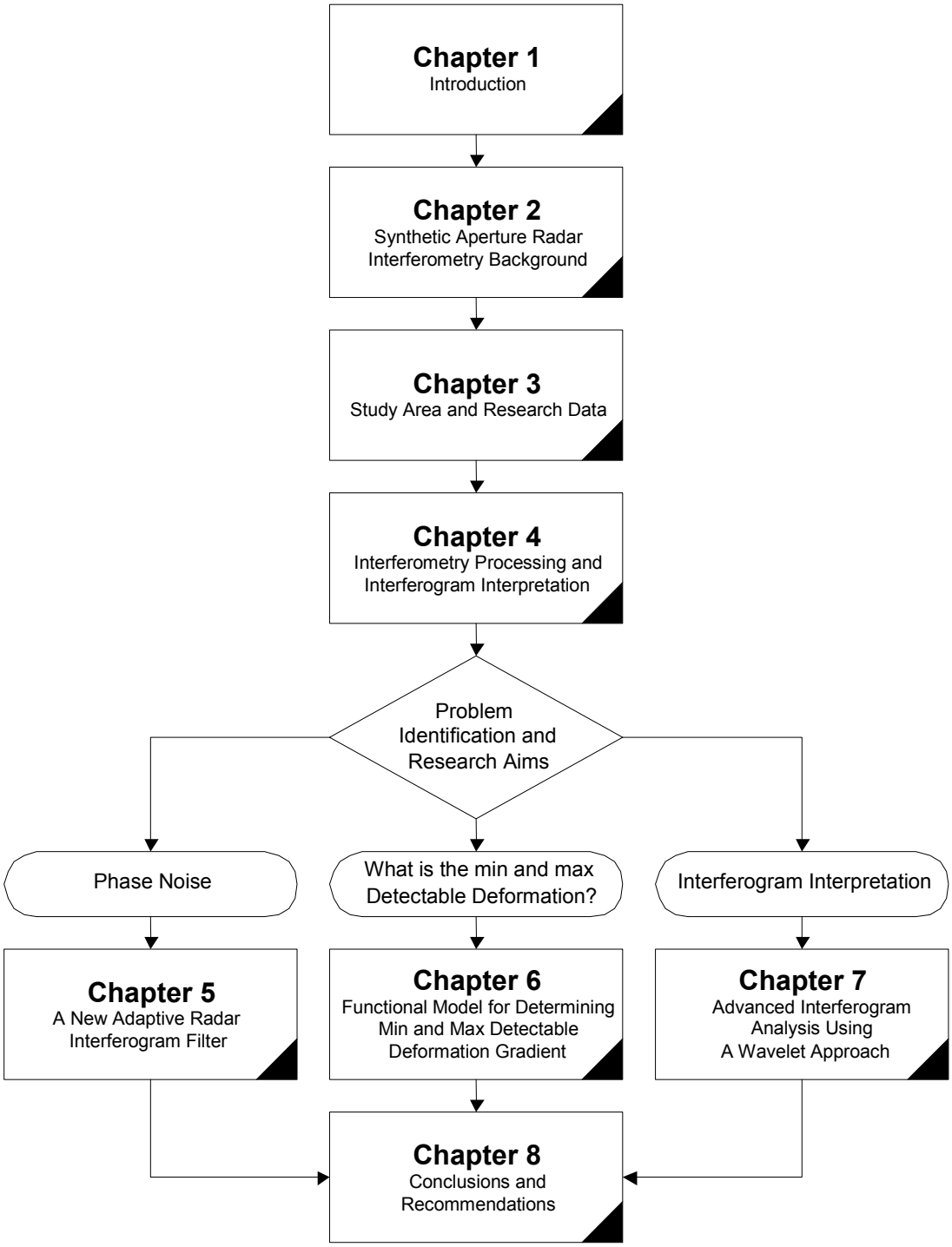

Figure 1.2 *Thesis structure.*

2 SYNTHETIC APERTURE RADAR INTERFEROMETRY BACKGROUND

This chapter presents a condensed overview of the background and theory required for understanding the InSAR technique. The theory presented here focuses on the definition of the principles of radar, synthetic aperture radar, and interferometry. Furthermore, the decorrelation effects as well as the satellite orbit errors and atmospheric heterogeneity responsible for increasing noise in the interferogram phase measurement are identified and discussed. Moreover, this chapter provides the basic theory necessary for simulations of the interferometric data undertaken in Chapter 5 and Chapter 6. For further details and background on SAR and radar interferometry, the reader is referred to the many textbooks available (*e.g.* Fitch, 1988; Franceschetti and Lanari, 1999; and Hanssen, 2001).

2. 1 Radar

As mentioned in the introductory chapter, radar is an example of an active image technology in which the sensor provides its own source of illumination. Radar, an acronym for Radio Detection and Ranging, refers to a technique and instrumentation that operate in the microwave portion of the electromagnetic spectrum, and which penetrate cloud cover and other atmospheric particles due to relatively long wavelength (Figure 2.1). Such a bandwidth increases the signal penetration capacity, which gives radar a strong advantage over optical sensors.

In many ways radar images resemble those from optical systems. However, optical imagery shows the terrain reflectivity response to visible light, whereas radar imagery shows the terrain response to radio waves. Thus, the response of objects and terrain to microwave radiation can be vastly different from optical waves.

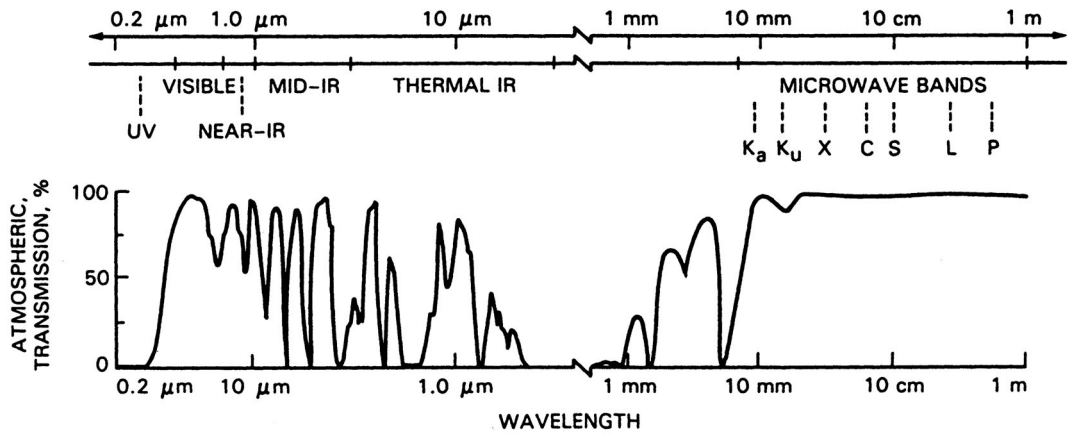

Figure 2.1 *The electromagnetic spectrum and atmospheric transmission capabilities (after Henderson and Lewis, 1998, p3).*

A radar instrument (antenna) emits a series of electromagnetic pulses and detects the reflections of these pulses from objects in its line of sight. The strength of the signal and the two-way travel time of the pulse are stored by the radar system. The backscatter amplitudes define the pixel brightness. The time delays and the speed of light are used to determine the range to the detected object (Fitch, 1988, pp1-18).

2. 2 Basic SAR principles

The SAR system generates a radar image by scanning the Earth's surface from an aircraft or spacecraft platform using an attached radar antenna. As the radar antenna moves at uniform speed (v) and altitude (H) along the flight path, it transmits at look angle (θ) the microwave pulses along direction (R) which is orthogonal to the direction of the flight path (Figure 2.2). Each pulse is shaped into a linear frequency modulated and transmitted at the pulse repetition frequency (PRF) towards the Earth. The same antenna receives the backscattered echoes reflected from the terrain. The signal is than stored and processed to synthesize a large aperture. Finally, the data are formed as the high-resolution image of the terrain response to the radio signals (Bamler and Schättler, 1993).

The transmitted and received signals are coherent. This means that the transmitted signals are generated from a stable local oscillator and can be referenced in time and space to a common point. The received signal has a precisely measurable time delay, which is dependent on the distance to the ground, and has a precisely measurable

phase difference in relation to the local reference phase (oscillator phase). The coherence allows for synthesising the effect of the large aperture (antenna) that permits imaging at a much higher resolution than could be achieved with the physically small antenna (Ghiglia and Pritt, 1998, pp8; Olmsted, 1993).

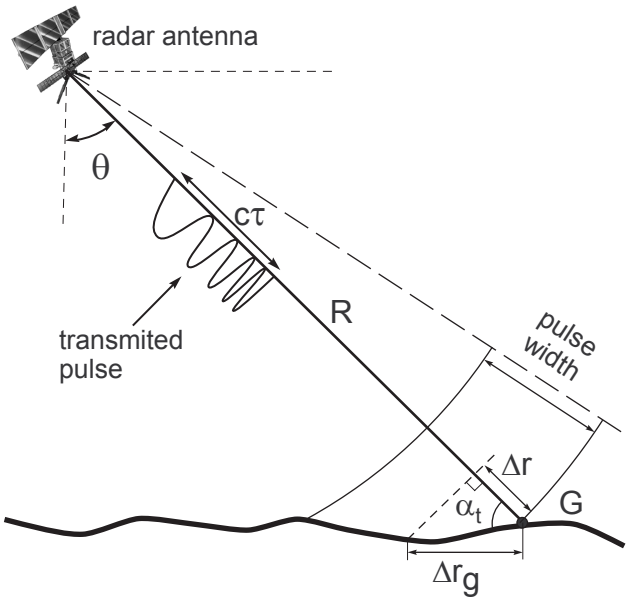

Figure 2.2 *Sensor-target geometry (single pass).*

The SAR imaging configuration determines the coordinate system in which the *azimuth* coordinate indicates position along the flight path, whereas the *range* refers to the position along the line perpendicular to the flight direction. The range coordinate is associated with the direction of the transmitted pulses. Figure 2.3 illustrates the whole imaging scene as it is created at the acquisition time. The spot on the Earth illuminated by a single pulse is referred to as the antenna footprint, while the imaged strip on the ground is called the swath. D and L are the dimensions of the physical radar antenna. The angles θ and β are the look angle and beam angle respectively. H indicates the altitude of the satellite and λ is the wavelength.

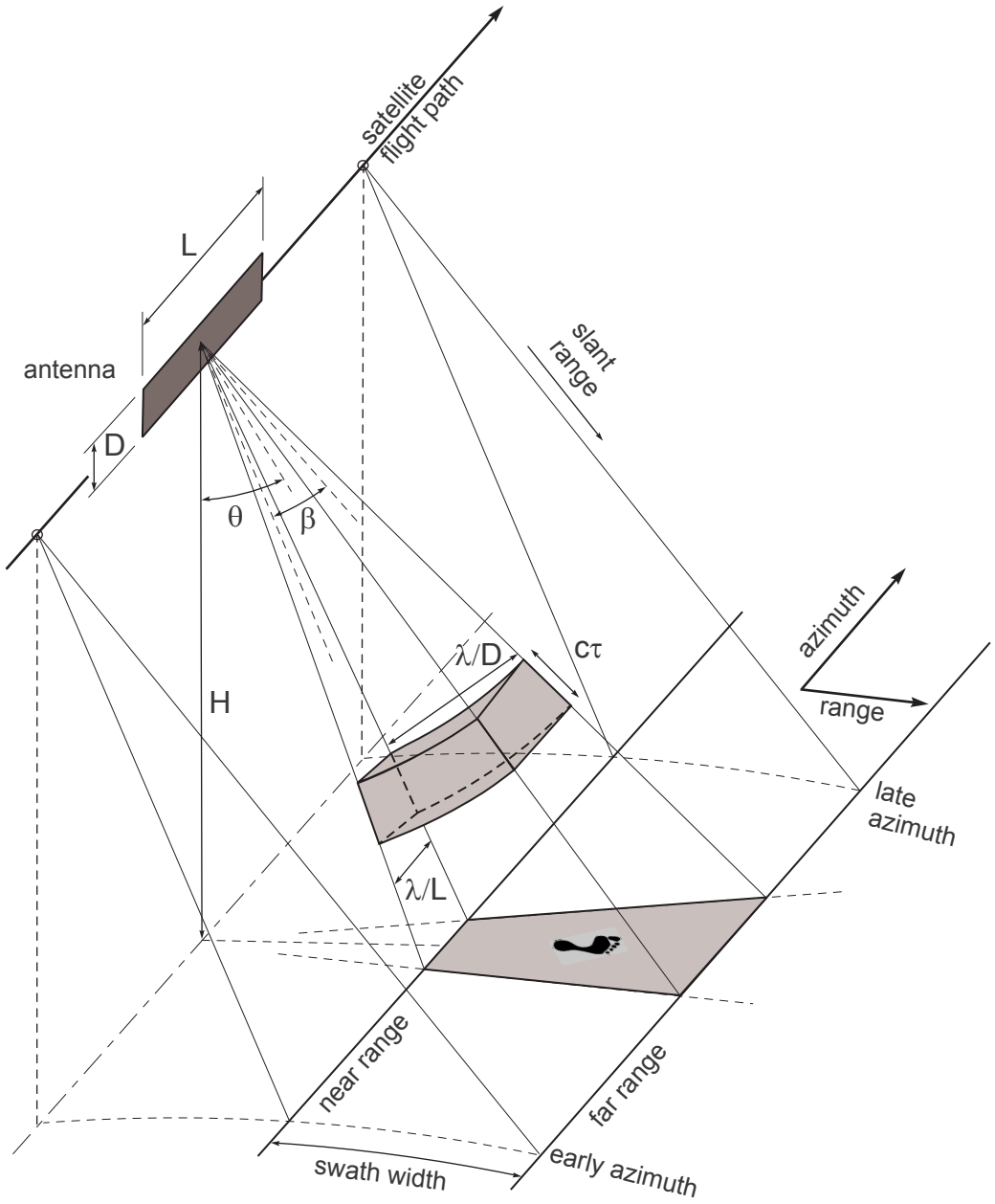

Figure 2.3 *Three-dimensional view of the scanning configuration for a side looking SAR system.*

The pulse duration τ of the transmitted signal determines the slant range resolution Δr of the SAR system (see Figure 2.2):

$$\Delta r = \frac{c\,\tau}{2} \tag{2.1}$$

where c is the speed of light.

On the other hand, the range resolution on the ground Δr_g, which describes the minimum distance between two objects that can be individually detected, is defined as follows:

$$\Delta r_g = \frac{c\tau}{2\cos\alpha_t} \tag{2.2}$$

where α_t is the terrain slope angle.

The range resolution can be easily changed and improved by managing the bandwidth of the transmitted pulse. The azimuth resolution, however, is limited by the azimuth antenna footprint size. Basic antenna theory states that the resolution of the signal detected by an antenna (ΔA) is inversely proportional to the length of the antenna:

$$\Delta A = \frac{\lambda}{L} \cdot R \tag{2.3}$$

In general, a larger sensor (antenna) can obtain more information about scanned objects and thus improve resolution. To increase the image resolution in the azimuth direction, the SAR system uses spacecraft movement and advanced signal processing techniques to simulate a larger sensor size (Figure 2.4).

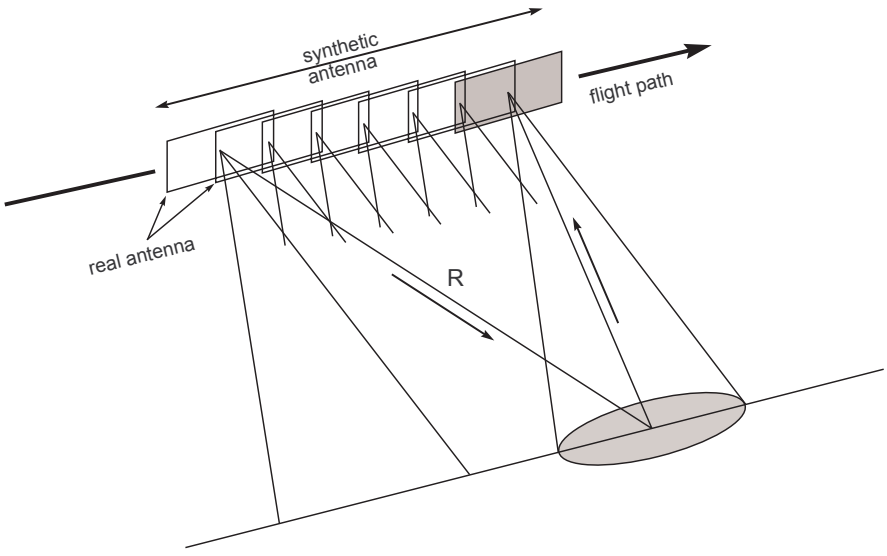

Figure 2.4 *Real antenna forming a synthetic aperture.*

The synthetic aperture technique was first demonstrated by Graham (1974), and improves azimuth resolution from the 4.5 km beam width for the single pulse to approximately 5 m. Since then, several algorithms for SAR focusing have been developed (*e.g.* Madsen, 1989; Massonnet *et al*., 1994; and Xiong *et al*., 1995; Jin, 1996; Debao *et al*., 1999). The ERS-1/2 SAR data used in this study were pre-processed (focussed) to the Single Look Complex (SLC) format by the ESA Processing and Archiving Centre.

In principle, the azimuth processing of SAR data requires an estimation of the Doppler Frequency Shift (also called Doppler Centroid Frequency (FDC)) of the returned echo signal. FDC is a change in wave frequency as a function of the relative velocities of the radar antenna and the target. In practice this means that the signal returned from the area ahead of the space-borne sensor has an upshifted (higher) frequency. Conversely, the signal from the area behind the sensor has a downshifted (lower) frequency.

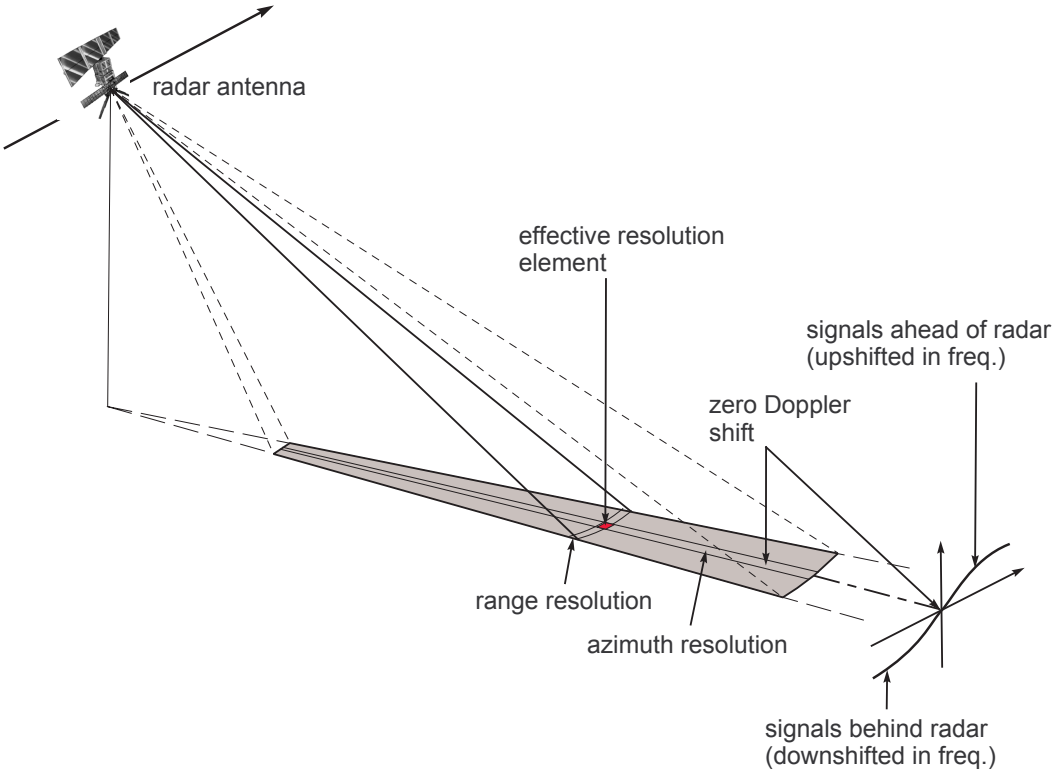

Figure 2.5 *Determination of the effective resolution element (adapted from Lillesand and Kiefer, 2000, p623).*

By processing (focusing) the returned signal using FDC, a very small effective beam width is obtained (Figure 2.5). In other words, the azimuth spectrum contains information about Doppler shift and its bandwidth, and is related to the spectral resolution in the azimuth direction. The FDC depends on the Earth's rotation and satellite yaw steering and it varies in slant range direction (Price, 1999, pp48-69; Barmettler *et al.*, 1996; Zebker *et al*., 1994).

A focused radar image is composed of many dots (pixels). Each pixel in the radar image represents the radar backscatter for the corresponding area of the ground surface. The quality of the image depends on the sensor-scene geometry and signal processing approach. One of the SAR imagery products called Single Look Complex Image (SLC) has preserved the amplitude and phase of the backscattered signal for each pixel, in complex number fashion. Such information makes the interferometry process possible and is described in detail later in this chapter.

2. 3 Factors Affecting Reflectivity

Four major factors affect the reflectivity of the radar signal, namely (i) geometry, (ii) topography, (iii) surface roughness, and (iv) dielectric constant (Mikhail *et al*., 2001).

The incidence angle (θ_{inc}) is the major geometrical factor affecting the strength of the radar signal (Figure 2.6). As θ_{inc} increases the radar energy spreads away and the reflectivity of the terrain decreases. Furthermore, the local incidence angle (θ_{lok}) is influencing the strength of the radar echo (Figure 2.6). Thus, an increase in the terrain slope in the range direction increases the strength of the returned signal. In addition, the backscattered signal increases if the surface roughness increases.

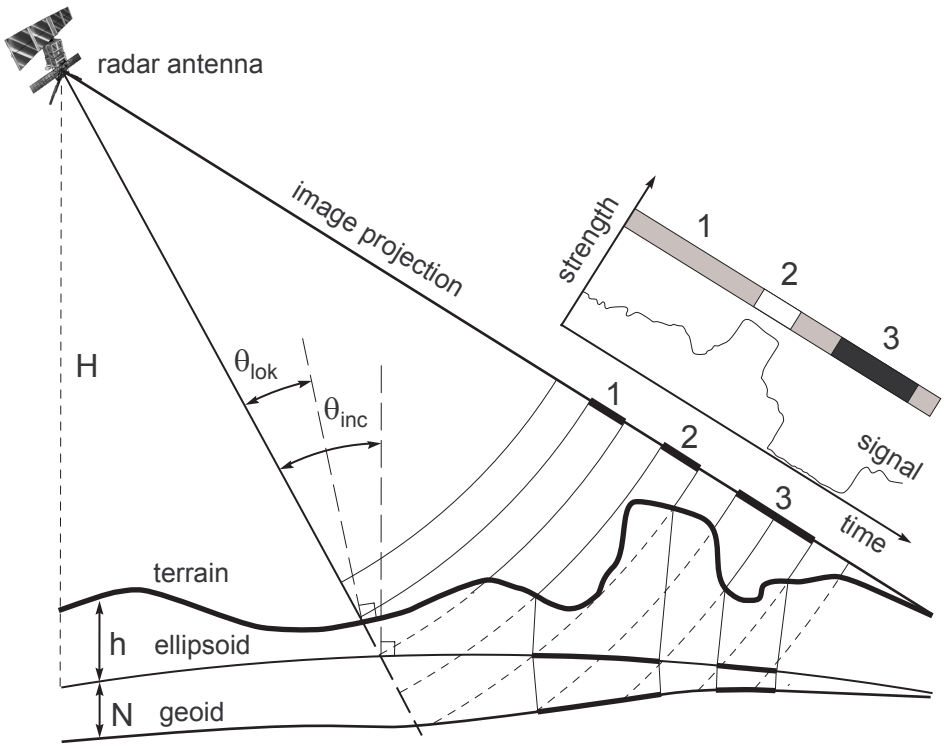

Figure 2.6 *Terrain elevation affecting the image geometry. Area (1) indicates foreshortening, (2) layover and (3) shadow. Black strip (3) indicates weak backscattered signal.*

The last factor affecting the radar reflectivity is the dielectric constant (d_c), which is a measure of the reaction of a material to the presence of an electric field. Materials with high dielectric constant are very good reflectors of radar energy. For instance, water has a d_c equal to 80, while the value of d_c for dry land surface ranges from 3 to 8 (Mikhail *et al*., 2001, p305). Since soil contains a high amount of water, it strongly reflects the radar energy away from the antenna and, again, it appears as a dark area on the image.

2. 4 Topographic Effects on Image Geometry

There are three effects on radar image geometry caused by the SAR configuration and topography of the observed scene: (i) foreshortening, (ii) layover, and (iii) shadow. These are illustrated in Figure 2.6.

Foreshortening refers to a compression of terrain slopes that face the incoming radar energy, which occurs due to the nature of radar as a ranging system.

The *layover* phenomenon is caused by the simultaneous return of radar signals from multiple fractions of the terrain that are at the same distance from the signal transmitter.

The *shadow* areas are caused by the absence of radar returns from portions of the terrain that are occluded, thus not illuminated by the transmitted radar signal.

2. 5 Principles of InSAR

As mentioned previously, the SAR system is capable of delivering a product called a single look complex image, which preserves the phase information as well as the amplitude of the backscattered signal. This information can be exploited and used for topography modelling or deformation detection. The *phase* refers to the relative position along the wave with respect to a reference point, or the relative displacement between two or more waves.

Waves interact with one another and the result of their interaction depends on the individual wave properties. There are two possible types of interaction between waves, firstly constructive (C) addition of the amplitudes when the waves are in phase and secondly, destructive (D) addition when the waves are out of phase (Figure 2.7). This constructive and destructive interaction among waves is known as *interference*.

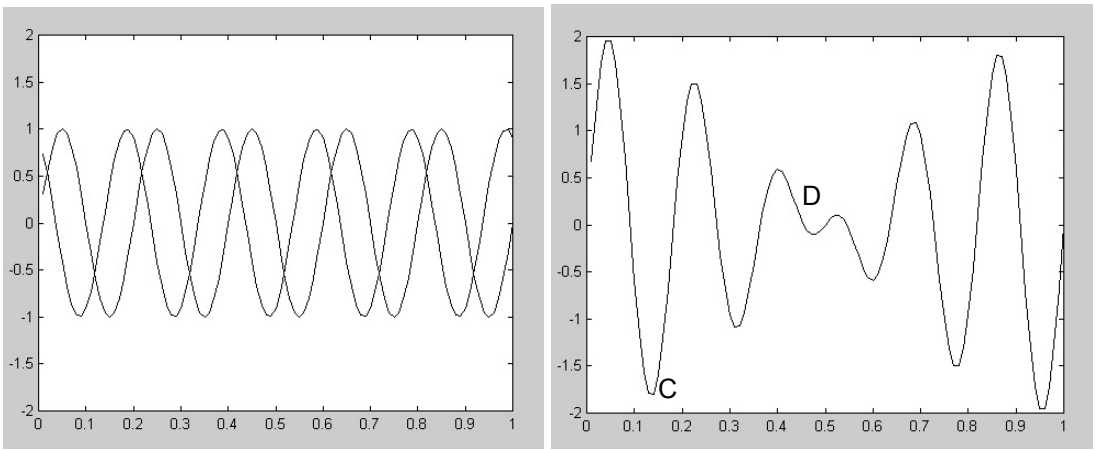

Figure 2.7 *Wave phase difference (left-hand side), and addition of two waves (right-hand side).*

In 1801, Young first studied the interference of light waves. His experiment, commonly known as the '*double-slit*' is illustrated on Figure 2.8a.

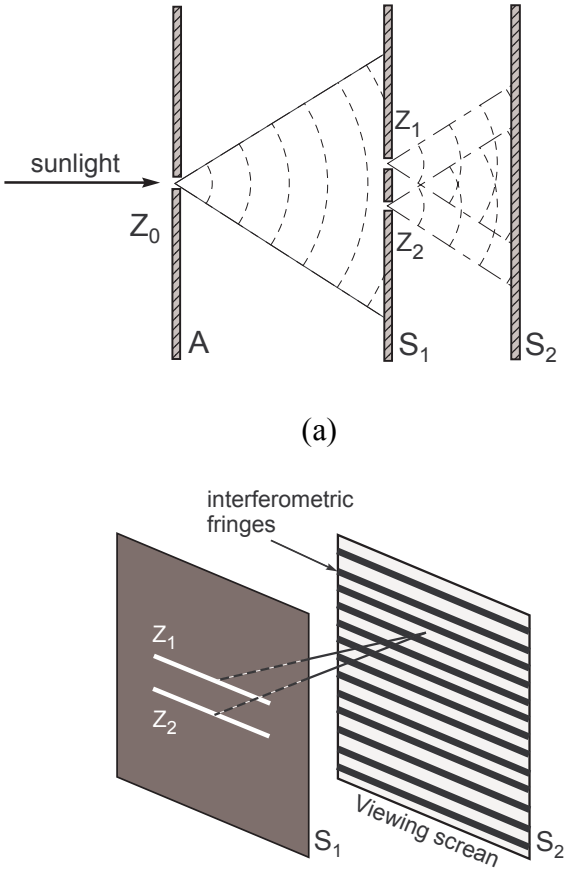

Figure 2.8 *a (left-hand side) Young's two-slit experiment set up and b (right-hand side) interferometric fringes (adapted from Ghiglia and Pritt (1998, p10 and p13).*

On the viewing screen S_2 (Figure 2.8b) a series of light and dark bands can be seen. The dark lines represent the minima of the combined wave disturbance, where destructive interference occurs and the waves cancel each other out. On the other hand, the bright lines represent the maxima, where constructive interference occurs and the wave amplitudes add to each other. The patterns of light and dark bands are commonly called *interferometric fringes.*

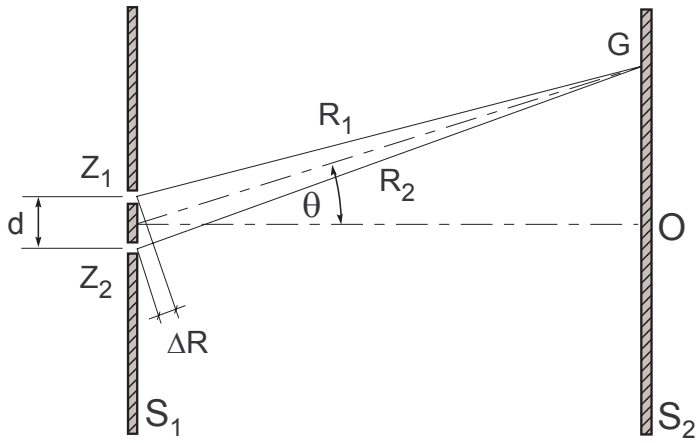

Figure 2.9 *Cross-section through Young's experiment set up (adapted from Ghiglia and Pritt; 1998, p11).*

In Figure 2.9 a cross-section through Young's experimental set up is illustrated. Young determined the mathematical relationship between all relevant quantities and determined the relationship between the phase difference $\Delta\varphi$ and the path difference ΔR given as:

$$\frac{\Delta R}{\lambda} = \frac{\Delta\varphi}{2\pi} \tag{2.4}$$

Nowadays, the principles of this classical experiment are applied to SAR interferometry. However, instead of the slits, two radar antennas S_M and S_S, coherent sources of electromagnetic energy, are applied and the surface of the Earth becomes the 'viewing screen'. The configuration of the side-looking SAR system is shown in Figure 2.10. The interference pattern can be seen on the ground due to path differences between the two sensors to any point that varies with position *G(x,y)*. Moreover, the fringes have a slight curvature because the path difference varies in both directions. The exact spacing and curvature of the fringes are a function of parameters, such as (i) radar wavelength, (ii) distance between antenna and Earth surface, (iii) shape of the surface, and (iv) spatial configuration (separation) of the two antennas in space.

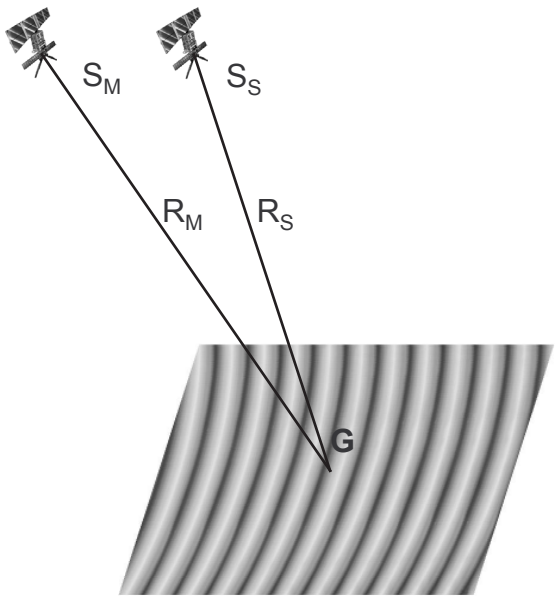

Figure 2.10 *Side-looking SAR set up with two radar antennas (perspective view).*

A SAR system produces images of the ground that comprise a regular grid of complex values *g(x,y):*

$$g(x,y) = u(x,y) + iv(x,y) \tag{2.5}$$

where *u(x,y)* and *v(x,y)* are the real and imaginary parts of the complex number as illustrated in Figure 2.11.

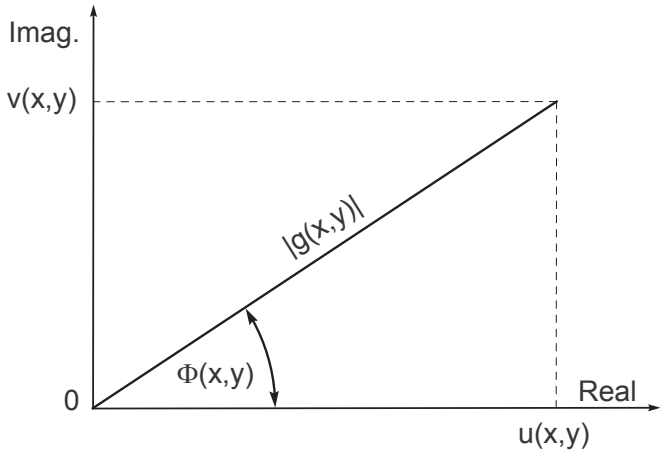

Figure 2.11 *Definitions of amplitude and phase.*

Such complex numbers can be represented in terms of amplitude $|g(x,y)|$ and phase $\Phi(x,y)$:

$$g(x,y) = |g(x,y)|e^{i\Phi(x,y)} \tag{2.6}$$

where amplitude is defined as:

$$|g(x,y)| = \sqrt{u^2(x,y) + v^2(x,y)} \tag{2.7}$$

and phase:

$$\Phi(x,y) = \arctan\frac{v(x,y)}{u(x,y)} \quad \text{when } u(x,y) \neq 0 \tag{2.8}$$

The surface area on the ground is represented by a single pixel, which generally contains hundreds of elementary returns from all scatters within the resolution cell. Thus, the pixel signal value is generated as the sum of hundreds of elementary returns.

To perform radar interferometry two SAR images are needed. In this thesis, the image acquired in the first pass is called the master (*M*) and the image acquired in the second pass is called the slave (*S*). Following Ghiglia and Pritt (1998, p14), the complex notation of the SAR images can be expressed as:

$$g_M(x,y) \cong |g_M(x,y)| \exp\{i\Phi_M\}, \quad \text{where: } \Phi_M = -\frac{4\pi R_M(x,y)}{\lambda} \tag{2.9}$$

$$g_S(x,y) \cong |g_S(x,y)| \exp\{i\Phi_S\}, \quad \text{where: } \Phi_S = -\frac{4\pi R_S(x,y)}{\lambda} \tag{2.10}$$

where $|g_M(x,y)|$ and $|g_S(x,y)|$ are the complex terrain reflectivities (amplitude), R_M and R_S are the ranges from the sensors to point *G(x,y)* on the ground, and λ is the wavelength.

After aligning and resampling the slave image to corresponding locations in the master grid, the two images can be interfered with each other by multiplication of the complex value of the master $g_M(x,y)$ by the complex conjugate of the slave $g_S^*(x,y)$:

$$g_M(x,y) \cdot g_S^*(x,y) \cong |g_M(x,y)||g_S(x,y)| \exp\{i(\Phi_M - \Phi_S)\} \tag{2.11}$$

where '·' denotes the point wise multiplier. The result of such a multiplication is a *complex interferogram*.

If the position of the radar antennas and the SAR system quantities are known very precisely and the images are highly spatially correlated (that is, $|g_M(x,y)| \cong |g_S(x,y)|$), then the interferogram measures the phase difference (modulo 2π) in slant range to the common ground point *G(x,y),* illuminated during both acquisitions.

Figure 2.12 shows a typical interferometry cross-section that indicates all quantities required to obtain topographic heights or surface deformation, based on two radar images.

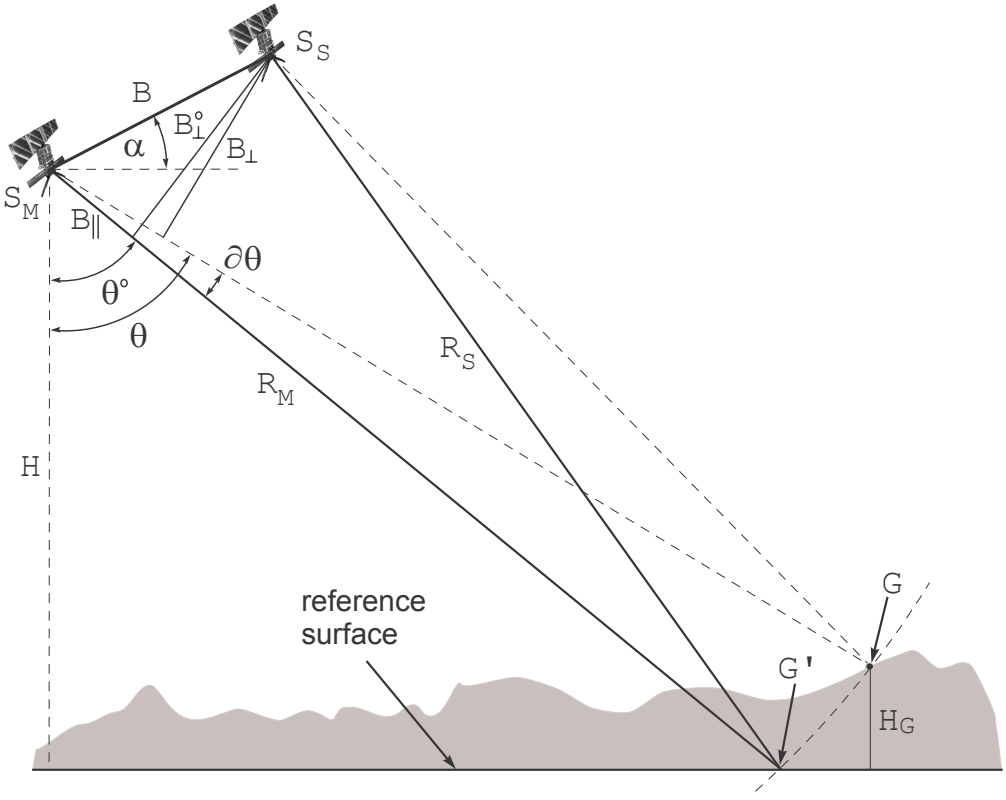

Figure 2.12 *InSAR geometry in the plane orthogonal to the satellite trajectories.*

Using the observed phase difference (ϕ) at point *G(x,y),* range R_M, the sensor's separation baseline (B), and the sensor height (H), it is possible to determine the height (H_G) of point *G(x,y)* above a reference surface.

When the exterior conditions are equal during acquisitions of master (first pass) and slave (second pass) images, the interferometric phase can be written as:

$$\phi = \Phi_M - \Phi_S = -\frac{4\pi(R_M - R_S)}{\lambda} = -\frac{4\pi}{\lambda} B_{||} \tag{2.12}$$

If the range (R_i) is much larger than the baseline (B), we can assume that both ray paths are approximately parallel. Therefore, using this approach known as the *parallel-ray* approximation (Zebker and Goldstein, 1986), the path difference ($B_{||}$) can be approximated as:

$$B_{||} = B\sin(\theta - \alpha) \tag{2.13}$$

Due to orbit inaccuracies and the 2π phase ambiguity it is not possible to derive $B_{||}$ directly from the geometry. However, the relation between changes in $B_{||}$ and θ can be described as:

$$\partial B_{||} = B\cos(\theta^0 - \alpha)\partial\theta \tag{2.14}$$

where θ^0 is the initial value obtained at the reference surface (*e.g.* ellipsoid).

Knowing precisely the height of the satellite H above the reference surface and the derivative for a resolution cell G with range $R_{MG,}$ the relationship between the changes in look angle θ due to a height difference ∂H can be found. Finally, the height H_G of the pixel location above a reference surface and the phase difference $\partial\phi_G$ can be defined as (Hanssen, 2001, p37):

$$H_G = \frac{\lambda R_{MG}\sin(\theta_G^0)}{4\pi B_{\perp,G}^0}\partial\phi_G \quad \text{where:} \quad B_{\perp,G}^0 = B\cos(\theta_G^0 - \alpha) \tag{2.15}$$

where R_{MG} is the range from the satellite to the resolution cell G determined in the configuration of the master image, B is the baseline and θ_G^0 is the initial value found for an arbitrary reference surface, for instance an ellipsoid.

Rearranging Equation (2.15), the functional relationship between the absolute interferometric phase ϕ_G and the terrain height H_G above a reference surface can be defined as:

$$\phi_G = -\frac{4\pi H_G B^0_{\perp,G}}{\lambda R_{MG} \sin\theta^0_G} \tag{2.16}$$

A recursive scheme is used to determine a new value at a specific height above the arbitrary reference surface. The component $\partial\phi_G$ in Equation (2.15) can be replaced by 2π that yields the *height ambiguity*. In other words, it is the linear interval that corresponds to a 2π phase shift:

$$h_{2\pi} = \left| \frac{\lambda R_{MG} \sin\theta^0_G}{2B^0_{\perp,G}} \right| \tag{2.17}$$

Since the measured interferometric phase is the sum of the expected reference phase ϕ_{R_G} on the reference surface, often called the '*flat Earth pattern*':

$$\phi_{R_G} = \frac{4\pi}{\lambda} B \sin\left(\theta^0_G - \alpha\right) \tag{2.18}$$

and the observed phase changes due to topography (H_G) and deformation (D_G), the reference phase has to be removed from Equation (2.16). Thus, the final interferogram contains both the interferometric phase that represents a map of the relative terrain elevation with respect to the slant range direction and deformation (D_G) can be written as (Rocca *et al.*, 2002; Hanssen 2001, p38):

$$\phi_G = \frac{4\pi}{\lambda}\left(B \sin\left(\theta^0_G - \alpha\right) - D_G - \frac{H_G B^0_{\perp,G}}{R_{MG} \sin\theta^0_G} \right) \tag{2.19}$$

If the ground is flat, the achieved fringe pattern is very uniform. However if the surface has variable topography, the point *G(x,y)* moves in the range and azimuth directions as well as up and down, causing path differences in 3D. Thus, terrain height disrupts the uniform fringe pattern as shown schematically in Figure 2.13.

The interferometric fringes do not directly represent the surface height. The wrapped discontinuities must be solved. This can be done during the *unwrapping process*, which, in general, is a process of finding the correct number of whole phase cycles and scaling them by the height ambiguity value. The different unwrapping approaches and algorithms can be studied for example in Zebker *et al.* (1986),

Goldstein *et al.* (1988), Spagnolini (1995), Ghiglia and Pritt (1998), Loffeld and Krämer (1999), Fornaro and Sansosti (1999) and Stramaglia *et al*. (1999).

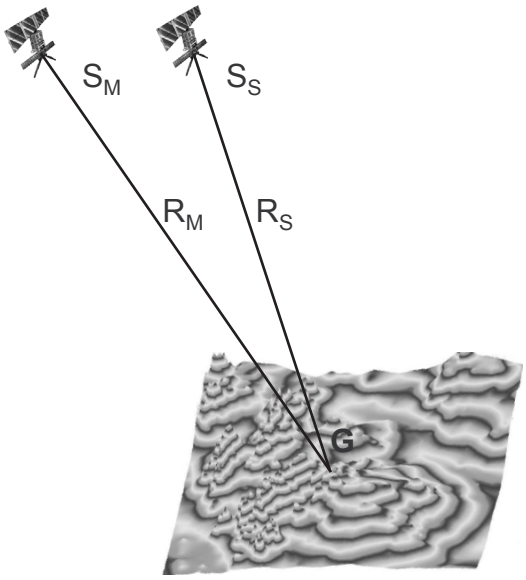

Figure 2.13 *Interferometry pattern caused by topography.*

In addition, the interferogram contains changes in phase due to atmospheric heterogeneity and decorrelation sources which occur between acquisitions times. These issues are discussed in Section 2.8 to Section 2.10.

2. 6 Differential Interferometry

Deformation observations using InSAR are made possible by the fact that surface motion caused by natural and human activities generates a local phase shift in the resultant interferogram. In fact, DInSAR can detect local and relative motions in slant range (satellite-ground).

Ground displacements have a direct impact on the interferogram phase shift and are independent of the satellite separation. The quantity of surface displacement can be estimated directly as a fraction of the wavelength. The ideal condition for deformation detection occurs when the satellites are in the same position in space during both acquisitions to ensure that only deformation will cause phase shifts in the interferogram. Unfortunately, it is very difficult to ensure such a condition and the non-zero perpendicular baseline ($B_\perp \neq 0$) will cause interferometric fringes, due to

the surface topography as well as deformation. However, DInSAR eliminates the phase signal due to topography to yield a differential interferogram in which the signature of surface deformation can be seen. Such an interferogram contains only the fringe patterns caused by deformation and possible decorrelation sources.

There are several ways to generate a differential interferogram, but commonly all techniques involve the generation of two interferograms: one spanning some surface change and topography, the other indicating only the surface topography. The topography related interferogram could either be calculated from a conventional DEM (2-pass differential interferometry), or from an independent interferometric pair without the phase component due to displacement (three- and four-pass differential interferometry). Finally, the topography interferogram is used to subtract the topographic signal from the interferogram that includes the deformation related signal. According to Franceschetti and Riccardo (1999, p. 219) taking a given (or generated) DEM with an accuracy 30 m and the satellite parameters of the ERS-1, example baseline perpendicular component $B_{\perp}$ = 100 m, we get an accuracy on the displacement equal to 1 cm.

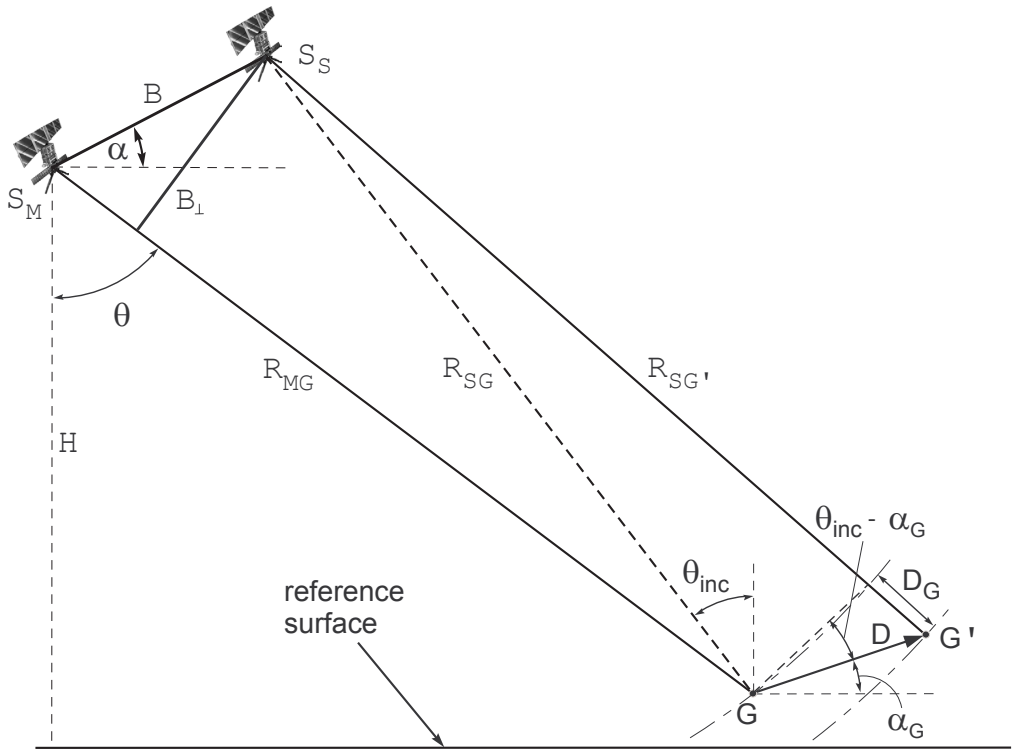

Figure 2.14 *Two-pass DInSAR geometry in the plane orthogonal to the satellite trajectories.*

Figure 2.14 shows the two-pass DInSAR set-up geometry. D indicates the displacement of point G that took place between two radar acquisitions. The range in the second pass (slave) is indicated with $R_{SG'}$, while R_{SG} is the range in the absence of displacement. The interferometric phase is given by:

$$\phi_G = \frac{4\pi}{\lambda}\left(R_{SG'} - R_{MG}\right) \tag{2.20}$$

By rearranging Equation (2.20), the contributions to the path difference due to the target displacement (D_G) and the topographic height (H_G) can be distinguished (Franceschetti and Lanari, 1999, p219):

$$\frac{\phi_G \lambda}{4\pi} = \left(R_{SG'} - R_{SG}\right) + \left(R_{SG} - R_{MG}\right) = D_G + H_G \tag{2.21}$$

If the baseline B = 0 (the same satellite position during both acquisitions), the topographic contribution will equal zero and the interferometric phase would be related only to the displacement term (D_G).

Using the far field approximation, a parallel look direction can be assumed. Thus the displacement vector D in direction α_G will create a slant range deformation component D_G as follows:

$$D_G = |D| \sin\left(\theta_{inc} - \alpha_G\right) \tag{2.22}$$

In practice, such a situation is very difficult to obtain due to difficulties in satellite navigation. Thus, the topographic influence has to usually be removed. However, in order to reduce the topography influence, radar images with the smallest possible perpendicular baseline ($B_\perp \rightarrow \min$) are preferred if the study focuses on the surface deformation detection.

2. 7 Interferometric Phase Statistics

2.7.1 Coherence

The complex coherence γ (complex correlation coefficient) between two complex SAR images g_M and g_S (the interferometric pair) is defined as (Lee *et al*. 1994; Bamler and Just, 1993):

$$\gamma = \frac{E\left\{g_M g_S^*\right\}}{\sqrt{E\left\{\left|g_M\right|^2\right\} E\left\{\left|g_S\right|^2\right\}}} \tag{2.23}$$

where $E\{\}$ is the expectation operator.

Coherence is a measure of the correlation of the phase information of two corresponding signals. This value can be assigned to every pixel of the interferogram, which provides a matrix of coherence values often called a *coherence map.*

2.7.2 The Multilook Phase Difference Distribution

As long as the two radar images g_M and g_S have some degree of correlation, the probability density function (PDF) of the interferogram phase is not necessarily uniform. Following Tough *et al*. (1995) and Oliver and Quegan (1998, p334), the marginal PDF for the phase difference ϕ is given as:

$$PDF(\phi,\gamma,L,\phi_0) = \frac{\left(1-|\gamma|^2\right)^L}{2\pi}\left\{\frac{\Gamma(2L-1)}{[\Gamma(L)]^2 2^{2(L-1)}}\times\left[\frac{(2L-1)\varpi}{\left(1-\varpi^2\right)^{L+0.5}}\left(\frac{\pi}{2}+\arcsin\varpi\right)\right.\right.$$
$$\left.\left.+\frac{1}{\left(1-\varpi^2\right)^L}\right]+\frac{1}{2(L-1)}\times\sum_{r=0}^{L-2}\frac{\Gamma(L-0.5)}{\Gamma(L-0.5-r)}\frac{\Gamma(L-1-r)}{\Gamma(L-1)}\frac{1+(2r+1)\varpi^2}{\left(1-\varpi^2\right)^{r+2}}\right\} \tag{2.24}$$

where ϕ_0 is the expected phase of the interferogram (ϕ_0 = 0), L is the number of independent looks, and $\varpi = |\gamma|\cos(\phi-\phi_0)$. The gamma function is defined as:

$$\Gamma(L) = (L-1)! \tag{2.25}$$

If L = 1, the summation contains no terms and the distribution reduces to single-look. The value of the PDF depends only on the number of looks and the complex correlation coefficient. Figure 2.15 shows the changes of the PDF functions (Equation (2.24)) for a constant value of coherence and different multilook values (L).

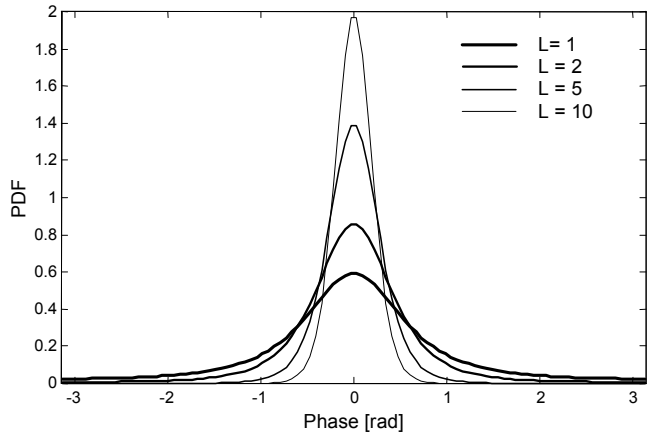

Figure 2.15 *Probability Density Functions for different multilook (L) values (γ = 0.75, ϕ_0 = 0).*

It can be seen that as the multilook factor increases the PDF increases. Thus the phase statistics can be improved, but at the expense of the spatial resolution of the interferogram. Figure 2.16 shows the changes of the PDF for different coherence values but using a constant multilook value.

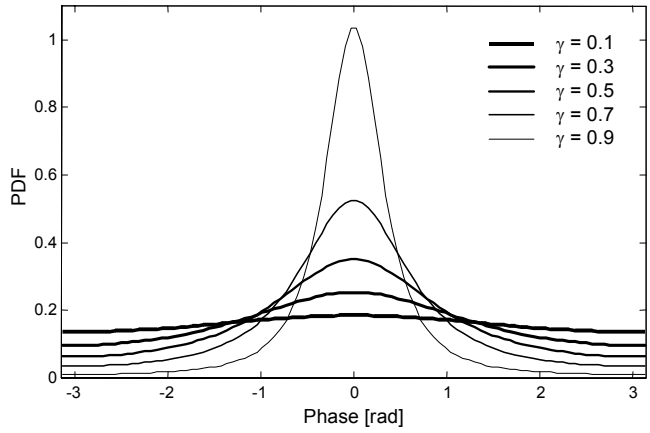

Figure 2.16 *Probability Density Functions for different coherence levels (L=1).*

As can be seen from Figure 2.16, high coherence increases the PDF value. Thus, coherence has a significant impact on the accuracy and reliability of the interferometric products. Low coherence can affect the phase differences related to topography or deformation in the way that its correct qualitative and quantitative interpretation may be impossible.

2. 8 Sources of Decorrelation

The interferometric phase can be affected by many decorrelation effects (factors), which can be categorised as follows: (i) thermal decorrelation, (ii) temporal decorrelation, (iii) geometrical decorrelation, (iv) Doppler centroid decorrelation and (v) processing induced decorrelation (Hanssen, 2001, p98; Ferretti *et al.*, 2001, 1999a; Franceschetti and Lanari, 1999, pp173-176). These effects increase the interferometric phase noise, thus decrease the suitability of radar interferometry for surface deformation detection or DEM generation.

When considered together, the above decorrelation factors are multiplicative so the total decorrelation value (γ_{total}) can be estimated as (Zebker and Villasenor, 1992):

$$\gamma_{total} = \gamma_{thermal} \cdot \gamma_{temporal} \cdot \gamma_{geom} \cdot \gamma_{FDC} \cdot \gamma_{proc} \tag{2.26}$$

The following sections describe all the listed decorrelation factors in more detail.

2.8.1 Thermal Decorrelation

The influence of thermal noise ($\gamma_{thermal}$) on the interferometric phase can be expressed by the signal-to-noise (*SNR*) ratio of the specific sensor (system) (Bamler and Just, 1993; Just and Bamler, 1994; Zebker and Villasenor, 1992):

$$\gamma_{thermal} = \frac{1}{1 + SNR^{-1}} \tag{2.27}$$

The value of the *SNR* ratio is defined as:

$$SNR = \frac{P_S}{P_N} \tag{2.28}$$

where P_S is the power of the signal and P_N the power of the noise.

According to Hanssen (2001, p101), the *SNR* value for the satellite ERS-1/2 is 11.7 [dB] and is mainly influenced by the design of the radar system, and the scattered scene.

2.8.2 Temporal Decorrelation

Temporal decorrelation ($\gamma_{temporal}$) occurs in the case of repeat-pass interferometry and it is one of the major constraints of radar interferometry. Temporal decorrelation is the function of all physical changes occurring on the terrain surface between two data acquisitions. It includes changes of soil moisture content, surface roughness and vegetation. Analytical modelling and numerical assessment of the temporal decorrelation is almost impossible due to the wide range of possible influencing factors. Changes in the environment caused by human activities can be a good example of the temporal decorrelation factor, which cannot be modelled quantitatively due to its unpredictable and discrete nature.

2.8.3 Geometric Decorrelation

Zebker and Villasenor (1992) provide the geometric (spatial) baseline decorrelation function γ_{geom} as the result of the phase offset due to the difference in the incidence angle θ_M and θ_S (Figure 2.17) between the two radar antennas (S_M, S_S) on the Earth's surface:

$$\gamma_{geom} = 1 - \frac{2|B|R_g \cos^2 \theta}{\lambda R} \tag{2.29}$$

where θ is the average look angle, λ the radar wavelength, B the baseline separation in the horizontal direction (in meters), R_g the ground range resolution, and R the slant range.

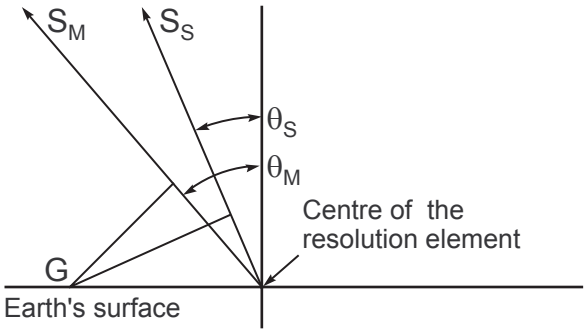

Figure 2.17 *Interferometric image geometry on the Earth's surface.*

A modified version of Equation (2.29), given by Lee and Liu (1999), includes the terrain slope α_t and baseline component $B_\perp$:

$$\gamma_{geom} = 1 - \frac{cB_\perp}{\lambda R B_w} \left| \cot(\theta_0 - \alpha_t) \right| \tag{2.30}$$

where c is the speed of light, θ_0 the nominal incidence angle on the ellipsoidal Earth (23° for ERS-1 and ERS-2), $B_\perp$ the perpendicular baseline (in meters), α_t is the local terrain slope, and B_w the frequency bandwidth of the transmitted signal.

Figure 2.18 shows the quantity of the geometric decorrelation γ_{geom} for the satellites ERS-1/2 as a function of the perpendicular baseline $B_\perp$ and the terrain slope angle α_t.

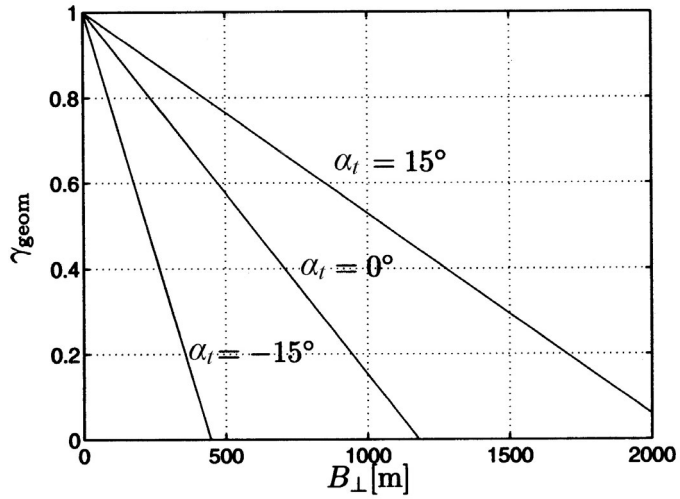

Figure 2.18 *Geometric decorrelation for ERS-1/2 (after Hanssen, 2001, p103).*

As Figure 2.18 shows, if the length of the perpendicular baseline ($B_\perp$) increases, the phase leads to a decorrelation and lower level of coherence. The coherence is completely lost and the interferometry cannot be performed if the $B_\perp$ reaches its critical length $B_{\perp,C}$:

$$B_{\perp,C} = \frac{\lambda B_w R}{c} \tan(\theta_0 - \alpha_t) \tag{2.31}$$

For the satellite ERS-1/2 the value of $B_{\perp,C}$ is approximately 1100 m.

2.8.4 Doppler Centroid Decorrelation

The difference in Doppler centroid frequencies $\Delta f_{DC} = f_{DC}^{M} - f_{DC}^{S}$ between the master and slave images causes a Doppler centroid decorrelation γ_{FDC}:

$$\gamma_{FDC} = \begin{cases} 1 - \dfrac{\Delta f_{DC}}{B_A} & if \quad |\Delta f_{DC}| \le B_A \\ 0 & if \quad |\Delta f_{DC}| > B_A \end{cases} \tag{2.32}$$

where B_A is the bandwidth in the azimuth direction. Therefore, a large value of Δf_{DC} will increase the phase noise.

2.8.5 Processing Induced Decorrelation

Incorrect alignment (coregistration) of two images during the interferometry processing generates an additional source of noise referred to as processing decorrelation γ_{proc}. Moreover, according to Hanssen and Bamler (1999) the interpolation kernels are also a potential source of interferometric decorrelation. However, Just and Bamler (1994) state that coregistration accuracy higher than 1/8 of pixel size leads to a negligible decorrelation.

2. 9 Orbital Error

In order to determine the interferometric baseline and to refer the interferometric products to a reference datum, the satellite orbit ephemerides are required. Any orbital errors will propagate directly as an error in DEMs or deformation maps.

The state vector error can be decomposed into three components, namely the radial (σ_R) (in the state vector direction), along-track (σ_A), and across-track (σ_X) (Figure 2.19a). According to Hanssen (2001, p121), the along-track error (σ_A) is usually sufficiently corrected during the coregistration of the master and slave images and can be neglected as a factor influencing the interferogram phase. Thus, the problem is two-dimensional and focuses on radial and across-track errors that propagate as systematic phase errors into the interferogram.

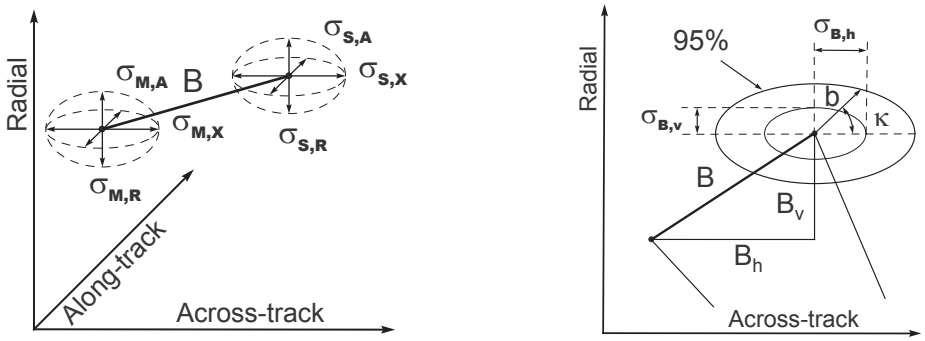

Figure 2.19 *a (left-hand side) Two orbits (master and slave) and associated error ellipses, b (right-hand side) radial and across-track errors influencing the baseline vertical (B_v) and horizontal (B_h) components (after Hanssen, 2001, p121).*

Assuming that the errors between master and slave orbits are uncorrelated, the radial (σ_R) and across-track (σ_X) errors propagate directly into the baseline (B) according to the relationships given in Equations (2.33) and (2.34).

$$\sigma_{B,h} = \sqrt{\sigma_{M,X}^2 + \sigma_{S,X}^2} \tag{2.33}$$

$$\sigma_{B,v} = \sqrt{\sigma_{M,R}^2 + \sigma_{S,R}^2} \tag{2.34}$$

Increasing the confidence interval to 95%, the baseline error b lies with sufficient confidence level within the larger error ellipse, as shown on Figure 2.19b. Only the length of the error vector b is known. The orientation of vector b remains unknown, thus the influence of this error on the interferogram phase can be any kind of behaviour. The orbital error b creates a residual reference phase trend, which has the largest effect when the orientation angle κ of b vector is close to 0 and π. However, if angle κ is close to $\pm\frac{\pi}{2}$, the effect is almost negligible.

2. 10 Atmospheric Heterogeneities

It is most likely that conditions in the atmosphere are not identical as the images are acquired at different times. Therefore, the length of the measured ray path between the sensor and the ground can change due to the time delay caused by any differences in the tropospheric and ionospheric disturbances. Any atmospheric heterogeneity will appear as a phase distortion in an interferogram and thus limit the confidence of

the results. Hanssen and Feijt (1996) quantitatively evaluate the atmospheric effects on SAR interferometry using an existing tropospheric model. A quantitative assessment of the influence of three major atmospheric parameters, such as pressure, relative humidity and temperature on the interferometric phase has been derived.

According to Zebker *et al.* (1997), interferograms derived from repeat-pass radar interferometry can be affected due to the time and space variation of atmospheric water vapour. Furthermore, variation of pressure and temperature do not induce distortion significantly as they are more evenly distributed through an interferogram than the wet troposphere term. Zebker *et al.* (1997) state that dry regions have fewer variations than wet regions. Although night time acquisition can reduce atmospheric artefacts more than daytime, due to more quiescent vegetation and a statistically more stable atmosphere at night (Massonnet and Feigl, 1998), the user has no control over the acquisition time for any given region on the Earth.

Weather balloon and surface data can be valuable sources of information to estimate and eliminate the tropospheric effect (Hopfield, 1971), but very often there is not sufficient data over the area of interest. Ground-based meteorological and GPS measurements can be used to estimate the tropospheric delay and calibration of radar interferograms as demonstrated by Bonforte *et al*. (2001), Ge *et al*. (2000b), Williams *et al*. (1998).

The ionospheric effect is extremely difficult to remove from the radar observation. Used in GPS technology, and based on the dispersive nature of the ionosphere, the combination of phase measurements at two different frequencies could eliminate the ionospheric contribution. This approach would require two radar images acquired simultaneously at different frequencies. Unfortunately, such a radar system does not exist. However, according to Gray *et al*. (2000) the ionospheric disturbance influences radar interferometry causing an azimuth offset which results in azimuth shift modulations at a kilometre scale for C-band wavelength. Therefore, it is assumed that the ionospheric effect will not influence the interferometric phase significantly over a single radar frame.

Taking into account the fact that radar interferometry is very sensitive to any changes in atmospheric conditions, it creates a potential tool for meteorological study. As shown in Hanssen *et al*. (1999), if the topography and deformation effects are known, the interferometric delay measurements can be used to infer high-resolution maps of integrated atmospheric water vapour distribution.

2. 11 Summary

In this chapter, the Synthetic Aperture Radar Interferometry background and theory have been presented. The chapter has included a short introduction to radar and synthetic aperture radar theory, followed by factors affecting the signal reflectivity. Furthermore, by introducing the Young 'double-slit' classical experiment, the principles of optical interferometry and its analogy to radar interferometry have been established. In addition, repeat-pass interferometry and differential radar interferometry as deformation monitoring techniques have been discussed.

The issue of interferometric phase statistics and sources of errors (decorrelations) affecting radar interferometry have been introduced. Moreover, the major decorrelation factors have been identified and discussed. These factors dramatically reduce the capability of the satellite radar interferometry for deformation monitoring as well as DEMs production in two different ways: first, by degrading the entire signal so the interferometry process cannot be performed; second, by introducing additional information to the analysed signal, which can lead to misinterpretation.

3 STUDY AREAS AND RESEARCH DATA

Deformation detection analysis requires a thorough knowledge of the characteristics of the study area so that the interpretation of the results is relevant to the actual surface deformation that has occurred. An understanding of the specific satellite data, such as radar images or satellite orbit ephemerides is also required.

In this chapter, the two data samples used for small-scale deformation detection studies, validation of the new developed filter algorithm, developing the functional model for determining the minimum and maximum detectable deformation gradient and the advanced analysis of the interferometric phase image are described. Furthermore, the key characteristics of the reference data, such as DEM and meteorological data are also outlined.

3. 1 Location and Characteristic of the Study Areas

In order to determine and enhance the ability of radar interferometry to detect small-scale surface deformation, two different study areas, namely Leinster and Silesia, have been selected. Leinster is located in the middle of the Western Australian desert. While the vast majority of the area is stable, a surface mine site located in its centre has experienced some surface deformation. Nevertheless, it can be recognised as an example of stable area. On the other hand, the Silesia study area, located in Poland, is an example of extremely unstable area as numerous underground mines have influenced the surface topography. The following section characterises the study areas in greater detail.

3.1.1 The Leinster Study Area

The Leinster study area is located 370 km north of Kalgoorlie and 700 km northeast of Perth in Western Australia (Figure 3.1a). The main advantage of choosing Leinster was its very stable and dry weather conditions, as well as limited vegetation

cover, that insure the high quality of SAR data. Furthermore, Leinster is located on the Yilgarn craton (Figure 3.1b), therefore it can be recognised as highly stable.

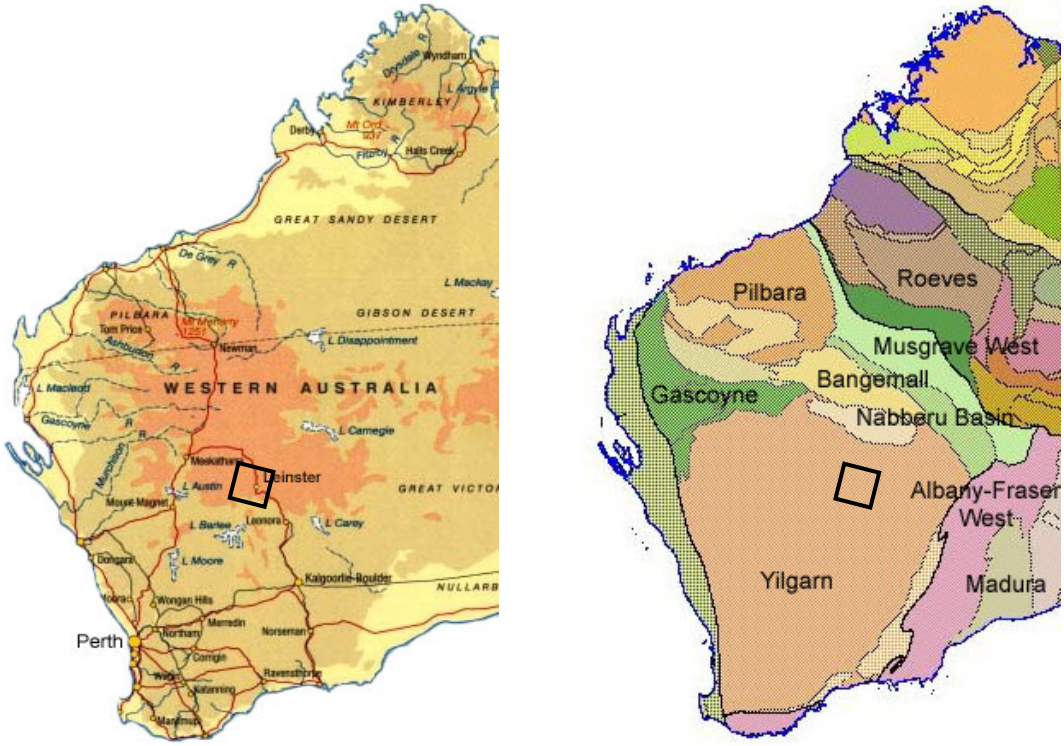

(a) (b)

Figure 3.1 *(a) Location of the Leinster study area and (b) map of crustal elements (cratonic regions) in Western Australia (after Geoscience Australia 2003). The rectangular frame indicates the location of image frame 4164 (relative scale).*

While the majority of this study area is stable, a nickel surface mine located in the centre of this study area does experience some surface deformation. A nickel sulphide deposit was discovered there in 1971 and, since December 1988, the Leinster nickel operation has belonged to the Western Mining Corporation (WMC). The current mine plan estimates continued operation for another 16 years, and this will extend even further if the exploration continues to be successful in replacing depleted ore (WMC Leinster, 2002).

Underground mining commenced in 1996 and since 1997 some significant surface deformation around and inside the open pit has been experienced. At present, the surface deformation occurs approximately 400 m from the crest of the pit as well as on its steep slope, and approximately 800 m along the east crest of the pit. As the underground mining develops below the pit, the spatial extent of the surface

deformation increases. Underground transport is conducted via a vertical shaft located in the vicinity of the pit. Due to the close proximity of the mine shaft and ventilation shaft to the apparent surface deformation, it is extremely important that a deformation monitoring program is implemented. Figure 3.2 illustrates the type and Figure 3.3 the spatial extent of deformation experienced at Leinster Mine site.

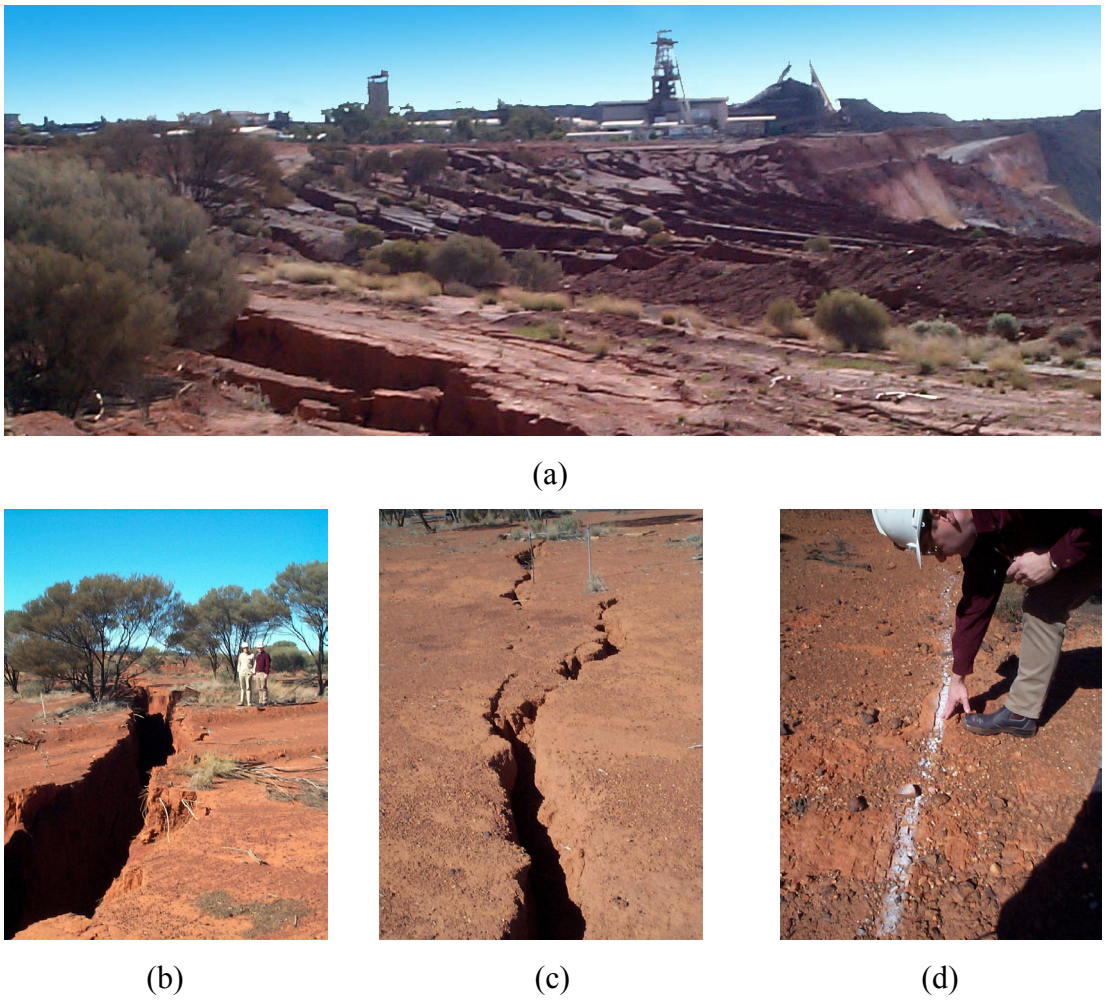

(a)

(b) (c) (d)

Figure 3.2 *(a) Deformation at the Leinster mine site, and different scale of surface cracks observed at (b) 100 m, (c) 200 m, and 400 m from the pit crest.*

Figure 3.3 shows a high-resolution (0.15 m) aerial photograph obtained from the Department of Surveying of the WMC Leinster Nickel Operation. Three different zones are identified (i) the surface deformation zone visible at the west crest of the pit, (ii) open pit zone and (iii) waste zone.

Figure 3.3 *Aerial photograph showing the Leinster mine site taken in 2001. Sparse vegetation cover over the deformation zone can be seen.*

3.1.2 The Silesia Study Area

The Upper Silesian Coal Basin is located almost in the south of Poland (Figure 3.4). Since the 19th century the Upper Silesian Coal Basin has been one of the largest mining centres in Europe, producing over 100 million tonnes of coal from 65 underground mines each year (Perski and Jura, 1999). However, due to coal deposits running out and the recent restructure of the Polish coal mining industry, the number of active coalmines in this region has declined.

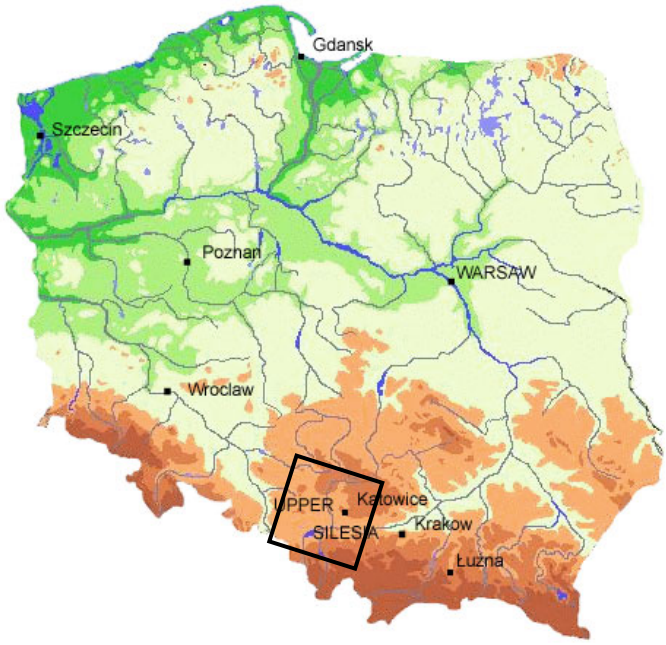

Figure 3.4 *Location of the Silesia study area in Poland (relative scale). The rectangular frame indicates the location of image frame 2592.*

Over two hundred years, the mining industry has made this region highly urbanized and environmentally degraded. The major part of the environmental damage is caused by surface deformation due to underground mining activities. There are two different types of surface deformation (i) continuous and (ii) discontinuous, experienced in the Upper Silesia region. Vast sag subsidence and local pit subsidence are examples of continuous forms of deformation. Cracks, faults and slides are examples of the discontinuous form of deformation.

Continuous surface deformation (subsidence) is the most common cause of changes in topography and hydrography. These changes affect human made structures, such as buildings, roads, railways and pipelines. The velocity of surface subsidence is usually a few centimetres per month, but there are areas where the velocity is up to 1 cm per day (Perski and Jura, 1999). In 1970, mining was commenced under densely urbanized cities, such as Katowice or Bytom, situated at the centre of the Silesia coalfields. Moreover, rapid urban expansion in the city of Katowice, lead to the development of suburban housing over the sites of relatively shallow abandoned mines or deeper active mines. Since then, mining deformation has become an important problem for the local community and the mining industry. In some cases, subsidence developed resulting in structural damage varying from minor cracking to

the collapse of some dwellings. A deformation-monitoring scheme is required to validate the deformation prediction models and to construct land classification maps. Such maps can help in the planning of infrastructure development as well as in redesigning mining techniques to minimise their impact on the surface.

3. 2 Satellite Radar Data

3.2.1 Sensor Characteristics

In this section the essential hardware components of the SAR instrument carried on board the ERS-1/2 satellites are discussed.

The first European Remote Sensing Satellite ERS-1 was launched on 17 July 1991 and finished its mission in July 1996. The second satellite ERS-2, launched on 20 April 1995, still operates in a sun-synchronous, near-polar orbit. Both satellites are almost identical; in particular the SAR instrument is the same. Therefore, the description of the satellite ERS-2 covers both sensors.

ERS-2 carries on-board a number of active microwave sensors supported by additional, complementary instruments that are capable of measuring, on a global scale, the Earth's atmospheric and surface properties with a high degree of accuracy. The main instruments are the Active Microwave Instrument (AMI), which combines a SAR operating in image or wave mode and a wind scatterometer, the Radar Altimeter (RA), the Precise Range and Range-rate Equipment (PRARE), the Along-Track Scanning Radiometer and Microwave Sounder (ATSR-2), Laser Retroreflectors (LRR) and the Global Ozone Monitoring Experiment (GOME) device. The SAR system consists of an antenna of area 10x1 m, a SAR processor, a pulse generator, a transmitter, and other supporting systems to collect measurements. The main SAR sensor parameters are listed in Table 3.1. In addition, ERS-2 satellite measures many additional parameters not covered by the existing satellite systems, including those of sea state, sea surface winds, ocean circulation and sea and ice levels (ESA Service, 2002).

Table 3.1 *ERS-1/2 SAR sensor parameters (after Franceschetti and Lanari, 1999, p11)*

Country	European Union
Platform	Satellite
Launch date	7/1991 (ERS-1), 4/1995 (ERS-2)
Designed Life time (years)	3
Frequency (GHz)	5.3 (C-band)
Polarization	VV
Orbit altitude (km)	785
Orbit inclination (deg)	98.5
Look angle (deg)	2.3
Swath width (km)	100
SAR Antenna dimensions (m)	10 x 1
Pulse duration (μs)	37.1
Pulse bandwidth (MHz)	15.5
Pulse repetition frequency (Hz)	1640-1720
Transmitted peak power (kW)	4.8
Data rate (Mb/s)	105 (5 b/sample, I/Q)

3.2.2 Satellite Data Selection

Suitable image selection is one of the vital decisions in the application of InSAR assuming that several images are available. The main criteria for image selection can be based on (i) deformation quantity (ii) the availability of the SAR data, (iii) the temporal and spatial distribution of the baseline, and (iv) characteristics of the atmospheric conditions during the image acquisitions.

To determine the availability of archival data sets, the Display Earth Remote Sensing Swath Coverage (DESCW) version 4.37 software was used (ESA Descw, 2002). It allows a user to perform multi-mission inventory searches on the major ESA supported missions by displaying the satellites' coverage over an Earth map (Figure 3.5). In addition, it provides the exact location and baseline information of all acquired and planned images (location only).

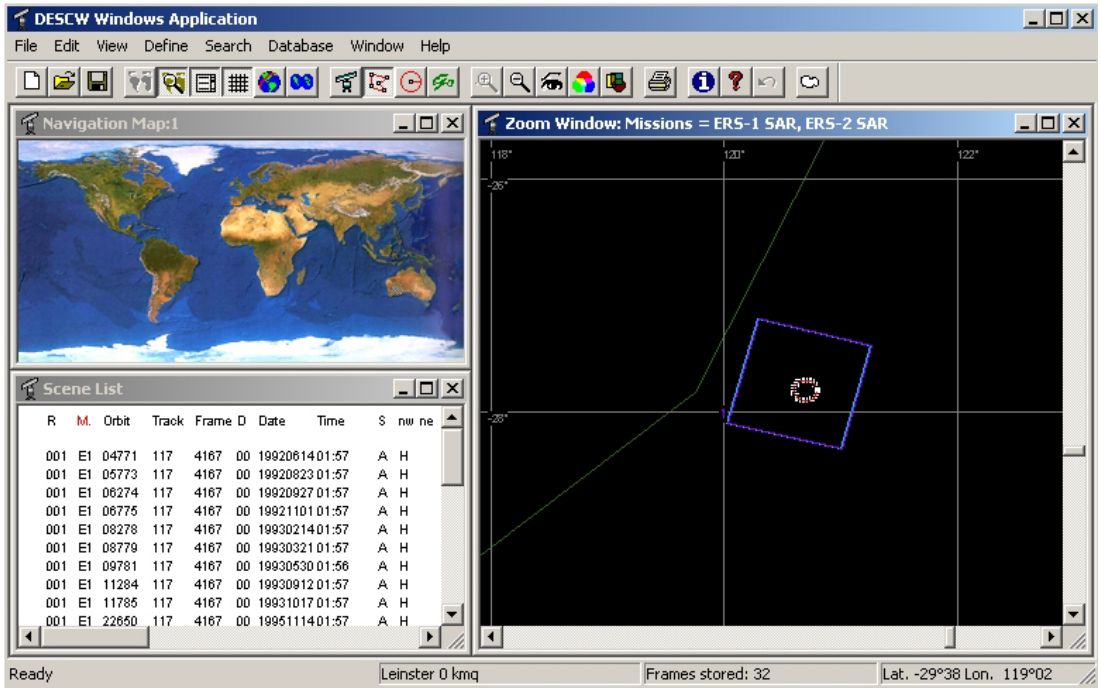

Figure 3.5 *DESCW graphical interface.*

For the Leinster study area two archival ERS-1/2 SAR SLC images (quarter of the frame) were selected and three new acquisitions were scheduled. Image details are listed in Table 3.2. Selected radar images were requested from ESA Remote Sensing Services. For the Silesia study area two archived images (whole frame) were selected. Image details are listed in Table 3.3.

Table 3.2 *Satellite data for Leinster study area (SLC images)*

AQ-No	Satellite	Date/Time [UT]	Track	Orbit	Frame
AQ-I	ERS-1	14.11.1995 / 1:57:07	117	22650	4164
AQ-II	ERS-2	19.03.1997 / 1:57:04	117	9991	4164
AQ-III	ERS-2*	24.10.2001 / 1:57:00	117	34039	4164
AQ-IV	ERS-2*	01.02.2002 / 1:55:00	117	35041	4164
AQ-V	ERS-2*	13.03.2002 / 1:57:00	117	36043	4164

{*} scheduled acquisition

Table 3.3 *Satellite data for Silesia study area (SLC images)*

AQ-No	Satellite	Date/Time [UT]	Track	Orbit	Frame
AQ-SI	ERS-1	04.10.1992 / 9:38:05	222	6379	2592
AQ-SII	ERS-1	08.11.1992 / 9:38:01	222	6880	2592

3.2.3 SAR Data Limitations at Leinster Study Area

After researching the ESA image database it was found that there is not sufficient archival data sets covering the Leinster study area. Only the images acquired between 1991 and 1997 were available. Therefore, the new acquisitions and synchronised terrestrial measurements were scheduled. However, due to a defect in the gyroscope onboard the ERS-2 satellite, since March 2001 ESA has experienced difficulties with the ERS-2 satellite navigation. Since then, correct navigation has been impossible and keeping the satellite on the track with high accuracy has been very difficult (ESA Service, 2002). Therefore, none of the planned acquisition has created a suitable couple for interferometry analysis. The shortage of suitable radar images over the Leinster study area was the major limiting factor preventing proper observation of small-scale deformations at mine site and its validation against terrestrial measurements.

3.2.4 Satellite Orbit Coordinates

The radar interferometry process requires satellite orbit ephemerides or state vectors to determine the interferometric baseline vector and to refer the interferometry products to a geodetic reference datum.

According to Closa (1998), accuracy of the satellite position determination directly affects the interferometry process and the quality of its products. Moreover, he indicates the high quality of the Delft Institute for Earth-Oriented Space Research (DEOS) and the ESA orbits and the similar impact of both sources of orbits on the quality of interferometry products.

Precise orbit determination incorporates data adjustment using observations and models. In a result, a set of state vectors consisting of time, velocity and position

vectors is computed. For example, the Delft precise orbits of the satellites ERS-1/2 are computed using Satellite Laser Ranging (SLR) altimeter tracking data and a new improved Delft Gravity Model (DGM-E04). According to Scharroo and Visser (1998) the radial and across-track RMS errors of Delft precise orbits are on the order of 5 and 8 cm respectively. In this thesis for the interferometry processing purposes, the Delft precise orbits of the satellites ERS-1/2 were used.

The Delft orbits are provided in a binary format called Orbital Data Records (ODRs) and contain the position of the satellite at a 60 second interval. For the ERS-1 satellite precise orbits were available from 11 April 1992 to 6 June 1996, and for ERS-2 satellite from May 1995 and they were realised with a few months delay. All the ODR files are provided via a DEOS ftp services and were downloaded together with the supporting software GETORB (Delft Precise Orbits Service, 2002).

The GETORB software contains several utilities to handle the Delft orbit files, such as tools to list and interpolate the orbits at any given time. The software provides accurate time as well as the latitude and longitude coordinates of the satellite in 10^{-7} degrees (Delft Getorb Software, 2002).

3. 3 Other Reference Data

3.3.1 Digital Elevation Model

In order to reduce the topographical effect during the interferometry processing (differential interferometry) over the Leinster study area a part of the GEODATA 9 Second DEM Version 2 was acquired from the Geoscience Australia. The DEM is a grid of ground level elevation points with a grid spacing of 9 seconds in longitude and latitude (approximately 250 m). The height values are with respect to the Australian Height Datum (AHD) reference system. The DEM is a model of the terrain in which each data point represents the approximate elevation at the centre of each cell. Theoretical estimates and tests of the DEM against trigonometric data distributed evenly across Australia indicate that the standard deviation error of the DEM varies between 7.5 m and 20 m for most of the continent (Hutchinson, 2001).

The radar interferometry derived ellipsoidal heights are referenced to the surface of the WGS84 ellipsoid. However, the AHD heights are essentially normal orthometric heights defined over the geoidal reference system (Holloway, 1988). Therefore, in order to use the 9”DEM, the ellipsoidal heights need to be provided. To obtain the required ellipsoidal heights, the AHD heights were transformed using the geoid-WGS84-ellipsoid separation (Featherstone and Alexander, 1996). The Winter v.5.04 software provided by Geoscience Australia was used to interpolate a geoid-ellipsoid separation value (*N* value) from existing AUSGeoid98 regular grid of *N* values. Then, at each grid point location of the 9”DEM, the *N* value was subtracted. AUSGeoid98 is a gravimetric geoid model of Australia that has been computed using data from EGM96 global geopotential model, the 1996 release of the Australian gravity database, a national DEM, and satellite altimeter-derived marine gravity anomalies (Featherstone *et al.*, 2001). Finally, the DEM was interpolated to a 20 m grid interval using bicubic interpolation.

3.3.2 Meteorological Data

In order to assist in the selection of archival images and the interpretation of interferometry results at the Leinster study area, the meteorological data such as (i) daily rainfall, (ii) relative humidity, (iii) temperature, and (iv) pressure were obtained and analysed. The interferometric phase difference caused by atmospheric heterogeneity is very often present in the interferometry results. Thus, the correct interpretation of the phase image is sometimes impossible and an additional source of information is necessary. Therefore, the analysis of meteorological data can significantly reduce the likelihood of possible misinterpretation of the interferometric phase image. Consequently the meteorological data were obtained from the Bureau of Meteorology, Climate and Consultancy Section, West Perth. All data were acquired at the Leinster Aerodrome meteorological station nr: 12314, Latitude: 27°50'19"S, Longitude: 120°42'11"E, Elevation: 497.0 m.

Table 3.4 and Table 3.5 show the rainfall records at the time of two image acquisitions AQ-I and AQ-II (image details in Table 3.2). These data represent the magnitude of daily rainfall ten days before the image acquisition and one day after the image acquisition.

Table 3.4 *Daily Rainfall data at Leinster study area (AQ-I)*

Date: 1995/Nov/	04	05	06	07	08	09	10	11	12	13	14	15
Rainfall [mm]	0.0	0.0	0.0	0.0	0.0	0.0	n/a	0.0	n/a	n/a	0.0	0.0

Table 3.5 *Daily Rainfall data at Leinster study area (AQ-II)*

Date: 1997/Mar/	09	10	11	12	13	14	15	16	17	18	19	20
Rainfall [mm]	0.0	0.0	0.0	0.0	0.0	0.0	5.0	0.0	0.0	0.0	0.0	0.0

As can be seen from Table 3.4 and Table 3.5, the rainfall record at the time of the image acquisition indicates no rainfall at all. There were only 5 mm of rainfall recorded 5 days prior the acquisition time. Moreover, relative humidity, temperature and mean sea level (MSL) pressure data sampled six times a day are plotted in Figure 3.6. At the time of the image acquisitions (AQ-I, AQ-II), all the meteorological quantities were almost identical. Therefore, it leads to a conclusion that weather conditions during both image acquisitions were very much comparable and should not affect the interferogram interpretation.

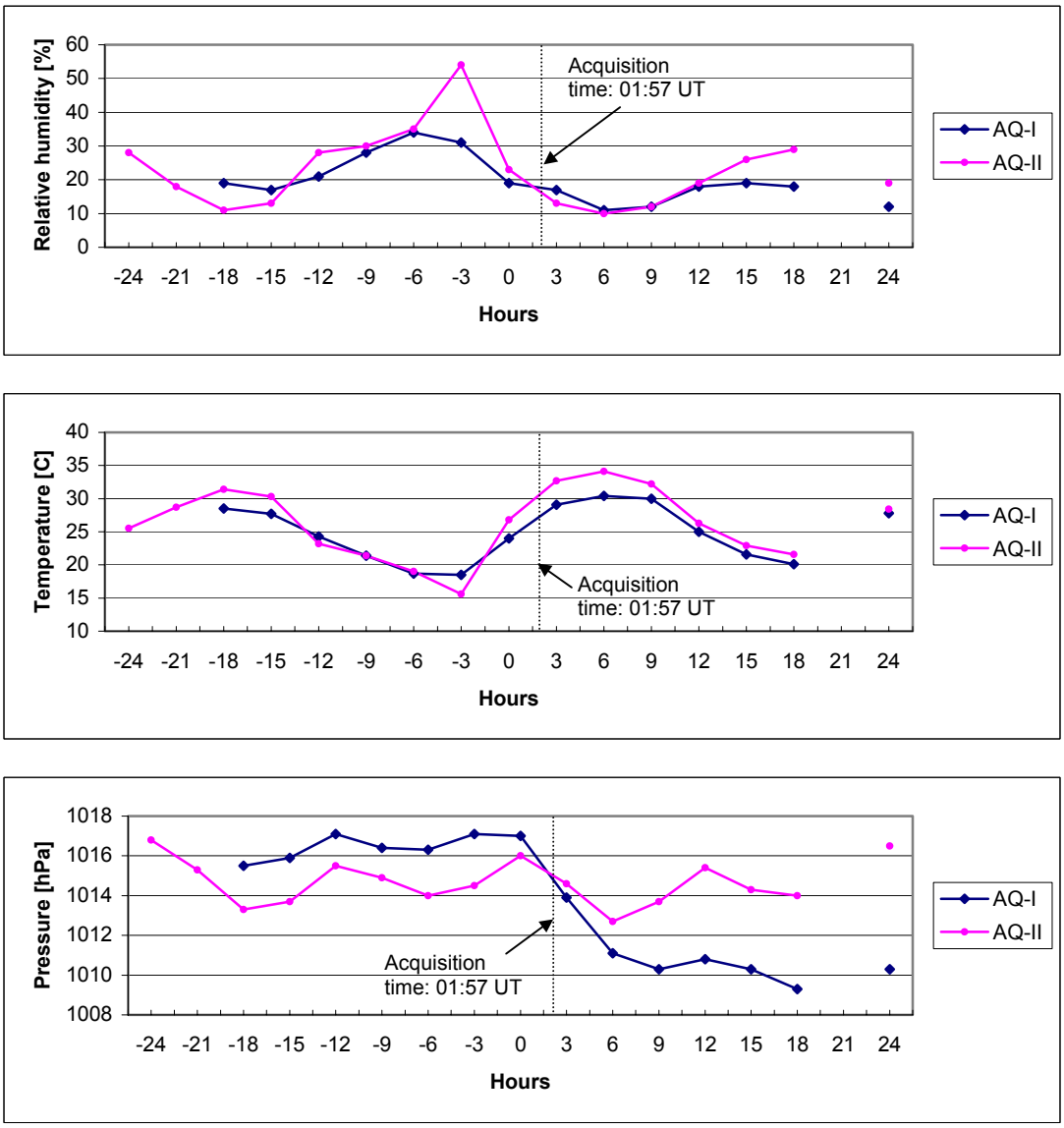

Figure 3.6 *Meteorological data (relative humidity, temperature, and MSL pressure) 24 hours before and after the image acquisitions AQ-I and AQ-II.*

3. 4 Summary

In this chapter the research data and study areas have been introduced and discussed. The selection process of the radar images as well as its limitations were outlined. Moreover, the reference data related to the Leinster study area, such as DEM and methodological observation were described and interpreted.

4 INTERFEROMETRY PROCESSING AND INTERFEROGRAM INTERPRETATION

This chapter investigates the processing steps necessary to create a repeat pass interferogram, a differential interferogram and a coherence map from the SLC SAR data. Apart from particular software available to perform interferometry processing, the fundamental technique and algorithms as well as the most important decisions and problems during the interferometry processing are identified and discussed in detail. Finally, the interferometric data of the Leinster and Silesia study areas are analysed in terms of small-scale surface deformation detection.

4. 1 Processing Software and Hardware

To perform the interferometry processing procedure, the Delft Object-oriented Radar Interferometric Software (Doris) in conjunction with Matlab 6.0 (Matlab, 2004), Snaphu v1.4.2 (Snaphu, 2004), and GMT v3.4 (GMT, 2004) software have been used.

The Doris interferometry software was developed at Delft University of Technology and is available for all popular platforms. It is written in C++ and has a modular structure. Each module identifies a different algorithm for a different processing step. The user can select the modules and algorithms that best suit their needs for a certain interferometric application. The current version of Doris v.3.7 is capable of processing SLC images for the basic interferometric products (Kampes and Usai, 1999).

All the interferometry processing has been performed on a SunBlade 100 UNIX Workstation. The major hardware specifications are listed in Table 4.1.

Table 4.1 *UNIX workstation specifications*

Architecture	500-MHz Ultra SPARC-IIe
Memory (RAM)	1152-MB
Hard Drive	20-GB, 7200-rpm, EIDE
CD-Rom	48X-speed
Graphics	On-board, 24bit, Sun(TM) PXG64 2D Graphics
Monitor	21-inch, colour, 1600x1200 max resolution
Operating System	Solaris 8 release (07/2001)

4. 2 Interferometry Processing

Figure 4.1 illustrates the entire interferometry processing chain. It contains all the interferometry stages including image acquisition and SAR focusing processing. There are six major processing stages necessary to compute a coherence map, interferogram and differential interferogram, which are considered in this chapter, assuming that radar data have already been acquired and pre-processed (focused) to SLC images by a data supplier (PAF centres in the case of ESA). Thus, the interferometry processing stages can be divided into (i) data preparation, (ii) coregistration of the radar images, (iii) products generation (coherence, interferogram), (iv) filtering of the phase image, (v) topography correction and unwrapping and (vi) geocoding. In the following sections these stages are illustrated by following the processing procedures for the Leinster data set.

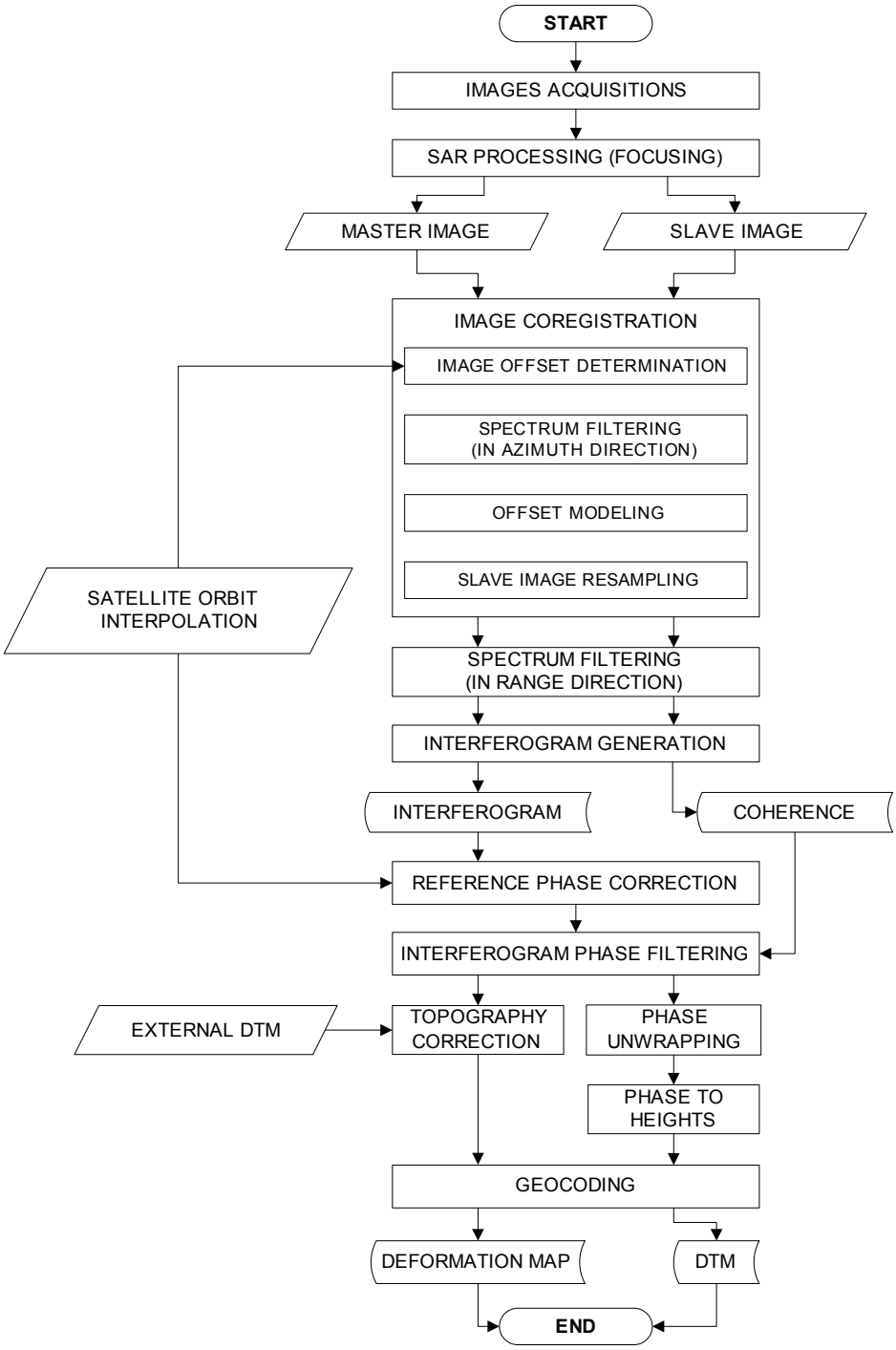

Figure 4.1 *Interferometry processing chain.*

4.2.1 Image Reading

For the analysis of interferometry processing steps, two radar images acquired over the Leinster study area AQ-I and AQ-II (image details in Table 3.2) were chosen as the master and slave, respectively. The ERS SLC SAR images were delivered on a CD-ROM. In order to perform interferometry processing, parts of the images have

been cropped and saved. Figure 4.2 shows the intensity image (E) of the selected part of the master image defined as:

$$E = \left|g(x,y)\right|^2 \tag{4.1}$$

where $\left|g(x,y)\right|$ is the amplitude of a complex number (Equation 2.7).

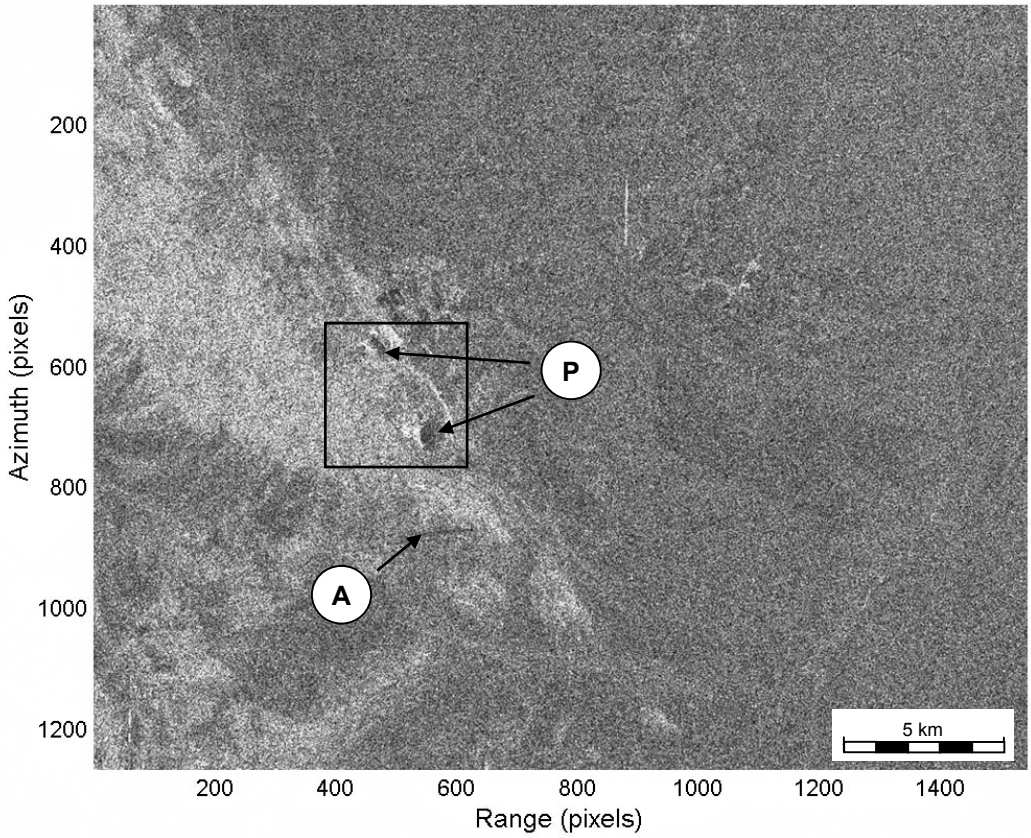

Figure 4.2 *Intensity image. The rectangular shape shows the mine site area. Two open pits (P) and the airstrip (A) are clearly visible. The white colour represents high intensity whereas the dark indicates areas of low intensity of the returned signal.*

4.2.2 Satellite Orbit Interpolation

To obtain the precise orbit of the satellites, the DEOS program Getorb and satellite orbit ephemeredes described in Section 3.2.4 have been used. Based on the image acquisition time and the image size in azimuth direction, the satellite ephemeredes were extracted from ODR files and interpolated (cubic splines) into one-second intervals. Accurate time and image size are provided in the image header file. The

satellite ephemeredes are then converted into the output table in the following order: second_of_day, x, y, z. The orbit coordinate system is WGS84. To avoid boundary effects due to the interpolation process, a 6 second interval was applied before and after the required image acquisition time.

4.2.3 Image Coregistration

Before interferogram computation, the coregistration process of lining up two images (master and slave) covering the same area must be undertaken. Coregistration can be defined as a geometric image transformation function and subsequent resampling of the slave image in such a way that each ground point is located at the same position in both images (Franceschetti and Lanari, 1999, p178). The sub pixel accuracy of the coregistration process is necessary to obtain coherent interferometric products. The following sections describe the coregistration procedures.

4.2.3.1 Image Offset Estimation

If images of the same scene are produced from several acquisitions, which is the case for repeat pass interferometry, they will not overlay exactly. Due to the different starting time of image acquisition and nonparallel orbits, the shift in azimuth direction can reach several thousands of pixels while the shift in range direction is usually smaller and can reach up to several pixels. Therefore, the offset in range and azimuth direction must be evaluated in order to shift the slave image to best fit the master image. Moreover, sometimes a rotation is required to better match both images. Therefore, to estimate the offset between two images, the following steps are taken: (i) coarse offset determination, (ii) coarse registration, (iii) azimuth filtering and (iv) fine registration.

The *coarse offset* between the master and slave images can be determined based on precise orbit information. This is the fastest approach to obtain the coarse offset within an accuracy of about 30 pixels. For an arbitrarily chosen point $G^{M}_{A,R}$ (usually in the centre) on the master image, the position *G(x,y,z)* in the satellite orbits coordinate system is determined. Next, given this position, an iterative algorithm searches along the slave orbit until the correct Doppler position is found from which

point *G(x,y,z)* was observed, and the coordinates of the corresponding point in the slave image $G^{S}_{A,R}$ are determined (Kampes, 2000, p26). Finally, the difference between the azimuth and range coordinates of the slave and master images define the offset $O^{C}_{A,R}$ as:

$$O^{C}_{A,R} = G^{S}_{A,R} - G^{M}_{A,R} \tag{4.2}$$

where *A* and *R* are the coordinates in azimuth and range direction, respectively.

After determining the coarse offset, the coarse registration procedure is applied. The purpose of coarse registration is to determine one offset for the entire image, but with an accuracy of about one pixel. To perform this task, the cross-correlation technique (Gabriel and Goldstein, 1988) based on the magnitude (squared amplitude) of both images, for a number of evenly distributed locations over the entire image, is applied. The procedure consists of presenting a set of different offsets for a given position and determining the correlation between the images for each offset. The initial coarse offset has been estimated in the previous step based on the satellite ephemerides. The offset with the highest correlation is the estimation for a particular position. Finally, the offset with the highest number of occurrences over the entire number of different positions is recognised as the approximate offset between master and slave image. Although the computations can be performed in the space domain, the FFT method in the spectral domain is applied in order to decrease computation time.

Due to differences in Doppler centroid frequency, the spectrum of the master does not overlap entirely with the spectrum of the slave image. This is very often the case if the raw radar data have been focused (pre-processed) to SLC format using a fixed and different Doppler centroid frequency. Therefore, by applying band pass filtering, the spectrum (in azimuth direction) of the master image that does not overlap with the spectrum of the slave image can be filtered out. This approach improves the coherence between both images and reduces the noise in the interferogram. At the same stage, the spectrum of the slave image is also filtered. Figure 4.3 shows this process for the master and slave spectrums.

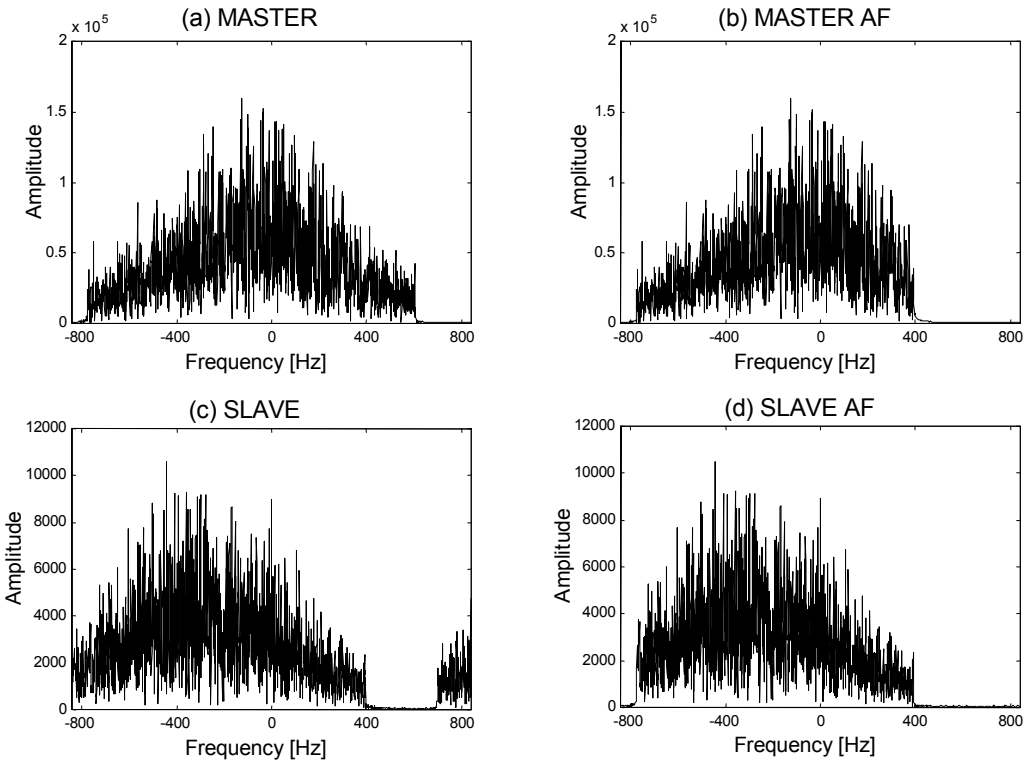

Figure 4.3 *The spectrum of master (a) and slave (c) images before azimuth filtering. Plots (b) and (d) show the overlaying spectrum of both images as a consequence of the spectral filtering.*

As a result of coarse registration, the offset between master and slave images has been determined with an accuracy of approximately one pixel. Next, the *fine registration* step is performed in order to deliver a large number of offsets at evenly distributed locations with sub pixel accuracy. The same cross-correlation technique as described in coarse registration is used. However, the number of correlation windows is significantly increased to a few hundred. The number of windows depends on the size of the image. Moreover, the distribution of the correlation windows should be dense enough to evenly cover the entire image.

To avoid aliasing due to the doubled bandwidth of the cross-correlation product compared to master and slave images, both images are oversampled before cross-correlation. As suggested by Prati and Rocca (1990) the oversampling factor of 8 has been applied for the FFT interpolation. This will ensure a coregistration accuracy of about 1/8 of a pixel. According to Just and Bamler (1994), the coregistration error does not introduce a phase bias. However, it does introduce

additional phase variance. Furthermore, coregistration to the accuracy of about 1/8 of a pixel is sufficiently accurate and yields almost negligible decrease in coherence.

4.2.3.2 Offset Vector Modelling

To determine the offset vector for every pixel in the slave image, the transformation model is determined based on the offsets established in the fine registration step. Only offsets characterised by coherence values greater than a given threshold are selected to determine the model parameters. As a result, the number of available observations is decreased while the accuracy of the model is increased, as the offsets characterised by very low coherence are disregarded. To model the offsets, a two-dimensional polynomial of degree one is applied. The observation equations are defined as:

$$\begin{bmatrix} O_1 \\ O_2 \\ \vdots \\ O_N \end{bmatrix} = \begin{bmatrix} 1 & A_1 & R_1 & A_1^2 & \cdots & R_1^d \\ 1 & A_2 & R_2 & A_2^2 & \cdots & R_2^d \\ \vdots & & & & & \\ 1 & A_N & R_N & A_N^2 & \cdots & R_N^d \end{bmatrix} \cdot \begin{bmatrix} C_{A=0,R=0} \\ C_{10} \\ C_{01} \\ C_{20} \\ \vdots \\ C_{0d} \end{bmatrix} \tag{4.3}$$

where O_i are the observed offsets (product of fine registration step), A_i and R_i are the locations in azimuth and range direction, respectively, of the observed offsets, and C_{AR} are the unknown coefficients of the polynomial.

Figure 4.4 and Figure 4.5 show the absolute errors defined as estimated offsets minus the observed offsets for the processed data set, in range and azimuth direction respectively. The absolute errors (e) are small and equally distributed in the range and azimuth direction. However, the correlation of the offset is rather poor, though it is sufficiently high for interferometry processing studies.

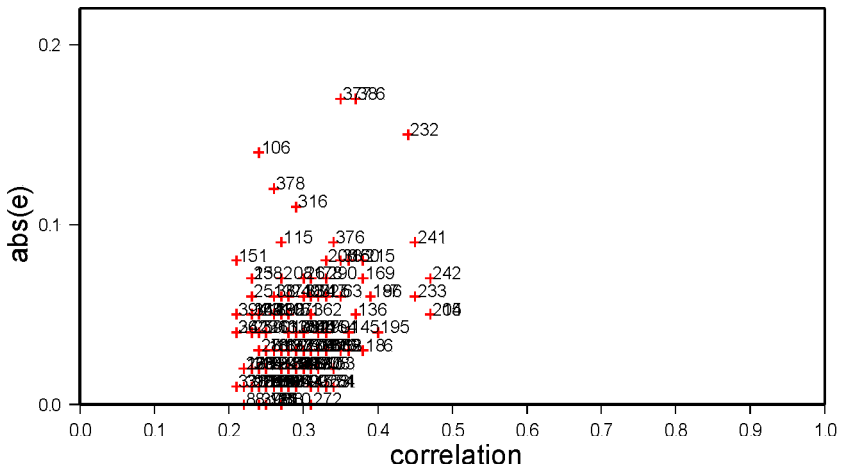

Figure 4.4 *The absolute error (e) in range direction (estimated offset minus observed offset) for the number of correlation windows.*

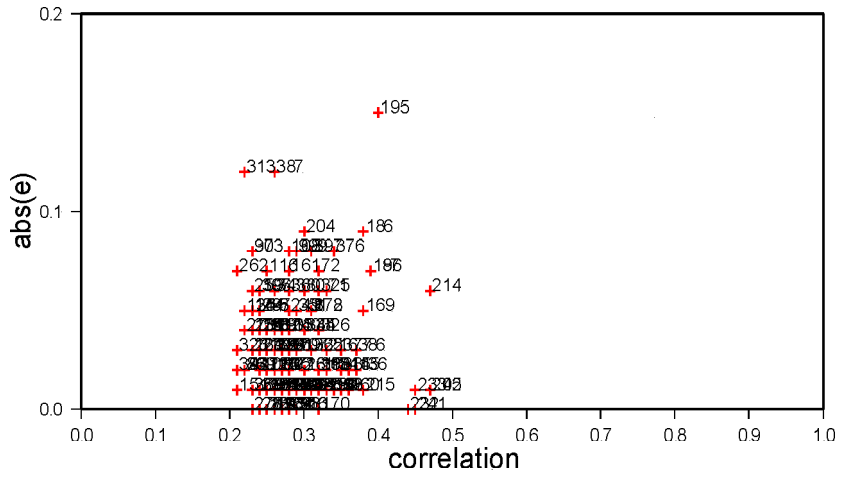

Figure 4.5 *The absolute error (e) in azimuth direction (estimated offset minus observed offset) for the number of correlation windows.*

4.2.3.3 Resampling

In this procedure, the slave image is resampled according to the estimated transformation model. This step involves the reconstruction of the continuous signal of the slave image from its sampled version, and sampling of the reconstructed signal at the new grid location. The reconstruction of the slave image signal is usually achieved by convolution with an interpolation kernel. The six-point cubic spline interpolation kernel is applied, which according to the study conducted by Hanssen and Bamler (1999), creates minimal decorrelation and a low level of phase noise in the resulting interferogram.

Moreover, due to the difference (220.243 Hz) between the Doppler Centroid Frequency (FDC) of the master and slave image, the resampling procedure is processed with the azimuth spectrum shifted to the zero Doppler frequency before interpolation. Then, the interpolated signal is shifted back to the original FDC.

Slightly different viewing angles of the SAR sensor (different local incidence angles) will create a spectral shift in the range direction of the radar data. It is yet another potential source of phase noise in the interferogram. Thus, *range filtering* is performed before the generation of interferometric products. The idea of range spectral filtering is the same as azimuth spectral filtering described in Section 4.2.3.1 and consists of filtering out the non-overlapping parts of the spectrum using a band pass filter.

4.2.4 Interferometric Product Generation

In the following section, interferometry products, such as interferogram, coherence map and differential interferogram, are generated and discussed in detail.

4.2.4.1 Interferogram

As defined in Equation 2.11, a complex interferogram is constructed by a point-wise multiplication of corresponding pixels in the master and the complex conjugate of slave image. The phase image of the complex interferogram represents the phase difference between two SAR data sets while the amplitude image contains the useful information on the SNR of the observed phase. If the images are delivered from two repeat SAR acquisitions, usually the resulting phase image is called a *repeat pass interferogram* or *interferogram* for short. Figure 4.6 shows the phase image of the complex interferogram for the Leinster study area. The magnification of a small area reveals the details of the interferogram. Vertical fringes corresponding to the uniform surface of the Earth are clearly visible and in some places are disturbed by the topography or some decorrelations. Before further analysis and computation, the phase corresponding to a reference surface needs to be removed. This processing step is described in the following section.

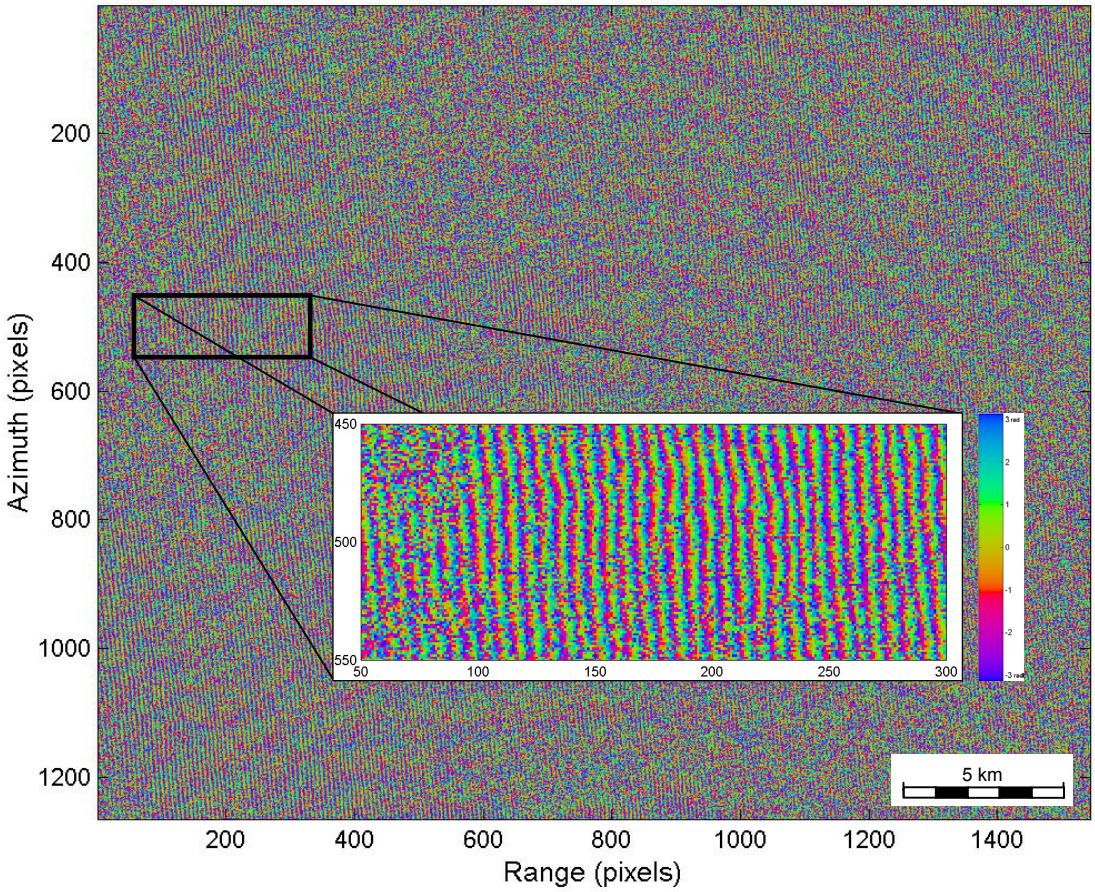

Figure 4.6 *Phase image with visible flat Earth pattern (pixel size is 20x20 m).*

4.2.4.2 Reference Phase Correction

The usefulness of the interferometric phase starts at the time when the component called the '*flat Earth*' caused by the reference surface is removed. The theoretical background of the interferometric phase was provided in Chapter 2. However, at the pixel level, the interferometric phase $\phi_{i,j}^{I}$ can be defined as:

$$\phi_{i,j}^{I} = \phi_{i,j}^{M} - \phi_{i,j}^{S} - \phi_{i,j}^{R} \tag{4.4}$$

where the $\phi_{i,j}^{M}, \phi_{i,j}^{S}, \phi_{i,j}^{R}$ are the phase value of master image, slave image and reference phase, respectively, at pixel location *i*,*j*.

Since the values of both images are complex, the phase difference also has to be evaluated in complex fashion as:

$$\phi_{i,j}^{I} = \arctan_2\left(I_{i,j}^{imag}, I_{i,j}^{real}\right) \quad \text{where} \quad I_{i,j} = M_{i,j} \cdot S_{i,j}^{*} \cdot R_{i,j}^{*} \tag{4.5}$$

where I is the complex interferogram, $\arctan_2$ is the four-quadrant arc tangent, and (*) is the complex conjugate.

The reference phase is computed for a number of points distributed over the master image based on precise satellite orbits. The reference phase for the entire image is than estimated based on those points. Finally, the reference phase is subtracted at each pixel to produce an interferogram as shown in Figure 4.7.

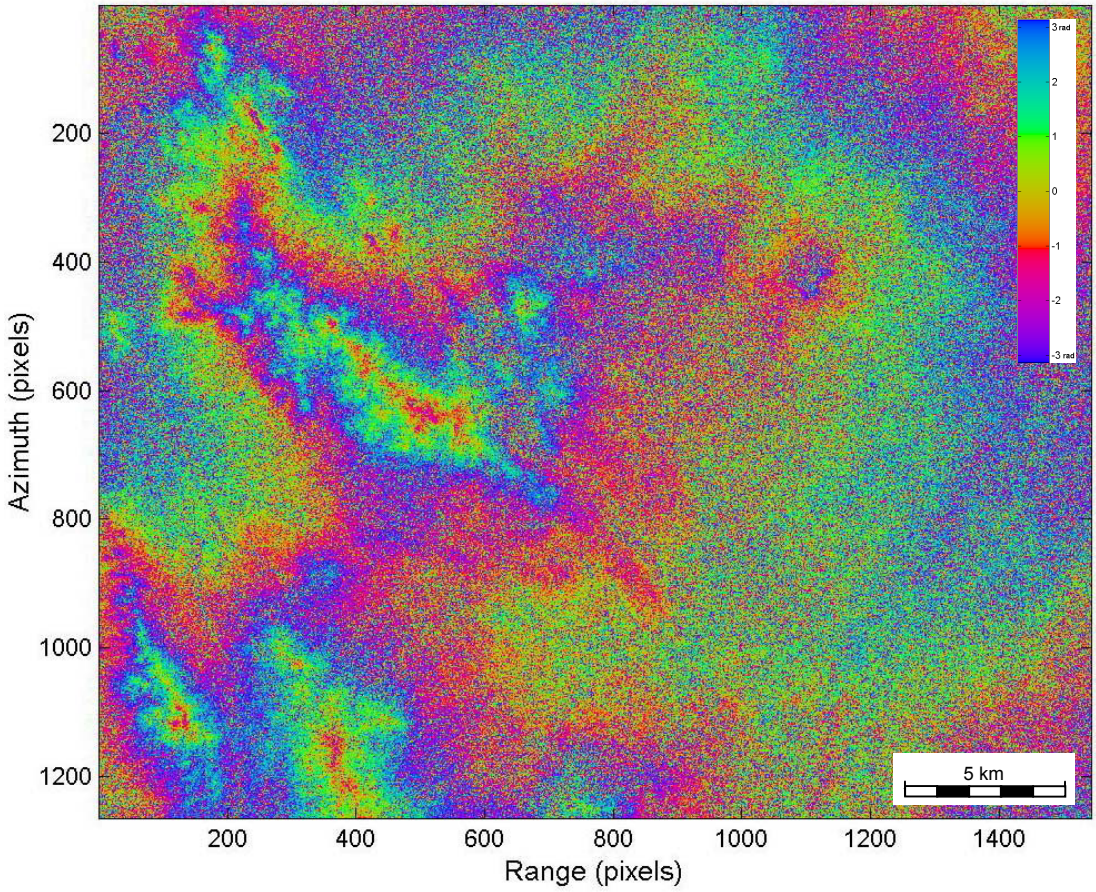

Figure 4.7 *The phase image of the complex interferogram. The reference phase has been subtracted. Visible fringes corresponding to local topography (1 fringe ≈ 41 m)*

The remaining fringes correspond to the local topography as well as possible deformation. The colour bar shows the interferometric phase in radians. One whole phase cycle corresponds to approximately 41 m difference in elevation. In this

interferogram two fringes are visible, which indicates a maximum terrain elevation of up to 80 m.

The resolution of the interferogram plays a very important role, especially when the purpose of interferometry is to detect deformations of small spatial phenomena, for instance, mining related surface subsidence. Commonly used multilooking requires a compromise between reduction of the phase noise and the spatial resolution. By applying the multilooking factor 5:1, only the resolution in the azimuth direction is reduced and a pixel of equal size (approximately 20x20 m for ERS-1/2 SLC data) is created.

4.2.4.3 Coherence Map

In the process of coherence map computation it is assumed that the reference phase has been subtracted from the interferogram. The complex coherence (Equation 2.23) between two images is estimated based on the assumption that the accuracy of the phase observation of a uniform region is stationary. Therefore, it allows the computation of the local complex correlation between any two coregistered complex images by complex correlation computation over a small moving window. To estimate the coherence, the maximum likelihood estimator given by Seymour and Cumming (1994) is applied:

$$\hat{\gamma} = \frac{\left|\sum_{i=1}^{Nr} g_{M_i} g_{S_i}^{*}\right|}{\sqrt{\sum_{i=1}^{Nr}\left|g_{M_i}\right|^2 \sum_{i=1}^{Nr}\left|g_{S_i}\right|^2}} \tag{4.6}$$

where *Nr* is the number of pixels within the correlation window (*e.g.* 25 pixels for 5x5 pixels window). The maximum likelihood estimation is a technique for estimating constant parameters associated with random observations or for estimating random parameters from random observations when the distribution of the parameters is known.

Not only is coherence useful for assessing the accuracy of the interferometric phase, the coherence map is also a suitable tool for land classification and change detection

in the biomass as shown by Engdahl and Hyyppä (2000), Martinez *et al.* (1998), Strozzi and Wegmüller (1998), and Borgeaud and Wegmüller (1996).

As radar imagery is highly sensitive to changes in soil moisture content, coherence maps are particularly useful for soil classification, in terms of highlighting different moisture content over arid and dry deserts. Therefore, such maps can be recommended for use as an additional tool in the agriculture industry. Figure 4.8 shows the coherence map of the Leinster study area.

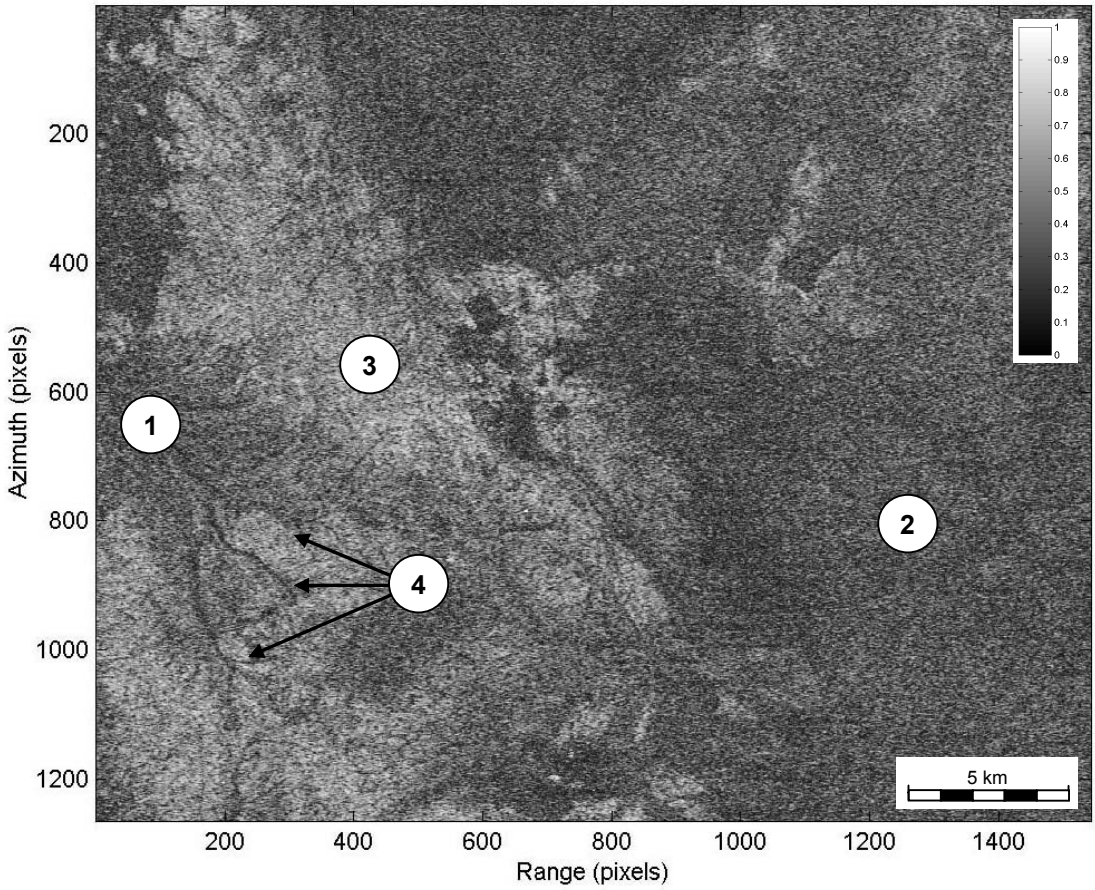

Figure 4.8 *Estimated coherence map over the Leinster study area. The white colour indicates area where the coherence is high. Simple land classification based on coherence value: (1) valley, (2) bush, (3) hills, and(4) streams.*

Four distinct areas were recognised and designated certain values according to their soil moisture content: (1) valley and (2) bush where the coherence value is low due to accumulation of moisture. This factor intensifies the vegetation and the biomass, as compared to (3) hills, where dry soil dominates. Furthermore, areas of stream

flows (4) could be recognised despite the dry season during image acquisitions (meteorological data are discussed in Section 3.3.2).

4.2.4.4 DEM Radar Coding

In order to achieve a differential interferogram, the topography component must be removed from the complex interferogram. Therefore, an additional source of information about the surface topography is needed. In this processing stage, an existing 9"DEM is modified via radar coding according to the grid of the interferogram. Radar coding is a process of converting the DEM heights (differences in heights, precisely) into the related unwrapped phase value (ϕ^{DEM}) at each pixel location. It is important that both the interferogram and DEM have the same sampling size.

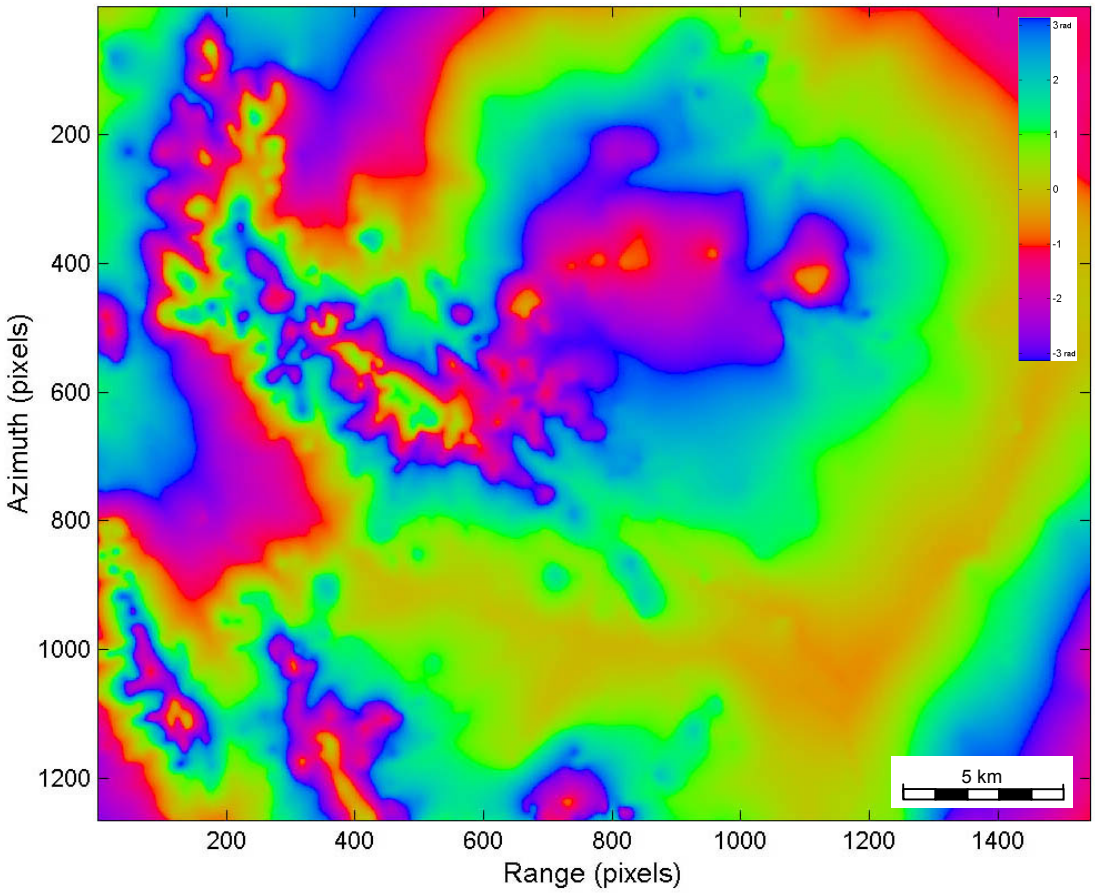

Figure 4.9 *Wrapped phase of the radar coded 9"DEM.*

Figure 4.9 shows the wrapped phase of the DEM. As can be seen, the topography fringes match very well with the interferogram (Figure 4.7) generated from SAR images.

4.2.4.5 Differential Interferogram

The differential interferogram (*DF*) is computed by subtracting the topography-related phase (ϕ^{DEM}) from the complex radar interferogram (*I*). This is performed at each pixel location (*i,j*) according to the following equation:

$$DF_{i,j} = I_{i,j} \cdot \exp(-i \cdot \phi_{i,j}^{DEM}) \tag{4.7}$$

The resulting differential interferogram can be seen in Figure 4.10. Since no major deformation occurred between image acquisitions, the differential interferogram did not reveal any deformation-related phase changes. However, a residual phase trend, which spanned diagonally over the entire differential interferogram, has been detected. Proper identification of such a phase trend would help to eliminate it from the differential interferogram, as proposed by Hanssen (2001, p123), or Massonnet and Feigl (1998). However, the correct interpretation of the origin of the diagonal strip is not immediately obvious. Three possible reasons that could cause this long wavelength trend in the differential interferogram have been identified. These are (i) atmospheric artefacts, (ii) DEM error, and (iii) satellite orbit error.

Atmospheric artefacts may be rejected because weather conditions were comparable during both image acquisitions. The interpretation of weather conditions over the entire scene has been made based on meteorological data collected at one ground weather station located in the centre of the imaging scene (see Section 3.3.2). Such an approach is considered to be very reliable. Although, only one source of meteorological data was available, the regular shape of the trend is unlikely to be the product of turbulent weather nature.

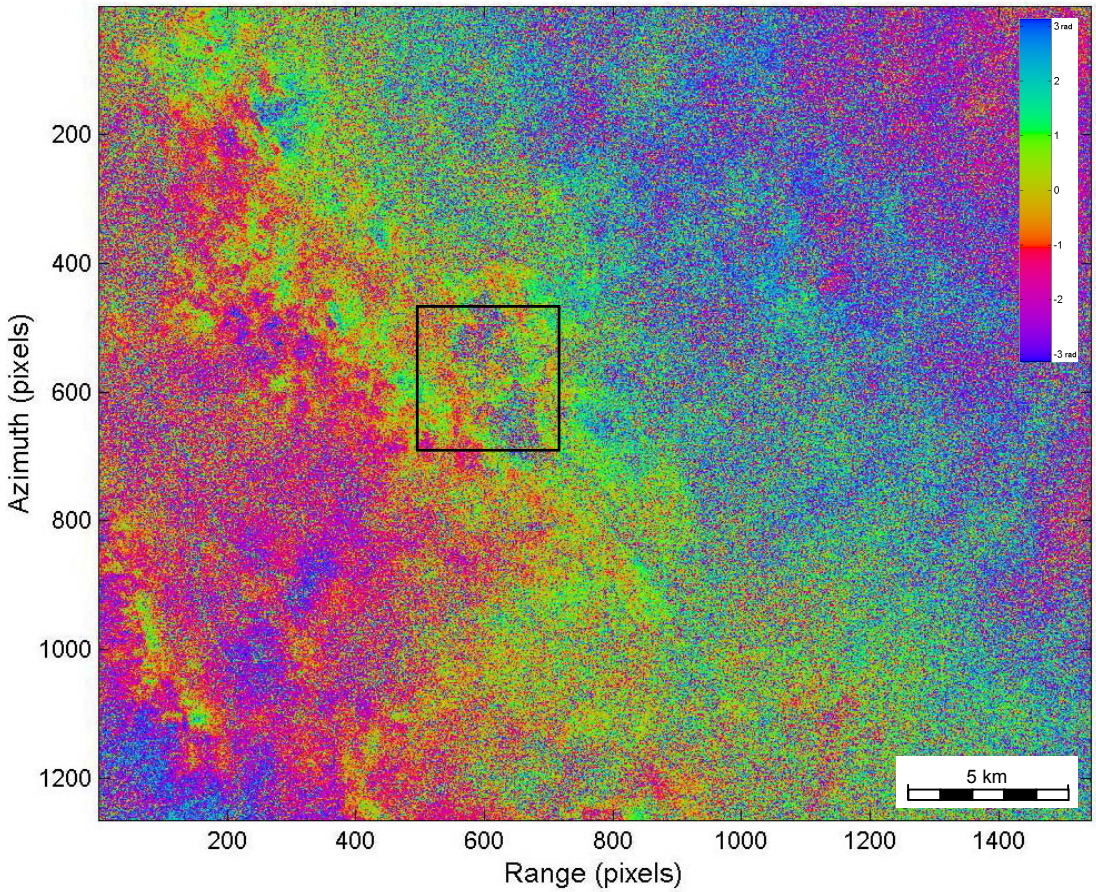

Figure 4.10 *Differential interferogram. Topographic information has been removed from the complex interferogram using 9"DEM. The rectangular window indicates the mine site location.*

A series of tests were carried out in order to determine if the 9"DEM is the source of the long wavelength trend in the differential interferogram. These tests rely on a number of processing steps using the same DEM, but slightly shifted in different directions from its original location. Each time the DEM was shifted, the process of radar coding and phase subtraction was performed and the resultant differential phase image analysed. The DEM was shifted from its original location by 120, 240, 440 and 960 metres in eight different directions (vertical, horizontal and crosswise). Each version of the new differential interferogram appeared to increase the phase trend. Thus, the error due to DEM, especially its misregistration with the interferogram, was also rejected. Therefore, the residual phase is most likely caused by an orbital error of the satellites.

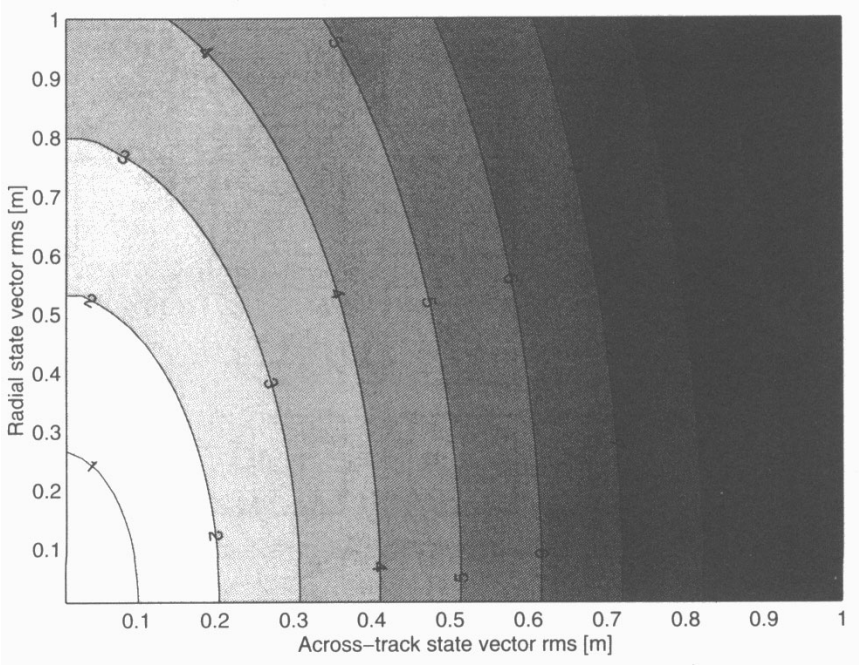

Figure 4.11 *Residual fringes due to radial and across-track state vector RMS errors with 95% confidence level that the maximum amount of fringes is less than shown (after Hanssen, 2001, p124).*

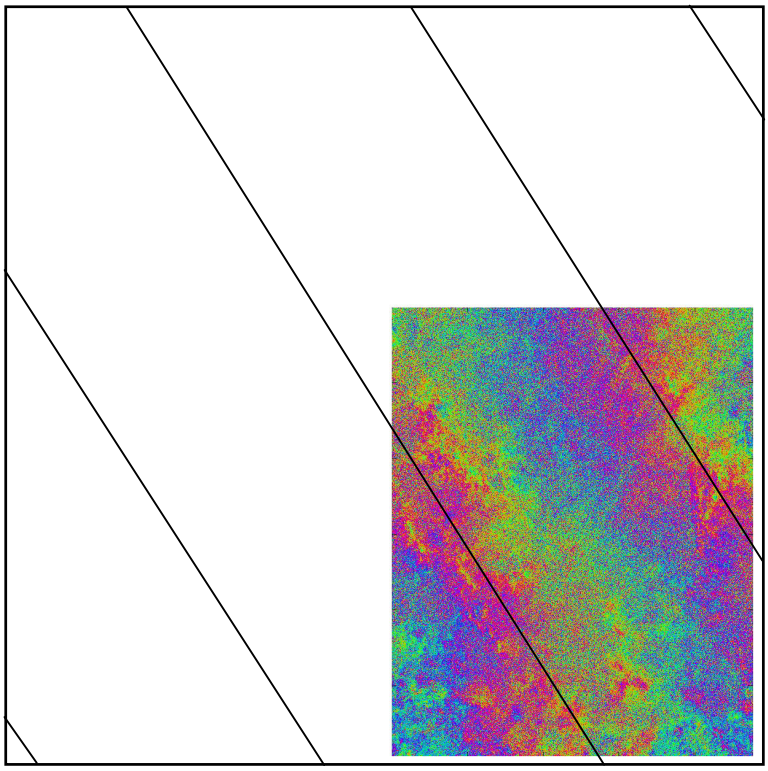

Figure 4.12 *Reconstructed residual phase trend for the whole frame 4164.*

As mentioned in Section 2.9, orbital errors are capable of creating residual phase trends in interferograms. Therefore, such an error was concluded to be the most

likely cause of the residual phase trend in Figure 4.10. The number of residual fringes can than be used to estimate the magnitude of the orbital error. To this aim, the graph (Figure 4.11) proposed by Hanssen (2001, p124) was utilised. Notably, the Hanssen graph was build based on the satellite orbits provided by Delft Institute for Earth-Oriented Space Research (DEOS), a source that is identical to that used in this research.

Since the research images cover one quarter of the whole scene, the residual phase has been reconstructed for the whole frame as shown in Figure 4.12. As a result, four residual fringes have been identified for frame 4164. According to the graph (Figure 4.11), these fringes translate to a RMS of about 0.4 m across-track and more than 1.0 m along-track of the state vector.

4.2.5 Phase Unwrapping

The phase signal in the interferogram is given modulo 2π. Thus, the correct integer number of the whole phase cycles has to be found in order to obtain the absolute phase signal. However, due to the presence of the phase noise as well as the layover and shadow phenomena, the phase unwrapping process is the most complex and crucial of the entire interferometric processing chain.

Applying the filtering techniques to the wrapped phase interferogram will reduce the level of noise and improve the unwrapping process. Therefore, it can improve the quality of DEMs as well as deformation maps. However, while filtering reduces noise in the interferogram, it does not necessarily enhance or recover the signal. Moreover, the impact of the filter can significantly change the structure of the interferogram.

In order to reduce the phase noise, the adaptive radar interferogram filter proposed by Goldstein and Werner (1997) has been applied. However, while using this filter, the problem of losing resolution in the filtered phase was identified, which agrees with the observation of Goldstein and Werner (1998).

Figure 4.13 and Figure 4.14 show the wrapped phase interferogram before and after applying the Goldstein radar interferogram filter. The reduced level of phase noise is clearly visible.

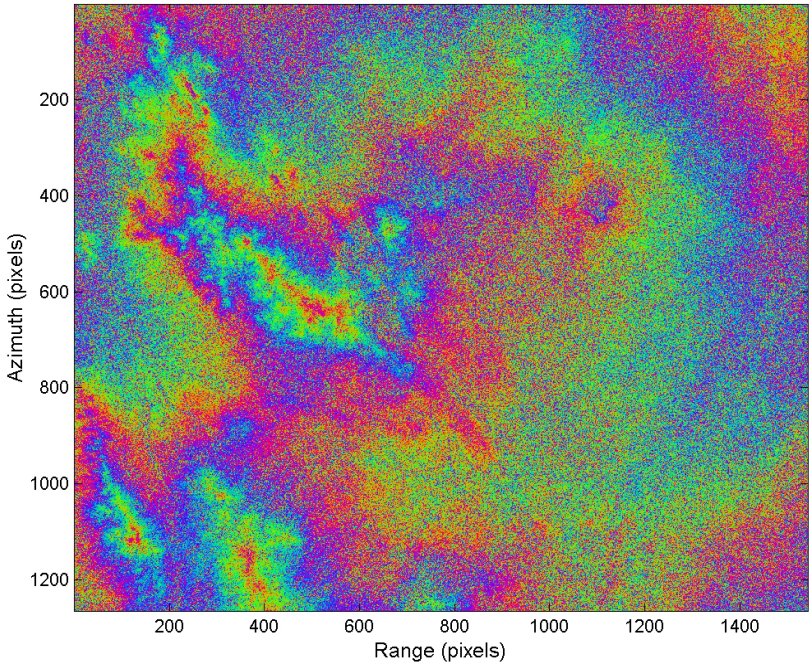

Figure 4.13 *Wrapped phase interferogram – unfiltered.*

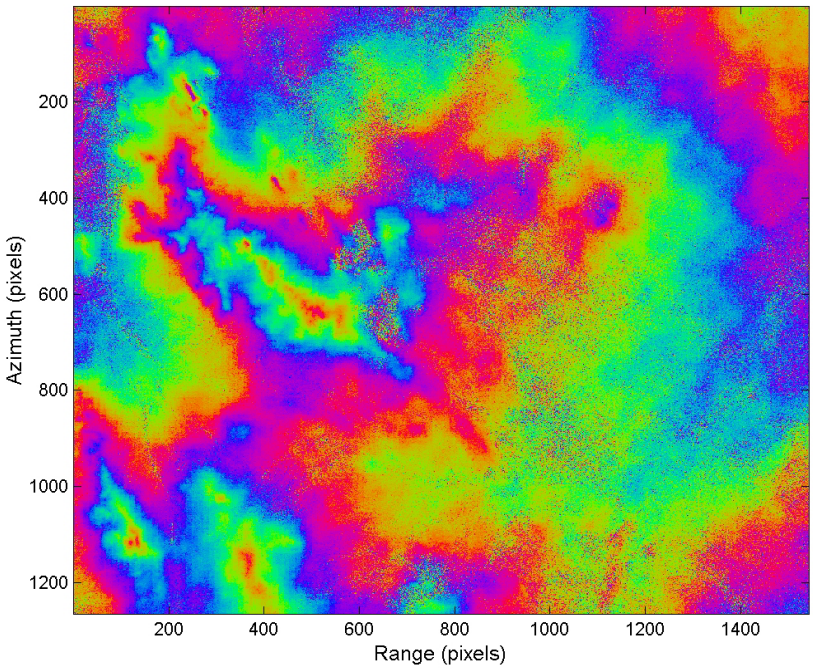

Figure 4.14 *Wrapped phase interferogram – filtered using Goldstein radar interferogram filter.*

The unwrapping process was performed using Snaphu v.1.4.2, software that uses a statistical-cost, network-flow algorithm proposed by Chen and Zebker (2001, 2000). Figure 4.15 shows the unwrapped phase image. Apart from an area of the interferogram that suffered from high decorrelation associated with mining development, the phase unwrapping algorithm did not encounter major problems.

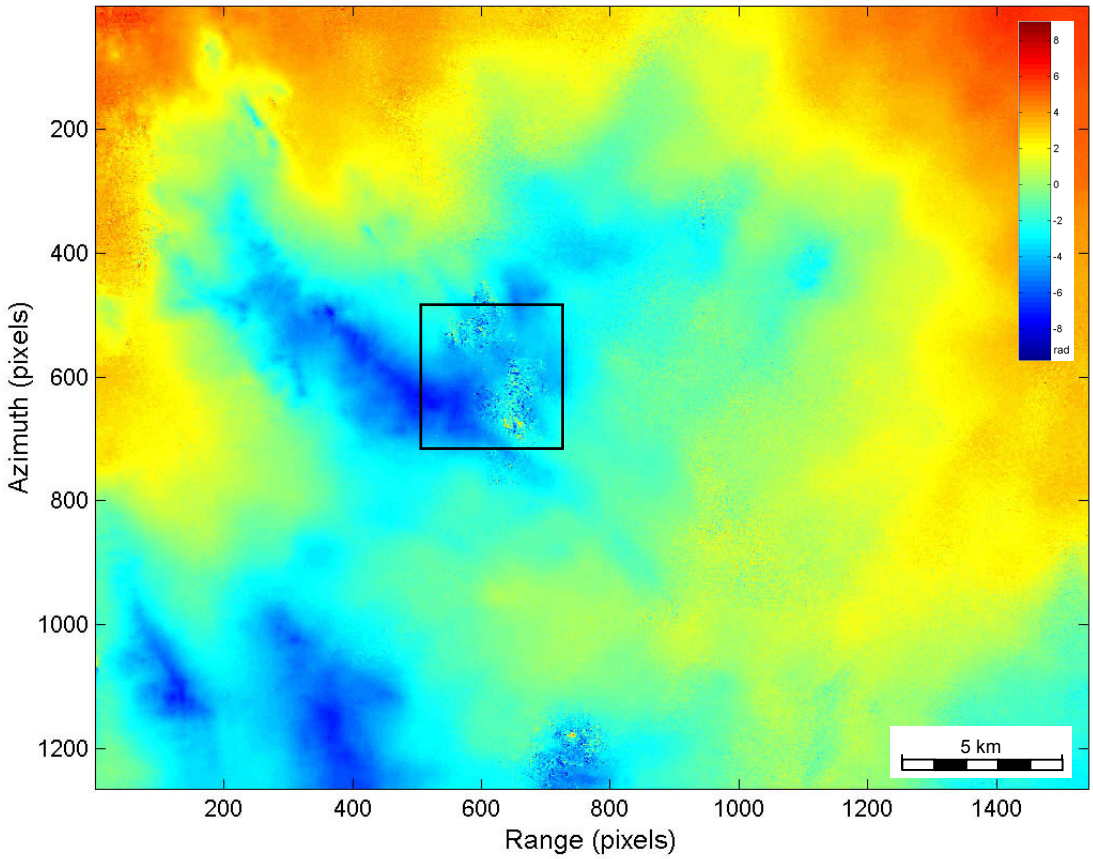

Figure 4.15 *Unwrapped phase image. Visible phase variation over the mine site area (rectangular box).*

4.2.6 Phase to Height Conversion

In this processing step, the interferometric phase is converted into the related topographic height. Different approaches exist to achieve this interferometric phase conversion (*e.g.* Rodriguez and Martin, 1992). However, the preferred method of computing topographic heights based on the height ambiguity has been used. The theoretical relationship between the topographical height and phase difference is given in Section 2.5. Nevertheless, it has to be stressed that the reference phase due to the *flat Earth* has to be removed prior to this processing step. Furthermore, the

topographical height remains in the radar coordinate system (range and azimuth) and therefore, a transformation procedure is required to provide data in a geo-referenced format.

4.2.7 Geocoding

Interferometry data are useful for further analysis, such as comparisons with external surveying and geological maps, as long as they are delivered in a common reference system. Thus, geocoding transforms the radar products from a coordinate system related to InSAR geometric configuration (range, azimuth and height) to a convenient geodetic reference.

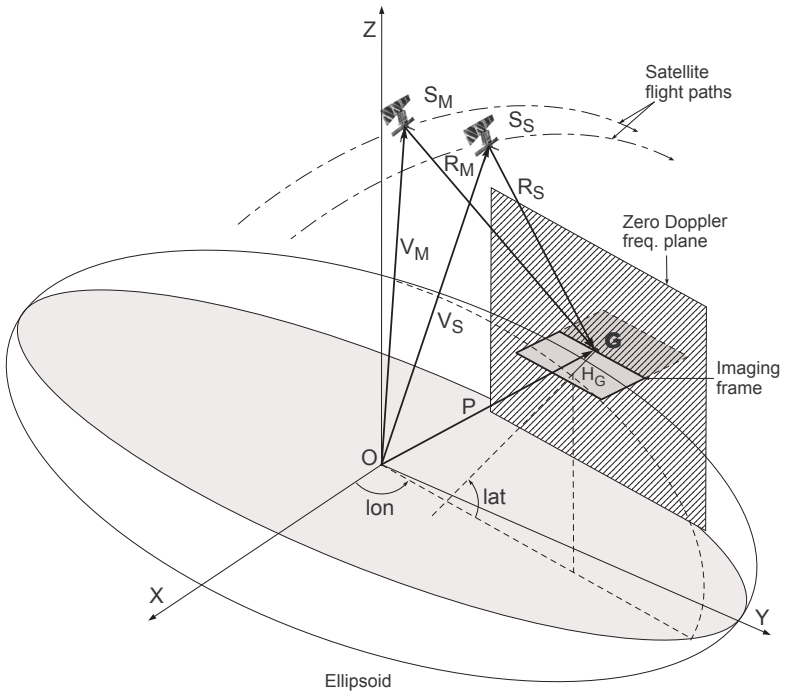

Figure 4.16 *InSAR geometry with respect to the Cartesian (x,y,z) and geodetic (lon,lat,h) reference systems.*

To geolocalise a given point *G*, the necessary set of information includes (i) the state vectors (V_M,V_S), (ii) satellite velocities, and (iii) the range distances (R_M, R_S) of the master and slave satellites. Figure 4.16 shows the InSAR geometry with respect to reference systems. Provided that the interferometric phase is unwrapped, the unknown coordinates of the point G(x,y,z) can be evaluated by solving the nonlinear system of four equations as shown by Franceschetti and Lanari (1999, p214).

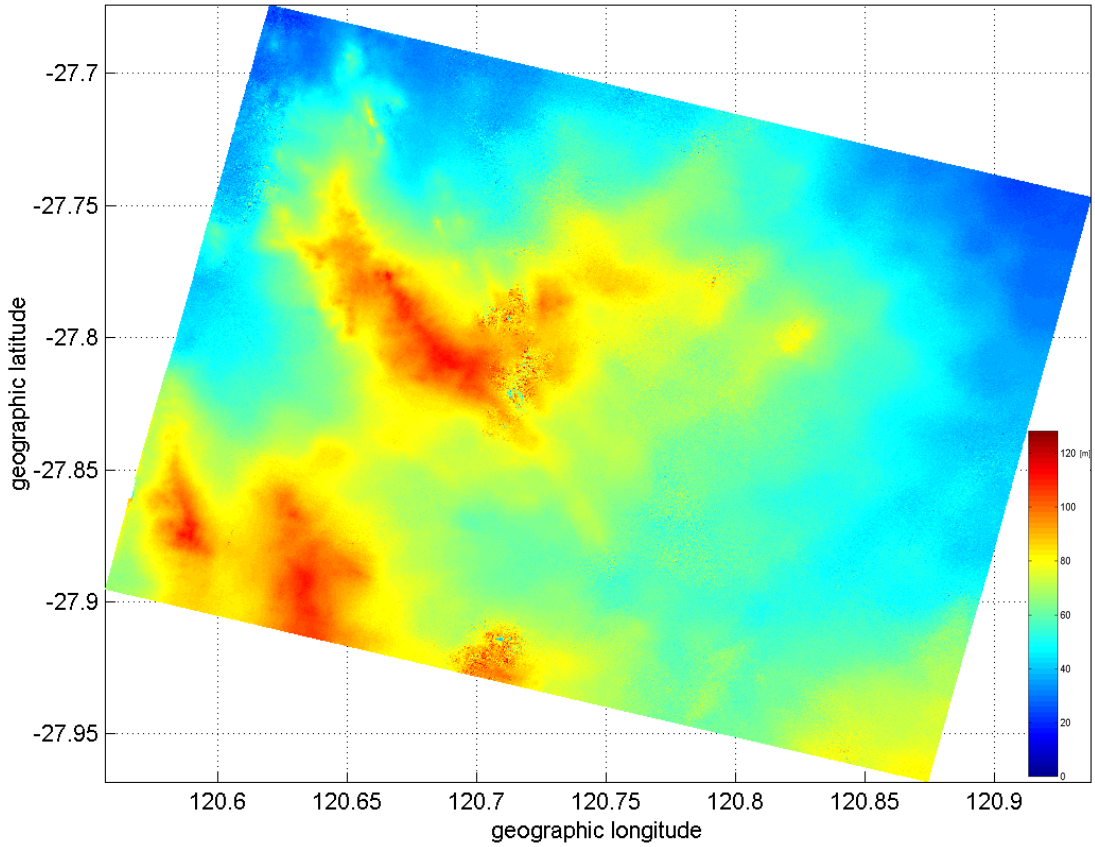

Figure 4.17 *DEM derived from InSAR over the Leinster study area.*

Once the position of the point *G* is known in the Cartesian coordinate system, the longitude and latitude can easily be derived using any of the available transformation methods.

Figure 4.17 shows the geolocalised DEM. However, since the InSAR technique is based on the observation of the relative changes of the interferometric phase values, the terrain heights inherit the same characteristic. Thus, in order to provide the DEM in a proper height reference system, the true terrain height has to be known for at least one point, so that the DEM can be properly transformed.

4. 3 Interferogram Interpretation of the Leinster Mine Site

The differential interferogram analysed is a product of two archived images AQ-I and AQ-II acquired on 14.11.1995 and 19.03.1997 respectively. During this period of time, no major deformation around the pit occurred. However, as shown in Figure 4.18a, the differential interferogram shows extremely large phase variation over the

open pit and waste. This is interpreted as the phase noise due to temporal decorrelation associated with the mining development and likely due to the deformation that was initiated at the beginning of 1997. Unfortunately, this cannot be proven due to the absence of suitable surveying data. The coherence map (Figure 4.18b) corresponding to the same areas also shows very low values (0.3 and less). Figure 4.18c illustrates the interferometric phase image superimposed on the intensity image for better orientation. The image acquisition and mine site geometry was found to be a major factor reducing the potential application of radar interferometry for open pit deformation detection. In particular, at the pit and waste steep walls where the layover and shadow phenomena occur (Figure 4.18d). Thus, the extremely large value of terrain slope reduces the reliability of InSAR as a detection method of small-scale deformation associated with surface mining. The slope angle for open pit walls varies between 45° and 65°, and sometimes exceeds 70° (Lilly, 2000).

Although the absence of proper radar images prevented small-scale deformation detection studies at Leinster mine site, the analysis of the available interferogram has led to some valid conclusions. The limited resolution of the interferometry data significantly reduces the capability of satellite radar interferometry as an effective tool for surface deformation detection over surface mines. For instance, the most common mine wall failure is about the same dimension as one interferogram pixel size (20x20 m assuming the finest resolution). Even larger failures of several pixels will be very difficult to recognise due to the presence of the interferometric phase noise, layover and shadow phenomena. Furthermore, the temporal decorrelation caused by the dynamics of the deformation will also increase the level of decorrelation. Moreover, the frequency of repeat image acquisition, which is limited to 35 days for satellites ERS-1/2 and ENVISAT, could not be sufficient for a particular deformation studies. Therefore, the satellite radar interferometry is not an optimal tool for slope stability monitoring with the currently available satellites.

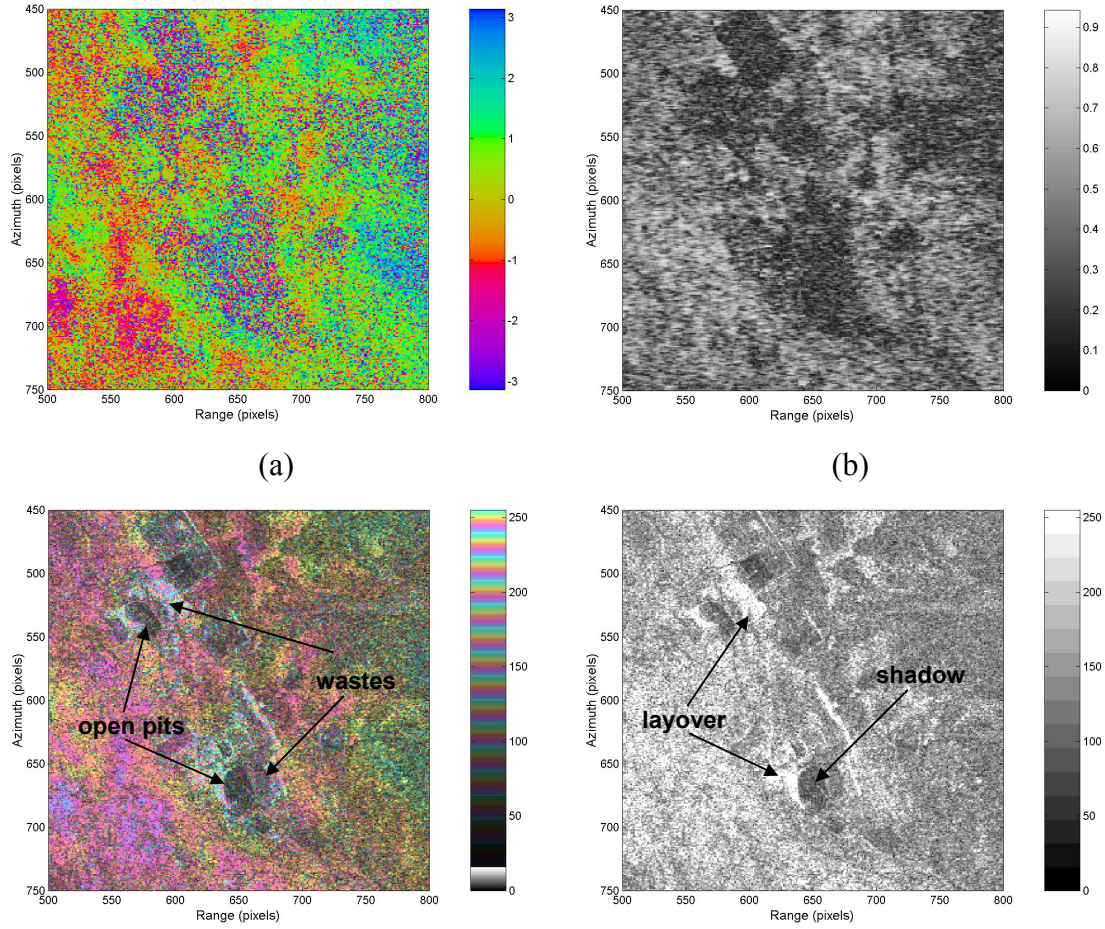

Figure 4.18 *(a) differential interferogram, (b) coherence map, (c) magnitude-phase mix, and (d) magnitude image of the differential interferogram over the Leinster mine site. Pixel size is 20x20 m.*

Certain alternative solutions, such as *permanent scatterer (PS)* developed by Ferretti *et al.* (2001, 2000, 1999a), can also be applied to detect small-scale deformations associated with surface mining. PS is based on the analysis of single coherent pixels on a series of interferograms. This method can provide reliable elevation and deformation measurements even in the absence of visible fringes on a single interferogram. However, the large number of radar images necessary for PS analysis can sometime be the limiting factor for this method.

Recently developed terrestrial radar interferometry, based on principles that are identical to the space borne InSAR, demonstrates its advantages for '*close range*' deformation detection studies. Its application to deformation monitoring of landslides (Tarchi *et al., 2003*), engineering constructions (Tarchi *et al., 1999*), and mine slope stabilities (Reeves *et al.*, 2000) proves the high quality of the

interferometric data gathered by the radar system. At present, this type of radar interferometry is recommended for open pit slope stabilities monitoring, as it has three great advantages over satellite radar interferometry. These are (i) very high spatial resolution of the system, (ii) the system can be set up at any convenient location, and (iii) the system is operational at all times (*e.g.* day or night).

4. 4 Interferogram Interpretation of the Silesia Study Area

The analysed interferogram is the product of two images AQ-SI and AQ-SII (image details are listed in Table 3.3). The shortest possible temporal separation (35 days) between image acquisitions, the urban character of the study area and the acquisition time (autumn season) that reduced the vegetation cover, acted to minimise decorrelation contributions. These conditions increased the overall coherence, as seen in Figure 4.19. In addition, the perpendicular baseline component in this case was only 56 meters and the topography variation over the Silesian basin is very low. The resultant interferogram did not show any topography related fringes, therefore, the differential interferometry step was omitted.

Only a part of the entire scene over the investigation area is analysed. At a number of different locations, interferometric fringes can be observed (Figure 4.20). These fringes are related to surface deformations due to the underground mining that spread over the investigation area. The number of fringes and spatial size of the deformation areas vary, although the shape of deformation remains common for most cases. Except when the surface deformation is formed by the superposition of many deformations, a circular or elliptical shape was found to be most common. These observations over this region correlate with previous studies conducted by Perski (*e.g.* Perski, 2000; Perski and Jura, 1999). According to these studies, the interferometric phase measurements agreed with the terrestrial surveying measurements as it was validated over the rural and urban areas near the city of Katowice. As reported, the interferometric data were able to detect subsidence of less than 1 cm/month.

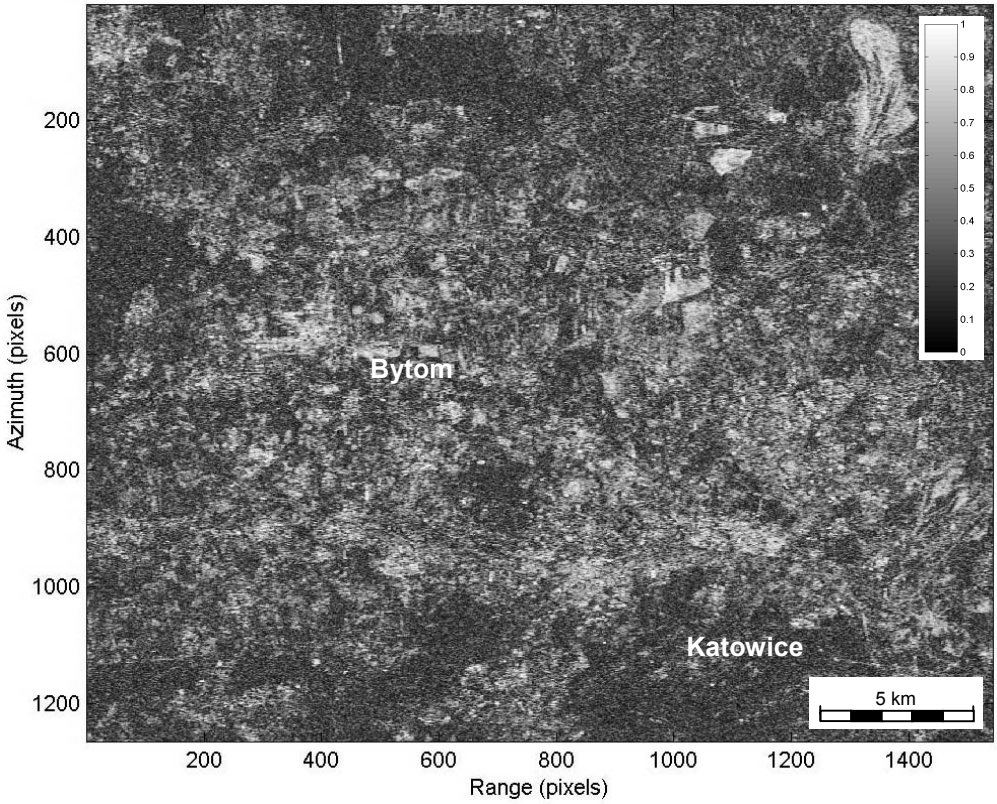

Figure 4.19 *Coherence map over the Silesia study area.*

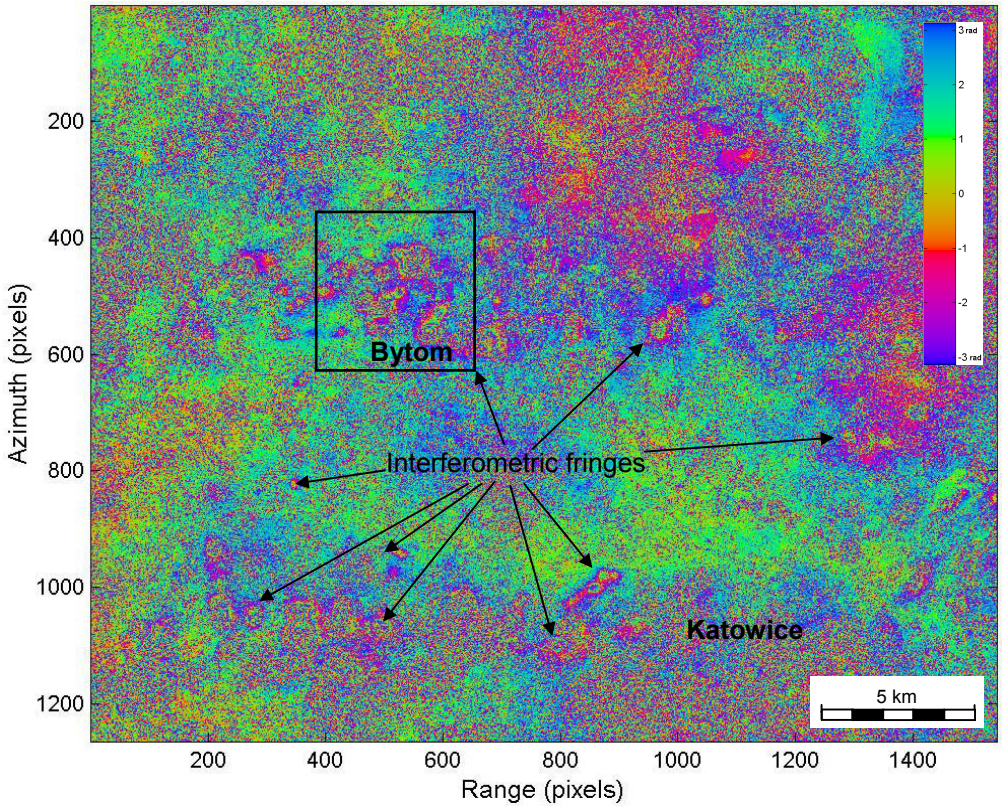

Figure 4.20 *Interferogram over the Silesia study area with a number of visible fringes corresponding to surface deformation due to underground mining activities.*

Figure 4.21 shows the set of interferometry-derived data selected over the city of Bytom. The interferometric phase image (Figure 4.21a) shows the group of fringes representing surface subsidence due to underground mining spanning over 35 days. The large aggregation of underground mining activities in this area contributes to the overall surface subsidence. Thus, a group of superposed elliptical shapes can be observed. Proper interpretation of such a deformation signature can be difficult, or even impossible, if the level of noise is too high. However, after filtering, it was possible to correctly interpret the magnitude as well as the spatial extent of most surface subsidence.

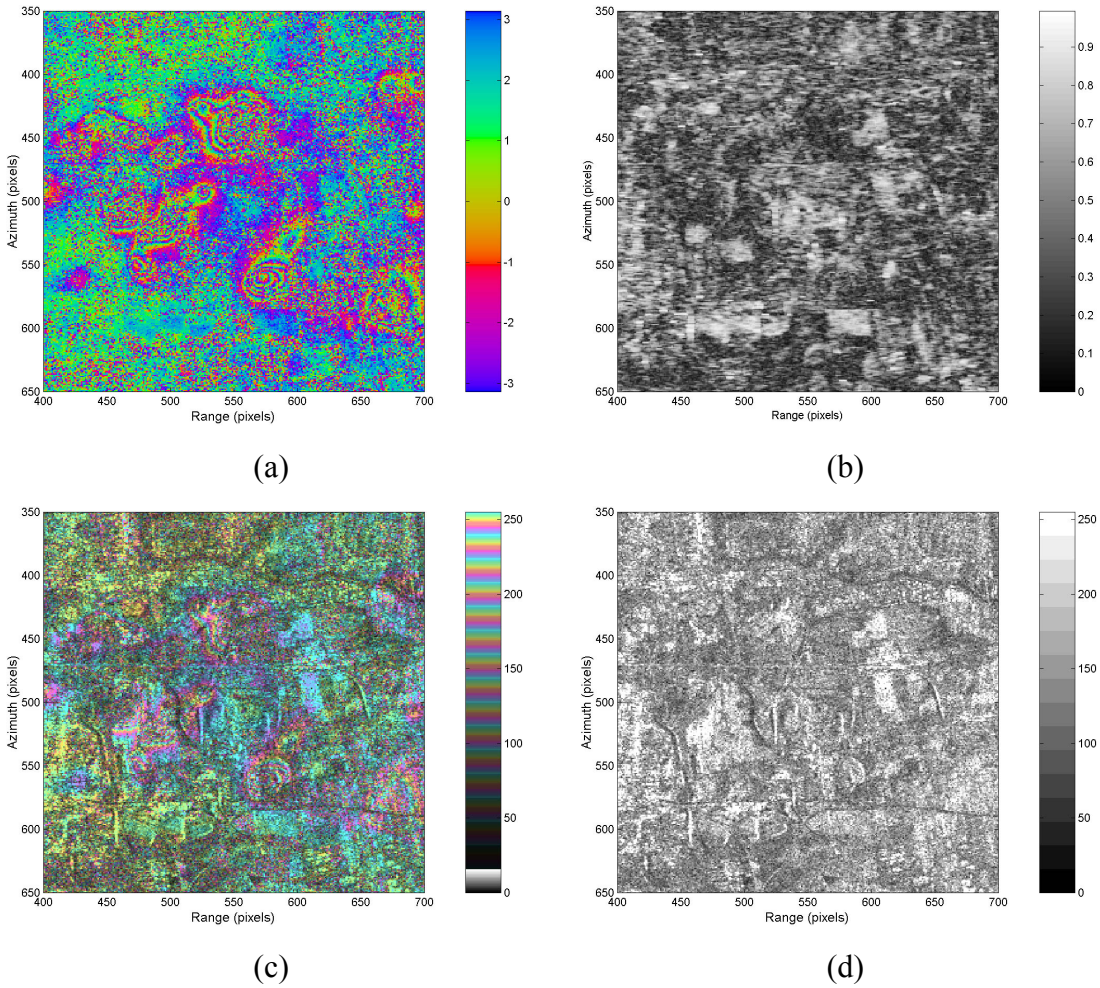

Figure 4.21 *(a) interferogram, (b) coherence map, (c) magnitude-phase mix, and (d) magnitude image of the interferogram over the part of Silesia study area (Bytom city). Pixel size is 20x20 m.*

Figure 4.22 shows an example analysis of interferometric phase image and the corresponding surface subsidence due to underground mining. Since a phase

difference equals 2π (one fringe) represents approximately 28 mm of surface changes along the satellite line of sight with respect to the stable area, the subsidence magnitude can be easy reconstructed. In this particular example, portion of a fringe has been identified, which corresponds to a maximum subsidence in the centre of the area of about 10 mm (Figure 4.22b). Moreover, the spatial extent of the deformation area can easily be outlined.

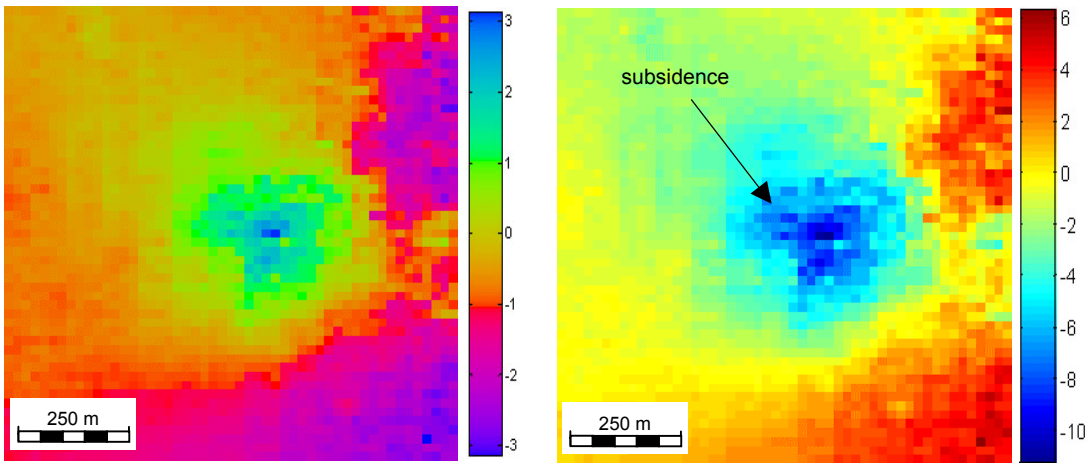

(a) (b)

Figure 4.22 *(a) Interferometric phase image (colour bar in radians) and (b) surface subsidence (colour bar in millimetres). Interferogram was filtered using Goldstein radar interferogram filter.*

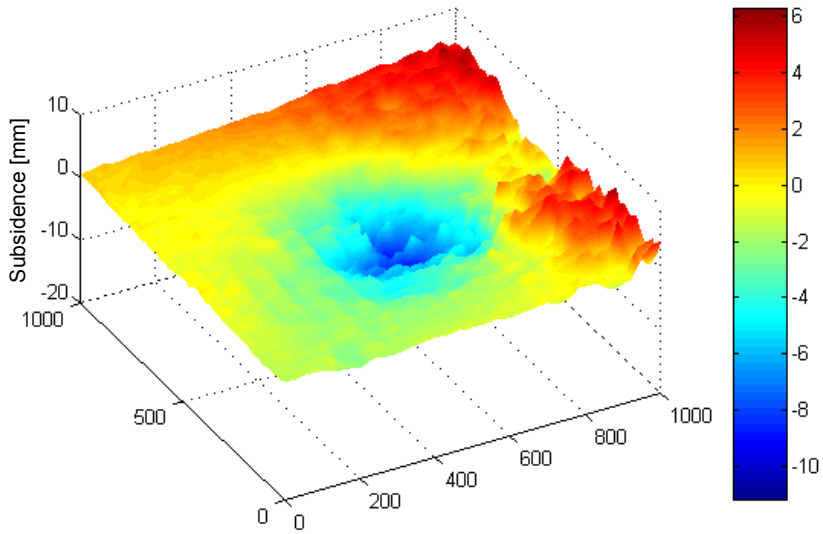

Figure 4.23 *Three-dimensional model of surface subsidence based on InSAR data (colour bar in millimetres).*

In addition, the +6 mm uplift in the vicinity of the subsidence has been revealed. According to Gren and Popiołek (1999, p.167) the uplift phenomenon is very often associated with the surface subsidence in the Silesia mining region. It is caused by the combination of a specific mining system and characteristics of the rock strata above the orebody, and occurs in the direct vicinity of surface subsidence. Finally, the surface subsidence is represented as the three-dimensional model that can be seen in Figure 4.23.

In conclusion, the analysis of the interferometric phase image over the Silesia study area has proven that space borne radar interferometry is able to detect small-scale surface deformation. However, the interferometric phase noise was found to be the major factor reducing the performance of phase unwrapping process and correct interpretation of the deformation magnitude. The interferogram filtering enhances the robustness of the phase unwrapping process but it reduces the deformation signal.

4. 5 Limitation and Weaknesses of InSAR

Based on the analyses of the interferometric processing stages and their subsequent products, several conclusions were derived and will be discussed in the followed section.

Although decorrelations related to the acquisition of radar images are more severe, the introduction of interferometric processing decorrelation can also be problematic as phase noise is elevated. Fortunately, certain counter measures may be implemented. For example, obtaining the proper solution in the coregistration step will improve the quality of the interferometric products. In addition, spectral filtering and spectrum shifting of the images before the resampling procedure will minimize the occurrence of phase noise.

Analysis of the differential interferogram of the Leinster study area revealed a long wavelength phase trend. The origin of this phase trend has been related to the satellite orbital error. Moreover, the high variations of the interferometric phase and low coherence values over the mine site have been associated with intensive mining

developments. Due to a failure in a satellite navigation system, new image acquisitions were not suitable for interferometric analysis.

Interferometric analysis of the Silesia study area revealed a number of locations where surface subsidence has been detected. For the majority, quantitative interpretation was possible. However, in cases where interferometric data could not be interpreted with confidence, significant phase noise was found to be the perpetrating factor. Application of interferogram filtering reduces the level of noise but it also decreases the interferogram resolution.

Based on the analysis of interferometry processing stages and its products, three outstanding problems may be identified, giving rise to the core aims addressed in the following chapters of this thesis. The first research aim is to reduce interferometric phase noise. This involves the use of a novel adaptive radar interferogram filter, which was developed based on a modification to the Goldstein filter (Chapter 5). This filter acts to minimise the loss of resolution in the interferogram. The second and third research questions emerged after analyses of the interferometric phase image. What is the minimum and maximum detectible deformation gradient that radar interferometry can detect? Moreover, does a method exist, which can replace visual inspection to analyse the interferometric phase related to a small-scale surface deformation? A methodology that leads to a functional model for determining minimum and maximum detectable deformation gradient is developed in Chapter 6. The extended analysis of the phase image is examined using a wavelet approach in Chapter 7.

4. 6 Summary

The interferometric processing chain has been shown. All the important stages of this process have been discussed and optimal solutions and decisions are proposed. Furthermore, the interferometry products, such as coherence maps, interferograms, differential interferogram as well as DEM, have been derived and analysed over the two study areas introduced in Chapter 3. Finally, the phase noise was found to be the major factor limiting the interpretation of the interferometric phase image.

5 A NEW ADAPTIVE RADAR INTERFEROGRAM FILTER

The quality of DEMs and displacement maps can be improved by numerous methods at different processing levels. One of them is filtering of the interferometric phase. However, while filtering reduces noise in the interferogram, it does not necessarily enhance or recover the signal. Furthermore, the impact of the filter can significantly change the structure of the interferogram. In this chapter the idea of filtering is investigated and applied to the wrapped phase interferogram. In addition, a new filter based on modifying the existing Goldstein radar interferogram filter is proposed. The proposed approach makes the filter parameter dependent on coherence, so that incoherent areas are filtered more than coherent areas. This modification minimises the loss of signal while still reducing the level of noise. Finally, the validation of the new filter is performed on simulated and real data sets. This chapter provides a more detailed description of the work that has already been published in Baran *et al*. (2003).

5. 1 Background to the Phase Filtering

As previously mentioned, a multilooking process can be used as an effective tool for phase noise reduction but only at the expense of spatial resolution. Therefore, in order to preserve spatial resolution, a filtering algorithm has to be applied. There are many available filtering techniques that can be applied to the interferometric phase. Some of them are more suitable for filtering the interferometric phase image. For instance, in the study conducted by Bezerra-Candeias *et al*. (1995) three different filtering methods based on (i) a morphological filter, (ii) a modified median filter, and (iii) a modified mode filter are combined considering the periodic character of the interferometric wrapped phase. The application of such modified filter algorithms to the unwrapped phase significantly aids the processing stages (*e.g.* phase unwrapping) and the quality of the interferometry products. Other filtering algorithms developed and applied to the interferometric phase are demonstrated in

Hubig (1999), Reeves *et al*. (1999), Bo *et al*. (1999) Lee *et al*. (1998) and Goldstein and Werner (1997, 1998).

5.1.1 Filtering in Space Domain

Filtering in the space domain is usually associated with a discrete convolution of the image with a *kernel*, often called the *convolution mask*. The kernel is usually a small array of numbers. An example of a mean kernel can be seen in Figure 5.1.

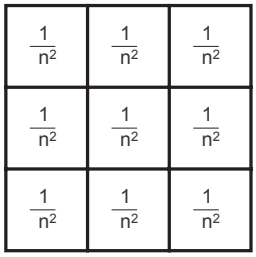

Figure 5.1 *Kernel of a mean filter with n x n neighbourhood.*

The convolution can be seen as a simple mathematical operation in linear system theory. In principle, it is an operation that takes a part of an image (*I*) at each pixel location and multiplies it by the kernel (*K*) to produce another pixel value on an output image (*O*). Usually the interaction is a form of multiplication, adding and shifting. Figure 5.2 illustrates the convolution process.

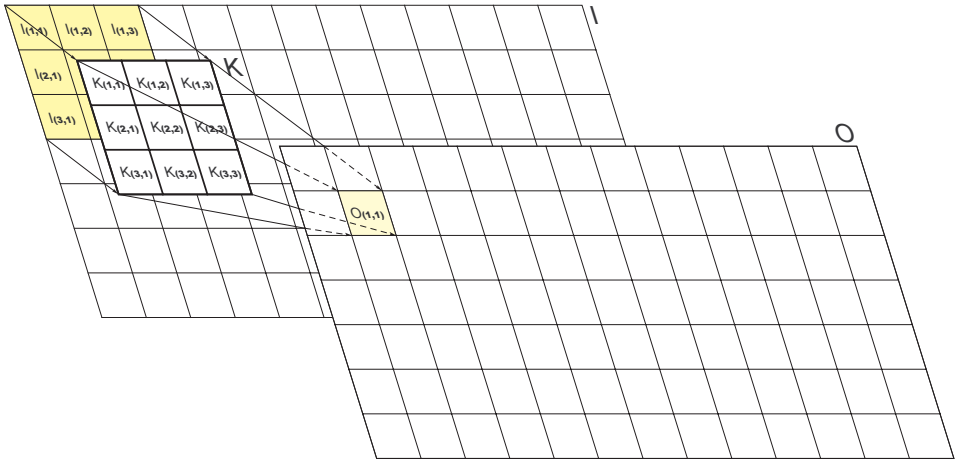

Figure 5.2 *An example convolution of the image (I) with kernel (K) with the boundary effect.*

The convolution is performed by sliding the kernel over the image, usually starting at the top left-hand corner of the image. The kernel moves through all the positions where it fits entirely within the boundaries of the image. Each kernel position corresponds to a single output pixel value. Multiplying the kernel value by the underlying image pixel value for each of the cells in the kernel, and taking the sum of all these values, calculates the value of the new pixel. If image I has M x N pixels and the odd kernel dimension is m x n, the convolution can be written as:

$$O(i,j)=\sum_{k=1}^{m}\sum_{l=1}^{n}\left(i-\frac{m-1}{2}+k, j-\frac{n-1}{2}+l\right)K(k,l) \tag{5.1}$$

where i and j run from 1 to M and N while k and l run from 1 to m and n respectively.

In addition, the implementation of convolution produces a smaller output then the original size because the kernel has to fit entirely within the image. This constraint can be overcome by centring the kernel on an edge pixel and inventing the input pixel value for the location where the kernel extends off the image. A typically chosen value for regions outside the true image is zero.

Figure 5.3 illustrates that case. Such a solution has the advantage that the output image is the same size as the original one, but the disadvantage is that the output image is distorted at the edges. Therefore, the convolution will sacrifice the edge pixels in order to achieve true values in the output result.

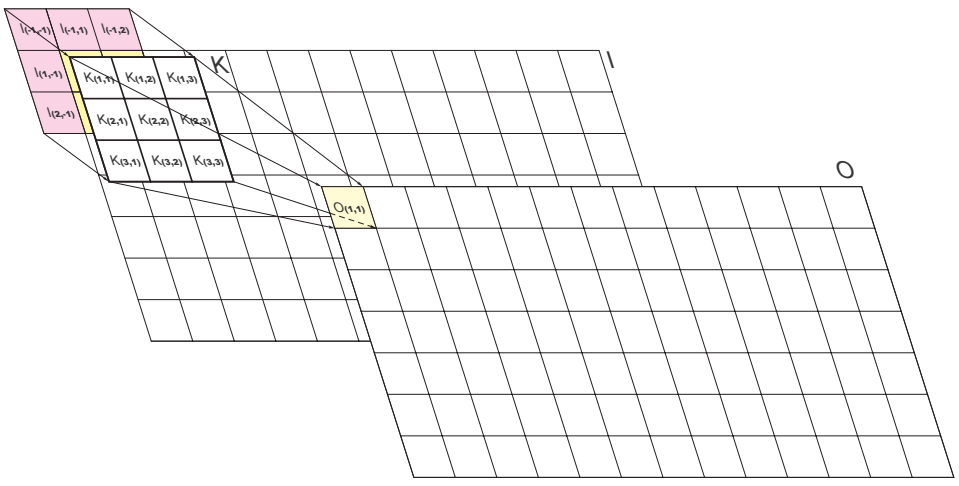

Figure 5.3 *An example convolution of image (I) with kernel (K) with no boundary effect.*

Convolution can be used to implement many different operations. The most common are feature detection and spatial filtering. The basic examples of spatial filtering are the mean and median filters. The *mean filter* is a simple method of smoothing the image by replacing each pixel value in an image with the average value of its neighbours, including itself. The *median filter* is the most common non-linear image filter technique. It is a one or two-dimensional processing operation in which the value of the pixel is replaced by the median value of its neighbours, including itself.

The advantage of mean and median filters is their simplicity. However, the main disadvantage is that they do not adapt to local noise level variations and the geometrical shapes of the objects within the image.

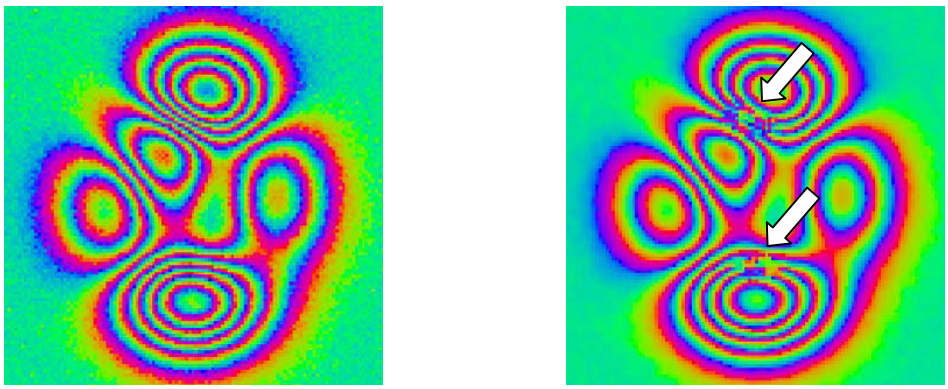

(a) (b)

Figure 5.4 *(a) Simulated noisy interferogram (120x120 pixels), (b) Interferogram after applying of the mean filter (kernel 3x3).*

Figure 5.4 shows the simple example of a simulated phase interferogram with some Gaussian noise before and after filtering using the mean filter. It is clearly visible that in the two areas (arrows) the fringe structure was destroyed. Figure 5.5 shows the effect of the median filter on the interferogram structure. The fringes were heavily corrupted especially in areas where high fringe density is experienced. These simple examples demonstrate the effect of spatial filtering on fringe structures.

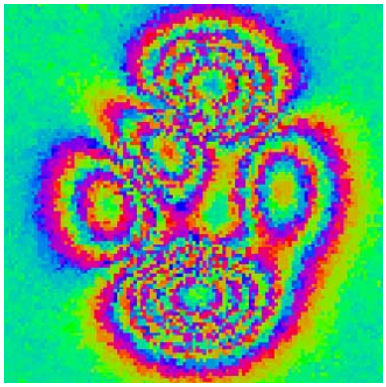

Figure 5.5 *Interferogram after applying of the median filter (kernel 3x3).*

In the case of the phase unwrapping process, when the correct number of phase cycles is crucial, it is extremely important that a filtering algorithm does not change the spatial structure of the fringes. Thus there is a demand for a better filtering algorithm which significantly reduces the phase noise but has no or minimum impact on the image structure.

5.1.2 Filtering in the Frequency Domain

A more advanced filtering technique called *spatial frequency filtering* is based on manipulation of the spectral components contained within an image. To find the spatial frequencies within an image, the Discrete Fourier Transform (DFT) is used. In principle, DFT is a process of decomposing a signal into a set of sine and cosines with the frequency and amplitude of each representing spatial frequencies. However, such process is time consuming due to the large number (order N x N) of complex multiplications and additions required to compute the DFT. To reduce the computation time, the more efficient tool called Fast Fourier Transform (FFT) can be applied. The FFT algorithm decomposes the DFT taking into account the periodicity of the sine and cosine functions, thus reducing the number of necessary computations to order N $\log_2$ N. Since the FFT algorithm works by dividing the input image by 2 repeatedly, the size of the input image should be the power of 2. The most important part of the FFT process is that, after manipulation of the frequency components, the inverse Fourier transform can reconstruct the filtered object in the space domain. More details about DFT and FFT can be found in, for example, Buttkus (2000, pp59-84).

By modifying the frequency components, periodic noise can be removed from the image using a simple low-pass filter. Figure 5.6 shows the frequency responses of four basic types of ideal one-dimensional frequency filters. The four filters can be described by the following set of equations:

Ideal low-pass filter

$$F_l(f) = \begin{cases} 1 \; for \; f \le f_c \\ 0 \; for \; f > f_c \end{cases} \tag{5.2}$$

Ideal high-pass filter

$$F_l(f) = \begin{cases} 1 \; for \; f > f_c \\ 0 \; for \; f \le f_c \end{cases} \tag{5.3}$$

Ideal band-pass filter

$$F_l(f) = \begin{cases} 1 \; for \; f_{\min} \le f \le f_{\max} \\ 0 \;\; otherwise \end{cases} \tag{5.4}$$

Ideal notch filter

$$F_l(f) = \begin{cases} 0 \; for \; f \le f \le f_c \\ 1 \; otherwise \end{cases} \tag{5.5}$$

The main purpose of ideal filters is to remove certain frequency components and leave other frequency components unmodified.

To apply the above filters to a two-dimensional data set, such as an image, two different approaches can be taken. The first approach is based on the idea of applying a one-dimensional ideal filter separately to both frequency directions. The second approach is to use single one-dimensional filter and to apply it radially to all frequencies. In the second solution, all frequency components that lie on a circle of a given radial distance from the zero frequency are filtered.

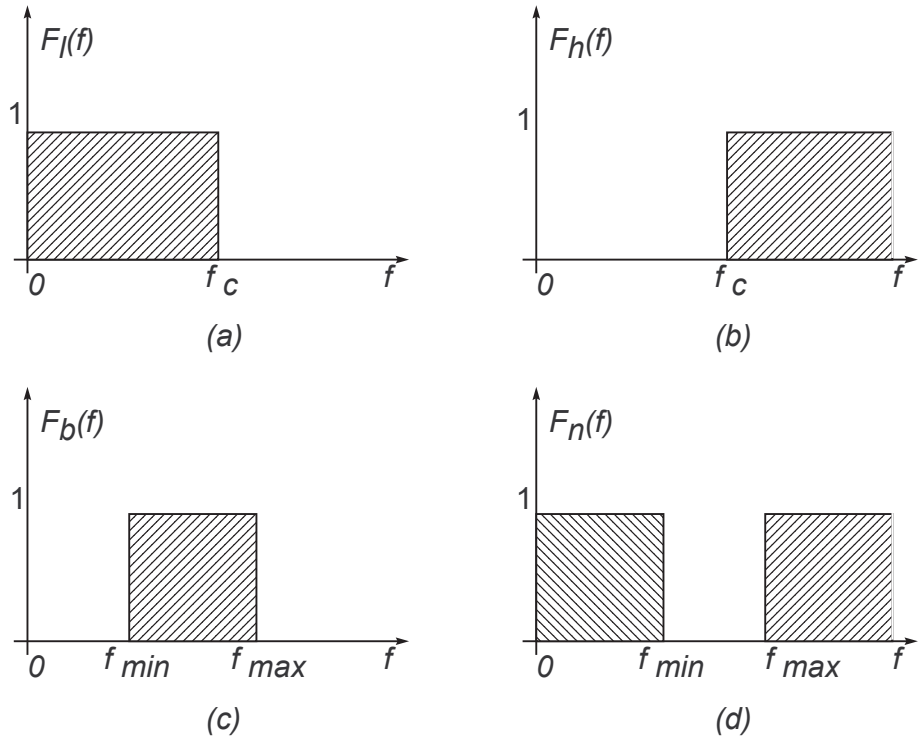

Figure 5.6 *Four types of ideal filters: (a) low-pass filter, (b) high-pass filter, (c) band-pass filter, (d) notch filter.*

5.1.3 Adaptive Filters

The idea behind adaptive filtering is that a filter changes its characteristics depending on the type of noise and image content within a local window. An adaptive filter usually consists of two steps. In the first step a decision of what type of filtering should be applied is made. Such a decision is based on the presented type of noise and the content of an image. In the second step, the final filtering is applied.

Although, there are many different types of adaptive filtering in both the space and frequency domains, description and application of all filters are beyond the scope of this dissertation. Thus, in the following section, the most widely used adaptive radar interferogram filter, proposed by Goldstein and Werner (1997, 1998), is investigated, and analysed. Furthermore, a modification to this filter is proposed.

5. 2 Goldstein Radar Interferogram Filter

Goldstein and Werner (1997) proposed an adaptive radar interferogram filter based on the concept of multiplication of the Fourier spectrum *Z(u,v)* of a small interferogram patch by its smoothed absolute value $S\{|Z(u,v)|\}$ to the power of an exponent α:

$$H(u,v) = S\{|Z(u,v)|\}^{\alpha} \cdot Z(u,v) \tag{5.6}$$

where *H(u,v)* is the filter response (the spectrum of the filtered interferogram), *S{}* is a smoothing operator, *u*, *v* are spatial frequencies, and α is the filter parameter. Patches are defined as a small part of the interferogram and are overlapped to prevent discontinuities at the boundaries. The filter parameter α is an arbitrarily chosen value between 0 and 1, and has the biggest impact on the filter performance. For the value of $\alpha = 0$, the multiplication factor becomes one, and no filtering occurs. However, for large values of α, filtering is significant. A problem using Goldstein radar interferogram filter occurs when a high value of parameter α is applied. By subtracting the filtered from unfiltered interferogram a residual systematic phase trend appears, which indicates the loss of resolution in the filtered phase (Goldstein and Werner, 1998).

5. 3 A New Interferogram Phase Filter

As explained in Section 2.7.1, the quality of the interferometric phase between two complex SAR images (the interferometric pair) can be estimated directly from interferometric data as a function of the absolute value of complex coherence |γ| (Equation 2.23). Alternatively, the phase noise can be estimated theoretically based on the sensor characteristics, signal processing algorithms, and acquisition conditions.

Bamler and Hartl (1998) define the phase standard deviation for a single-look (*L=1*) interferogram as a function of the absolute value of the complex coherence |γ| given by:

$$\sigma^2_{\varphi,L} = \frac{\pi^2}{3} - \pi \arcsin(|\gamma|) + \arcsin^2(|\gamma|) - \frac{Li_2(|\gamma|^2)}{2} \tag{5.7}$$

where Li_2 is the Euler's dilogarithm, defined as:

$$Li_2\left(|\gamma|^2\right) = \sum_{k=1}^{\infty} \frac{|\gamma|^{2k}}{k^2} \tag{5.8}$$

Figure 5.7 shows the relationship between the coherence $|\gamma|$ and phase standard deviation (σ_φ). It indicates that by either reducing the number of looks or increasing the coherence the phase standard deviation can be improved.

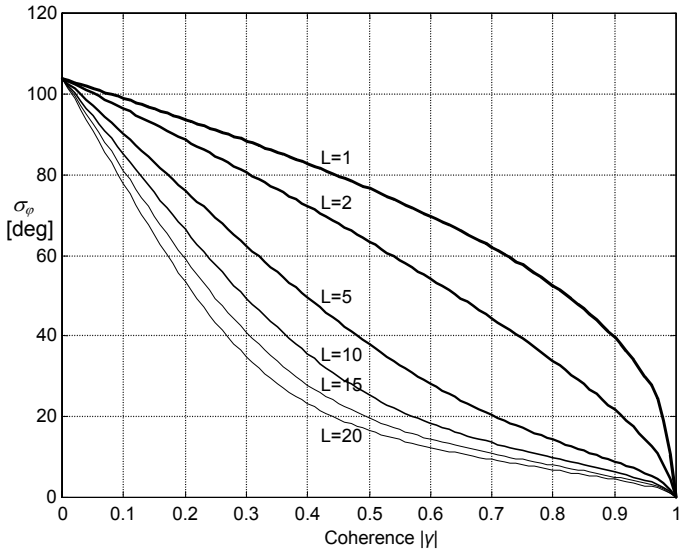

Figure 5.7 *Phase standard deviation (σ_φ) versus coherence (L indicates the multi-look number).*

From the relationship expressed in Equation (5.7), coherence can be recognised as a direct measure of the interferogram phase noise. Therefore, it can be used to modify the Goldstein interferogram filter. The new filter is created by making the parameter α in Equation (5.6) dependent on the coherence:

$$H(u,v) = S\left\{\left|Z(u,v)\right|\right\}^{1-\bar{\gamma}} \cdot Z(u,v) \tag{5.9}$$

Equation (5.9) shows the new radar interferogram filter, where exponent α has been replaced by $1-\bar{\gamma}$. Parameter $\bar{\gamma}$ is the mean value of the absolute coherence computed from the effective corresponding patch (patch size minus overlap) on the coherence map. This approach ensures that the coherence and filter response are of the same size and in the same place. Furthermore, it prevents $\bar{\gamma}$ being affected by

the coherence from the overlapped part of the patch. Such a modification adapts the Goldstein interferogram filter by preventing areas of high coherence (less noise) being over-filtered, but allows stronger filtering in areas where there is low coherence (high noise). Thus, the loss of resolution in the interferogram due to the filtering process can be reduced in the areas where coherence is high.

The author of this thesis developed all the necessary filtering functions using Matlab 6.0 software. The concept of the new radar interferogram filter is shown in Figure 5.8. The interferogram and the coherence map are divided into overlapping rectangular patches. Patches are defined as a small part of the interferogram of even size (power of 2) to aid efficiency of the FFT algorithm. The overlap between patches is required to prevent discontinuities at the boundaries. The maximum overlap size is described as the half of the patch size minus one. Moreover, the trade off between the computation time and the minimization of the boundary effect has to be taken into account. For each patch of the interferogram, the spectrum $Z(u,v)$ is computed (using the two-dimensional FFT). At the same time, from the effective corresponding patch (patch size minus overlap) on the coherence map, the mean value $\bar{\gamma}$ is computed. Finally, the spectrum of the interferogram patch is weighted by multiplying it by its smoothed and scaled absolute spectrum to the power of exponent $1-\bar{\gamma}$. Smoothing of the absolute spectrum is performed by spatial convolution with a block kernel $S\{\}$. As the block kernel, the Fourier spectrum of the spatial moving average has been applied. The size of the smoothing kernel must be small to prevent the spectrum being over-smoothed.

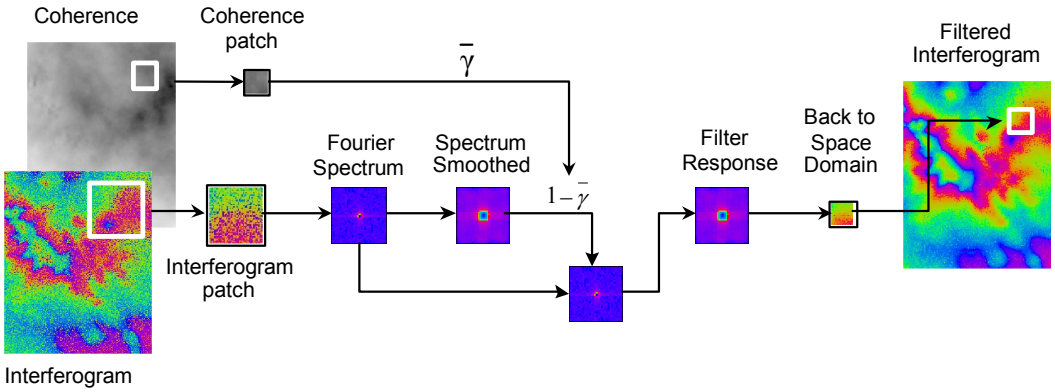

Figure 5.8 *New adaptive radar interferogram filter diagram.*

5. 4 Data Simulations

The validation of the new radar interferogram filter was performed using simulated and real interferometry data sets. In the following section the concept of simulation of the interferogram and the coherence map is developed.

5.4.1 Simulation of the Interferogram

The wrapped phase interferogram was simulated by radar coding a given 9"DEM (Figure 5.9) and wrapping its phase (Figure 5.10).

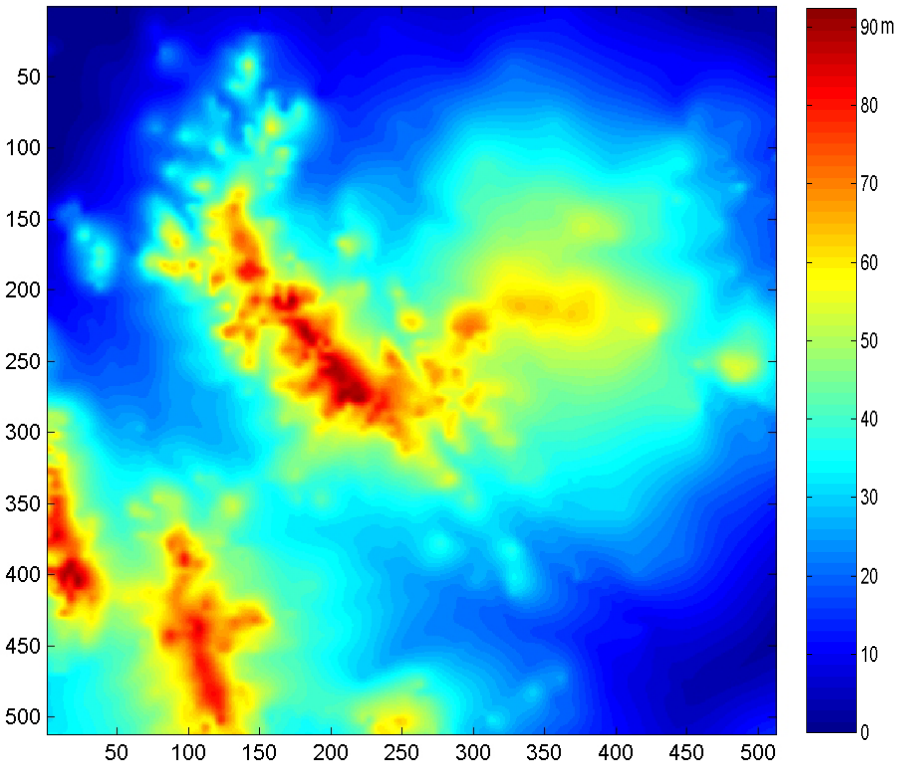

Figure 5.9 *Digital Elevation Model (pixel size is 50 m).*

The DEM is a grid of 512 x 512 pixels. The pixel size is 50 m that creates a scene of approximately 25 x 25 km. All figures in this section are in pixel units in both directions unless indicated differently.

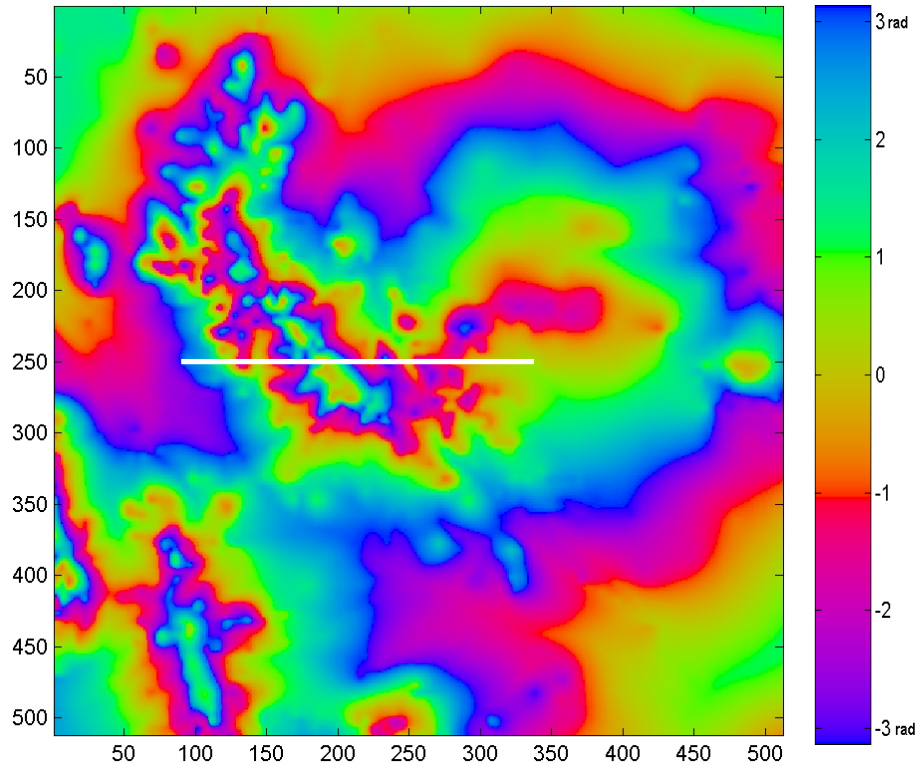

Figure 5.10 *Simulated wrapped phase interferogram based on DEM. The horizontal line indicates the cross-section location (see Section 5.5).*

5.4.2 Simulation of the Coherence Map

To model the coherence map three different decorrelation factors: (i) geometrical, (ii) thermal, and (iii) temporal were taken into account (for more details about decorrelation factors refer to Section 2.8). The final coherence map was estimated as a product of multiplication of each the above decorrelation factors.

5.4.2.1 Geometrical Decorrelation

Geometrical decorrelation (γ_{geom}) is estimated based on Equation (2.29) and Equation (2.30). The terrain slopes (α_t) were delivered directly from the DEM. Figure 5.11 shows the map of the terrain slopes.

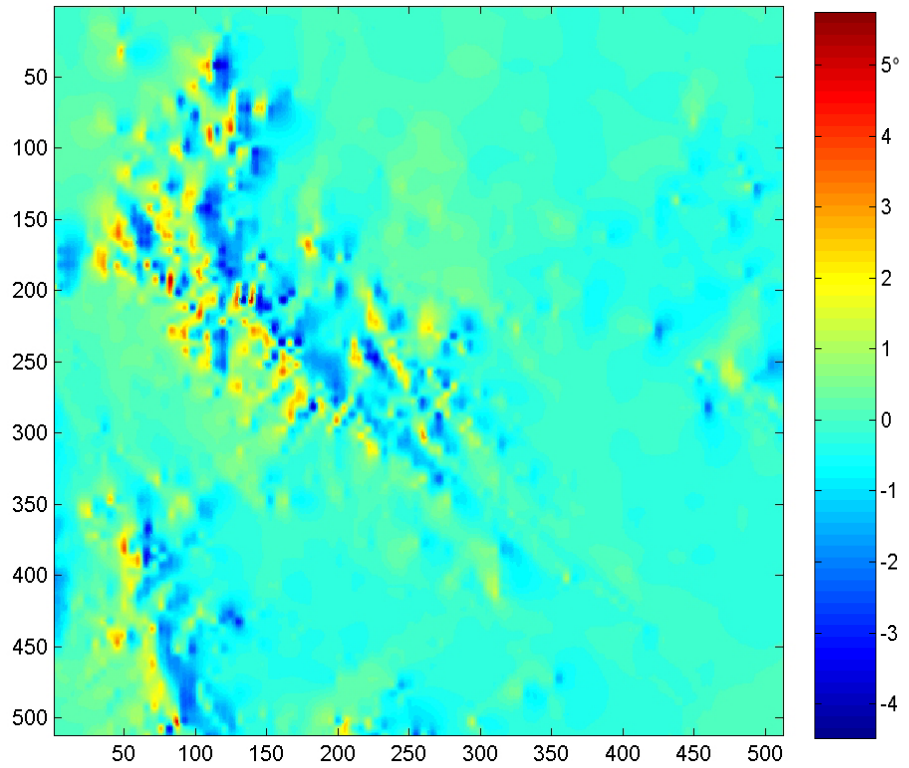

Figure 5.11 *Map of slopes (in degrees) based on the given DEM.*

The remaining parameters necessary to simulate the geometrical decorrelation were taken from the header of the real ERS-1 SLC radar image (AQ-I) and are listed in Table 5.1.

Table 5.1 *Geometrical decorrelation simulation parameters*

Perpendicular baseline ($B_{\perp}$):	200 m
Wave length (λ):	0.05666 m
Range bandwidth (B_w):	15550 kHz
Speed of light (c):	300000000 m/s
Range (R):	837560 m

The simulated coherence map based on geometrical decorrelation can be seen in Figure 5.12.

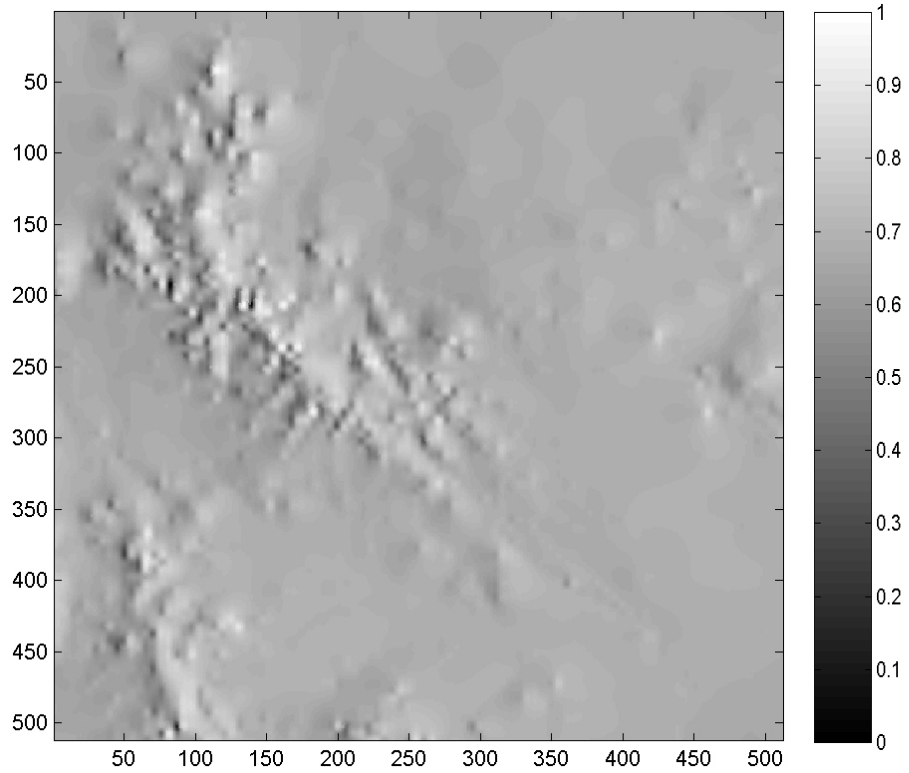

Figure 5.12 *Simulated coherence map based on geometrical decorrelation.*

5.4.2.2 Thermal Decorrelation

Thermal decorrelation ($\gamma_{thermal}$) is estimated based on Equation (2.27). The value of Signal-to-Noise (SNR = 11.7 dB) evaluated for satellites ERS-1/2 is taken from Hanssen (2001, p101).

$$\gamma_{thermal} = \frac{1}{1+11.7^{-1}} = 0.92 \tag{5.10}$$

Thermal decorrelation is to be assumed equal over the entire interferogram.

5.4.2.3 Temporal Decorrelation

The temporal decorrelation ($\gamma_{temporal}$) is a function of all physical changes on the Earth's surface, which can occur between data acquisitions. Since this decorrelation factor is extremely difficult to model, a fractal surface was adopted to simulate this type of decorrelation. For simplicity of coherence modelling additional decorrelation factors, such as Doppler Centroid decorrelation and processing decorrelation are assumed to be included in the temporal decorrelation.

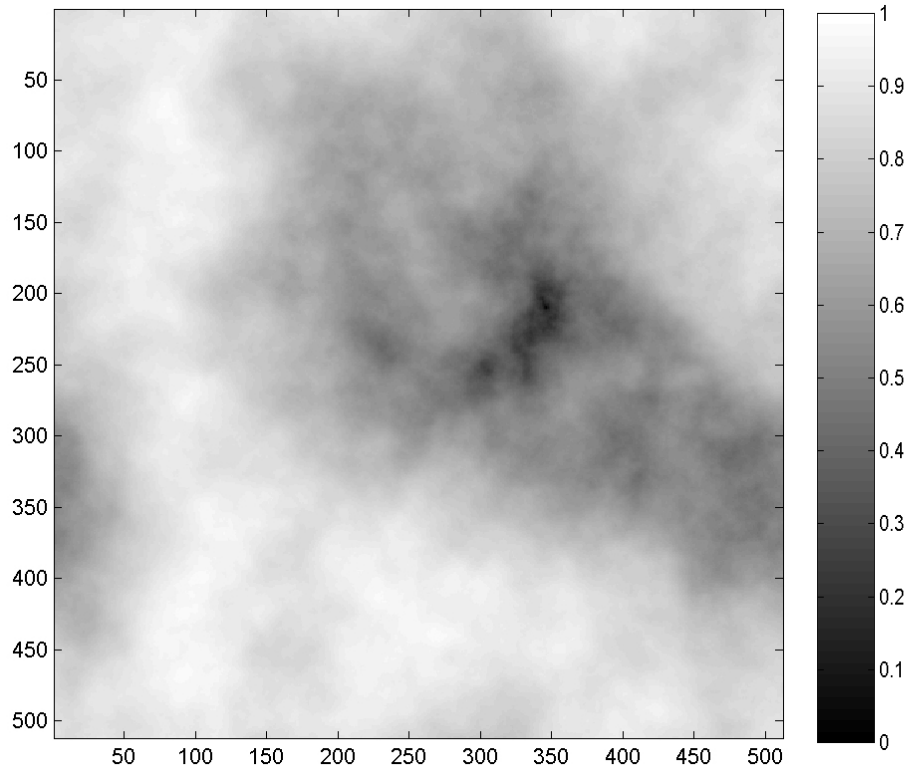

Figure 5.13 *Simulated coherence map based on fractal surface.*

Figure 5.13 shows the coherence map, which is simulated by the use of an isotropic two-dimensional fractal surface with power law behaviour of normally distributed random numbers. The extremely low coherence (black area) can be associated, for instance, with surface water, high soil moisture content, or human activities. The mid coherence values (grey area) could be related, for instance, to changes in vegetation cover. Finally, the white areas simulate very high coherence values where the temporal decorrelations are not experienced.

5.4.2.4 Total Decorrelation

In the final stage, the coherence map is modelled based on total decorrelation (γ_{total}) according to Equation (5.11) based on each simulated decorrelation factors.

$$\gamma_{total} = \gamma_{geom} \cdot \gamma_{thermal} \cdot \gamma_{temporal} \tag{5.11}$$

Figure 5.14 shows the simulated coherence map.

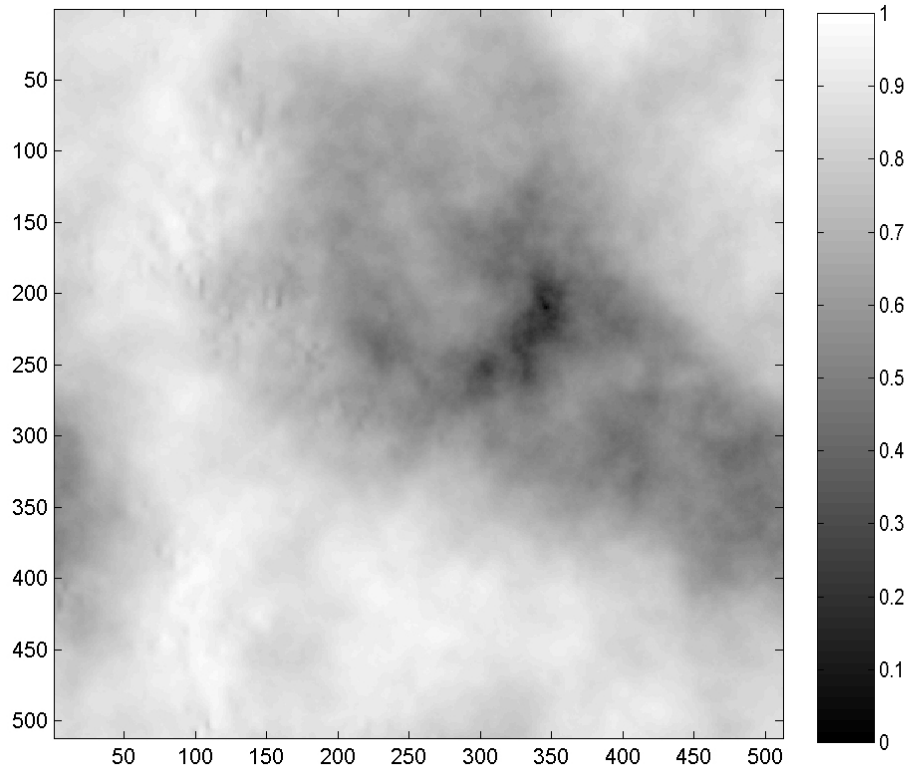

Figure 5.14 *Modelled coherence map based on all decorrelation factors.*

5.4.3 Phase Noise Modelling

Based on the concept discussed in Section 5.3 that links phase variance (σ_φ^2) in an interferogram with the absolute value of the complex coherence (|γ|), a matrix ($M_{\sigma\varphi}$) of the standard deviations (Figure 5.15) is generated based on the modelled coherence map ($|\gamma_{total}|$) (Figure 5.14).

A simulated phase noise N_G (Figure 5.16) is generated by point wise multiplication of the phase standard deviations matrix ($M_{\sigma\varphi}$) with a matrix of normally distributed random numbers with mean zero and variance one (R_N).

$$N_G = M_{\sigma\varphi} .* R_N \tag{5.12}$$

Some of the statistics of the simulated phase noise are shown in Figure 5.17. Finally, the noise is added to the simulated interferogram as shown in Figure 5.18.

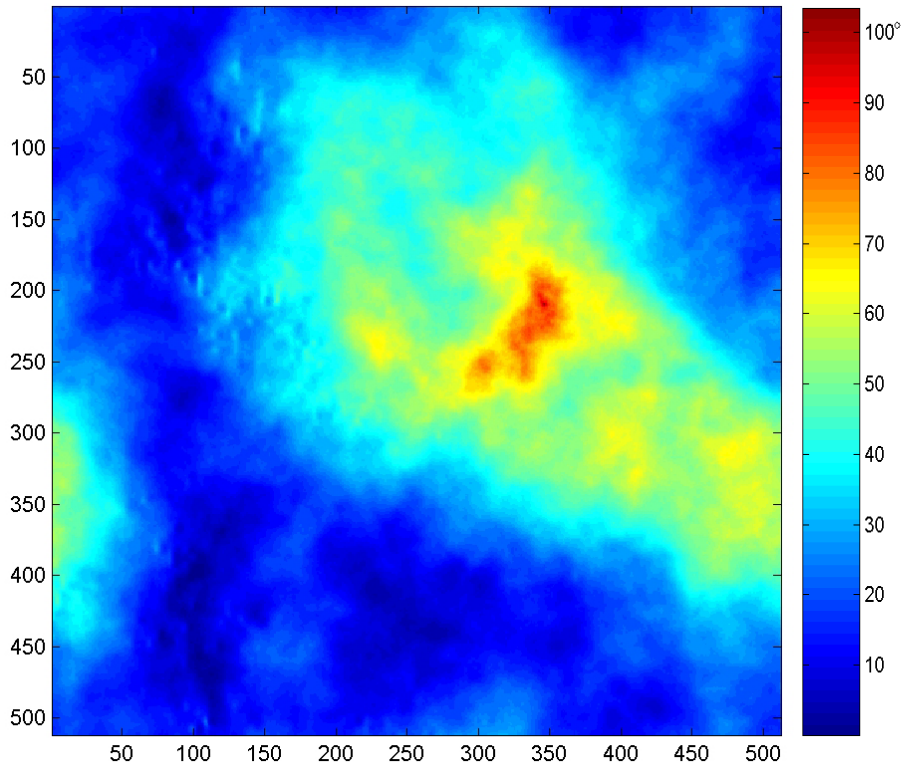

Figure 5.15 *Phase standard deviation (σ_φ) based on coherence map (L=1).*

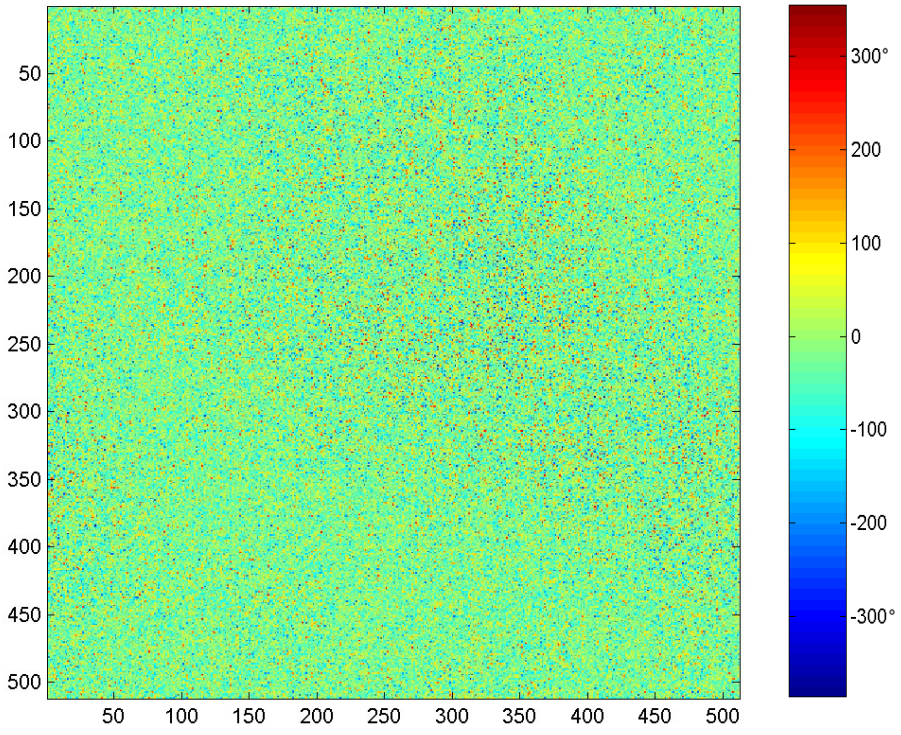

Figure 5.16 *Simulated interferometric phase noise.*

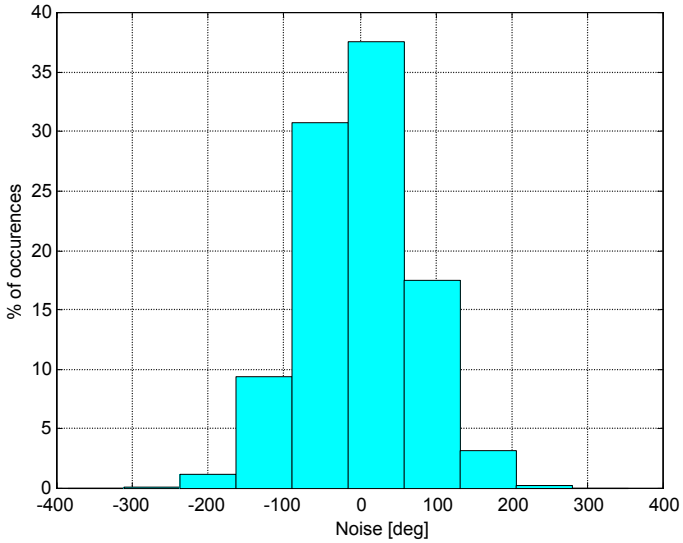

Figure 5.17 *Histogram showing noise distribution (mean = 0.2, STD = 72.9).*

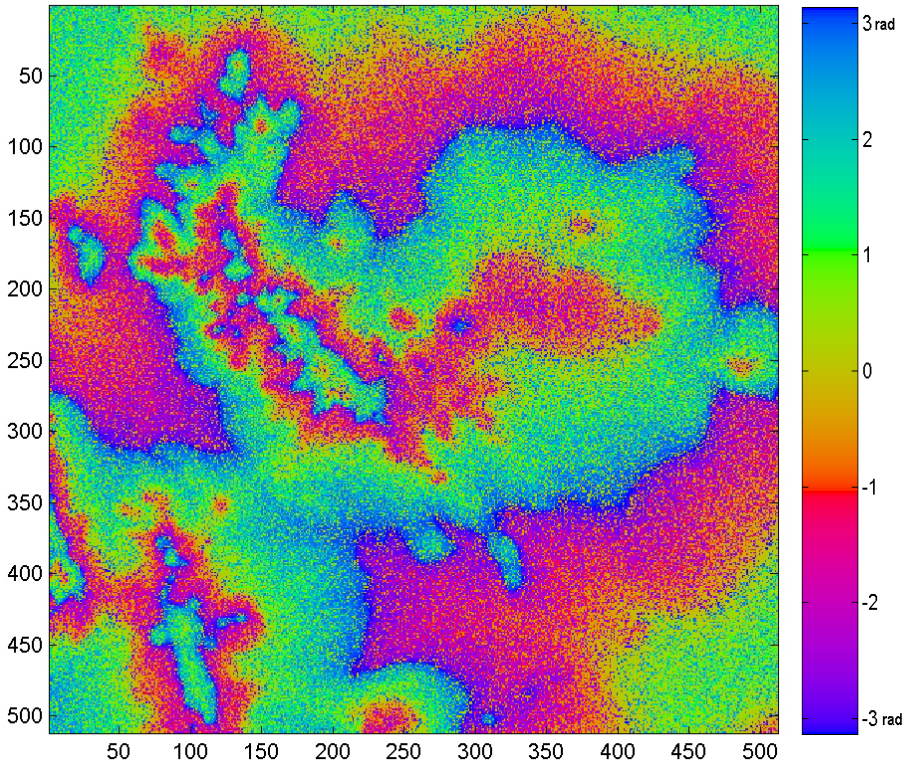

Figure 5.18 *Simulated interferogram with added noise.*

5. 5 Numerical Validation Using Simulated Data Set

In the first test, the new radar interferogram filter is used to filter the interferogram without any noise at all (Figure 5.10) to assess the filter impact on the wrapped phase itself in terms of filter parameter $1-\bar{\gamma}$. The filter parameters for this test are listed in

Table 5.2. The uniform coherence value is assumed to be over the entire interferogram each time the filtering is applied.

Table 5.2 *Filter parameters*

Filter type	Patch size	Overlap	Smoothing operator S{}	Filter param.
Goldstein	32x32	14	Mean kernel (3x3)	$\alpha = 0.9$
New filter	32x32	14	Mean kernel (3x3)	$1-\bar{\gamma}$

The filtering was performed for coherence equal 0.0 up to 0.9 with a step of 0.1. Figure 5.19 shows a cross-section over the simulated wrapped phase interferogram without noise, which is a sample of a number of cross sections analysed. The location of the cross-section is indicated in Figure 5.10.

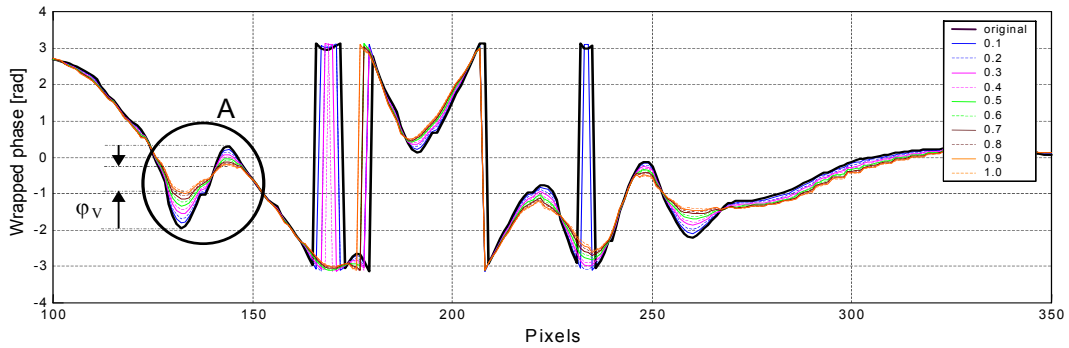

Figure 5.19 *A cross-section over the simulated interferogram without noise. Each line shows the phase after filtering for different value of the filter exponent. The phase offset (φ_V) is clearly visible.*

Vertical offsets (φ_V) between the original and filtered phase due to the impact of the filter can be seen. The magnitude of the offsets increases as the filter parameter $1-\bar{\gamma}$ increases. Furthermore, the biggest vertical offsets are experienced in the areas of large curvature and they always occur in the direction of concavity. An example of this behaviour is shown in Figure 5.19, circle A.

Figure 5.20 shows the characteristics of the Goldstein filter and the new interferogram filter in terms of the ±max phase offset caused by the filters, versus the mean absolute coherence ($\bar{\gamma}$). The graph constructed is based on the differences between the interferogram without noise and its filtered versions. The dashed line on

the graph shows the ±max phase differences versus the coherence for the new radar interferogram filter. It can be seen that for high coherence values the phase offsets become small.

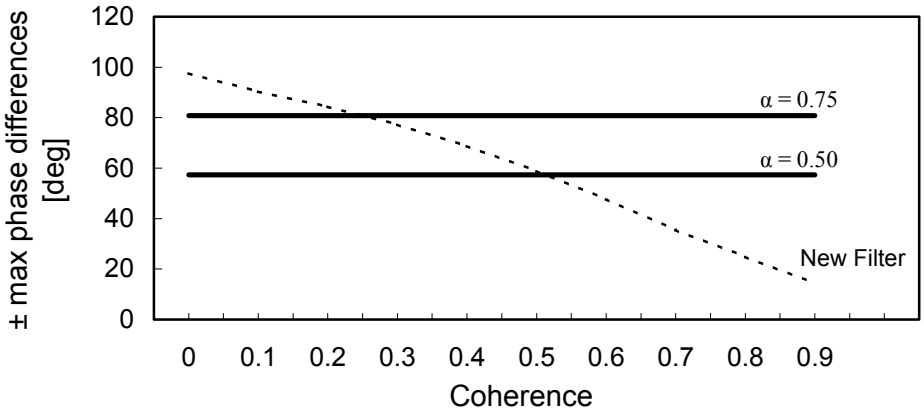

Figure 5.20 ±*max phase differences versus coherence caused by the Goldstein filter for α = 0.75 and α = 0.5 (bold lines), and the new filter (dashed line).*

After analysing the whole interferogram the maximum differences between the original and filtered phase were found to be ±98° for $\bar{\gamma}$ = 0 and ±14° for $\bar{\gamma}$ = 0.9. On the other hand, the two bold lines show the expected ±max phase offset for the Goldstein filter for two different values of parameter *α:* ± 80° for α = 0.75 and ± 59° for α = 0.50. In this case, the differences between the original and filtered phase are high, constant, and strongly dependent on the chosen α value.

In the next test, both filters are used to filter the simulated phase interferogram with noise. The simulated coherence map (Figure 5.10) is also used with the new filter. The filter parameters for all tests are listed in Table 5.2. The filtered interferograms were generated and are shown in Figure 5.21 and Figure 5.23 for Goldstein and the new filter respectively.

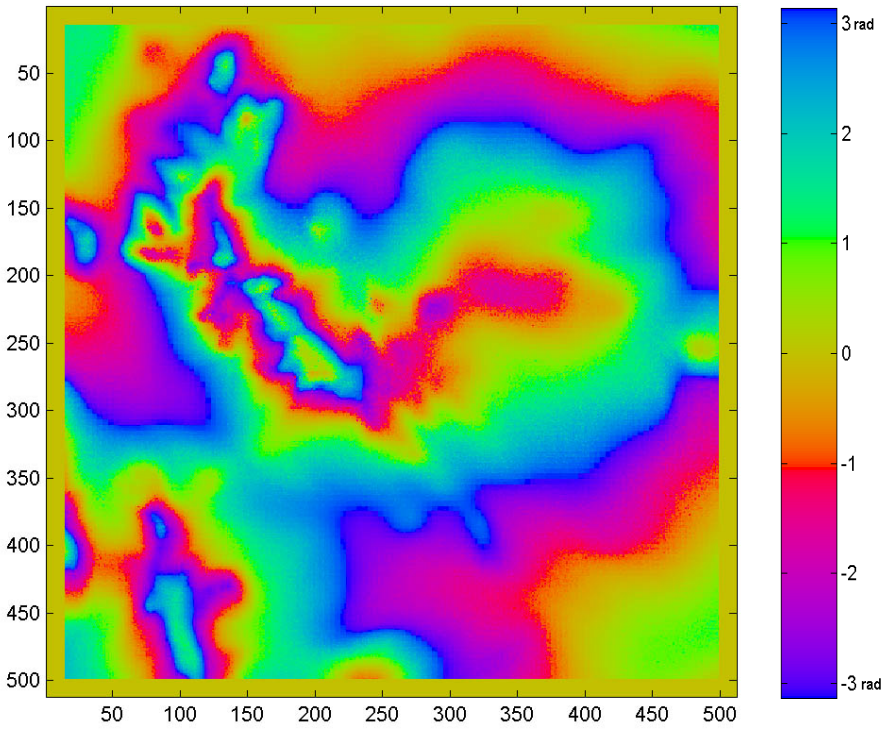

Figure 5.21 *Filtered wrapped phase of the simulated interferogram using Goldstein radar interferogram filter.*

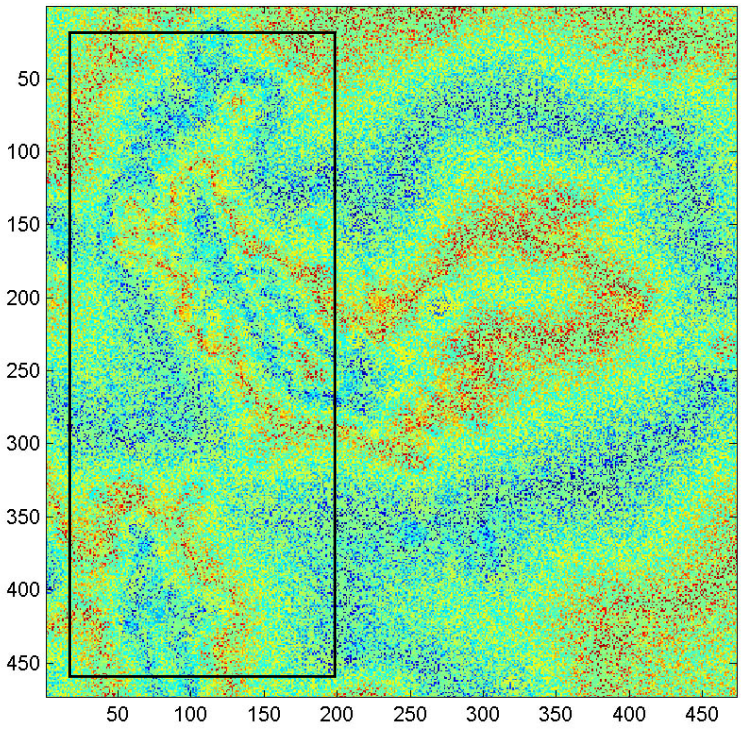

Figure 5.22 *Difference between filtered and not filtered interferogram for Goldstein radar interferogram filter. Remaining features indicate loss of resolution.*

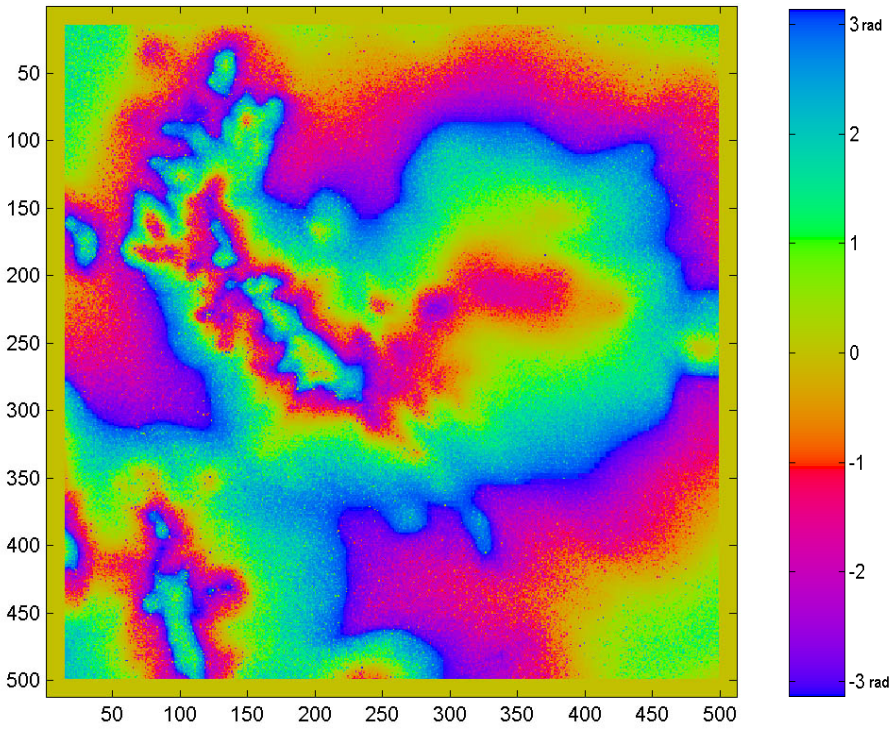

Figure 5.23 *Filtered wrapped phase of the simulated interferogram using the new filter.*

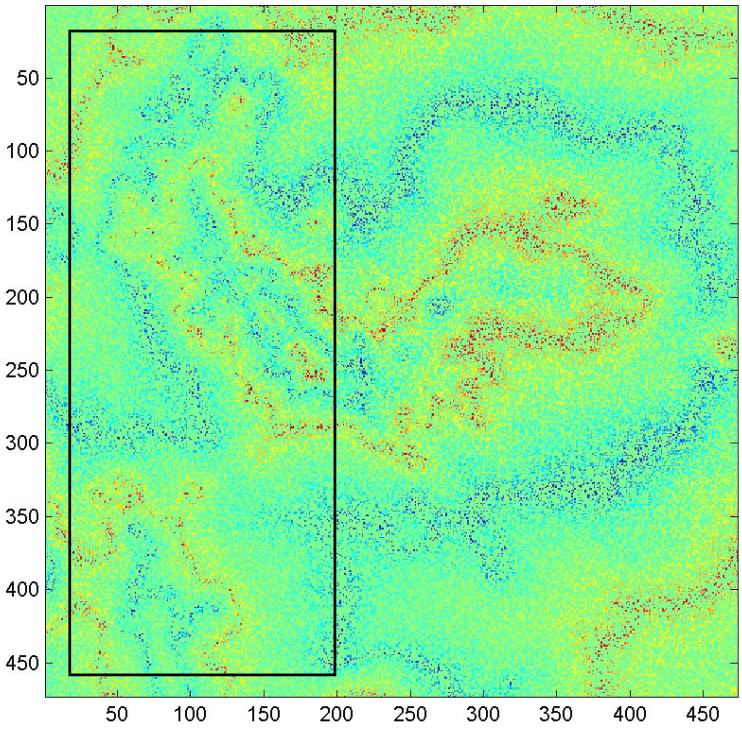

Figure 5.24 *Difference between filtered and not filtered interferogram for the new filter. Remaining features indicate loss of resolution.*

The maps of the differences between filtered and original interferogram show the systematic phase pattern (trend) indicating some loss of resolution in the filtered interferogram. Both filters lead to some loss of resolution. However, the new filter reduces the loss of resolution over the part of the interferogram that is characterised by higher coherence. The rectangular windows in Figure 5.22 and Figure 5.24 show the area where the major differences between the filters occur.

5. 6 Numerical Validation Using Real Data Set

In the following sections the Goldstein and new filter are applied to the real data sets to evaluate their impact on InSAR derived surface heights and small-scale deformation detection. The same filers parameters are used as in previous tests.

5.6.1 Filter Impact on DEMs

To assess the filters impact on DEMs both filters are applied to the real interferogram from the Leinster study area formed by two images (see Chapter 4). After filtering the interferogram, the reduction of the phase noise relative to raw interferogram (Figure 4.7) is clearly visible for both filters (Figure 5.25 and Figure 5.26).

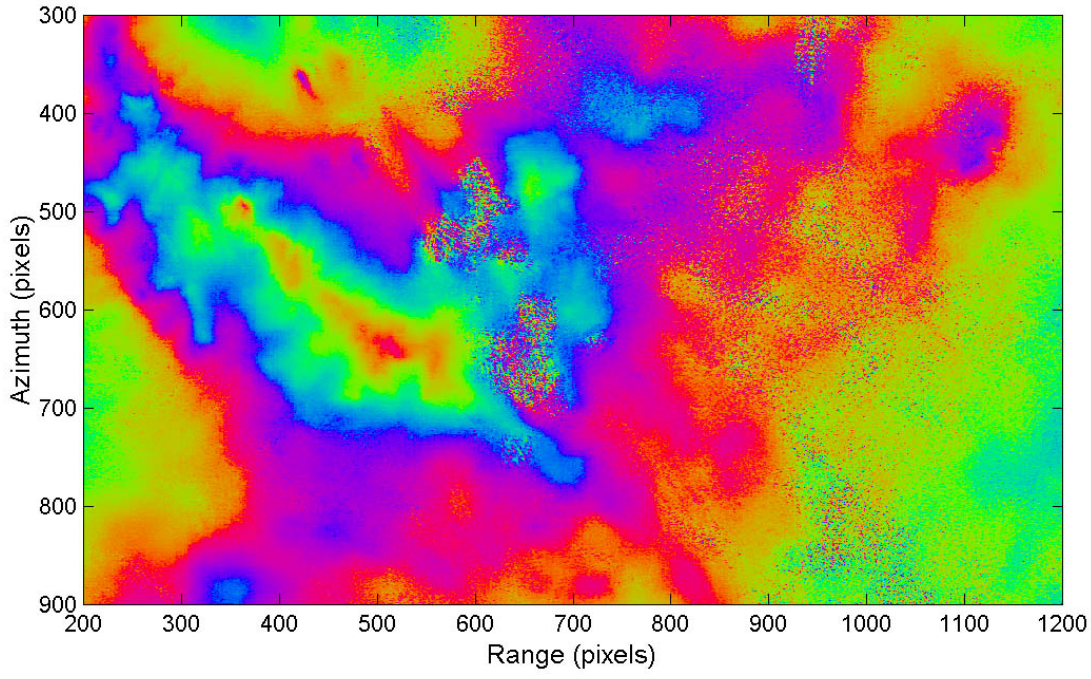

Figure 5.25 *Filtered wrapped phase interferogram using the Goldstein radar interferogram filter.*

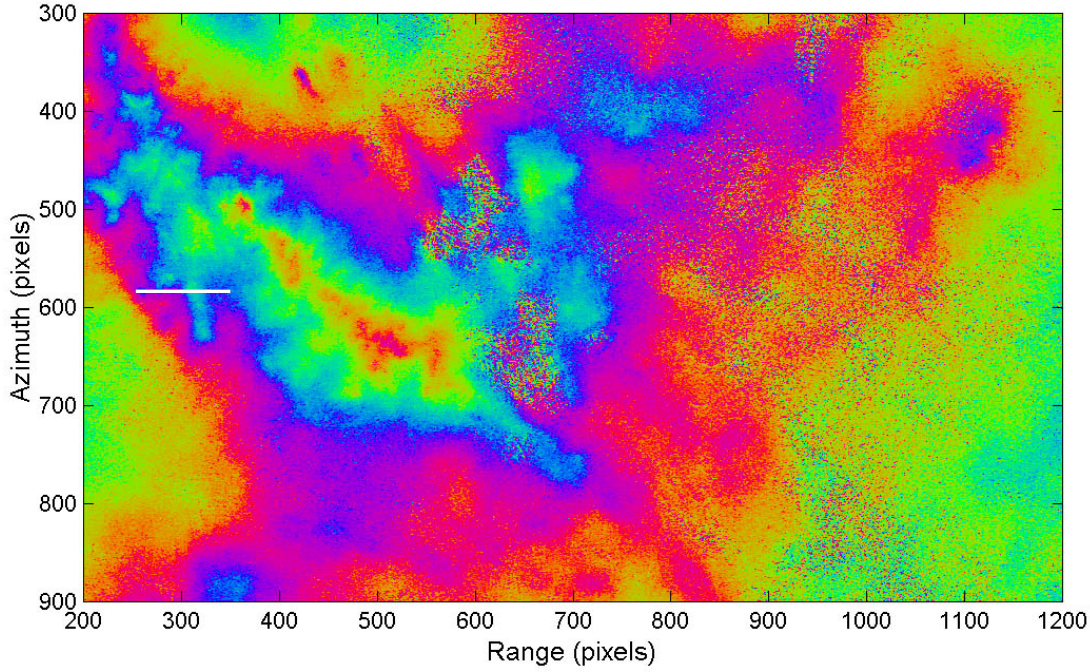

Figure 5.26 *Filtered wrapped phase interferogram using the new filter. Horizontal line indicates cross-section location.*

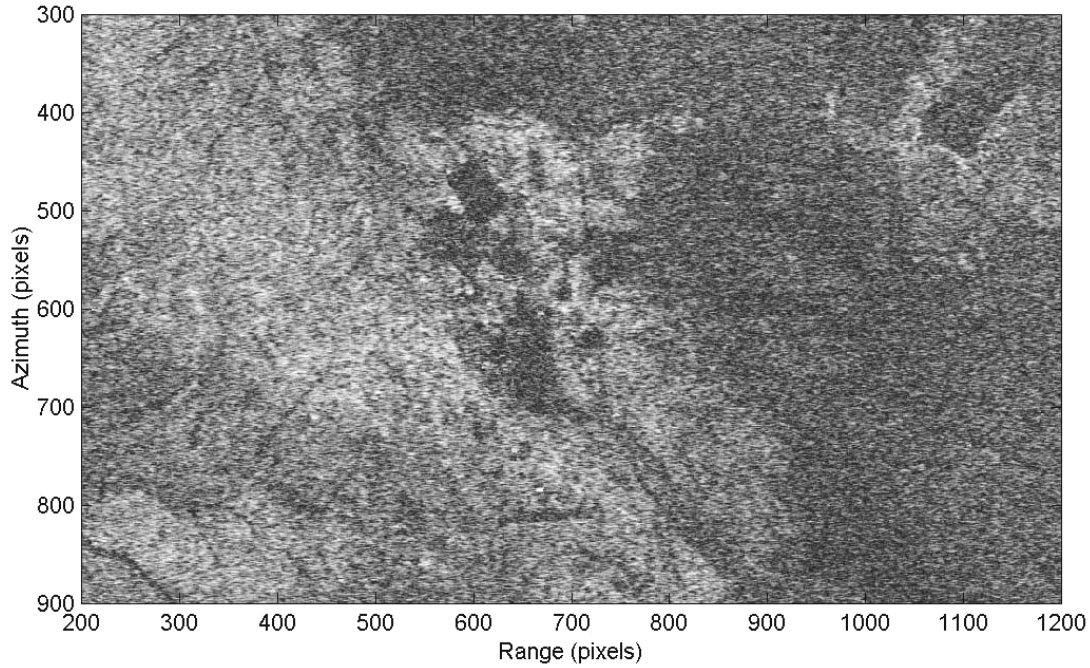

Figure 5.27 *Coherence map.*

A closer look at the example cross-section (Figure 5.28) over the wrapped phase interferogram shows the same characteristics of the Goldstein filter and the new filter as observed when used with simulated data set. The horizontal line on Figure 5.26 indicates the cross-section location. In Figure 5.28 circle A, large vertical phase

offset (φ_V) can be observed for the Goldstein filter. At the same time due to the high coherence ($\bar{\gamma} > 0.7$) in this region (Figure 5.27), the new filter does not create a high phase offset.

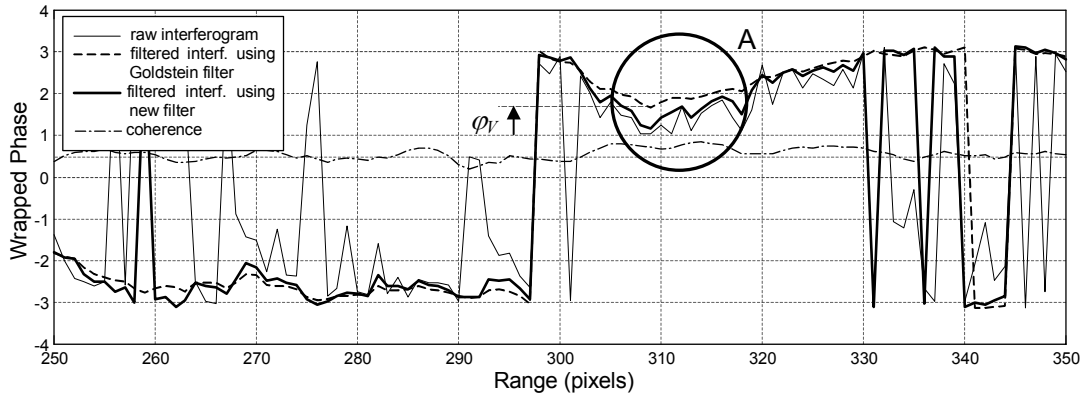

Figure 5.28 *The cross-section over the unfiltered and filtered wrapped phase interferogram.*

To check how the phase offset affects terrain heights, phase unwrapping and height computation were performed. Figure 5.29 shows the cross-section over the surface heights corresponding to the same location as the wrapped phase indicated in Figure 5.28.

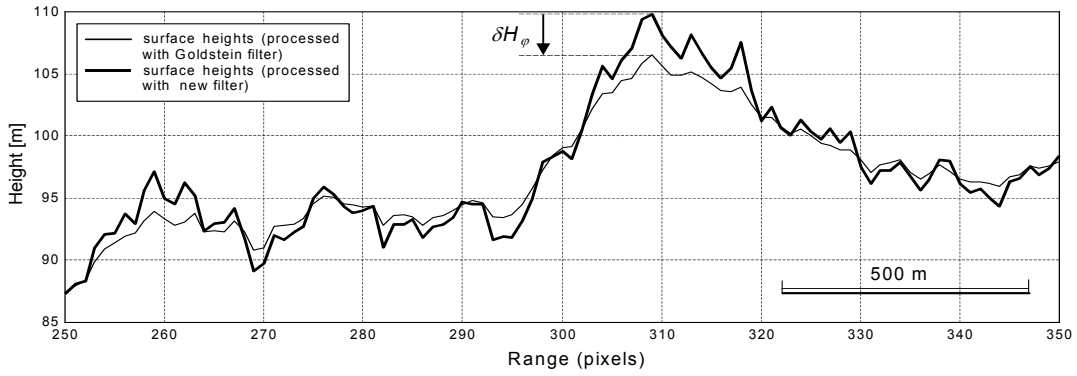

Figure 5.29 *The cross-section over the reconstructed surface heights.*

As expected, the vertical phase offset propagates directly into the height of the DEM introducing additional systematic error (δH_φ). The quantity of this error depends strongly on the φ_V and is proportional to the height ambiguity.

5.6.2 Filter Impact on Small-Scale Deformation Detection

To evaluate the impact of the filter on small-scale surface deformation detection both filters are applied to the real interferogram from the Silesia study area formed by two images (AQ-IS and AQ-IIS see Chapter 4). The part of the interferogram that has already been analysed in Section 4.4, Figure 4.22 is selected for this test. It represents an example of small-scale surface subsidence due to underground mining. Figure 5.30c and d show the interferometric phase images after applying the Goldstein and new radar interferogram filter respectively. The reduction of the phase noise is clearly visible for both filters as compared to the raw interferogram (Figure 5.30a).

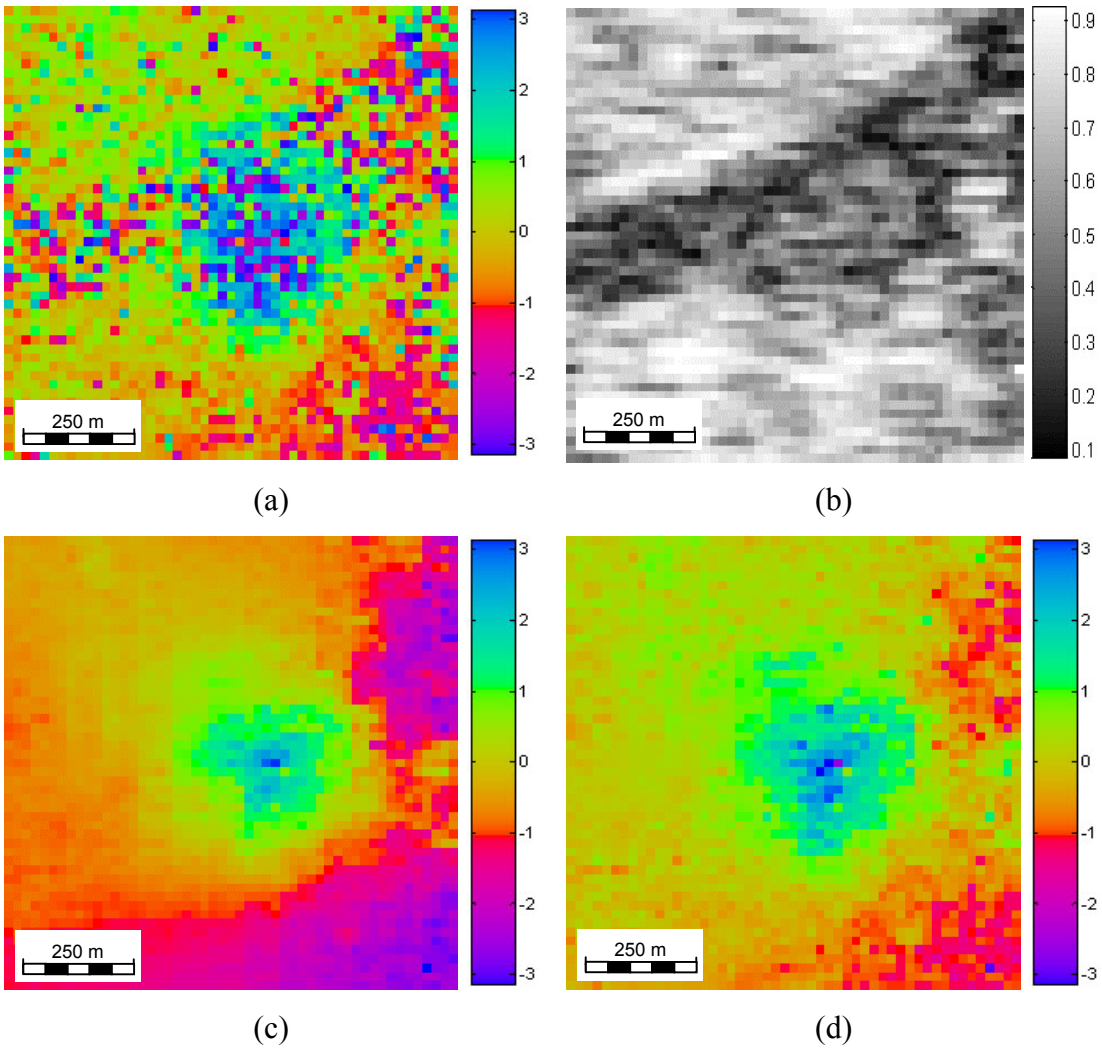

Figure 5.30 *(a) Raw interferogram, (b) coherence map, (c) filtered interferogram using the Goldstein (α = 0.9) and (d) the new radar interferogram filter (colour bars in radians).*

The reconstructed surface subsidences show the impact of both filters on the deformation signal. The overall magnitude of reconstructed subsidence (Figure 5.31a) based on the filtered interferogram using the Goldstein filter is up to 40% less than the magnitude of reconstructed subsidence (Figure 5.31b) based on the filtered interferogram using the new filter.

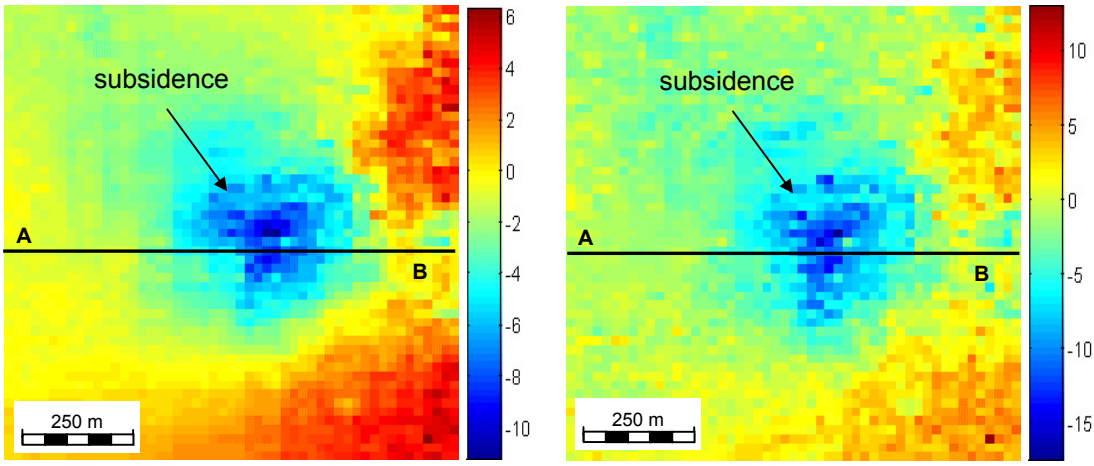

(a) (b)

Figure 5.31 *(a) Surface subsidence reconstructed from the filtered interferogram using the Goldstein and (b) the new radar interferogram filter (colour bars in millimetres). Horizontal line indicates the cross-section location.*

The example cross-section (A-B) along both surface subsidences (Figure 5.32) illustrates the quantity of deformation signal that has been lost due to over-filtering. As can be seen the largest difference (δD) between both surface subsidences is experienced in the centre of the deformation sag.

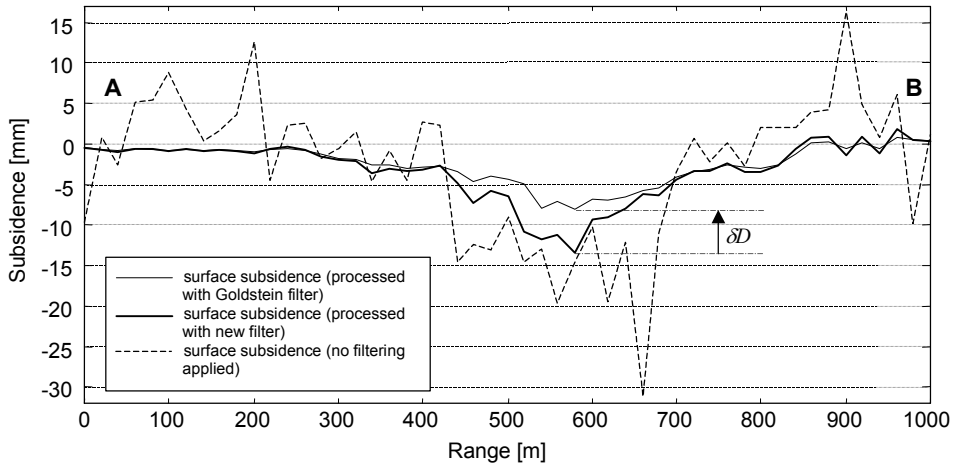

Figure 5.32 *The cross-section along the reconstructed surface subsidences.*

Figure 5.33 shows the map of differences between two reconstructed surface subsidences based on filtered interferograms using the new and Goldstein radar interferogram filter. It reveals the loss of deformation signal in the centre part of the subsidence sag.

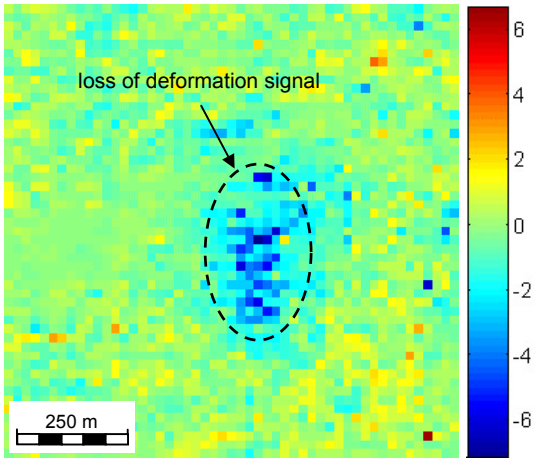

Figure 5.33 *Loss of deformation signal due to over-filtering. Based on differences between the reconstructed surface subsidences based on filtered interferograms using the new and Goldstein radar interferogram filter (colour bar in millimetres).*

In conclusion, the phase offset due to filtering using the Goldstein radar interferogram filter propagates directly into the deformation map leading to some loss of deformation signal. If the deformation signal is very low, the impact of the filter can be severe as it can significantly reduce the quantity of the signal or even destroy the entire signal. The proposed filter, however, reduces the loss of deformation signal due to over-filtering. As it is led by the coherence value it adopts better to the actual level of noise. The high coherence value prevents the phase being over-filtered. Therefore, it prevents the loss of small-scale deformation signal.

Figure 5.34 shows the new redefined three-dimensional model of subsidence based on the filtered interferogram using the new radar interferogram filter. As compared to the previous model shown in Figure 4.23 the magnitude of subsidence is significantly larger in the centre of the deformation sag but the spatial extent of the subsidence has not changed much.

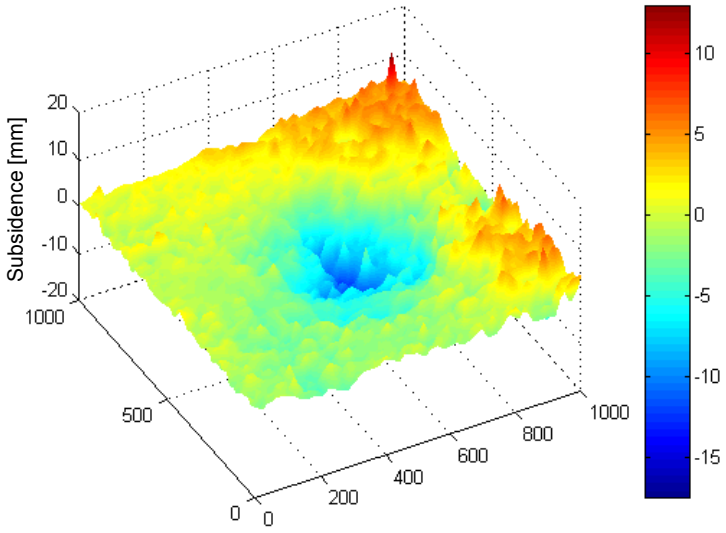

Figure 5.34 *New three-dimensional model of surface subsidence (colour bar in millimetres).*

5. 7 Discussion

In this chapter, a new adaptive radar interferogram filter based on the modification to the Goldstein filter was proposed. The Goldstein filter parameter α was replaced with a new parameter $1-\bar{\gamma}$, which is dependent on the value of absolute coherence. The effectiveness of the new filter has been evaluated based on simulated and real data sets. As the experiments show, both filters create some phase offset in the filtered interferogram. The phase offset has direct impact on quality of DEMs and deformation detection studies as it introduces additional error to the surface heights and deformation signal. However, the new filter reduces the magnitude of the phase offset as it prevents the areas characterised by high coherence (less noise) from being over-filtered. On the other hand, it allows stronger filtering in the areas with low coherence (high noise). Therefore, the new filter adapts to the wrapped phase interferogram more effectively. Furthermore, both filters perform almost identically in the areas where coherence is low (less then 0.3).

In conclusion, interferograms characterised by high coherence will benefit from the new radar interferogram filter, as it decreases the loss of resolution. In particular, regions of rough terrain and small-scale surface deformation (small magnitude) will benefit from the new filter being used.

5. 8 Summary

This chapter provides the basic filters theory followed by the development of a new adaptive radar interferogram filter. The new filter is based on the modification to the Goldstein radar interferogram filter. In order to evaluate the filter, the interferometry data such as the interferogram and coherence map have been simulated. Finally, the Goldstein and the new filters have been applied to the simulated and real wrapped phase interferogram. The results have shown that the new filter performs better as it minimises the loss of signal while still reducing the level of noise.

6 A NEW FUNCTIONAL MODEL FOR DETERMINING MINIMUM AND MAXIMUM DETECTABLE DEFORMATION GRADIENT

In this chapter a functional model for determining the minimum and maximum detectable deformation gradient in terms of coherence is proposed. Moreover, this model is developed based on a new methodology that incorporates both real and simulated data. Finally, the new model is validated and its advantages and disadvantages discussed.

6. 1 Introduction

Radar interferometry measures the change in range distance between the sensor and the ground. If a part of the ground covered by the imaging scene experiences a displacement (D_G) along the sensor-ground direction, it changes the round trip distance by $2D_G$, and creates a phase shift with respect to the stable part of the scene. Any displacement along the radar viewing direction equal to half a wavelength creates one fringe in the interferogram. Assuming that the wavelength (λ) equals 0.056 m (ERS-1/2 SAR sensor), one fringe corresponds to 0.028 m of surface displacement. Thus, in the interferogram, within each fringe a given colour represents a particular phase difference. Therefore the accurate displacement for each point can easily be established.

However, not all deformations can be detected using radar interferometry. The necessary condition for deformation detection given by Massonnet and Feigl (1998) implies that the maximum detectable deformation gradient is one fringe per pixel. Furthermore, Massonnet and Feigl (1998) define the maximum detectable deformation gradient (d_x) as a dimensionless ratio of half the wavelength (λ) to the pixel size (ps):

$$d_x = \frac{0.5 \cdot \lambda}{ps} \tag{6.1}$$

Therefore, for the satellites ERS-1/2, the maximum detectable deformation gradient (d_x) is equal to 1.4×10^{-3}, assuming the interferogram pixel size 20x20 m.

According to the definition, radar interferometry should be able to detect quite a wide range of different deformation gradients. Unfortunately, radar interferometry suffers from noise in the interferogram phase measurement, which is caused by the decorrelation effects discussed in Section 2.8. Moreover, the interferogram contains biases due to satellite orbit errors, atmospheric heterogeneity and filtering. Thus, very small and large deformation gradients become undetectable if the level of noise is too high.

The current definition of the maximum detectable deformation gradient does not include the noise factor. Thus, it does not describe the problem realistically. In addition, a definition describing the minimum deformation gradient does not exist at all. Therefore, to determine the minimum and maximum detectable deformation gradient, a new methodology is proposed. This approach consists of (i) simulation of deformation, (ii) generation of deformation phase values, (iii) insertion of the simulated deformation phase information into a real SLC image, (iv) DInSAR processing, and (v) the analysis of the differential interferogram to estimate the signature of the recovered deformation signal, in relation to the original simulated deformation model. Finally, a theoretical set of observations that lead to the functional model defining the minimum and redefining the maximum detectable deformation gradient is created.

6. 2 Small-Scale Surface Deformation Simulation

A common shape for small-scale surface deformation is a circular or elliptical trough (by mining subsidence). Thus, to model a small-scale deformation the two-dimensional elliptical Gaussian function has been adopted:

$$f(R,A) = \frac{1}{2\pi\sigma_R\sigma_A} \exp -\left[\frac{(R-\mu_R)^2}{2\sigma_R^2} + \frac{(A-\mu_A)^2}{2\sigma_A^2} \right] \tag{6.2}$$

where R and A are the coordinates of the model in the range and azimuth direction respectively. Assuming the mean values (μ_R, μ_A) equal to 0, by changing the standard

deviation components σ_R and σ_A, an elliptical shape for the simulated deformation is achieved *f(R,A)*. Furthermore, by scaling the entire model, the amplitude of vertical deformation is simulated. For simplicity, it has been assumed that vertical deformation derived from the model expresses surface subsidence along the direction of the satellite line of sight.

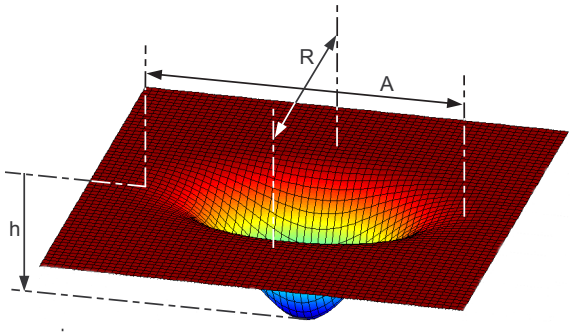

Figure 6.1 *Geometry of the simulated deformation model.*

Several models, varying in spatial extent (*R/A*) and the deformation amplitude (*h*), have been generated (Figure 6.1). The details of the simulated models are listed in Table 6.1.

Table 6.1 *Deformation models parameters*

Name	**M0**	**M1**	**M2**	**M3**	**M4**	**M5**	**M6**	**N0**	**N1**	**N2**	**N3**	**N4**	**O0**	**O1**	**O2**	**O3**
Fringe	1/8	1/4	1/2	1	2	3	4	1/8	1/4	1/2	1	2	1/8	1/4	1/2	1
h[mm]	3.5	7	14	28	56	84	112	3.5	7	14	28	56	3.5	7	14	28
R/A[m]	480/960							280/480					140/220			

By converting (wrapping) the simulated deformation model into their associated phase values (28mm = 2π), the change in phase (Φ_{SR}) along the radar line of sight is computed. Next, the simulated signal is added as a patch into the phase (Φ_S) of a real radar image (*e.g.* slave image). Finally, the phase (Φ_{SN}) of the new created image is defined as:

$$\Phi_{SN} = \Phi_S + \Phi_{SR} \tag{6.3}$$

If the new phase value (Φ_{SN}) is greater than ±π, the phase is wrapped again. However, the amplitude of the real image is not changed ($|a_{SN}|=|a_S|$). Figure 6.2 indicates the related phase and amplitude values.

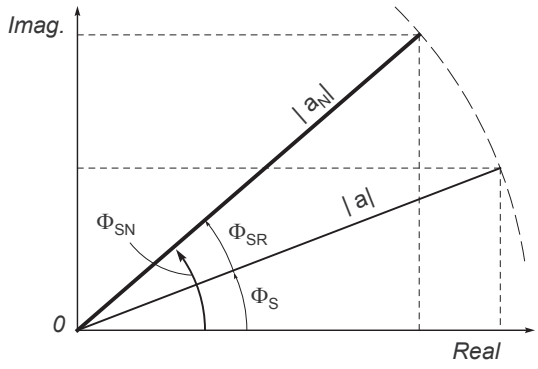

Figure 6.2 *Definitions of amplitude and phase for the new image.*

The simulated phase patches are added to areas characterised by different coherence values. It is assumed that no other deformation signal exists in the areas where the patches are added. This approach of incorporating simulated phase according to a deformation model into the real image ensures realistic noise over the simulated deformation. For the purpose of testing this methodology, two radar images (AQ-I and AQ-II) acquired over the Leinster study area are used. After the phase information of the simulated deformation model is introduced into the slave image, both images are processed and a differential interferogram is achieved. The interferometry processing and parameters used are discussed in Chapter 4. Finally, the interferometric phase difference ($\Delta\Phi$) is defined as:

$$\Delta\Phi = \Phi_M - \left(\Phi_S + \Phi_{SR}\right) + n \tag{6.4}$$

where $\Delta\Phi_M$ is the phase of the master image, *n* describes the noise preserved in both images as well as the noise introduced during the interferometry processing procedure.

If the perpendicular baseline component is sufficiently short, the topography contribution can be neglected. In practice, however, it is very difficult to obtain radar images with a very small perpendicular baseline and usually the topography contribution has to be removed from the interferogram in order to obtain the signature of deformation. Therefore, assuming subtracted topography contribution, Equation (6.4) can be rewritten as:

$$\Delta\Phi = -\Phi_{SR} + n \tag{6.5}$$

Finally, the differential interferogram should contain the phase signal related to the simulated deformations (Φ_{SR}) and the noise (n). If the phase of the simulated deformation model is recovered on the differential interferogram, it is assumed that a particular deformation can be detected.

In the following sections, the phase images of particular deformation models are analysed and the functional model determining the min/max detectable deformation gradient developed. Figure 6.3 shows the basic concept of the new methodology.

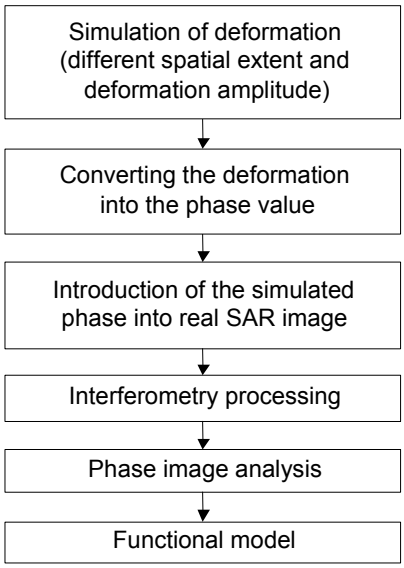

Figure 6.3 *Proposed methodology.*

6. 3 Interferometry Analysis of the Simulated Deformation Models

The phase images of the simulated deformation models are compared visually with the signatures from their respective differential interferograms after interferometry processing. The visual inspection was aided by the image editing software using magnifying tools. Figure 6.4 to Figure 6.6 show the interferometric phase of the simulated deformation models M, N, O (model parameters are defined in Table 6.1) and the signature of these models onto the differential interferogram after interferometry processing. The phase related to the modelled deformation was introduced into the slave image over the areas characterised by different coherence values ranging from 0.3 to 0.55.

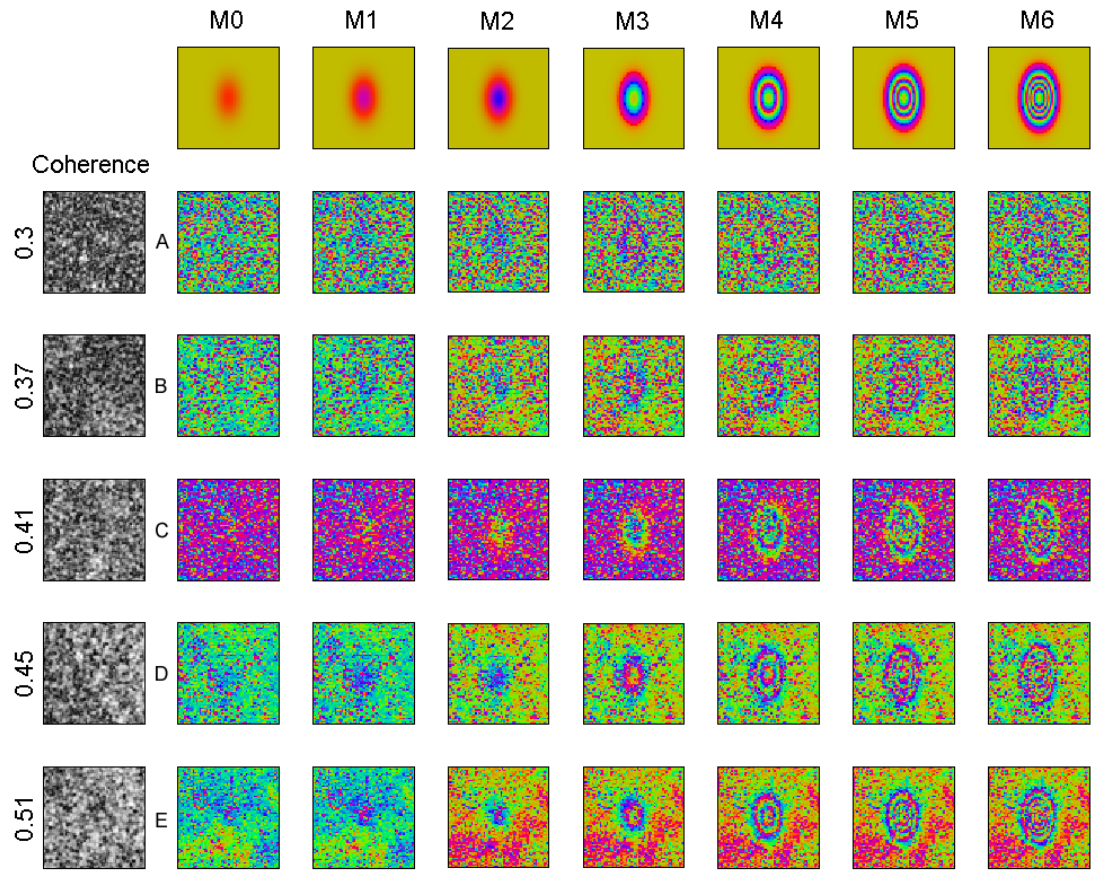

Figure 6.4 *Phase images of the simulated models M0 to M6 and their signature after interferometry processing for different coherence value (rows A to E). The left-hand side column shows the corresponding coherence map and the average value over the area.*

The interferogram based on the given radar images (AQ-I, AQ-II) is characterised by overall low coherence, due to the long temporal baseline. This factor results in the limited range of coherence values covered. However, the covered coherence range is good enough to develop a model as the low coherence values play the crucial role in determining the model parameters.

It was found that for constant coherence, it becomes increasingly difficult to correctly interpret the interferometric phase ($\Delta\Phi$), as the amount of vertical deformation increases. For instance, for the interferometric phase related to models M2, M3, M4, which represent a half, one and two fringes respectively, the number of fringes can be measured correctly for given coherence value. However, for the interferometric phase related to model 'M6' (4 fringes), it was not possible to unequivocally determine the number of fringes. In addition, as the increasing magnitude of deformation becomes more difficult to retrieve, the overall deformation

contour pattern is more easily recognised. The extent of the deformation for the 'M' family of models could be recognised on the interferogram for coherence values of 0.35 and above, while for models 'N', the coherence threshold was determined at the level of 0.40 (Figure 6.5).

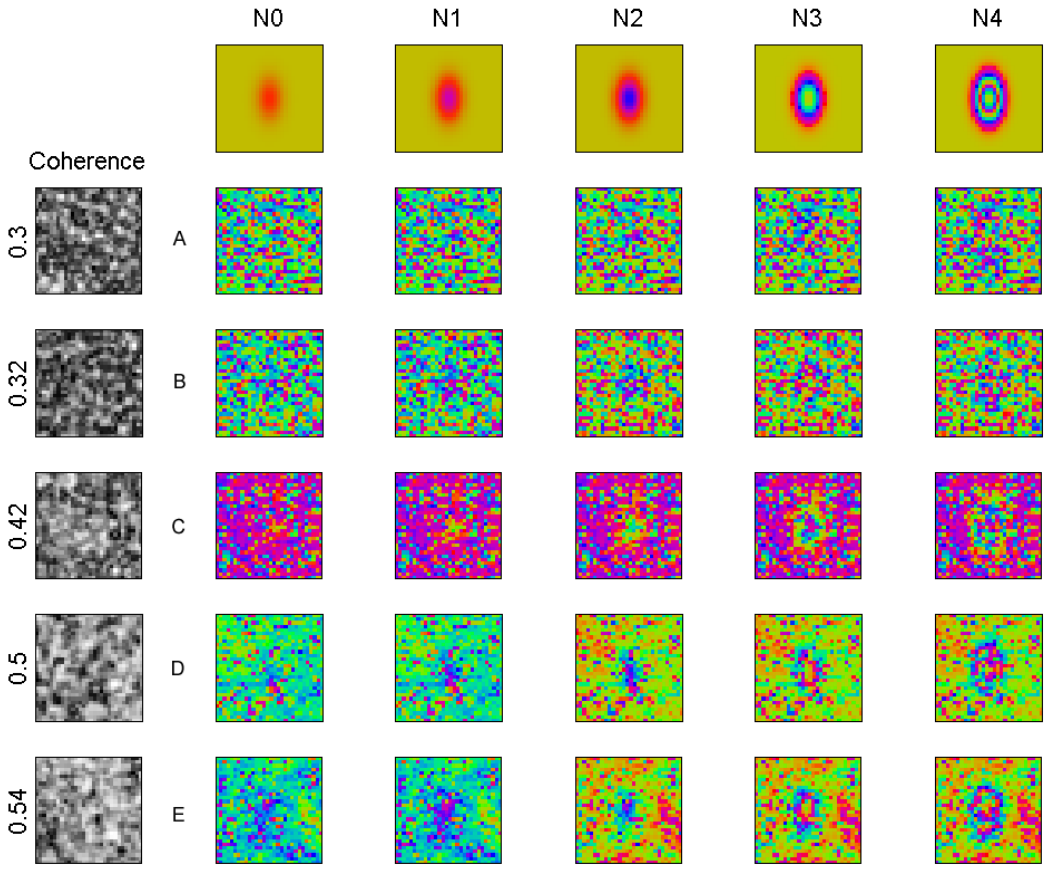

Figure 6.5 *Phase images of the simulated models N0 to N4 and their signature after interferometry processing for different coherence value (rows A to E). The left-hand side column shows the corresponding coherence map and the average value over the area.*

Furthermore, the smallest deformation models 'O' could be detected only at coherence level greater than 0.50. The spatial extent of this model (140 x 220 m) and deformation amplitude 0.5 and 1 fringe could only be recognised at coherence level 0.55 (Figure 6.6).

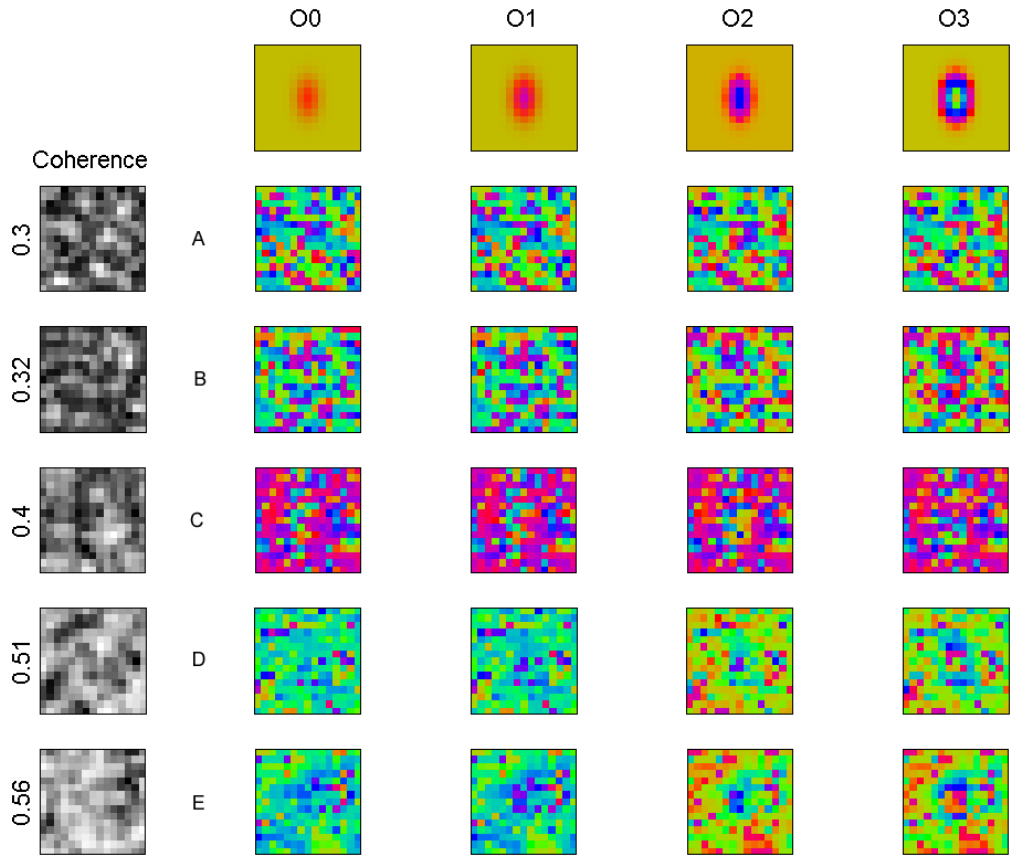

Figure 6.6 *Phase images of the simulated models O0 to O3 and their signature after interferometry processing for different coherence value (rows A to E). The left-hand side column shows the corresponding coherence map and the average value over the area.*

6. 4 Functional Model

In this section a functional model defining the minimum (d_{min}) and the maximum (d_{max}) detectable deformation gradient is proposed. The new model extends the definition of the maximum detectable deformation gradient by including the coherence (γ) factor in its definition. Moreover, this model defines the previously undefined minimum detectable deformation gradient also in terms of coherence value.

6.4.1 Model Parameters

Two parameters of the model are defined: (i) deformation gradient and (ii) coherence.

The first parameter, deformation gradient (*d*), is defined as:

$$d = \frac{h}{L_{\min}} \tag{6.6}$$

where h is the deformation magnitude and L_{min} is the shortest distance from the edge of the deformation model to the place where the maximum deformation magnitude occurs. According to the simulated models, L_{min} is equal to the half of the range dimension ($L_{\min} = 0.5 \cdot R$). Both variables are in the same units, therefore the deformation gradient is dimensionless.

The second parameter, coherence (γ), defined in Equation 2.23 and its estimator in Equation 4.6, describes the interferometric phase accuracy. In other words, coherence is an indicator of the amount of interferometric phase noise caused by many decorrelation factors.

In order to develop the functional model, a set of observations (Table 6.2) based on the proposed methodology described in previous sections has been prepared. Each time the simulated model could be detected on the resulting interferogram, a decision value (Ω) is set to 1. Moreover, if the model could not be detected, the decision value (Ω) is set to 0. The correct detection of the model implies that the spatial extents as well as the correct number of fringes could be identified.

The detection of the simulated deformation is undertaken by visual inspection of the interferogram. This approach is the major weakness of the resultant model. However, no automatic method that could be used for deformation detection analysis exists. In the following chapter one possible approach of using a wavelet transform for advanced analysis of the phase image is examined. If the wavelet approach proves successful, the model could be better defined.

Table 6.2 *Model parameters (observations)*

No.	Model	Deformation Gradient (*d*)	Coh. (γ)	Decision (Ω)	No.	Model	Deformation Gradient (*d*)	Coh. (γ)	Decision (Ω)
1	M0A	0.000015	0.30	0	41	N1A	0.000050	0.30	0
2	M0B	0.000015	0.37	0	42	N1B	0.000050	0.32	0
3	M0C	0.000015	0.41	0	43	N1C	0.000050	0.42	0
4	M0D	0.000015	0.45	0	44	N1D	0.000050	0.50	1
5	M0E	0.000015	0.51	0	45	N1E	0.000050	0.54	1
6	M1A	0.000029	0.30	0	46	N2A	0.000100	0.30	0
7	M1B	0.000029	0.37	0	47	N2B	0.000100	0.32	0
8	M1C	0.000029	0.41	0	48	N2C	0.000100	0.42	1
9	M1D	0.000029	0.45	1	49	N2D	0.000100	0.50	1
10	M1E	0.000029	0.51	1	50	N2E	0.000100	0.54	1
11	M2A	0.000058	0.30	0	51	N3A	0.000200	0.30	0
12	M2B	0.000058	0.37	1	52	N3B	0.000200	0.32	0
13	M2C	0.000058	0.41	1	53	N3C	0.000200	0.42	1
14	M2D	0.000058	0.45	1	54	N3D	0.000200	0.50	1
15	M2E	0.000058	0.51	1	55	N3E	0.000200	0.54	1
16	M3A	0.000117	0.30	0	56	N4A	0.000400	0.30	0
17	M3B	0.000117	0.37	1	57	N4B	0.000400	0.32	0
18	M3C	0.000117	0.41	1	58	N4C	0.000400	0.42	0
19	M3D	0.000117	0.45	1	59	N4D	0.000400	0.50	1
20	M3E	0.000117	0.51	1	60	N4E	0.000400	0.54	1
21	M4A	0.000233	0.30	0	61	O0A	0.000050	0.30	0
22	M4B	0.000233	0.37	0	62	O0B	0.000050	0.32	0
23	M4C	0.000233	0.41	1	63	O0C	0.000050	0.40	0
24	M4D	0.000233	0.45	1	64	O0D	0.000050	0.51	0
25	M4E	0.000233	0.51	1	65	O0E	0.000050	0.56	1
26	M5A	0.000350	0.30	0	66	O1A	0.000100	0.30	0
27	M5B	0.000350	0.37	0	67	O1B	0.000100	0.32	0
28	M5C	0.000350	0.41	0	68	O1C	0.000100	0.40	1
29	M5D	0.000350	0.45	0	69	O1D	0.000100	0.51	1
30	M5E	0.000350	0.51	1	70	O1E	0.000100	0.56	1
31	M6A	0.000467	0.30	0	71	O2A	0.000200	0.30	0
32	M6B	0.000467	0.37	0	72	O2B	0.000200	0.32	0
33	M6C	0.000467	0.41	0	73	O2C	0.000200	0.40	1
34	M6D	0.000467	0.45	0	74	O2D	0.000200	0.51	1
35	M6E	0.000467	0.51	0	75	O2E	0.000200	0.56	1
36	N0A	0.000025	0.30	0	76	O3A	0.000400	0.30	0
37	N0B	0.000025	0.32	0	77	O3B	0.000400	0.32	0
38	N0C	0.000025	0.42	0	78	O3C	0.000400	0.40	0
39	N0D	0.000025	0.50	0	79	O3D	0.000400	0.51	0
40	N0E	0.000025	0.54	0	80	O3E	0.000400	0.56	1

6.4.2 Model Determination

Figure 6.7 shows the value of the deformation gradient (d) plotted against the coherence value (γ) for the observations listed in Table 6.2. The dots on the plot indicate the simulated models that are not detected after the interferometry processing. The asterisks indicate the models that are properly detected after the interferometry processing. As it can be seen, the point clouds related to the models that are identified as detected ($\Omega = 1$) form the wedge-like shape among the observations. This very important observation provides the possibility to define a model that can relate the deformation gradient and the coherence value defining: d_{min}, and d_{max}.

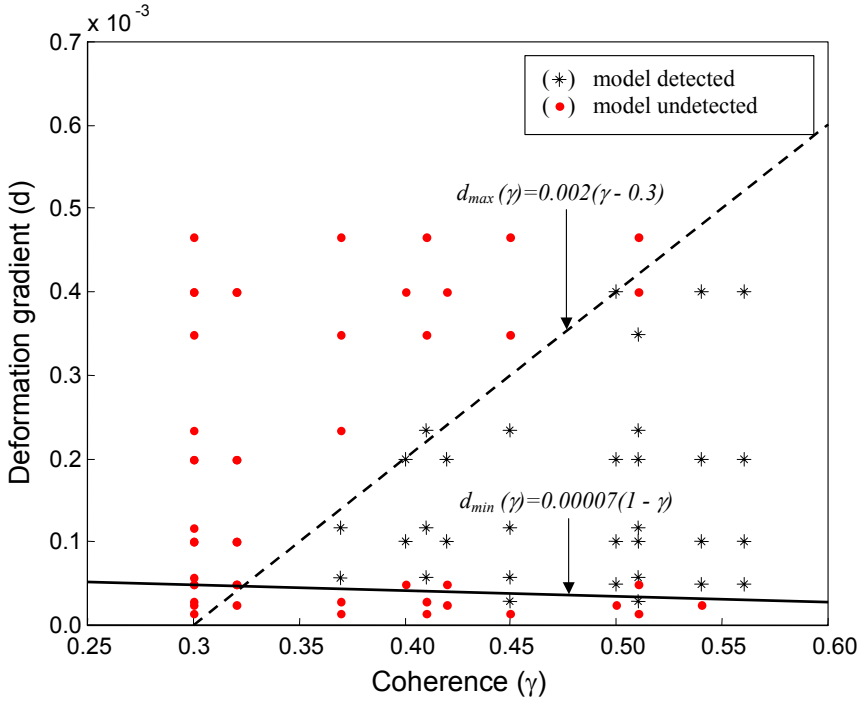

Figure 6.7 *Observations and the linear models: $d_{min}(\gamma)$ and $d_{max}(\gamma)$.*

To define the maximum detectable deformation gradient function $d_{max}(\gamma)$, the observations data set and the constraint defined in Equation (6.7) have been taken into account.

$$d_{\max} = d_x \quad for \quad \gamma = 1 \tag{6.7}$$

This constraint ensures that for a coherence value equal to one, the extended definition of the model holds for the maximum detectable deformation gradient

already defined in Equation (6.1). Therefore, the linear formula for the new function is defined as:

$$d_{\max} = S_m(\gamma - 1) + d_x \tag{6.8}$$

where S_m is the slope of the linear function $d_{max}(\gamma)$, which defines the boundary between the upper edge of the point clouds (Figure 6.7).

On the basis of Figure 6.7, the value of the slope S_m was empirically determined to be approximately 0.002. Therefore, the new definition of the maximum detectable deformation gradient in terms of the coherence value is defined as:

$$d_{\max} = \frac{\gamma - 1}{500} + d_x \tag{6.9}$$

Furthermore, to define the minimum detectable deformation gradient function $d_{min}(\gamma)$, the observations data set and the constraint defined in Equation (6.10) have been taken into account.

$$d_{\min} = 0 \quad for \quad \gamma = 1 \tag{6.10}$$

This constraint will ensure that for a coherence value equal to one, the minimum detectable deformation gradient is zero. In other words, if there is no deformation at all, the phase value should be constant. Therefore, the linear formula for the new function is defined as:

$$d_{\min} = S_n(\gamma - 1) \tag{6.11}$$

where S_n is the slope of the linear function $d_{min}(\gamma)$, which defines the boundary between the lower edge of the point clouds (Figure 6.7).

On the basis of Figure 6.7, the value of the slope S_n was empirically determined to be approximately 0.7×10^{-5}. Therefore, the new definition of the minimum detectable deformation gradient in terms of the coherence value is defined as:

$$d_{\min} = -0.00007(\gamma - 1) \tag{6.12}$$

Combining the Equation (6.9) and Equation (6.12) the functional model for determining the minimum and maximum detectible deformation gradient is created. Figure 6.8 shows a new graphical summary of the functional model. The horizontal axis of the graph indicates the coherence value from 0 to 1 while the vertical axis indicates the range of possible deformation gradients from 0 to d_x. The value of d_x is equal to 1.4×10^{-3} and it is the old definition of the maximum detectable deformation gradient for satellite ERS-1/2 as defined in Equation (6.1).

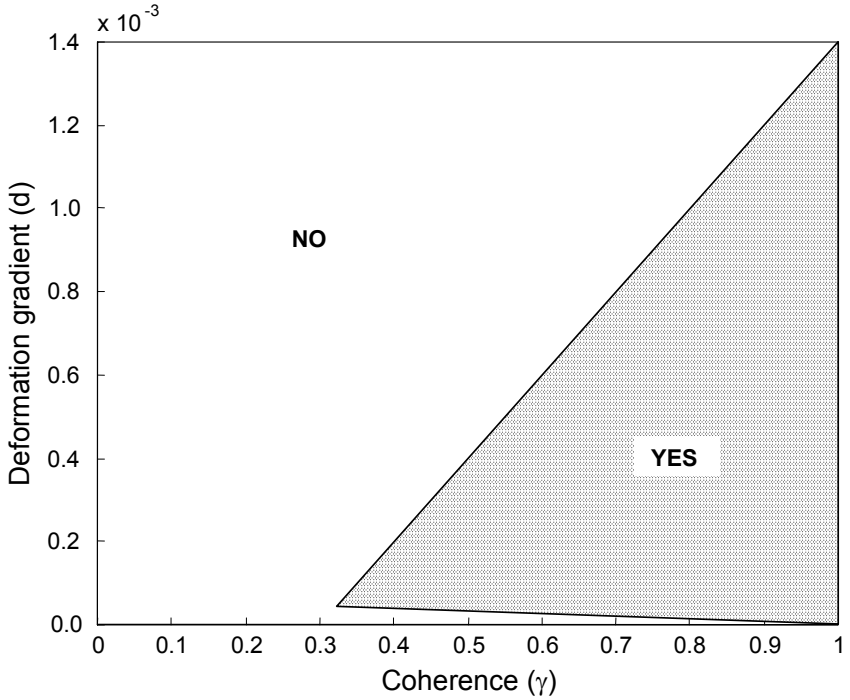

Figure 6.8 *The new functional model for determination of the min/max detectable deformation gradient (d) in terms of coherence value (γ). This model is valid for the satellites ERS-1/2 (λ=5.66 cm) and interferogram resolution 20x20 m.*

Figure 6.8 illustrates two zones named YES and NO. The zone YES shows the values of coherence (γ) and deformation gradient (d) for which the deformations on the surface can be detected by radar interferometry. The zone NO, however, shows the values of γ and d for which the surface deformation cannot be detected. Equation (6.13) defines the deformation gradient as detectable or not for certain coherence values:

$$\begin{cases} d_{\min} \le d \le d_{\max} & \Rightarrow \quad Yes \\ d > d_{\max} \; or \; d < d_{\min} & \Rightarrow \quad No \end{cases} \tag{6.13}$$

In addition, for $d_{min}(\gamma) = d_{max}(\gamma)$ the minimum coherence value, below which any deformations cannot be detected, was found to be 0.32.

6.4.3 Validation of the Functional Model

The purpose of model validation is to establish if the relationship between the model's parameters (coherence and deformation gradient) is valid for other interferometry data. To validate the proposed functional model, the interferogram from the Silesia study area based on images AQ-IS and AQ-IIS is used. The interferogram was processed to 20x20 m pixel size. Since the data from Silesia was not used for the model generation it ensures independent validation of the model.

Two different areas over the interferogram to validate the functional model have been identified. Figure 6.9 illustrates the first case (K_1), which shows one fringe related to the surface deformation caused by the underground mining activities. The task for this assessment is to find out if the deformation gradient and coherence taken from this example lies within the YES zone as defined by the model.

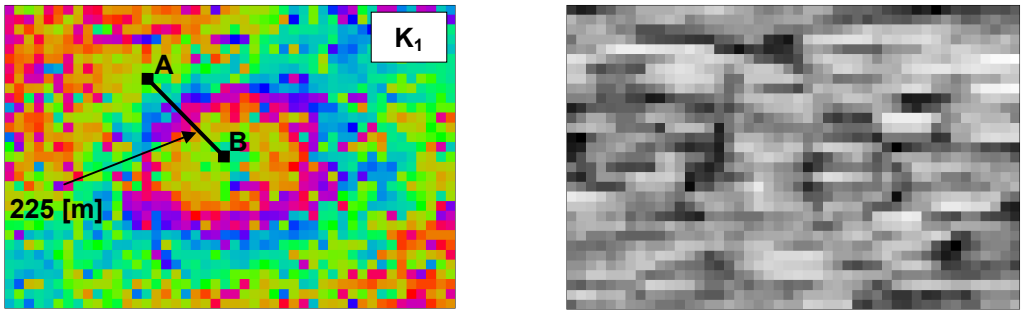

(a) (b)

Figure 6.9 *(a) Deformation fringe over the Silesia study area and (b) the corresponding coherence map (mean coherence over the area is 0.61).*

To perform this validation, two parameters of the model are established. Firstly, the deformation gradient between points A and B is found to be 0.12×10^{-3} (0.028/225). Secondly, the average coherence over the area is found to be 0.61. Finally, the two parameters are plotted on the graph as shown on Figure 6.11. Point $K_1(\gamma,d)$ falls into the YES zone what indicates that this deformation gradient can be easily detected at this coherence value. Thus, this example has confirmed the suitability of the new

functional model for determining the min/max deformation gradient in terms of coherence.

Figure 6.10 shows the second case (K_2). This example interferogram presents the four fringes in form of an elliptical shape that are related to surface deformation caused by the underground mining activities. However, a segment of the fringes is too noisy and the correct interpretation of the number of fringes is impossible in that area.

The task of this assessment is to find out if the same deformation gradient and different coherence taken from this example lies within the proper zone as defined by the model. Therefore, two sub-cases are selected over the area. The first sub-case, K_{2A}, shows a part of the interferogram where the correct number of fringes can be identified and the deformation magnitude established. Sub case K_{2B} indicates a part of the interferogram where the correct number of fringes could not be identified at all. Assuming the elliptical shape of the deformation area, the deformation gradients between points AB and AC are the same in both sub-cases and are equal to 0.26×10^{-3} (Figure 6.10.a).

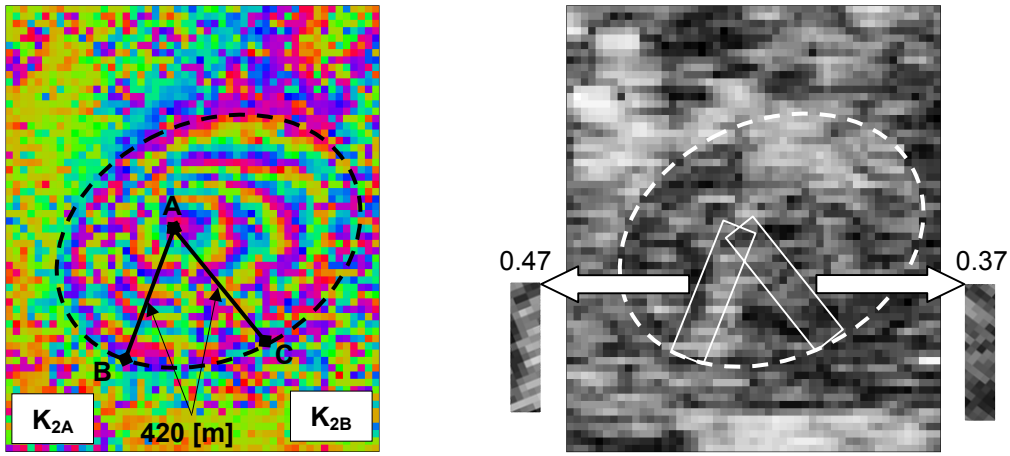

(a) (b)

Figure 6.10 *(a) Deformation fringes over the Silesia study area and (b) the corresponding coherence map.*

However, the coherence value calculated over the two areas is different and equal to 0.47 in sub case K_{2A} and 0.37 in sub case K_{2B}. The coherence is the average value calculated over the strips covering the investigation areas as shown in Figure 6.10.b.

Finally, the observed parameters related to both sub cases (K_{2A} and K_{2B}) are plotted on the graph as shown in Figure 6.11. As can be seen, the analysed examples have further confirmed the prediction of the functional model.

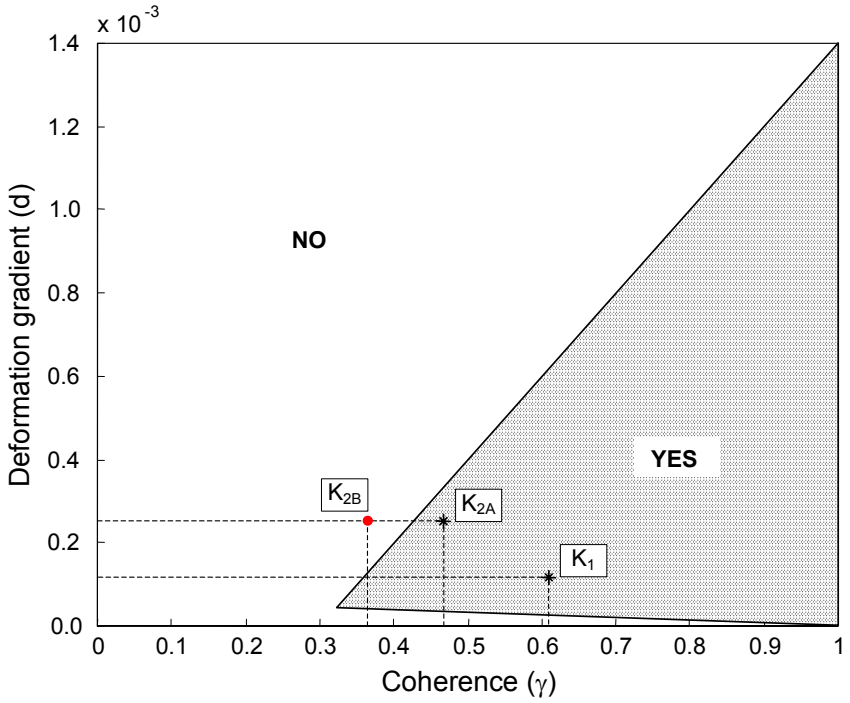

Figure 6.11 *Validation of the functional model. (The three test cases (K_1, K_{2A}, K_{2B}) agree with the new functional model).*

6. 5 Discussion

A new methodology that leads to a functional model for determining the minimum and maximum detectable deformation gradient by radar interferometry has been proposed. This methodology is based on both simulated and real data. The advantage of using simulated deformation is that full control over the spatial extent and vertical magnitude of deformation is available. Furthermore, introducing the phase information of the simulated deformation models into a real radar image ensures the realistic noise within the final differential interferogram. By comparison of the deformation signatures on the differential interferogram with their corresponding models, a set of observations that lead to a new model has been established. The new functional model extends the existing definition of the maximum detectable deformation gradient by introducing dependence on the coherence value γ. Thus, the new definition decreases the maximum detectable deformation gradient as the coherence decreases. The new and old definitions are

identical only for coherence equal to one. On the other hand, the proposed model introduces the previously undefined minimum detectible deformation gradient. It is important to notice that an increasing amount of noise also affects the ability of the interferometry technique to detect very small deformation gradients. For instance, taking into account the parameters of the satellites ERS-1/2, the maximum detectable deformation gradient is 1.4×10^{-3} for coherence equal to one and decreases to 0.04×10^{-3} at coherence level 0.32. Moreover, the range of minimum detectable deformation gradients decreases from its largest value of 0.04×10^{-3} to zero as the coherence increases to one. The zero deformation gradient can be explained as no deformation at all. Therefore, according to the conditions of the new model, radar interferometry should be able to detect deformations at their maximum detectable deformation gradient and resolve the stable areas with the maximum confidence level for the coherence value equal to one. Any coherence smaller than one would result in narrowing the range of detectable deformation gradients. Moreover, below coherence value of 0.32, detection of any deformation is virtually impossible.

Even though the developed methodology is consistent, two weaknesses within the proposed model may be identified. These weaknesses should be taken into account when using the model in order to prevent any misinterpretations. The first weakness is the model's dependence on visual inspection. All the interferometric analyses and comparisons between phase images were based on a visual inspection of the differential interferogram. Therefore, the set of observations can be very subjective. Thus, the boundaries of the functional model are somewhat uncertain. However, the lowest confidence level is at the lowest coherence values and increases gradually to 100% when coherence reaches one. In order to improve the confidence level at the boundaries of the model, the visual interpretation of the phase image should be replaced by some sort of automatic technique. Such a technique could provide unbiased results. Moreover, it could extend the image interpretation and reveal additional information invisible for the human eye. Therefore, the definition of the functional model could be further adjusted. In the next chapter the new wavelet approach for the extended analysis of phase image is proposed and analysed.

The second concern is related to the spatial geometry of the modelled deformations. Although the surface deformation is simulated as an elliptical trough, the resultant

functional model determining min/max detectable deformation gradient can be applied to any other deformation modes. However, using the same methodology and simulating a specific mode of deformation (*e.g.* local tectonic motion), the functional model could be more suitable for a specific application. Moreover, the functional model could be refined by increasing the number of observations base on data from different parts of the world.

Although, the proposed model is not perfect, its application can still be very beneficial. By using the model, a user could find out a range of deformation gradients that can be detected assuming a given range of coherence values. Moreover, the minimum coherence value can be determined for a given deformation gradient. This can be a superb tool for the initial assessment of the suitability of the radar interferometry technique for surface deformation monitoring. The deformation gradient can be easily determined from existing knowledge about deformation geometry. The coherence could also be approximated assuming some influence of the decorrelation factors. It is well known that agricultural, forestry, urban, and desert areas as well as seasonal weather changes and time between data acquisition affect the coherence. Studies on using coherence for land-cover classification have already proved the close link between the coherence value and the land properties (*e.g.* Martinez *et al*., 1998; Morley *et al.*, 1997). Therefore, by reversing this approach, coherence could be estimated a priori for a particular region of interest.

Having both parameters (deformation gradient and coherence) and using the model, it can be easily determined whether the surface deformation is detectable or not. Thus, this model can serve as a decision-support tool to determine whether or not to apply satellite radar interferometry to study a given surface deformation. Therefore, this model can save money and time.

6. 6 Summary

This chapter has presented the methodology that led to a functional model defining the minimum and redefining the maximum detectable deformation gradient. Sets of representative surface deformation models have been simulated and the associated phase from these models introduced into real SAR data acquired by ERS-1/2

satellites. Subsequently, interferograms have been derived and surface deformations are estimated. A number of cases of surface deformation with varying magnitudes and spatial extent have been simulated. In each case, the resultant surface deformation has been compared with the 'true' surface deformation as defined by the deformation model. Based on these comparisons, a set of observations that leads to a new functional model has been established. Finally, the proposed model has been validated against external data sets and proven viable. The major weakness of the model is its reliance on visual interpretation of interferograms. One method for potentially automatic deformation detection in interferograms is explored in the following chapter.

7 ADVANCED INTERFEROGRAM ANALYSIS USING A WAVELET APPROACH

Small-scale surface deformation detection using radar interferometry can sometimes be a challenging task due to the presence of noise in the interferogram. Most importantly, however, the interpretation of interferometric phase measurements based on a visual inspection of the phase image is very much user-dependent, thus, it can be biased. This can lead to a misinterpretation of the interferogram, especially if the deformation signal is very weak. In this chapter, the wavelet approach is proposed for the extended analysis of the interferometric phase related to the small-scale surface deformation. The ability of the continuous wavelet transform to reveal the content of the wrapped phase interferogram, such as (i) discontinuities, (ii) extent of the deformation signal, and (iii) the magnitude of the deformation signal, is examined.

7. 1 The Wavelet Transform

The wavelet transform is a relatively new mathematical tool, developed in the mid-1980s by Grossmann and Morlet (1984). Subsequently improved, today it is widely used in many applications from compression and enhancement (*e.g.* Wu and Su, 2000), pattern recognition (*e.g.* Arivazhagam and Ganesan, 2003), geophysics (*e.g.* Weng and Lau 1994) and any kind of signal analysis. Recently, the wavelet technique has been applied for speckle noise (multiplicative Gaussian noise) reduction and enhancement of SAR images (Sveinsson and Benediktsson, 1996; Bao, 1999; Achim and Bezerianos, 2003). As the outcomes of these studies show, a significant improvement in the change detection and automatic image classification after denoising of radar images can be achieved. Furthermore, the application of the wavelet transform has improved the reconstruction of DEMs derived from multiple InSAR data, as demonstrated by Ferretti *et al*. (1999b).

A wavelet is a specially defined wavelike function for which several conditions must be satisfied (*e.g.* Addison, 2002, p9). Such a function can be recognised as a basic

element (wavelet) that can be used to describe any complex function in a process called the wavelet transform. The wavelet transform is in fact a process very similar to the Fourier transform although, when using the Fourier transform, it is impossible to detect and characterize very narrow transient signal whose spectrum is not resolved. The wavelet transform, however, has the required capability to describe and analyse highly localised transient signals (in real space).

Mathematically, the two-dimensional continuous wavelet transform $W(\vec{b},s)$ of a function *f(x,y)* with respect to a wavelet function $\Psi(\vec{b},s)$ can be defined as:

$$W(\vec{b},s) = w(s)\int_{-\infty}^{\infty}\int_{-\infty}^{\infty} f(\vec{\mathrm{X}})\,\Psi^{*}\left(\frac{\vec{\mathrm{X}}-\vec{b}}{s}\right)d^{2}\vec{\mathrm{X}} \tag{7.1}$$

where $\vec{b} = (b_x, b_y)$ is the coordinate vector indicating the location of the wavelet over *f(x,y)*, $\vec{\mathrm{X}} = (x, y)$ is the coordinate vector, *s* is the scale ('width') of the wavelet, and *w(s)* is a normalisation function that ensures all wavelets at each scale have the same unit energy. Ψ^{*} is the complex conjugate of the wavelet function $\Psi(\vec{b},s)$. The above definition of the wavelet transform can be extended to higher dimensions simply by extending the length of vectors $\vec{\mathrm{X}}$ and $\vec{b}$. Figure 7.1 shows the basic concept of a wavelet transform.

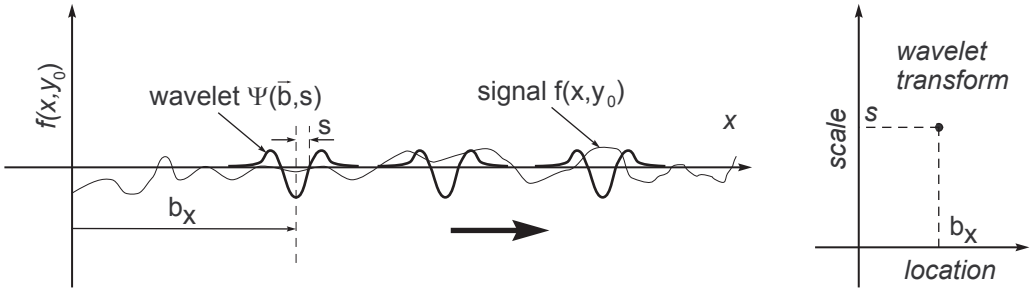

Figure 7.1 *Basic concept of the wavelet transform (one-dimension case at y_0).*

A signal *f(x,y)* is convolved with a wavelet kernel $\Psi(\vec{b},s)$ at different locations ($\vec{b}$) and different scales (*s*) of the wavelet. This procedure generates wavelet coefficients $W(\vec{b},s)$. In general, the wavelet coefficients are always one dimension greater than that of the signal itself. Due to scaling, some of the dilated wavelets correlate better

with the signal than the others. Therefore, the wavelet transform reveals different scale components of the analysed signal.

In small-scale surface deformation using radar interferometry, the signature of deformations (fringes) is highly localised in the space domain, thus the wavelet transform has a desirable advantage over the Fourier transform in analysing such a signal. Therefore, by transforming the interferometric phase image into the wavelet space, deformation signatures that may be hidden to the naked eye can be revealed. If this approach proves viable, the deformation detection procedure could be enhanced or even automated. The ability of the wavelet transform to identify abrupt discontinuities may even support phase unwrapping procedures.

7. 2 Wavelet Selection

Some wavelets are more suitable for particular applications than others as they correlate better with a specific signal. The continuous wavelet transform is particularly well suited for analysing the local differentiability of a signal, and for detecting and characterising its possible discontinuities (Farge, 1992). Therefore, four real (isotropic) two-dimensional continuous wavelet functions were chosen in order to select the most suitable for extended analysis of the wrapped phase image. These are, the Halo (Dallard and Spedding, 1993), Perrier, Paul (Perrier *et al*., 1998) and Poisson (Grossman and Morlet, 1984) wavelets.

To perform the wavelet analysis, a collection of Matlab functions (Wavelab, 2003) and in-house Fortran 2D Wavelet Transform Routines (Kirby, 2003) have been used. To ensure identical conditions, all the wavelets were applied to the same uniform and representative deformation signal related to the ‘M4’ model (Figure 7.2a). The ‘M4’ model details were listed in Table 6.1.

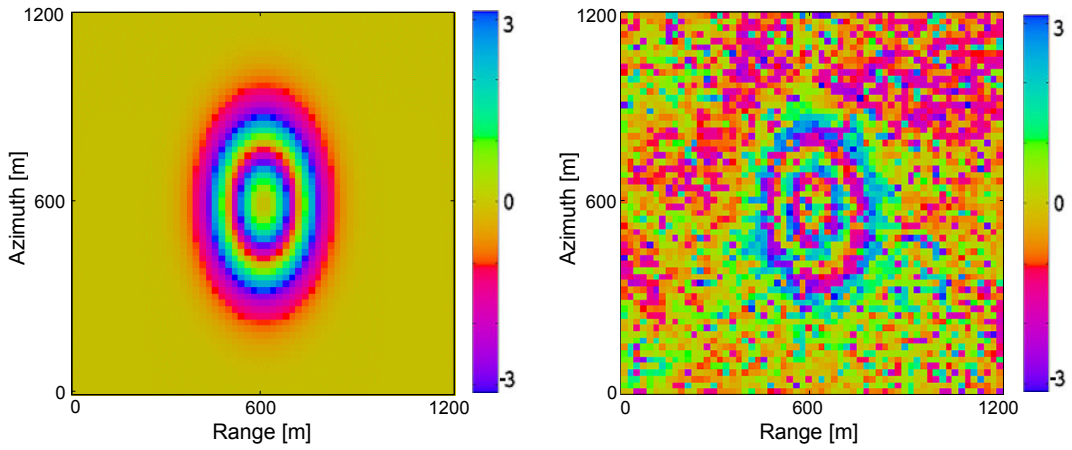

Figure 7.2 *(a) Wrapped phase of the 'M4' deformation model and (b) its interferogram signature 'M4E' (colour bars in radian).*

Two criteria, which the wavelet function has to satisfy in order to become the appropriate for further studies, have been established. They are as follows:

(A) The wavelet power spectrum should match the Fourier power spectrum as accurately as possible because Fourier methods is widely accepted as a method of computing power spectrum;

(B) The overlap between frequency bands determined by the Fourier power spectrum of the wavelet for differed range of scales should be minimal to prevent leakage of frequency bands.

The assessment of the wavelet functions against the criterion A is based on the comparison of the global wavelet power spectrum with the radially-averaged Fourier power spectrum of the deformation signal (interferogram). The global wavelet power spectrum *E(s)* is defined as the sum of squared amplitude of the wavelet coefficients:

$$E(s) = \sum_{b} \left| W(\vec{b}, s) \right|^2 \tag{7.2}$$

As can be seen on the plotted charts (Figure 7.3), the Halo wavelet (Figure 7.3a) gives the best match between their respective global wavelet power spectrum and the radially-averaged Fourier power spectrum over the whole range of frequencies.

Power spectra of the Perrier and Paul wavelets (Figure 7.3b and Figure 7.3c respectively) also correspond well. However, the match is weaker for medium frequencies. On the other hand, the Poisson wavelet (Figure 7.3d) power spectrum does not match the Fourier power spectrum over all frequency components of the analysed signal.

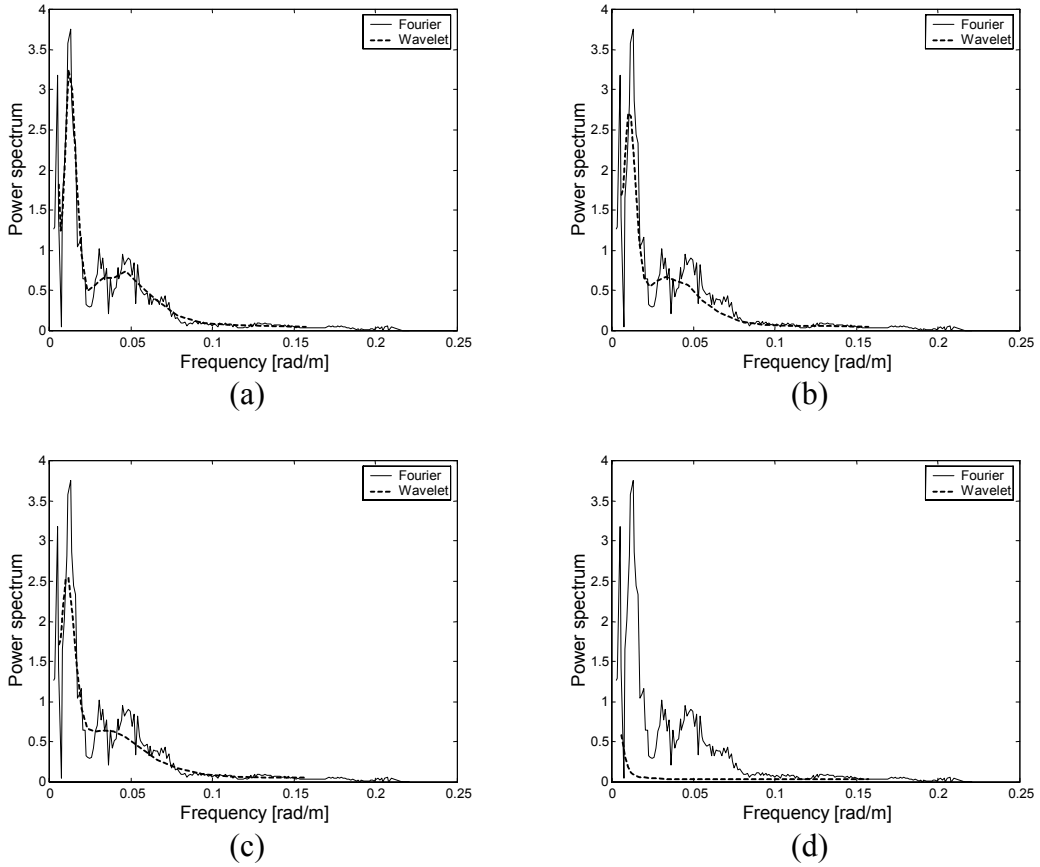

Figure 7.3 *The global wavelet power spectrum in comparison to the radially-averaged Fourier power spectrum for (a) Halo, (b) Perrier, (c) Paul, (d) Poisson wavelets. Power spectrum is shown in arbitrary units.*

The assessment against the criterion B is based on the analysis of the Fourier power spectrum of the wavelets for different scale values (s). The scales have been arbitrarily set up to 25, 50, 100, 150 and 250 metres. Since the overlap between the power spectra for different scale values cannot be fully eliminated, it is the main limiting factor of the continuous wavelet transform. However, the Halo wavelet appears to have the best ability to separate different frequency components of the analysed signal, as can be seen in Figure 7.4. For the chosen scales, the Halo

wavelet (Figure 7.4a) has the minimum overlap between the corresponding Fourier power spectra.

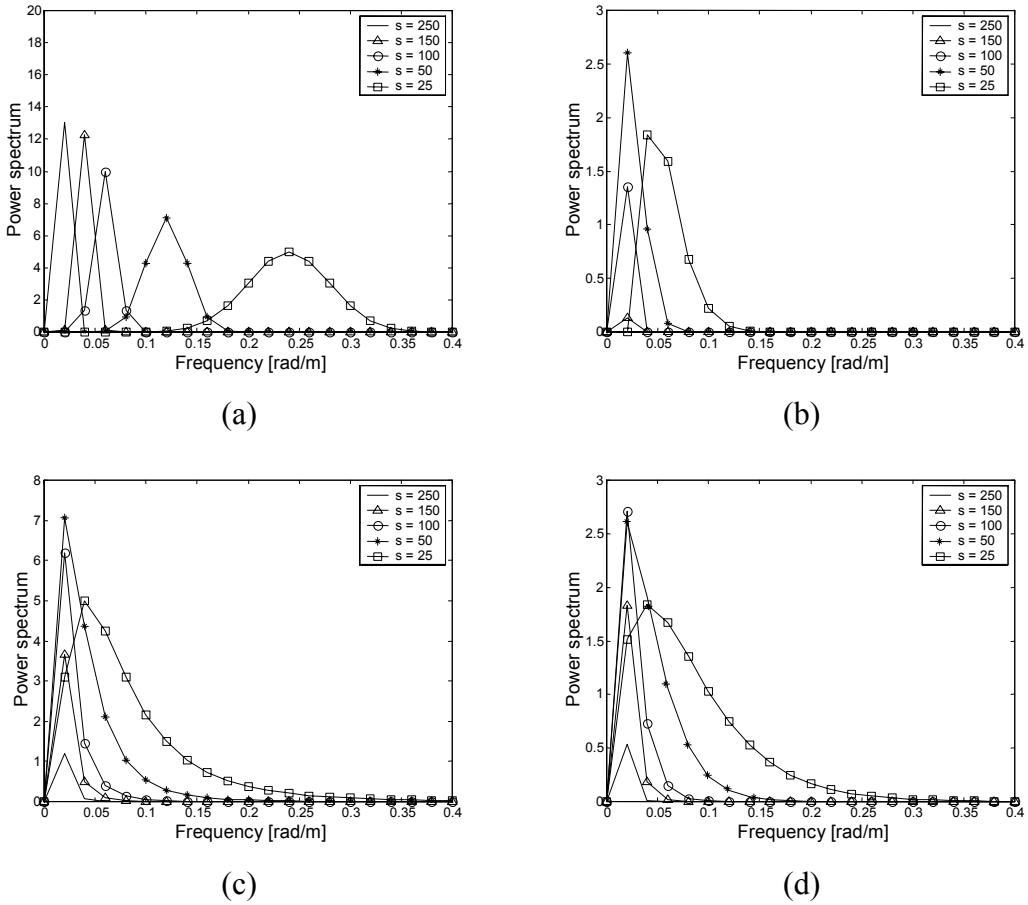

Figure 7.4 *Fourier power spectra of the wavelets (a) Halo, (b) Perrier, (c) Paul, and (d) Poisson at different scale values (s). Scales are shown in meters while the power spectrum is shown in arbitrary units.*

To undertake the ultimate decision on which wavelet to choose for the enhanced analysis of the interferometric phase image, *wavelet scalogram* plots have been computed and analysed for each wavelet function. The scalogram of a two-dimensional signal is a three-dimensional graph showing the wavelet power spectrum of the signal. The vertical axis of the scalogram indicates different scale (s) components of the signal. The horizontal plane shows the power spectrum for a particular scale, while the vertical plane indicates the power spectrum for all range of scales.

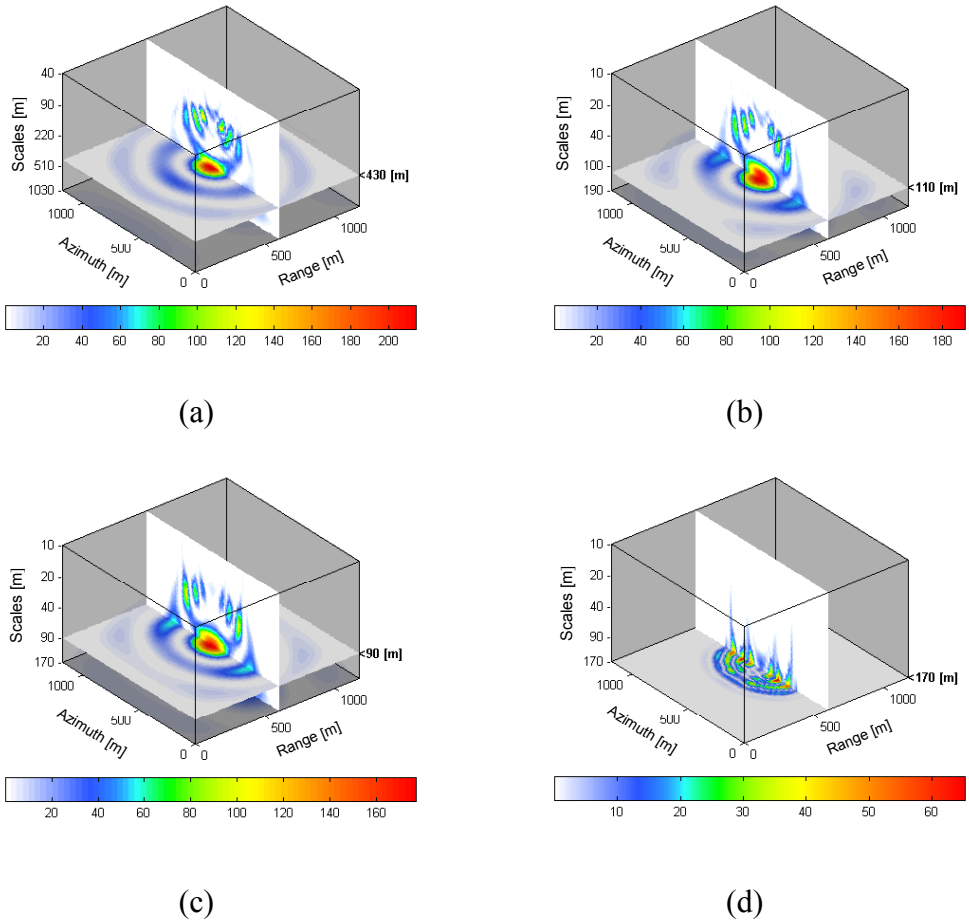

Figure 7.5 *The scalograms showing the wavelet power spectra of the interferometric wrapped phase image of the 'M4' deformation model for the (a) Halo, (b) Perrier, (c) Paul, and (d) Poisson wavelet. The horizontal scale bar illustrates the magnitude of the power.*

Many different cross-sections of the scalograms have been analysed. Figure 7.5 shows the scalograms illustrating the wavelet power spectra of the interferometric phase image (wrapped phase) of the 'M4' deformation model. All scalograms revealed different scale components of this deformation signature. However, each wavelet shows the power spectrum of the signal in a slightly different way.

The horizontal plane on the scalogram shows the distribution of the wavelet power in the azimuth and range direction. Choosing a particular scale or cross-section over the whole range of scales, the phase image can be analysed through studies of its wavelet power spectra. For the highest scale values, the Halo wavelet (Figure 7.5a) shows distribution of the wavelet power spectrum in form of circular rings around the central kernel, which contains most of the total energy. Moreover, the vertical cross-section reveals the energy over the whole range of scales forming characteristic

patterns. The magnitude of the wavelet power can be related to the deformation signal and/or noise. Furthermore, the patterns of the power spectra show discontinuities within the signal where the phase changes its value from $-\pi$ to $+\pi$. A similar distribution of the wavelet power spectra is shown by the Perrier and Paul wavelets Figure 7.5b and Figure 7.5c respectively. However, at the highest scales both wavelets exhibit larger energy in the azimuth direction. Figure 7.5d shows the power spectrum for the Poisson wavelet. This is the worst wavelet power spectrum as its energy distribution is very limited, especially at the smallest scale values.

Based on the initial assessment using criteria A and B, as well as the analysis of the wavelet power spectrum undertaken in the above section, the Halo wavelet has been chosen as the most suitable for the extended analysis of the interferometric phase image.

7. 3 Extended Analysis of the Interferogram Using the Halo Wavelet

The following analysis consists of three stages. First, the scalograms of the phase images of the deformation models and their interferogram signatures are computed. Second, the representative horizontal cross-sections over the highest, medium and the smallest scale values for corresponding scalograms are analysed. Finally, the most suitable scale is chosen and studied in detail. All the analyses are performed on simulated and real interferometric phase images.

7.3.1 Simulated Interferometric Phase Images

Although, detailed analysis of the simulated phase images are demonstrated only for deformation model ‘M4’ and its interferogram signature ‘M4E’ the final conclusions are made based on analyses of all the chosen cases as shown in Figure 7.8 to Figure 7.13. Analysing the scalogram plots of the simulated deformation model ‘M4’ without noise (Figure 7.6, left-hand side), it appears that the wavelet power at the highest scale (1030 m) corresponds to the spatial extent of the model. As the scales gradually decrease, the spectral energy forms into four elliptical strips.

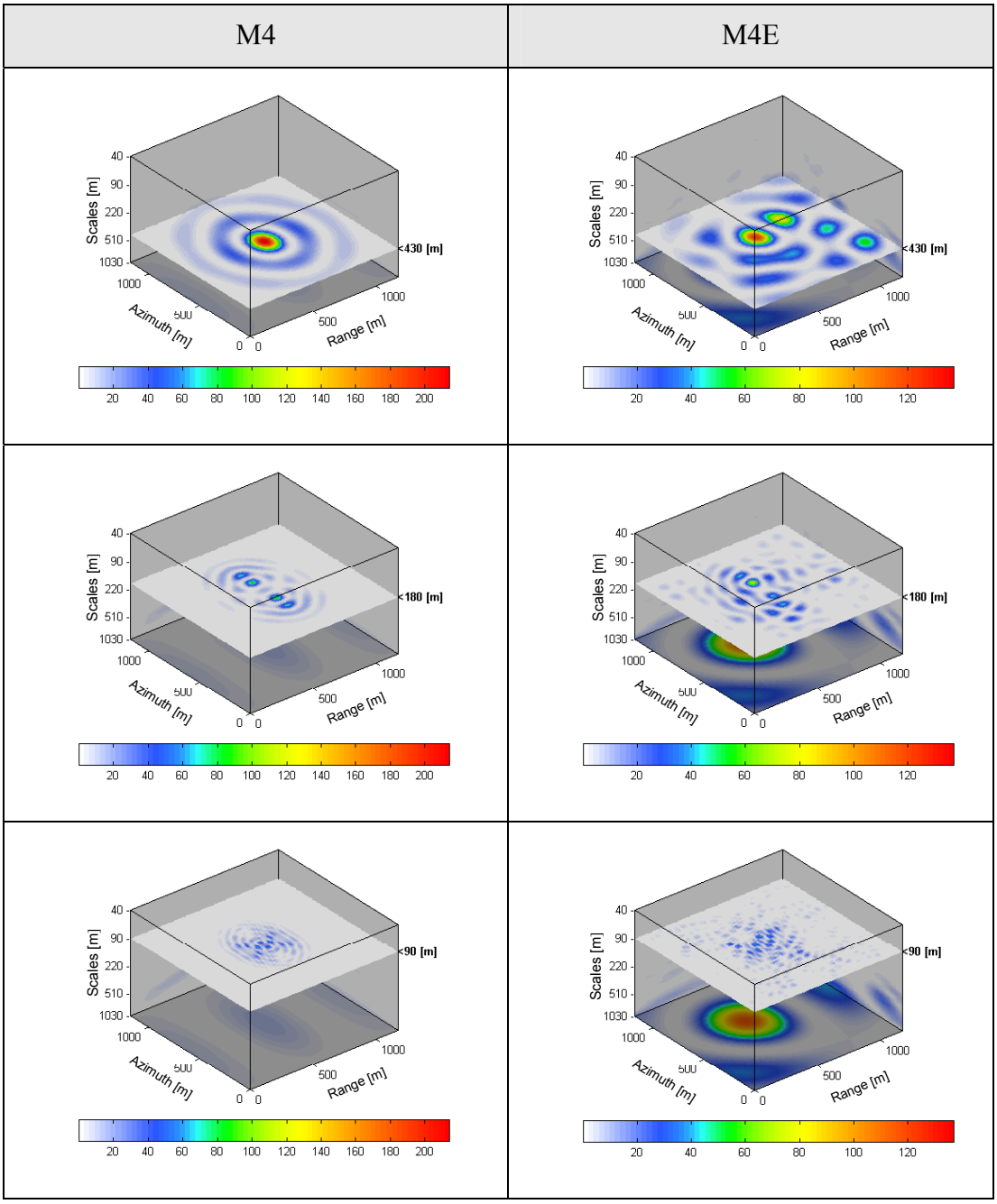

Figure 7.6 *Scalograms of the deformation model 'M4' (left-hand side) and its interferogram signature 'M4E' (right-hand side) indicating a series of cross-sections at different scale values using the Halo wavelet. Horizontal scale bar shows the magnitude of the power.*

At an approximate scale of 180 m, these strips are very clearly formed and they correspond to the interferometric phase change from value -π to +π. As the scales get smaller, the energy patterns disappear and their interpretation become impossible. The right-hand side of Figure 7.6 shows the scalograms and the cross-sections along the wavelet power spectrum of the deformation signature 'M4E'. The noise within

the interferogram disrupts the spectral energy, which does not form a regular shape. However, at the medium scales (110 to 150 m) the wavelet energy seems to correspond with the phase discontinuity. Therefore, the following extended analysis of the interferometric phase image will focus on the wavelet energy related to the medium scales in particular. Figure 7.7A shows the scalogram of the deformation model 'M4' and its interferogram signature 'M4E' (Figure 7.7A'). The horizontal planes illustrate the wavelet power spectrum for the 150 m scale. Figure 7.7B and B' show the cross-sections over the scalograms in azimuth direction, while Figure 7.7C and C' show the cross-sections along the corresponding wrapped phase interferograms. The scalogram plots (A and A') reveal the spatial distribution of the wavelet power. A comparison of the corresponding spectral density can provide an indication of how the noise is affecting the signal. Furthermore, the parts of the spectrum that are less affected by the noise can be identified and the corresponding scale values determined. Such scales could be recognised as the most suitable for analysis of any other interferometric phase images.

The wavelet power spectrum of the model 'M4' is almost twice as strong as its noisy interferogram signature 'M4E'. However, at some scales the same spectral features can be still recognised on both scalograms. For the medium scales the wavelet energy seems to be less affected by the noise than for extremely long and short scales. At the scale value of 150 m the wavelet energy forms four rings that in some parts can be recognised on the scalogram of phase image 'M4E' (Figure 7.7A'). The cross-section in Figure 7.7B shows the vertical distribution of the wavelet energy of the model 'M4'. The high-energy values form into the two groups of spots (2 and 3). Since the deformation model is symmetrical its wavelet power spectrum inherited the same attribute. Figure 7.7B' shows the corresponding cross-section showing the vertical distribution of the wavelet energy of the deformation signature 'M4E'. The group of spots 2' corresponds with the group 2. The group of spots 3', however, have different vertical distribution but they still can be recognised.

The spectral features (2,2' and 3,3') are interpreted as related to the discontinuities within the interferometric phase image (phase changes from the $+\pi$ to $-\pi$ value and inversely).

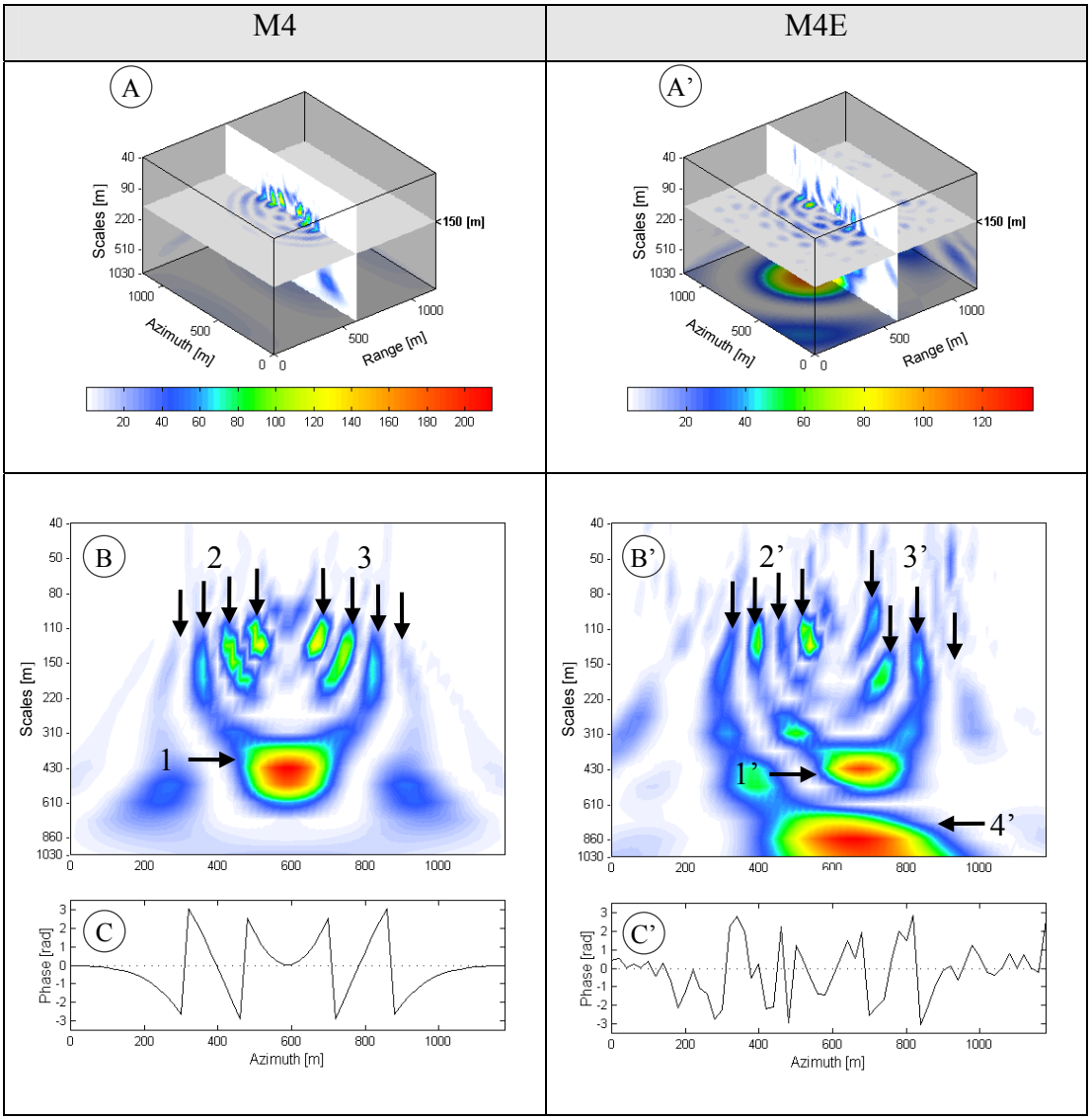

Figure 7.7 *The scalograms of the deformation model 'M4' representing two fringes (left-hand side) and its interferogram signature 'M4E' (right-hand side). (A,A') show horizontal cross-section for scale equal to 150 m, (B,B') vertical cross-section along the Azimuth direction (Range = 600 m), and (C,C') corresponding cross-sections along the azimuth direction over the wrapped phase. Numbers 1 to 4 indicates spectral features. The vertical axis illustrates different scale values, while the horizontal scale bar is the magnitude of the power.*

Furthermore, the largest concentration of wavelet energy (1) is observed in the centre of the cross-section (Figure 7.7B) that is slightly shifted (1') on the scalogram of the deformation signature 'M4E'. An additional concentration of energy has been observed on the scalogram of the deformation signature 'M4E' indicated by the number 4'. This is most likely due to the large concentration of the phase noise in the upper right corner of the deformation signature 'M4E' visible in Figure 7.2b.

Following are all the analysed scalograms of different deformation models varied in spatial extent, deformation magnitude and level of noise. The parameters of the deformation models can be found in Table 6.1 and its interferometric signatures in Figures 6.4 and Figure 6.5. All the analysed scalograms (Figure 7.7 to Figure 7.13) consist of six subfigures: A,A' illustrating the vertical and horizontal cross-section over the scalogram, B,B' show the vertical cross-section in details, and C,C' illustrate the cross-section along the wrapped phase image.

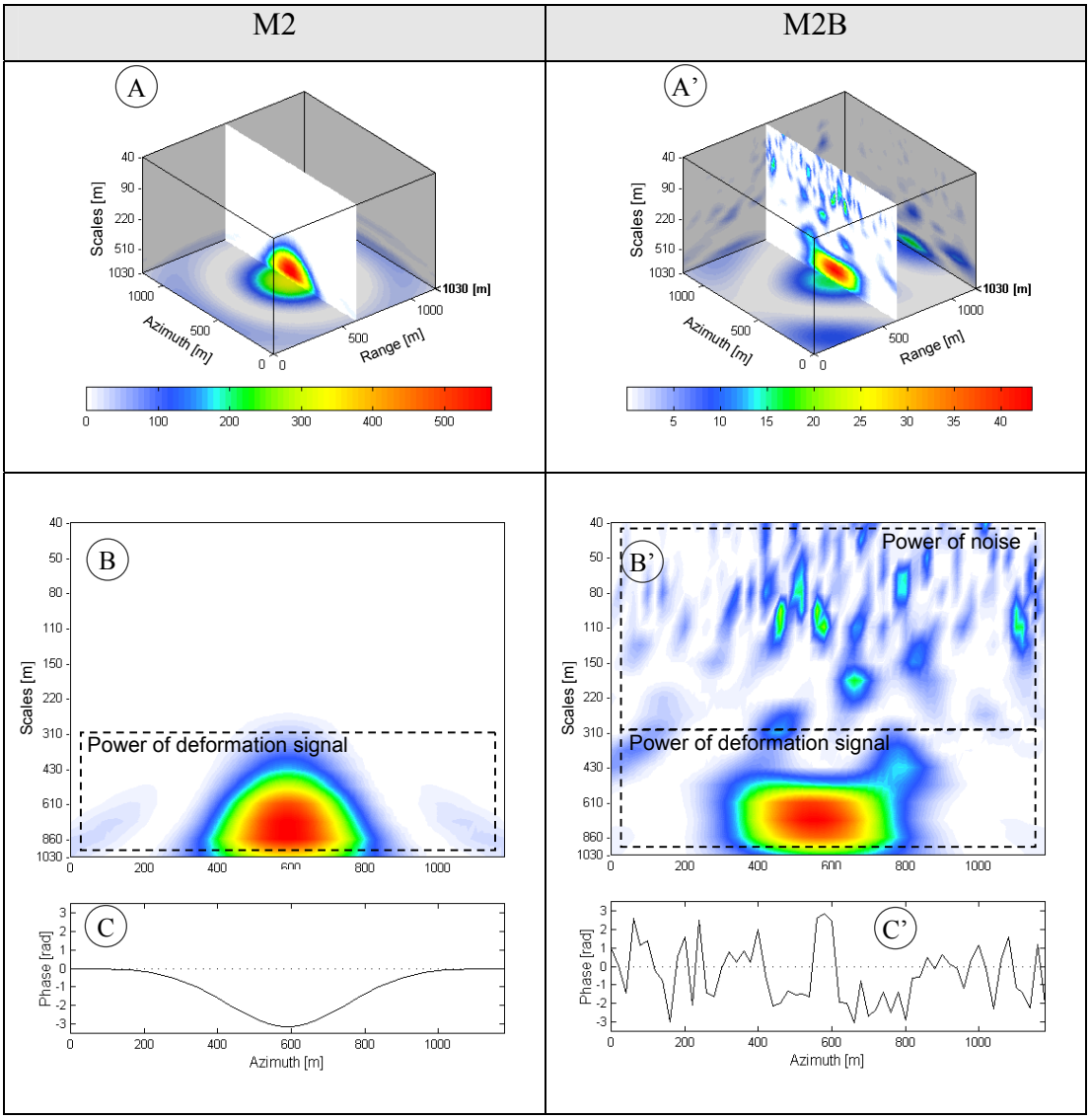

Figure 7.8 *The scalograms of the deformation model 'M2' representing half of the fringe (left-hand side) and its interferogram signature 'M2B' (right-hand side). The horizontal scale bar illustrates the magnitude of the wavelet power.*

The wavelet power spectrum illustrated in Figure 7.8 of the noise interferogram 'M2B', visible at the vertical cross-sections (A' and B'), reveals the power of the

deformation signal and noise. Both signals can be easily separated at the scale value equal to 310 m.

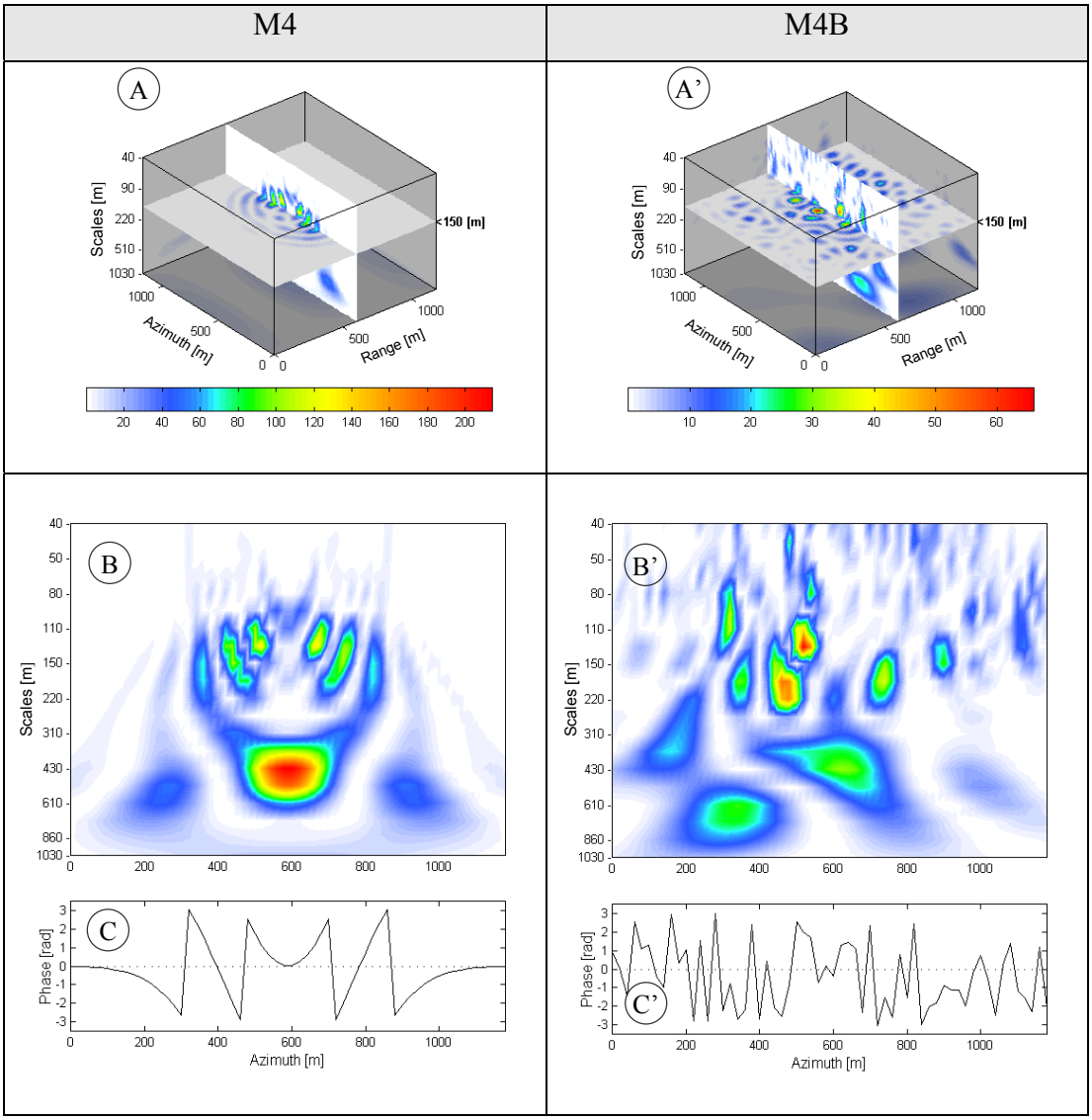

Figure 7.9 *The scalograms of the deformation model 'M4' representing two fringes (left-hand side) and its interferogram signature 'M4B' (right-hand side). The horizontal scale bar illustrates the magnitude of the wavelet power.*

The wavelet transform of the interferogram with the same amount of noise as in 'M2B' phase image in conjunction with higher deformation magnitude (two fringes) did not reveal any suitable information (Figure 7.9). The spectral features visible at the horizontal (A') and vertical (B') cross-sections of the noisy phase image do not match to those of without noise. Therefore the wavelet power spectrum of 'M4B' phase image is not useful.

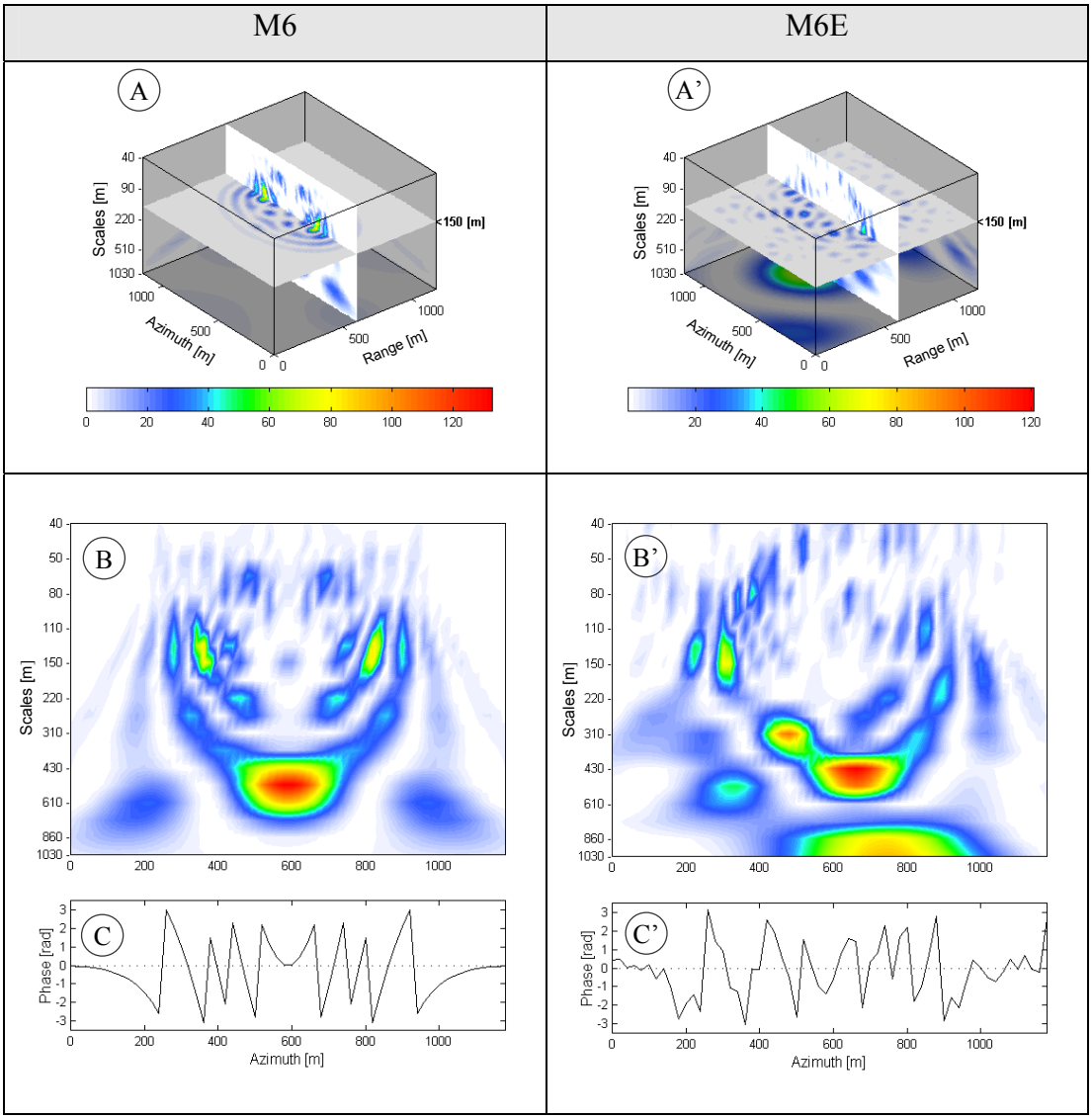

Figure 7.10 *The scalograms of the deformation model 'M6' representing four fringes (left-hand side) and its interferogram signature 'M6E' (right-hand side). The horizontal scale bar illustrates the magnitude of the wavelet power.*

The high fringe density makes it difficult to resolve the discontinuities within the interferometric phase, which appears in the scalogram (Figure 7.10B) at the smallest scale values (80-40m). However, this scale values usually correspond to noise. Thus the phase discontinuity information can be damaged as seen in Figure 7.10 on the scalogram of interferogram 'M6E' (B').

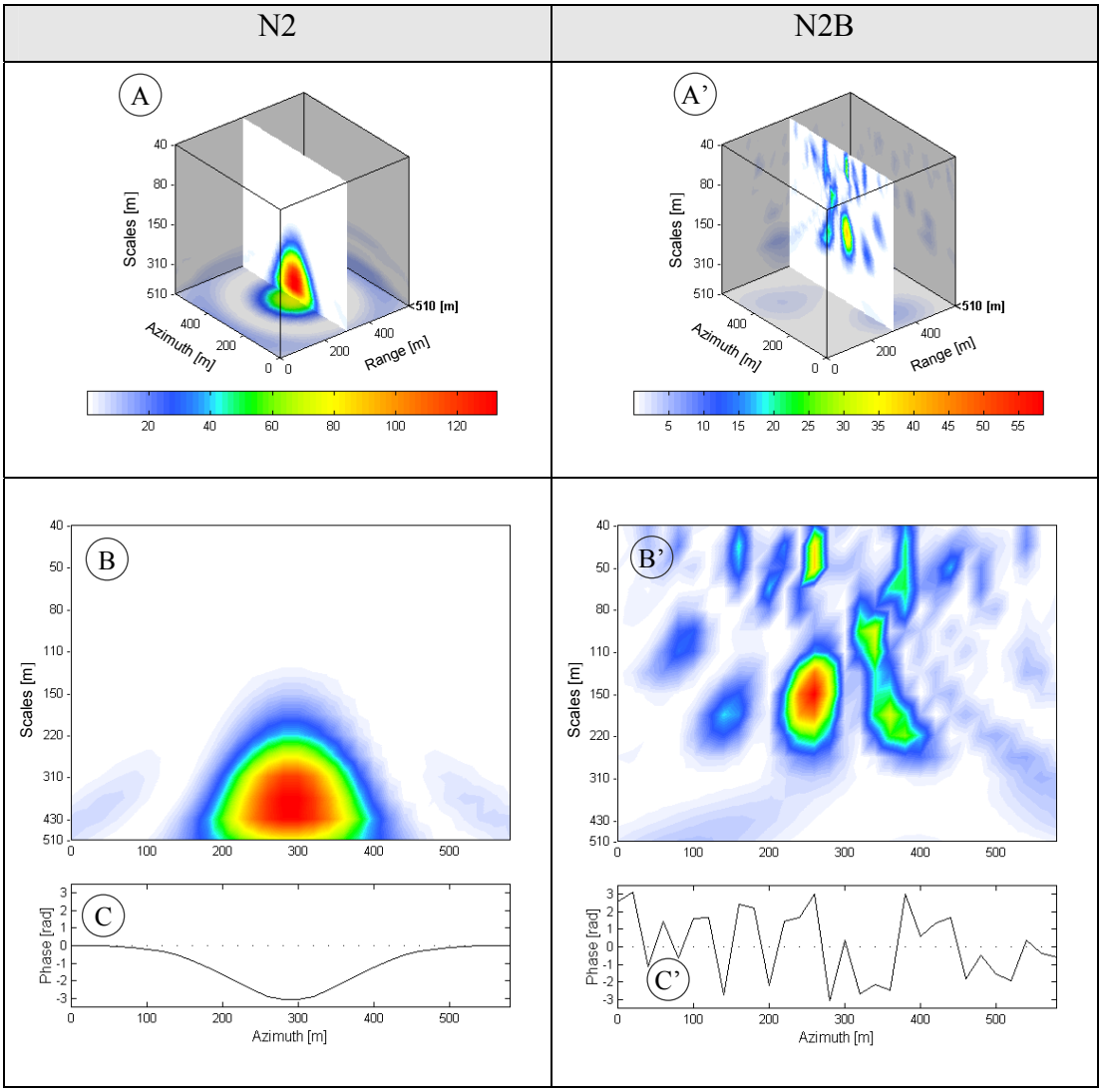

Figure 7.11 *The scalograms of the deformation model 'N2' representing half of the fringe (left-hand side) and its interferogram signature 'N2B' (right-hand side). The horizontal scale bar illustrates the magnitude of the wavelet power.*

When the spatial extent of the deformation signal gets smaller it does influence the wavelet analysis. As compared to the analysed phase image'M2B' (Figure 7.8) the same deformation magnitude and level of noise could not be resolved for deformation signature 'N2B' (Figure 7.11) using the wavelet. The wavelet power spectra of deformation signal and noise are mixed.

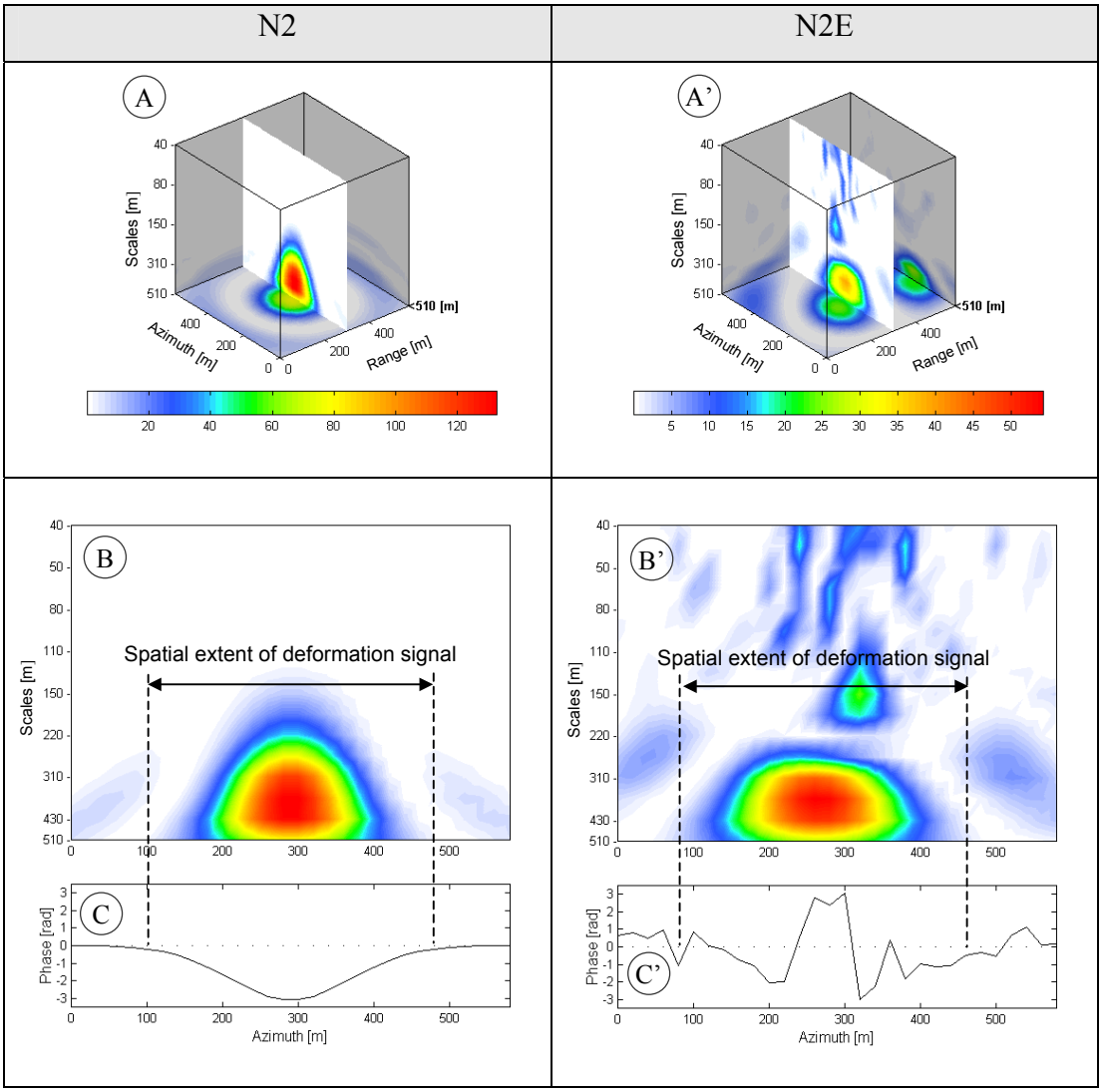

Figure 7.12 *The scalograms of the deformation model 'N2' representing half of the fringe (left-hand side) and its interferogram signature 'N2E' (right-hand side). The horizontal scale bar illustrates the magnitude of the wavelet power.*

However, the lower level of noise has improved the analysis of wavelet transform of the deformation model 'N2' (Figure 7.12). The scalograms (A',B') reveal the power spectra of deformation signal and noise. Moreover, analysing the horizontal extent and location of the deformation power (the longest scale value 510 m) it is possible to resolve the spatial location and extent of the deformation signal.

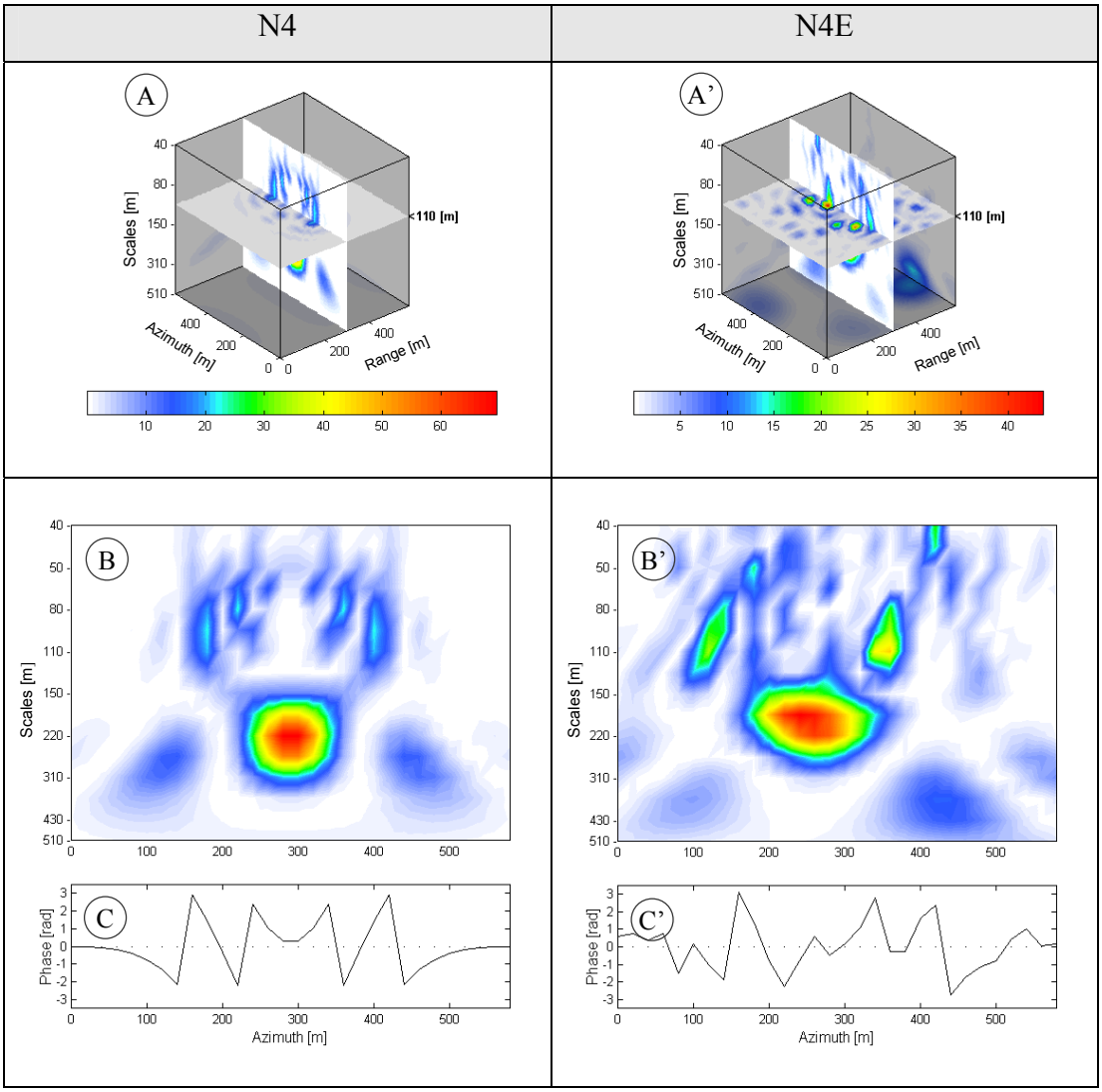

Figure 7.13 *The scalograms of the deformation model 'N4' representing two fringes (left-hand side) and its interferogram signature 'N4E' (right-hand side). The horizontal scale bar illustrates the magnitude of the wavelet power.*

In summary, there is a balance between deformation magnitude (number of fringes) and phase noise that affects the performance of the wavelet technique and interpretation of its power spectrum. If the number of fringes increases, their wavelet power spectrum interferes with the power of noise and therefore reduces the ability of the wavelet to resolve phase discontinuity and the spatial extent of deformation signal (*e.g.* Figure 7.13).

7.3.2 Real Interferometric Phase Image

In this section the Halo wavelet is used to analyse the real interferometric phase images that have been extracted from the wrapped phase interferogram derived over the Silesia study area (Figure 4.20). The selected images show four, two and one interferometric fringes in form of a circular and elliptical shape as can be seen on Figure 6.10a and Figure 7.14. The interferometric fringes are due to the surface subsidence induced by underground mining activities. Therefore, they represent a real deformation signal and level of noise.

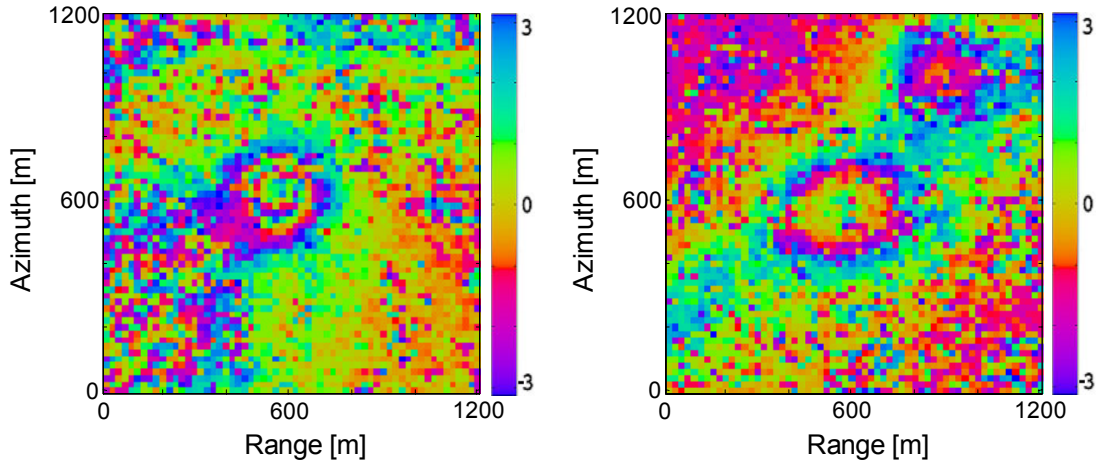

Figure 7.14 *Interferometric phase images extracted from wrapped phase interferogram over Silesia study area. (a) Represents two interferometric fringes and (b) one interferometric fringe (colour bars in radian).*

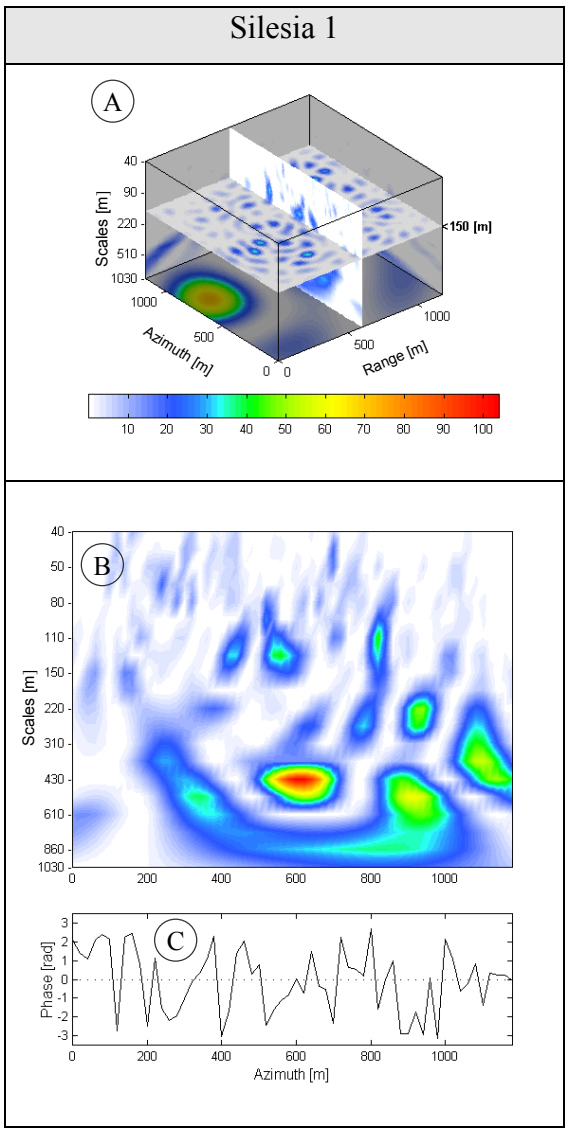

Figure 7.15 *The scalogram of the real phase image representing four fringes (Figure 6.10.a) related to surface subsidence over Silesia study area. The horizontal scale bar illustrates the magnitude of the wavelet power.*

Initially, the wavelet transform was applied to the phase image that reveals four deformation related fringes (Figure 6.10a). Unfortunately the phase discontinuities as well as the spatial extent of the deformation signal could not be resolved by the wavelet power spectrum visible on both horizontal (Figure 7.15A) and vertical (Figure 7.15B) cross-sections of the scalogram. This is due to high density of fringes and high level of noise preserved in the phase image. This confirms the conclusions based on the similar study conducted with the simulated deformation model 'M6' (Figure 7.10), which also contains four interferometric fringes.

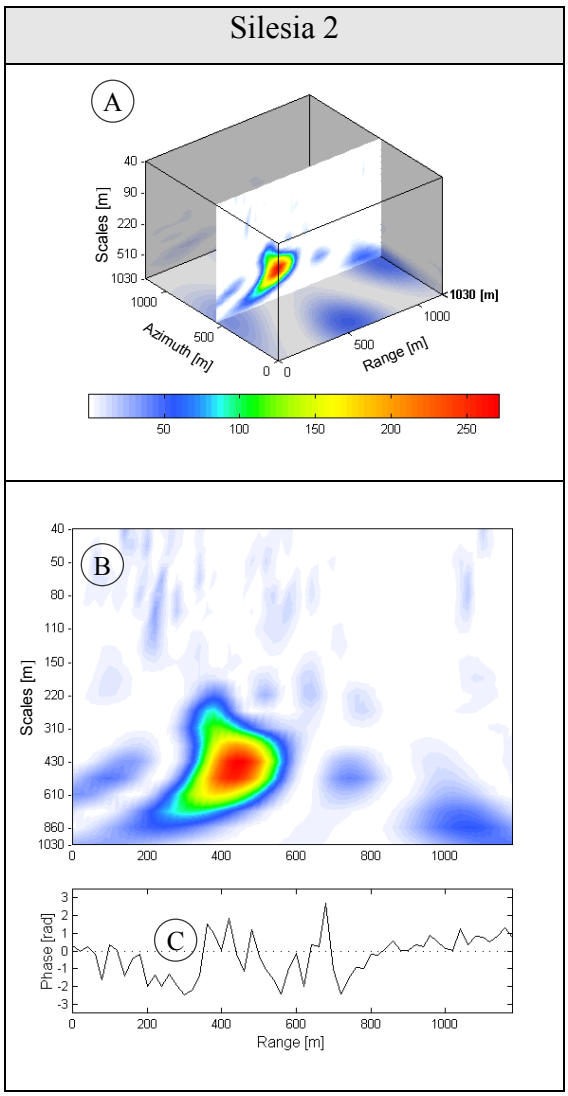

Figure 7.16 *The scalogram of the real phase image representing two fringes (Figure 7.14.a) related to surface subsidence over Silesia study area. The horizontal scale bar illustrates the magnitude of the wavelet power.*

The next two scalograms (Figure 7.16 and Figure 7.17) reveal the wavelet power spectrum of the phase images that contain two and one interferometric fringes respectively. Although, the number of fringes decreases, the phase discontinuities of the deformation signal and its spatial extent could not be resolved by the wavelet power spectrum visible on both horizontal and vertical cross-sections of the scalograms. The excessive level of noise has destroyed the discontinuities' patterns and the number of fringes cannot be established.

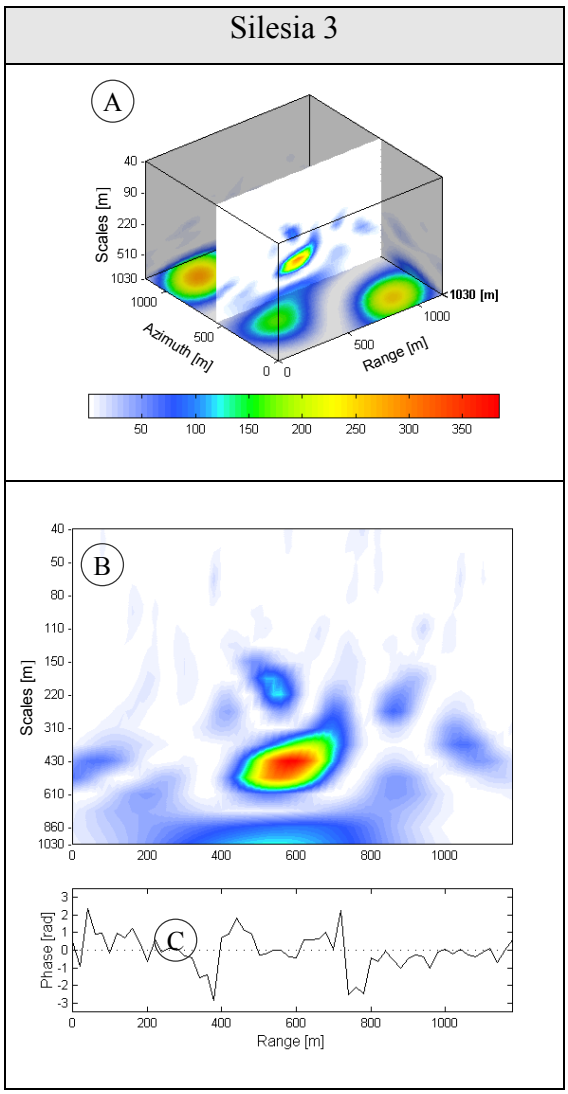

Figure 7.17 *The scalogram of the real phase image representing one fringe (Figure 7.14.b) related to surface subsidence over Silesia study area. The horizontal scale bar illustrates the magnitude of the wavelet power.*

7. 4 Discussion

The main aim of using the wavelet approach to analyse a wrapped phase image was to enhance small-scale deformation detection studies. Therefore, the ability to determine phase discontinuities as well as the extent of a deformation signal and its magnitude in wavelet space has been examined. The wavelet analysis of the interferometric phase images has shown some interesting results that are discussed in this section.

The Halo wavelet is able to determine discontinuities (phase change from -π to π value) within the wrapped phase interferogram. It is possible by analysing the wavelet energy distribution of the interferogram phase image visible at the vertical and horizontal cross-sections over the scalogram. At the medium and small-scale values the wavelet power spectrum corresponds directly to the spatial location of the signal thus, the observed phase discontinuities can be directly used to determine their spatial location. However, it was found that the effectiveness of the wavelet transform to reveal phase discontinuities depends strongly on the density of fringes and the level of noise within the interferogram. As the fringe density increases (deformation magnitude increases), the discontinuities within the phase image are resolved by medium to small-scale values of the wavelet function. Thus, the wavelet energy patterns corresponding to the phase discontinuity within the interferogram containing a high number of fringes over a small spatial extent are very small and difficult to recognise (*e.g.* Figure 7.10). Furthermore, the wavelet energy corresponding to the noise within the phase measurements is also revealed by the smallest scale values. Therefore this will often interfere with the signs of the phase discontinuity (*e.g.* Figure 7.10 and Figure 7.15) and will reduce the wavelet ability to resolve phase discontinuities within the wrapped phase interferogram.

Determination of the spatial extent of a deformation signal using wavelets can be problematic, as in principle the wavelet power spectrum at the longest scales does not correspond accurately to the spatial location of the signal. However, as long as the deformation magnitude does not exceed a value equal to half of the wavelength the analyses of the scalogram cross-sections show that identification of the spatial extent of the deformation signal is possible by determining the spatial extent of the wavelet energy at its largest scale value. The Halo wavelet was able to determine the spatial extent of the deformation signal (*e.g.* Figure 7.12) relatively easily as compared to the high magnitude deformation signal (*e.g.* Figure 7.10). The increasing level of noise also affects the ability of the wavelet to resolve the spatial extent of the deformation. For example, in the analysed model 'M4E' (Figure 7.7) the phase noise (speckle noise) has created a long wavelength phase trend in one part of the interferogram that has increased the wavelet energy for the longest scales. Therefore, it has damaged the information related to the spatial extent of the deformation signal.

Determination of the deformation magnitude using wavelets is complex, although, not impossible. Studying the discontinuities' patterns within the scalogram and hence identifying the phase discontinuities can help to establish the number of interferometric fringes. Therefore, deformation magnitude can be determined simply by counting the number of fringes. Unfortunately, a relationship between the wavelet energy and deformation magnitude for deformations smaller than half of the wavelength (one fringe) was not established. For this reason, ultimately the use of wavelet analysis to detect the deformation magnitude is not recommended, as some part of the deformation signal cannot be resolved.

In conclusion, transforming and analysing the wrapped phase image into the wavelet space have revealed the phase discontinuities and spatial extent of the deformation signal. Unfortunately, increasing levels of noise and fringe density reduce the effectiveness and applicability of the wavelet approach. Nevertheless, phase discontinuities and spatial extent detected by the wavelet transform are potentially a source of additional information helping to guide and improve the effectiveness of the phase unwrapping algorithms. In addition, the wavelet transform can also be used to identify and filtered out the noise in the interferogram.

7. 5 Summary

The wavelet transform has been applied for advanced analysis of the interferometric phase image. In order to choose the most suitable wavelet for the analysis, the selection criteria have been established. Based on the criteria the Halo wavelet has been chosen for the extended analysis of the wrapped phase interferogram. Using the Halo wavelet, the power spectrum of the simulated and real deformation models with and without noise, was derived. Following, the scalogram plots have been constructed and analysed. The wavelet transform was able to detect phase discontinuities and the extent of the deformation signal only under favourable conditions. However, this preliminary study using a rather simple analysis has demonstrated that the wavelet technique may have the potential to enhance interferometric deformation detection analysis in certain situations. Further development of this technique is a subject for future work.

8 CONCLUSIONS AND RECOMMENDATIONS

8. 1 Summary

Surface deformation monitoring is a vital component of many geotechnical and engineering operations. As the procedure provides geometrical description of deformations, it has become a useful tool in understanding the cause and progress of such distortions.

The use of standard monitoring techniques, such as surveying and geotechnical methods, can provide accurate and precise information on the positions and velocities of discrete points on a deforming surface. However, these techniques require expensive and highly specialised equipment. In addition, the setup of the monitoring system and its operation can be an arduous task. Thus, remote sensing techniques, such as satellite radar interferometry can provide a cheaper and less laborious alternative.

The use of InSAR has been demonstrated for DEMs generation and surface deformation detection. Although satellite radar interferometry applications are well established, the technique still suffers from problems due to noise associated with interferometric phase measurements and caused by a variety of decorrelation factors. Furthermore, the interferometry products contain biases due to satellite orbit error and atmospheric heterogeneity. These factors dramatically reduce the capabilities of radar interferometry in many applications and, in particular, compromise detection and analysis of small-scale surface deformations. Thus, improvement of the interferometry technique and the quality of its products is desirable to further enhance its capabilities. Therefore, the aims of this research were to apply, test and enhance the radar interferometry technique for the determination of surface deformation. The main focus was on small-scale surface deformations, such as surface subsidence associated with mining activities.

In an effort to identify and address the problems associated with radar interferometry products, two different study areas (Leinster in central Western Australia and the Upper Silesia region in Poland) were chosen. Satellite-borne radar data were obtained from ESA and processed to create a number of interferometry products, such as coherence maps, interferograms and differential interferograms. These products were analysed for the positive detection of surface deformations as well as to validate theoretical aspects developed in this thesis.

By studying the interferometry processing stages and analysing their outcomes, particular research problems were identified and improvements proposed. The use of a new adaptive radar interferogram filter, which minimises the loss of signal while still reducing the level of noise, was recommended. The validation of the filter algorithm was performed on simulated and real data sets. In order to determine the sensitivity of radar interferometry, that is, the minimum and maximum detectable deformation gradient, a new functional model has also been developed and tested. Finally, the wavelet approach for the advanced analysis of the interferometric phase related to small-scale surface deformation detection was examined.

8. 2 Research Outcomes

8.2.1 Application of InSAR for Small-Scale Deformation Detection

Satellite radar images acquired over two study areas were processed and analysed. However, for a direct assessment of the performance of InSAR in the detection of small-scale surface deformations, Silesia was selected as the more suitable. The primary aim of applying radar interferometry over the Silesia site was to determine the possibility of locating and assessing the magnitude of small-scale surface subsidence due to underground mining activities. Analysis of the resulting interferogram showed a number of locations where interferometric fringes, related to surface subsidence, occurred. The horizontal size of the detected deformations varied from several hundreds metres to a few kilometres, and the vertical magnitude ranged from a few centimetres up to a few decimetres. The circular or elliptical trough was found to be the most common shape of the deformations. However, more complex shapes occurred in areas affected by a superposition of several subsidences.

The associated interferometric phase noise was found to be the major factor reducing the reliability of the interferometric data. Thus, correct interpretation of the deformation signature was similarly compromised. In addition, the limited resolution of interferometry data (20 x 20 m) significantly undermined the use of InSAR in small-scale surface deformation detection studies.

The Leinster study area was recognised as highly stable. Therefore, it was mainly used to develop the functional model for determining the minimum and maximum detectable deformation gradient. However, the surface mine located in the centre of this study area has experienced some small-scale surface deformation at the crest of the open pit. The location and geometric distribution of deformation are well documented by terrestrial surveying comparisons between these distinct techniques were intended. However, poor archival data sets and the absence of new data prevented the validation of interferometry data against the findings of terrestrial surveying. Therefore, for periodical deformation monitoring, the current operational status of the satellite radar system (ERS-2) is unacceptable as it failed to provide new SAR data when prompted. Thus, in considering the application of radar interferometry for long-term deformation studies, it is recommended that the ESA SAR system be improved to ensure an uninterrupted supply of suitable data sets. Despite the fact that the only available data set did not reveal any deformation signatures around the investigation area, the analysis of the coherence map and differential interferogram did show some interesting results, which are listed below:

- Simple land classification, based on the coherence map, was possible as a result of the radar's ability to detect variations in soil moisture content.
- Intensive mining development between image acquisitions damaged the coherence and created large phase variations over the mining site area.
- Extreme influence of layover and shadow over open-cut mines and dumps would prevent deformation detection on steep slopes.
- The differential interferogram revealed a systematic phase trend (long wavelength) along the imaging scene that was associated with the satellite orbit error.

8.2.2 Improved Adaptive Radar Interferogram Filter

The interferometric phase filtering step was found to be an important determinant of the outcome of interferometry processing. Although, as filtering reduces noise in the interferogram, it does not necessarily enhance or recover the signal. This drawback was revealed by applying the Goldstein radar interferogram filter to the wrapped phase interferogram. By subtracting the filtered from the unfiltered interferogram, a residual systematic phase offset appears, which reflects the loss of resolution in the filtered phase. The magnitude of the offsets rises as the filter parameter alpha increases. In addition, the largest offsets occurred in areas of large curvature, which consistently aligned themselves in the direction of concavity. This phase offset reduces the magnitude of surface deformations and the heights of DEMs. In this thesis an improved radar interferogram phase filter has been proposed. This filter is based on a modification to the Goldstein filter and improves the quality of interferometry products. This novel approach converts the Goldstein filter parameter alpha into a parameter that is dependent on coherence, so that incoherent areas are filtered more than coherent areas. It has been shown that the new filter reduces phase offset as coherence increases. Therefore, this approach adapts the filter to the wrapped phase interferogram more effectively by ensuring that areas characterised by high coherence are not over filtered. Thus, it reduces the filter impact on the quality of DEMs and deformation maps. It has been shown that by filtering the interferometric phase related to small-scale surface deformation using the new radar interferogram filter, the magnitude of deformation signal was increased up to 40% in comparison to Goldstein filter while still reducing the level of noise.

8.2.3 New Functional Model for Determining Minimum and Maximum Detectable Deformation Gradient

According to the definition of maximum detectable deformation gradient, radar interferometry can detect a wide range of deformation gradients. However, radar interferometry suffers from the presence of noise in the interferogram phase measurement. In an effort to improve the existing definition, a new methodology was developed that not only led to the extension of the existing definition of maximum detectable deformation gradient but also defined the minimum detectable

deformation gradient. The resultant model includes the absolute value of coherence in its definition and therefore, describes the minimum and maximum detectable deformation gradient more realistically. Although the proposed model is very subjective, its application can still be beneficial. For example, it can be a valuable tool for the initial assessment of the suitability of radar interferometry for surface deformation detection. Thus, the information derived from this model can serve as a platform on which decisions of whether to use satellite radar interferometry to study a given surface deformation are made. This approach would be both cost- and time-effective.

8.2.4 Advanced Interferogram Analysis using a Wavelet Approach

There are numerous wavelet functions that could be potentially used to analyse the interferometric phase image. This study selected several continuous wavelet functions to test. The Halo wavelet was chosen as the most suitable for advanced interferogram analysis. The suitability of the wavelet was determined based on the fulfilment of certain selection criteria. The analysis of the cross-sections over the wavelet scalogram revealed a phase discontinuity within the wrapped phase interferogram. As the wavelet power spectrum corresponds directly to the spatial location of the signal, phase discontinuities can be used to determine the location and the number of interferometric fringes. Furthermore, information related to spatial extent of the deformation signal was determined by the wavelet energy distribution at the longest scale values. For deformation magnitude smaller than half of the wavelength the identification of the deformation extent was relatively easy. However, increasing level of noise and fringe density reduces the ability of wavelet to resolve phase discontinuity and the extent of the deformation signal.

8. 3 Recommendations for Future Research

There are many areas within radar interferometry that would benefit from continued research. Based on the findings of this research, the following recommendations for future work are proposed.

The research conducted has investigated the suitability of satellite radar interferometry for small-scale surface deformation detection, for instance, surface subsidence due to mining activities. As the studies show, there are limitations that have to be considered prior to the use of radar interferometry. One of the major concerns is the limited spatial resolution of the system. Therefore, hardware-based research that could improve the spatial resolution of interferometry products would be advantageous.

As interferometry products suffer from the effects of decorrelations, filtering techniques can improve phase statistics and therefore, the quality of DEMs and deformation maps. However, while filtering reduces noise, it does adversely affect the phase. Therefore, this thesis proposed the use of a new adaptive radar interferogram filter, which is reliant on coherence information and acts to minimise the loss of signal while still reducing the level of noise. The impact of the modified filter was demonstrated on both simulated and real data. Further evaluation of the effectiveness of the filter by use of ground truthing is a recommended research topic for further studies.

The methodology and functional model proposed in this research for the resolution of the minimum and maximum detectable deformation gradient, in terms of coherence, was developed for the ESA ERS-1/2 satellites. The same approach could also be applied to other SAR systems, such as JERS-1 and RADARSAT. Moreover, further studies could also produce a more general model for the establishment of the relationship between wavelength, pixel size and the coherence value.

As prior establishment of the coherence value is necessary for the use of the proposed model additional research is proposed to evaluate the coherence value based on land properties.

Finally, further investigation into the application of wavelet transforms to wrapped phase interferogram may enhance interferogram interpretation and even improve the capabilities of phase reconstruction. Since phase noise is spatially non-homogeneous, it damages only a part of the signal. Thus, reconstruction of the interferometric phase in this affected region would be appropriate. This would

significantly improve the robustness of the unwrapping algorithms and make automatic deformation detection possible. Therefore, wavelets could enhance the applicability of radar interferometry for deformation detection studies.

REFERENCES

Achim, A. and Bezerianos, A. (2003) SAR Image Denoising via Bayesian Wavelet Shrinkage Based on Heavy-Tailed Modeling, *IEEE Transactions on Geoscience and Remote Sensing,* Vol. 41, No. 8, pp. 1773-1784.

Addison, P.S. (2002) *The Illustrated Wavelet Transform Handbook*, Institute of Physics, London, 353p.

Amelung, F., Jónsson, S., Zebker, H. and Segall, P. (1999a) Prospects of Volcano Geodesy with ERS SAR Radar Interferometry, *Second International Workshop on ERS SAR Interferometry Fringe 99, Advancing ERS SAR Interferometry from Applications Towards Operations*, ESA Publications Division, Liège, Belgium, CD-ROM.

Amelung, F. and Bell, J.W. (2003) Interferometric Synthetic Aperture Radar Observations of the 1994 Double Spring Flat, Nevada, Earthquake (M5.9): Main Shock Accompanied by Triggered Slip on a Conjugate Fault, *Journal of Geophysical Research*, Vol. 108, No. B9, pp. 10.1-10.11.

Amelung, F., Jónsson, S., Zebker, H. and Segall, P. (2000) Widespread Uplift and 'trapdoor' Faulting on Galápagos Volcanoes Observed with Radar Interferometry, *Nature*, Vol. 407, pp. 993-996.

Amelung, F., Galloway, D.L., Bell, J.W., Zebker, H.A. and Laczniak, R.J. (1999b) Sensing the Ups and Downs of Las Vegas: InSAR Reveals Structural Control of Land Subsidence and Aquifer-System Deformation, *Geology*, Vol. 27, No. 6, pp. 483-486.

Arivazhagan, S. and Ganesan, L. (2003) Texture Segmentation Using Wavelet Transform, *Pattern Recognition Letters*, No. 24, pp. 3197-3203.

Bamler, R. and Hartl, P. (1998) Synthetic Aperture Radar Interferometry, Inverse Problems, No. 14, pp. R1-R54.

Bamler, R. and Just, D. (1993) Phase Statistics and Decorrelation in SAR Interferometry, *Proceedings of IGARSS'93*, Japan, pp. 980-984.

Bamler, R., Schättler, B., (1993) *SAR Geocoding: Data and Systems*, Schreier, G., (ed.), Wichmann, Karlsruhe, Germany, pp. 53-102.

Bao, M. (1999) Backscattering Change Detection in SAR Images Using Wavelet Techniques, *Proceedings of IGARSS'99*, Hamburg, Germany, pp. 1561-1563.

Baran, I., Stewart, M.P., Kampes, B. M., Perski, Z. and Lilly, P. (2003) A Modification to Goldstein Radar Interferogram Filter, *IEEE Transactions on Geoscience and Remote Sensing,* Vol. 41, No. 9, pp. 2114-2118.

Barmettler, A., Pasquali, P., Small, D. and Nüesch, D. (1996) Cross-Compatibility of ERS-SLC Products, *Proceedings of the 'Fringe 96' Workshop on ERS SAR Interferometry*, Zurich, Switzerland, Vol. 2, pp. 129-138.

Berardino, P., Borgia, A., Fornaro, G., Lanari, R., Sansosti, E. and Tesauro, M. (2000) Anticline Growing Beneath the Urban Area of Catania (Italy) Measured by SAR Interferometry, *Proceedings of IGARSS'00*, Hawaii, USA, pp. 2218-2220.

Berardino, P., Fornaro, G., Lanari, R., Sansosti, E. and Tesauro, M. (1999) Long Term Effects in Volcanic Areas Observed by Differential SAR Interferometry, *Second International Workshop on ERS SAR Interferometry Fringe 99, Advancing ERS SAR Interferometry from Applications Towards Operations*, ESA Publications Division, Liège, Belgium, CD-ROM.

Bezerra-Candeias, A.L., Mura, J.C., Dutra, L. and Moreira, J.R. (1995) Interferogram Phase Noise Reduction Using Morphological and Modified Median Filters, *Proceedings of IGARSS'95*, Firenze, Italy, pp. 166-168.

Bo, G., Dellepiane, S. and Beneventano, G. (1999) A Locally Adaptive Approach for Interferometric Phase Noise Reduction, *Proceedings of IGARSS'99*, Hamburg, Germany, pp. 264-266.

Bonforte, A., Ferretti, A., Prati, C., Puglisi, G. and Rocca, F. (2001) Calibration of Atmospheric Effects on SAR Interferograms by GPS and Local Atmosphere Models: First Results, *Journal of Atmospheric and Solar-Terrestrial Physics*, No. 63, pp. 1343-1357.

Borgeaud, M. and Wegmüller, U. (1996) On the Use of ERS SAR Interferometry for the Retrieval of Geo- and Bio-Physical Information, *Proceedings of the 'Fringe 96' Workshop on ERS SAR Interferometry*, Zurich, Switzerland, Vol. 1, pp. 83-94.

Buttkus, B. (2000) *Spectral Analysis and Filter Theory in Applied Geophysics*, Springer, Berlin, New York, 667p.

Campbell, J.B. (1996) *Introduction to Remote Sensing*, 2 ed., The Guilford Press, New York, USA, 622p.

Capes, R. (1999) Optimising the InSAR Data Supply Chain for Commercial Applications in Ground Displacement Detection, *Second International Workshop on ERS SAR Interferometry Fringe 99, Advancing ERS SAR Interferometry from Applications Towards Operations*, ESA Publications Division, Liège, Belgium, CD-ROM.

Carnec, C. and Delacourt, C. (1999) Three Years of Mining Subsidence Monitored by SAR Interferometry, near Gardanne, France, *Second International Workshop on ERS SAR Interferometry Fringe 99, Advancing ERS SAR Interferometry from Applications Towards Operations*, ESA Publications Division, Liège, Belgium, CD-ROM.

Chen, C.W. and Zebker, H.A. (2001) Two-Dimensional Phase Unwrapping With Use of Statistical Models for Cost Functions in Nonlinear Optymization, *Journal of the Optical Society of America A*, Vol. 18, pp. 338-351.

Chen, C.W. and Zebker, H.A. (2000) Network Approaches to Two-Dimensional Phase Unwrapping: Intractability and Two New Algorithms, *Journal of the Optical Society of America A*, Vol. 17, pp. 401-414.

Closa, J. (1998) The Influence of Orbit Precision in the Quality of ERS SAR Interferometric Data, *http://earth.esa.int/rootcollection/sysutil/ORB_QL.html*, Accessed: 26.11.2003.

Cohen, D.A., Deverel, S.J. and Johnson, L.A. (1998) Feasibility Study of Differential SAR Interferometry for Subsidence Monitoring in the Sacramento-San Joaquin Delta, *Proceedings of IGARSS'98*, Seattle, USA, pp. 1629-1631.

Cumming, I., Valero, J-L., Vachon, P., Mattar, K., Geudtner, D. and Gray, L. (1996) Glacier Flow Measurements with ERS Tandem Mission Data, *Proceedings of the 'Fringe 96' Workshop on ERS SAR Interferometry*, Zurich, Switzerland, Vol. 1, pp. 353-362.

Curran, P.J. (1985) *Principles of Remote Sensing*, John Wiley & Sons, Inc., Hong Kong, 282p.

Dallard, T. and Spedding, G.R. (1993) 2-D Wavelet Transforms: Generalisation of the Hardy Space and Application to Experimental Studies, *European Journal of Mechanics*, *B/Fluids*, Vol. 12, No. 1, pp. 107-134.

Dammert, P.B.G., Leppäranta, M. and Askne, J. (1997) Sea Ice Displacement Measurement by ERS-1 SAR Interferometry, *Proceedings of the Third ERS Symposium*, Florence, http://earth.esa.int/symposia//papers/dammert/, Accessed: 26.11.2003.

Debao, M., Wugao, L. and Zhongxin, L. (1999) A New Method to Estimate Doppler Parameters for Synthetic Aperture Radar in Target Echo Signals, *Proceedings of IGARSS'99*, Hamburg, Germany, pp. 521-523.

Delft Getorb Software (2002) *ERS Precise Orbit Determination: Tools and Software, http://www.deos.tudelft.nl/ers/precorbs/tools/,* Accessed: 26.11.2003.

Delft Precise Orbits Service (2002) *ERS Precise Orbit Determination*, http://www.deos.tudelft.nl/ers/precorbs/, Accessed: 26.11.2003.

Desnos, Y.L., Buck, C., Guijarro, J., Levrini, G., Suchail, J.L., Torres, R., Laur, H., Closa, J. and Rosich, B. (2000) The Envisat Advanced Synthetic Aperture Radar System, *Proceedings of IGARSS'00*, Hawaii, USA, pp. 1171-1173.

Ding, X., Montgomery, S.B., Tsakiri, M., Swindells, C.F. and Jewell, R.J. (1998) Integrated Monitoring Systems for Open Pit Wall Deformation, *Meriwa Report No. 186*, Australian Centre for Geomechanics, Perth, Australia, 114p.

Dzurisin, D. (2003) A Comprehensive Approach to Monitoring Volcano Deformation as a Window on the Eruption Cycle, *Reviews of Geophysics*, Vol. 41, No. 1, pp. 1.1-1.15.

Ehrismann, J., Marco van der Kooij and Hulshof, B. (1999) Commercial Application of SAR Interferometry for Change Detection, *Second International Workshop on ERS SAR Interferometry Fringe 99, Advancing ERS SAR Interferometry from Applications Towards Operations*, ESA Publications Division, Liège, Belgium, CD-ROM.

Engdahl, M. and Hyyppä, J. (2000) Temporal Averaging of Multitemporal ERS-1/2 Tandem InSAR Data, *Proceedings of IGARSS'00*, Hawaii, USA, pp. 2224-2226.

ESA Descw (2002) *Off-line Catalogue and Image Browser Home Page*, http://earth.esa.int/descw, Accessed: 26.11.2003.

ESA Service (2002) *ERS Mission Home Page*, http://earth.esa.int/missions/, Accessed: 26.11.2003.

Farge, M. (1992) Wavelet Transforms and Their Applications to Turbulence, *Annual Reviews, Fluid Mechanic*, No. 24, pp. 395-457.

Featherstone, W.E. and Alexander, K. (1996) An Analysis of GPS Height Determination in Western Australia, *The Australian Surveyor*, Vol. 41, No. 1, pp. 29-34.

Featherstone, W.E., Kirby, J.F., Kearsley, A.H.W., Gilliland, J.R., Johnston, G.M., Steed, J., Forsberg, R. and Sideris, M.G. (2001) The AUSGeoid98 Geoid Model of Australia: Data Treatment, Computations and Comparisons with GPS-levelling Data, *Journal of Geodesy*, Vol. 75, pp. 313-330.

Feigl, K.L., Gasperi, J., Sigmundsson, F. and Rigo, A. (1999) Crustal Deformation Near Hengill Volcano, Iceland 1993-1998: Coupling Between Volcanism and Faulting Inferred from Elastic Modelling of Satellite Radar Interferograms, *Second International Workshop on ERS SAR Interferometry Fringe 99, Advancing ERS SAR Interferometry from Applications Towards Operations*, ESA Publications Division, Liège, Belgium, CD-ROM.

Ferretti, A., Prati, C. and Rocca, F. (1999a) Permanent Scatters in SAR Interferometry, *Proceedings of IGARSS'99*, Hamburg, Germany, pp. 1528-1530.

Ferretti, A., Prati, C. and Rocca, F. (1999b) Multibaseline InSAR DEM Reconstruction: The Wavelet Approach, *IEEE Transactions on Geoscience and Remote Sensing*, Vol. 37, No. 2, pp. 705-715.

Ferretti, A., Prati, C. and Rocca, F. (2000) Nonlinear Subsidence Rate Estimation Using Permanent Scatters in Differential SAR Interferometry, *IEEE*

Transactions on Geoscience and Remote Sensing, Vol. 38, No. 5, pp. 2202-2212.

Ferretti, A., Prati, C. and Rocca, F. (2001) Permanent Scatters in SAR Interferometry, *IEEE Transactions on Geoscience and Remote Sensing*, Vol. 39, No. 1, pp. 8-20.

Fitch, J.P. (1988) *Synthetic Aperture Radar*, Springer-Verlag, New York, USA, 170p.

Fornaro, G. and Sansosti, E. (1999) A Two-Dimensional Region Growing Least Squares Phase Unwrapping Algorithm for Interferometric SAR Processing, *IEEE Transactions on Geoscience and Remote Sensing*, Vol. 37, No. 5, pp. 2215-2226.

Franceschetti, G. and Lanari, R. (1999) *Synthetic Aperture Radar Processing*, CRS Press, New York, USA, 307p.

Fruneau, B., Rudant, J-P., Obert, D. and Raymond, D. (1999) Small Displacement Detected by SAR Interferometry on the City of Paris (France), *Proceedings of IGARSS'99*, Hamburg, Germany, pp. 1943-1945.

Fruneau, B., Delacourt, Ch. and Achache, J. (1996) Observation and Modelling of the Saint-Etienne-de-Tinée Landslide Using SAR Interferometry, *Proceedings of the 'Fringe 96' Workshop on ERS SAR Interferometry*, Zurich, Switzerland, Vol. 1, pp. 21-27.

Geoscience Australia (2003), Mapping Section, http://www.agso.gov.au/map/, *Accessed: 26.11.2003.*

Gabriel, A.K., Goldstein, R.M. and Zebker, H.A. (1989) Mapping Small Elevation Changes Over Large Areas: Differential Radar Interferometry, *Journal of Geophysical Research*, Vol. 94, No. B7, pp. 9183-9191.

Gabriel, A.K. and Goldstein, R.M. (1988) Crossed Orbit Interferometry: Theory and Experimental Results from SIR-B, *International Journal of Remote Sensing*, Vol. 9, No. 5, pp. 857-872.

Ge, L., Chen, H.Y., Han, S. and Rizos, Ch. (2001a) Integrated GPS and Interferometric SAR Techniques for Highly Dense Crustal Deformation Monitoring, *Proceedings of the 14th International Technical Meeting of the Satellite Division of the U.S. Institute of Navigation*, Omni Press, 11-14 September, Salt Lake City, Utah, USA, CD-ROM.

Ge, L., Han, S. and Rizos, C. (2000a) Interpolation of GPS Results Incorporating Geophysical and InSAR Information, *Earth, Planets and Space*, Vol. 52, No. 11, pp. 999-1002.

Ge, L., Han, S. and Rizos, C. (2000b) The Double Interpolation and Double Prediction (DIDP) Approach for InSAR and GPS Integration, *19th*

International Society of Photogrammetry & Remote Sensing Congress, Amsterdam, Holland, pp. 205-212.

Ge, L., Rizos, Ch., Omura, M. and Kobayashi, S. (2001b) Integrated Space Geodetic Techniques for Monitoring Ground Subsidence due to Underground Mining, *5th International Symposium on Satellite Navigation Technology and Applications*, Canberra, Australia, CD-ROM.

Ge, L., Rizos, C., Han, S. and Zebker, H. (2001c) Mine Subsidence Monitoring Using the Combined InSAR and GPS Approach, *10th FIG International Symposium on Deformation Measurements*, Orange, California, CD-ROM.

Ghiglia, D.C. and Pritt, M.D. (1998) *Two-Dimensional Phase Unwrapping, Theory, Algorithms, and Software*, John Wiley & Sons, Inc., New York, USA, 493p.

GMT (2004) The Generic Mapping Tool, http://gmt.soest.hawaii.edu/, Accessed: 14.04.2004.

Goldstein, R.M., Engelhardt, H., Kamp, B. and Frolisch, R.M. (1993) Satellite Radar Interferometry for Monitoring Ice Sheet Motion: Application to an Antarctic Ice Stream, *Science*, Vol. 141, pp. 1171-1172.

Goldstein, R.M. and Werner, C.L. (1998) Radar Interferogram Filtering for Geophysical Applications, *Geophysical Research Letters*, Vol. 25, No. 21, pp. 4035-4038.

Goldstein, R.M. and Werner, C.L. (1997) Radar Ice Motion Interferometry, *Proceedings of the Third ERS Symposium*, Florence, Italy, Vol.2, pp. 969-972.

Goldstein, R.M., Zebker, H.A. and Werner C.L. (1988) Satellite Radar Interferometry: Two-Dimensional Phase Unwrapping, *Radio Science*, Vol. 23, No. 4, pp. 713-720.

Graham, L.C. (1974) Synthetic Interferometer Radar for Topographic Mapping, *Proceedings of the IEEE*, Vol. 62, No. 6, pp. 763-768

Gray, A.L., Mattar, K.E. and Sofko, G. (2000) Influence of Ionospheric Electron Density Fluctuations on Satellite Radar Interferometry, *Geophysical Research Letters*, Vol. 27, No. 10, pp. 1451-1454.

Gren, K. and Popiołek, E. (1999) *Wpływ Exploatacji na Powierzchnie i Górotwór [Eng. The influence of Underground Mining on the Surface and Formation]*, AGH, Kraków, Poland, 198 p.

Grossmann, A. and Morlet, J. (1984) Decomposition of Hardy Functions into Square Integrable Wavelets of Constant Shape, *SIAM Journal Mathematic Annual*, Vol. 15, pp. 723-736.

Guarnieri, A.M. and Rocca, F. (1999) Combination of Low- and High-Resolution SAR Images for Differential Interferogram, *IEEE Transactions on Geoscience and Remote Sensing*, Vol. 37, No. 4, pp. 2035-2049.

Haarpainter, J., Kergomard, C., Gascard, J-C. and Haugan, P.M. (2000) Sea Ice Dynamics Observed by ERS-2 SAR Imagery and ARGOS Buoys in Storfjorden, Svalbard, *Proceedings of IGARSS'00*, Hawaii, USA, pp. 467-469.

Hall, D.K. (1998) Remote Sensing of Snow and Ice Using Image Radar, in: *Principles and Applications of Imaging Radar: Manual of Remote Sensing*, 3 ed., Vol. 2, Henderson F. M. and Levis, A. J. (ed.), John Wiley & Sons, Inc., New York, USA, pp. 677-703.

Hanssen, R.F. (2001) *Radar Interferometry Data Interpretation and Error Analysis*, Kluwer Academic, Dordrecht, 308 p.

Hanssen, R.F. and Bamler, R. (1999) Evaluation of Interpolation Kernels for SAR Interferometry, *IEEE Transactions on Geoscience and Remote Sensing*, Vol. 37, No. 1 pp. 318-321.

Hanssen, R.F. and Feijt, A. (1996) A first Quantitative Evaluation of Atmospheric Effects on SAR Interferometry, *Proceedings of the 'Fringe 96' Workshop on ERS SAR Interferometry*, Zurich, Switzerland, Vol. 1, pp. 277-282.

Hanssen, R.F., Weckwerth, T.M., Zebker, H.A. and Klees, R. (1999) High-Resolution Water Vapor Mapping from Interferometric Radar Measurements, *Science*, Vol. 283, pp. 1297-1299.

Harris, R. (1987) *Satellite Remote Sensing: An Introduction*, Routledge & Kegan Paul Inc., New York, USA, 220p.

Haynes, M., Capes, R., Lawrence, G., Smith, A., Shilston, D. and Nicholls, G. (1997) Major Urban Subsidence Mapped by Differential SAR Interferometry, *Proceedings of the Third ERS Symposium*, Florence, http://earth.esa.int/florence/papers/capes/, Accessed: 26.11.2003.

Henderson F. M. and Levis, A. J. (1998) *Principles and Applications of Imaging Radar: Manual of Remote Sensing*, 3 ed., Vol. 2, John Wiley & Sons, Inc., New York, USA, 750p.

Holloway, R.D. (1988) *The Integration of GPS Heights into the Australian Height Datum*, Unisurv S33, School of Surveying, University of New South Wales, 151p.

Hopfield, H.S. (1971) Tropospheric Effect on Electromagnetically Measured Range: Prediction from Surface Data, *Radio Science*, Vol. 6, No. 3, pp. 357-367.

Hubig, M. (1999) A Maximum Likelihood a Priori Filter for Interferometric Phase, *Proceedings of IGARSS'99*, Hamburg, Germany, pp. 482-484.

Hutchinson, M. (ed) (2001) *User Guide for the GEODATA 9 SECOND Digital Elevation Model of Australia (2 ed.),* Australian Surveying and Land Information Group and Australian National University, Canberra.

Jin, M.Y. (1996) Optimal Range and Doppler Centroid Estimation for a ScanSAR System, *IEEE Transactions on Geoscience and Remote Sensing*, Vol. 34, No. 2 pp. 479-488.

Just, D. and Bamler, R. (1994) Phase Statistics of Interferograms with Applications to Synthetic Aperture Radar, *Applied Optics*, Vol. 33, No. 20, pp. 4361-4368.

Kampes, B. (2000) *Delft Object-Oriented Radar Interferometric Software, User's Manual and Technical Documentation*, Delft Institute for Earth-Oriented Space Research - Delft University of Technology, The Netherlands, 134p.

Kampes, B. and Usai, S. (1999) Doris: the Delft Object-Oriented Radar Interferometric Software, *2nd International Symposium on Operationalization of Remote Sensing*, Enschede, The Netherlands.

Kirby, J. (2003) *2D Wavelet Transform Routines*, Curtin University of Technology, The Western Australian Centre for Geodesy, personal communications.

Kobayashi, S., Fujii, N. and Okubo, S. (1999) Detection of Volcano Deformations and Coseismic Movements Using JERS-1 L-Band SAR Differential Interferometry: Combination with Other Geodetic Measurements, *Proceedings of IGARSS'99*, Hamburg, Germany, pp. 800-802.

Lanari, R., Lundgren, P. and Sansosti, E. (1998) Dynamic Deformation of Etna Volcano Observed by Satellite Radar Interferometry, *Geophysical Research Letters*, Vol. 25, No. 10, pp. 1541-1544.

Lee, H. and Liu, J.G. (1999) Spatial Decorrelation due to Topography in the Interferometric SAR Coherence Imagery, *Proceedings of IGARSS'99*, Hamburg, Germany, pp. 485-487.

Lee, J-S., Hoppel, K.W., Mango, S.A. and Miller, A.R. (1994) Intensity and Phase Statistics of Multilook Polarimetric and Interferometric SAR Imagery, *IEEE Transactions on Aerospace and Electronic System*, Vol. 32, No. 5, pp. 1017-1028.

Lee, J-S., Papathanassiou, P., Ainsworth, T.L., Grunes, R. and Reigber, A. (1998) A New Technique for Noise Filtering of SAR Interferometric Phase Images, *IEEE Transactions on Geoscience and Remote Sensing*, Vol. 36, No. 5, pp. 1456-1464.

Legg, Ch.A. (1994) *Remote Sensing and Geographic Information Systems: Geological Mapping, Mineral Exploration and Mining,* John Wiley & Sons, Inc., Chichester, England, 166p.

Lillesand, T.M. and Kiefer R.W. (2000) *Remote Sensing and Image Interpretation*, 4 ed., John Wiley & Sons, Inc., New York, USA, 724p.

Lilly, P.A. (2000) The Minimum Total Cost Approach to Optimum Pit Slope Design, *Proceedings of International Symposium on Mine Planning and Equipment Selection,* Athens, Greece, pp. 77-82.

Lintz, J. and Simonett, D.S. (1976) *Remote Sensing of Environment*, Addison-Wesley, Massachusetts, USA.

Loffeld, O. and Krämer, R. (1999) Phase Unwrapping for SAR Interferometry, *Proceedings of IGARSS'99*, Hamburg, Germany, pp. 1715-1717.

Logan, A.S., Villaescusa, E., Stampton V.R., Struthers, M.A. and Bloss, M.L. (1993) Geotechnical Instrumentation and Ground Behaviour Monitoring at Mount Isa, in: *Geotechnical Instrumentation and Monitoring in Open Pit and Underground Mining*, Szwedzicki, T. (ed.), A. A. Balkema, Rotterdam, Netherlands, pp. 321-329.

Loubser, P. (1993) Detection of Abandoned Mine Workings at KCGM's Open Pit Operations, *Geotechnical Instrumentation and Monitoring in Open Pit and Underground Mining*, Szwedzicki, T. (ed.), A. A. Balkema, Rotterdam, Netherlands, pp. 331-338.

Louet, J. and Bruzzi, S. (1999) Envisat Mission & System, *Proceedings of IGARSS'99*, Hamburg, Germany, pp. 1680-1682.

Madsen, S.N. (1989) Estimating the Doppler Centroid of SAR Data, *IEEE Transactions on Aerospace and Electronic System*, Vol. 25, No. 2, pp. 134-140.

Madsen, S.N., Mohr, J.J. and Reeh, N. (1999) Mapping Greenland by ERS-1/2 InSAR for Mass Ice balance and Dynamics Study, *Second International Workshop on ERS SAR Interferometry Fringe 99, Advancing ERS SAR Interferometry from Applications Towards Operations*, ESA Publications Division, Liège, Belgium, CD-ROM.

Mann, D., Freymueller, J. and Lu, Z. (2002) Deformation Associated with the 1997 Eruption of Okmok Volcano, Alaska, *Journal of Geophysical Research*, Vol. 107, No. B4, pp. 7.1-7.13.

Martinez, J.M., Beaudoin, A., Wegmüller, U. and Strozzi, T. (1998) Classification of Land-Cover and Forest Types Using Multidate ERS Tandem Data Acquired over Hilly Terrain, *Proceedings of IGARSS'98*, Seattle, USA, pp. 1809-1811.

Massonnet, D., Adragna, F. and Rossi, M. (1994) CNES General-Purpose SAR Correlator, *IEEE Transactions on Aerospace and Electronic System*, Vol. 32, No. 3, pp. 636-643.

Massonnet, D., Briole, P. and Arnaud, A. (1995) Deflation of Mount Etna Monitored by Spaceborne Radar Interferometry, *Nature*, Vol. 375, pp. 567-570.

Massonnet, D., Rossi, M., Carmona, C., Adragna, F., Peltzer, G., Feigl, K. and Rabaute, T. (1993) The Displacement Field of the Landers Earthquake Mapped by Radar Interferometry, *Nature*, Vol. 364, pp. 138-142.

Massonnet, D. and Feigl, K.L. (1998) Radar Interferometry and its Application to Changes in the Earth's Surface, *Reviews of Geophysics*, Vol. 36, No. 4, pp. 441-500.

Matlab (2004) The Language of Technical Computing http://www.mathworks.com/products/matlab/, Accessed: 14.04.2004.

Mikhail, E.M., Bethel, J.S. and McGlone, J.Ch. (2001) *Introduction to Modern Photogrammetry*, John Wiley & Sons, Inc., New York, USA, 479p.

Mohr, J.J. and Madsen, S.N. (1996) Multi-pass Interferometry for Studies of Glacier Dynamics, *Proceedings of the 'Fringe 96' Workshop on ERS SAR Interferometry*, Zurich, Switzerland, Vol. 1, pp. 345-352.

Morley, J., Muller, J-P. and Madden, S. (1996) Wetland Monitoring in Mali Using SAR interferometry, *Proceedings of the 'Fringe 96' Workshop on ERS SAR Interferometry*, Zurich, Switzerland, Vol. 1, pp. 151-166.

Nakagawa, H., Murakami, M., Fujiwara, S. and Tobita, M. (2000) Land Subsidence of the Northern Kanto Plains Caused by Ground Water Extraction Detected by JERS-1 SAR Interferometry, *Proceedings of IGARSS'00*, Hawaii, USA, pp. 2233-2235.

Oliver, Ch. and Quegan, S. (1998) *Understanding Synthetic Aperture Radar Images*, Artech House, Boston, USA, 479p.

Olmsted, C., (1993) *Alaska SAR Facility, Scientific SAR User's Guide*, Fairbanks, Alaska, 53p.

Peltzer, G. and Rosen, P. (1995) Surface Displacement of the 17 May 1993 Eureka Valley, California, Earthquake Observed by SAR Interferometry, *Science*, Vol. 268, pp. 1333-1336.

Peltzer, G., Rosen, P., Rogez, F. and Hudnut, K. (1996) Postseismic Rebound in Fault Step-Over Caused by Pore Fluid Flow, *Science*, Vol. 273, pp. 1202-1204.

Perrier, V., Philipovitch, T. and Basdevant, C. (1995) Wavelet Spectra Compared to Fourier Spectra, *Journal of Mathematical Physics*, Vol. 36, pp. 1506-1519.

Perski, Z. (2000) The Interpretation of ERS-1 and ERS-2 InSAR Data for the Mining Subsidence Monitoring in Upper Silesian Coal Basin, Poland, *International Archives of Photogrammetry and Remote Sensing*, Vol. 33, pp. 1137-1141.

Perski, Z. (1999) ERS InSAR data for Geological Interpretation of Mining Subsidence in Upper Silesian Coal Basin in Poland, *Second International Workshop on ERS SAR Interferometry Fringe 99, Advancing ERS SAR Interferometry from Applications Towards Operations*, ESA Publications Division, Liège, Belgium, CD-ROM.

Perski, Z. (1998) The Test of Applicability of Land Subsidence Monitoring by InSAR ERS-1 and ERS-2 in the Coal Mine Damaged Region (Upper Silesia), *International Archives of Photogrammetry and Remote Sensing*, Vol. 32, No. 7, pp. 555-558.

Perski, Z. and Jura, D. (1999) ERS SAR Interferometry for Land Subsidence Detection in Coal Mining Areas, *Earth Observation Quarterly*, No. 63, pp. 25-29.

Popiołek, E., Hejmanowski, R., Krawczyk, A. and Perski, Z. (2002) Application of Satellite Radar Interferometry to the Examination of the Areas of Mining Exploitation, *Surface Mining*, Braunkohle and Other Minerals, Vol. 54, No. 1, pp. 74-82.

Prati, C. and Rocca, F. (1990) Limits to the Resolution of Elevation Maps from Stereo SAR Images, *International Journal of Remote Sensing*, Vol. 11 No. 12, pp. 2215-2235.

Price, E.J. (1999) Coseismic and Postseismic Deformations Associated With the 1992 Landers California, Earthquake Measured by Synthetic Aperture Radar Interferometry, *PhD Thesis*, University of California, San Diego, USA, 160p.

Rack, W., Rott, H., Nagler, T. and Skvarca, A. (1998) Areal Changes and Motion of Northern Larsen Ice Shelf, Antarctic Peninsula, *Proceedings of IGARSS'98*, Seattle, USA, pp. 2243-2245.

Rees, G. (1999) *The Remote Sensing Data Book*, Cambridge University Press, Cambridge, UK, 262p.

Reeves, B., Homer, J., Stickley, G., Noon, D. and Longstaff, I.D. (1999) Spatial Vector Filtering to Reduce Noise in Interferometric Phase images, *Proceedings of IGARSS'99*, Hamburg, Germany, pp. 260-263.

Reeves, B.A., Stickley, G.F., Noon, D.A. and Longstaff, I.D. (2000) Developments in Monitoring Mine Slope Stability Using Radar Interferometry, *Proceedings of IGARSS'00*, Hawaii, USA, pp. 2325-2327.

Refice, A., Bovenga, F., Wasowski, J. and Guerriero, L. (2000) Use of InSAR Data for Landslide Monitoring: a Case Study from Southern Italy, *Proceedings of IGARSS'00*, Hawaii, USA, pp. 2504-2506.

Rocca, F., Prati, C. and Ferretti, A. (2002) *An Overview of SAR Interferometry*, http://earth.esa.int/florence/program-details/speeches/rocca-et-al/, Accessed: 26.11.2003.

Rodriguez, E. and Martin, J.M. (1992) Theory and Design of Interferometric Synthetic Aperture Radar, *IEE Proceedings-F; Radar and Signal Processing*, Vol. 139, No. 2, pp. 147-159.

Rott, H. and Siegel, A. (1999) Analysis of Mass Movements in Alpine Terrain by Means of SAR Interferometry, *Proceedings of IGARSS'99*, Hamburg, Germany, pp. 1993-1936.

Sansosti, E., Lanari, R. and Lundgren, P. (1998) Dynamic Deformation of Etna Volcano Observed by Satellite Radar Interferometry, *Proceedings of IGARSS'98*, Seattle, USA, pp. 1370-1372.

Scharroo, R. and Visser, P. (1998) Precise Orbit Determination and Gravity Field Improvement for the ERS Satellites, *Journal of Geophysical Research*, Vol. 103, No. C4, pp. 8113-8127.

Schmidt, A.A. and Bürgmann, R. (2003) Time-Dependent Land Uplift and Subsidence in the Santa Clara Valley, California, from a Large Interferometric Synthetic Aperture Radar Data Set, *Journal of Geophysical Research*, Vol. 108, No. B9, pp. 4.1-4.13.

Seymour, M.S. and Cumming, I.G. (1994) Maximum Likelihood Estimator for SAR Interferometry, *Proceedings of IGARSS'94*, Pasadena, CA, USA, pp. 2272-2275.

Snaphu (2004) Statistical-Cost, Network-Flow Algorithm for Phase Unwrapping, http://www-star.stanford.edu/sar_group/snaphu/, Accessed: 14.04.2004.

Spagnolini, U., (1995) 2-D Phase Unwrapping and Instantaneous Frequency Estimation, *IEEE Transactions on Geoscience and Remote Sensing*, Vol. 33, No. 3, pp. 579-589.

Stow, R. (1996) Application of SAR Interferometry to the Imaging and Measurement of Neotectonic Movement Applied to Mining and other Subsidence/Downwarp Modelling, *Proceedings of the 'Fringe 96' Workshop on ERS SAR Interferometry*, Zurich, Switzerland, Vol. 2, pp. 9-13.

Stow, R., Reddish, D., Wright, P., Peace, S., Doyle, G.S., Wilkinson, A.J. and Inggs, M.R. (1999) Geotechnical Applications of SAR Interferometry, *Second International Workshop on ERS SAR Interferometry Fringe 99, Advancing ERS SAR Interferometry from Applications Towards Operations*, ESA Publications Division, Liège, Belgium, CD-ROM.

Stow, R.J. and Wright, P. (1997) Mining Subsidence Land Surveying by SAR Interferometry, *Proceedings of the Third ERS Symposium*, Florence, http://earth.esa.int/florence/papers/stowetal/387c.htm, Accessed: 26.11.2003.

Stramaglia, S., Nico, G., Lovergine, F. and Guerriero, L. (1999) InSAR Phase Unwrapping Algorithm Based on Mean-Field Theory, *Proceedings of IGARSS'99*, Hamburg, Germany, pp. 1345-1347.

Stramondo, S., Salvi, S., Tesauro, M., Cocco, M., Lanari, R. and Anzidei, M. (1999) SAR Differential Interferometry (DInSAR) Applied to the 1997 Umbria-Marche, Italy, Seismic Sequence: Comparison with GPS and Modelling of the Coseismic Displacement Pattern, *Second International Workshop on ERS SAR Interferometry Fringe 99, Advancing ERS SAR Interferometry from Applications Towards Operations*, ESA Publications Division, Liège, Belgium, CD-ROM.

Strozzi, T., Wegmüller, U., Werner, Ch. and Wiesmann, A. (2000) Measurement of Slow Uniform Surface Displacement with mm/year Accuracy, *Proceedings of IGARSS'00*, Hawaii, USA, pp. 2239-2241.

Strozzi, T. and Wegmüller, U. (1999) Land Subsidence in Mexico City Mapped by ERS Differential SAR Interferometry, *Proceedings of IGARSS'99*, Hamburg, Germany, pp. 1940-1942.

Strozzi, T. and Wegmüller, U. (1998) A Forest Map of Part of Switzerland, *Proceedings of IGARSS'98*, Seattle, USA, pp. 1802-1804.

Sveinsson, J.R. and Benediktsson, J.A. (1996) Speckle Reduction and Enhancement of SAR Images in the Wavelet Domain, *Proceedings of IGARSS'96,* Nebraska, Lincoln, pp. 63-66.

Tarchi, D., Casagli, N., Fanti, R., Leva, D.D., Luzi, G., Pasuto, A., Pieraccini, M. and Silvano, S. (2003) Landslide Monitoring by Using Ground-based SAR Interferometry: An Example of Application to the Tessina Landslide in Italy, *Engineering Geology*, No. 68, pp. 15-30.

Tarchi, D., Rudolf, H., Luzi, G., Chiarantini, L., Coppo, P. and Sieber, A.J. (1999) SAR Interferometry for Structural Changes Detection: A Demonstration Test on a Dam, *Proceedings of IGARSS'99*, Hamburg, Germany, pp. 1522-1524.

Thompson, P.W. and Cierlitza, S. (1993) Identification of a Slope Failure Over a Year before Final Collapse Using Multiple Monitoring Methods, in: *Geotechnical Instrumentation and Monitoring in Open Pit and Underground Mining*, Szwedzicki, T. (ed.), A. A. Balkema, Rotterdam, Netherlands, pp. 491-511.

Timmen, L., Ye, X., Reigber, Ch., Hartmann, R., Fiksel, T., Winzer, W. and Knoch-Weber, J. (1996) Monitoring of Small Motions in Mining Areas by SAR Interferometry, *Proceedings of the 'Fringe 96' Workshop on ERS SAR Interferometry*, Zurich, Switzerland, Vol. 2, pp. 5-8.

Tokunaga, M. and Thuy, V.T. (2000) Estimation of Deformation Volume in Mt. Mayon in Philippine using Differential SAR Interferometry by using EERS Tandem, *Proceedings of IGARSS'00*, Hawaii, USA, pp. 2242-2244.

Tough, R.J.A., Blacknell, D. and Quegan, S. (1995) A Statistical Description of Polarimetric and Interferometric Synthetic Aperture Radar, *Proceedings of the Royal Society London Series A*, Vol. 449, pp. 567-589.

Vadon, H. and Massonnet, D. (2000) Earthquake Displacement Fields Mapped by Very Precise Correlation. Complementarity with Radar Interferometry, *Proceedings of IGARSS'00*, Hawaii, USA, pp. 2700-2702.

Wavelab (2003) WaveLab 802 Software for Matlab 5.x, http://www-stat.stanford.edu/~wavelab/, Accessed: 26.11.2003.

Wegmüller, U., Strozzi, T., Werner, Ch., Wiesmann, A., Benecke, N. and Spreckels, V. (2000) Monitoring of Mining-Induced Surface Deformation in the Ruhregebiet (Germany), *Proceedings of IGARSS'00*, Hawaii, USA, pp. 2771-2773.

Wegmüller, U., Strozzi, T. and Werner, Ch. (1999) Validation of ERS Differential SAR Interferometry for Land Subsidence Mapping: the Bologna Case Study, *Proceedings of IGARSS'99*, Hamburg, Germany, pp. 1131-1133.

Wegmüller, U., Strozzi, T. and Werner, Ch. (1998) Land Subsidence in the Po River Valley, Italy, *Proceedings of IGARSS'98*, Seattle, USA, pp. 1376-1378.

Weng, H. and Lau, K.M. (1994) Wavelets, Period Doubling, and Time-Frequency Localization With Application to Organization of Convection Over the Tropical Western Pacific, *Journal of Atmospheric Science,* Vol. 51, pp. 2523-2541.

Williams, S., Bock, Y. and Fang, P. (1998) Integrated Satellite Interferometry: Tropospheric Noise, GPS Estimates and Implications for Interferometric Synthetic Aperture Radar Products, *Journal of Geophysical Research*, Vol. 103, No. B11, pp. 27051-27067.

WMC Leinster (2002) Western Mining Corporation, Leinster Nickel Operation, *http://www.wmc.com.au/about/ourbusiness/nickel.htm#leinster, Accessed: 26.11.2003.*

Wodyński, A. and Kocot, W. (2000) Analysis of Structure Resistance of Typical Urban and Suburban Buildings to Mining Effects, *11th International Congress of the International Society for Mine Surveying*, Krakow, Poland, Vol. 1, pp. 517-526.

Wu, B-F. and Su, Ch-Y. (2000) Low Computational Complexity Enhanced Zerotree Coding for Wavelet-Based Image Compression, *Signal Processing: Image Communication*, No. 16, pp.401-411.

Xiong, X., Zhao, S. and Wen, F. (1995) Detection of the Doppler Frequency Shift in Acoustic Remote Sensing Systems, *IEEE Transactions on Geoscience and Remote Sensing*, Vol. 33, No. 3, pp. 523-527.

Yonezawa, Ch. and Takeuchi, S. (2000) Land Subsidence Detection Using Long Interval ERS/SAR Data Pairs, *Proceedings of IGARSS'00*, Hawaii, USA, July, pp. 1539-1541.

Zebker, H.A. and Goldstein, R.M. (1986) Topographic Mapping from Interferometric Synthetic Aperture Radar Observations, *Journal of Geophysical Research*, Vol. 91, No. B5, pp. 4993-4999.

Zebker, H.A., Rosen, P.A., Goldstein, R.M, Gabriel, A and Werner, C.L. (1994) On the Derivation of Coseismic Displacement Fields Using Differential Radar Interferometry: The Landers Earthquake, *Journal of Geophysical Research*, Vol. 99, No. B10, pp. 19617-19634.

Zebker, H.A., Rosen, P.A. and Hensley, S. (1997) Atmospheric Effects in Interferometric Synthetic Aperture Radar Surface Deformation and Topographic Maps, *Journal of Geophysical Research*, Vol. 102, No. B4, pp. 7547-7563.

Zebker, H.A. and Villasenor, J. (1992) Decorrelation in Interferometric Radar Echoes, *IEEE Transactions on Geoscience and Remote Sensing*, Vol. 30, No. 5, pp. 950-959.

Zeng, Q. and Ohkura, H. (2000) Observing the Ground Surface Deformation Before and After Taiwan Chichi Earthquake by JERS 1 and ERS 2 Differential SAR Analysis, *Proceedings of IGARSS'00*, Hawaii, USA, pp. 2251-2253.